$\Upsilon(1S)$ polarization measurement in PbPb collisions at $\sqrt{s_{NN}} = 5.02$ TeV using the CMS detector

By

SAEAHRAM YOO
DISSERTATION

Submitted in partial satisfaction of the requirements for the degree of

DOCTOR OF PHILOSOPHY

in
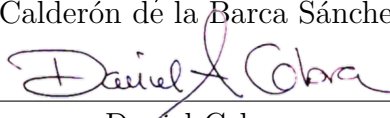
Physics

in the

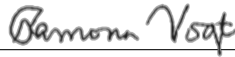OFFICE OF GRADUATE STUDIES

of the

UNIVERSITY OF CALIFORNIA

DAVIS

Approved:

_____
Manuel Calderón de la Barca Sánchez, Chair

_____
Daniel Cebra

_____
Ramona Vogt

Committee in Charge

2025

i

Contents

List of Acronyms

ALICE   A Large Ion Collider Experiment

AOD   Analysis Object Data

APD   avalanche photodiode

ATLAS   A Toroidal LHC Apparatus

BMTF   Barrel Muon Track Finder

BPIX   Barrel Pixel Detector

BS   beam spot

CSC   Cathode Strip Chamber

CondDB   Condition Database

CERN   European Organization for Nuclear Research

CEM   Color Evaporation Model

CPU   Central Processing Unit

CMS   Compact Muon Solenoid

CMSSW   CMS Software Framework

CNM   cold nuclear matter

CP   Charge-Parity

CS   Collins-Soper

CSM   Color Singlet Model

CP5   CMS Physics tune 5

DAS   Data Aggregation System

DCA   Distance of Closest Approach

DIGI   Digitization

DQ	Double Quality
DQM	Data Quality Monitoring
DT	Drift Tube
DSCB	Double-sided Crystal Ball
EB	ECAL Barrel
ECAL	Electromagnetic Calorimeter
ECR	Electron Cyclotron Resonance
EE	ECAL Endcap
EMTF	Endcap Muon Track Finder
ES	ECAL Preshower
FPIX	Forward Pixel Detector
GEM	Gas Electron Multiplier
GEN	Generation
GJ	Gottfried-Jackson
GMT	Global Muon Trigger
GO	Global Observable
GT	Global Tag
GMT	Global Muon Trigger
HB	Hadron Barrel
HCAL	Hadron Calorimeter
HE	Hadron Endcap
HF	Hadron Forward
HIN	Heavy Ion
HO	Hadron Outer
HX	helicity
HLT	High-Level Trigger
ID	Identification
ICEM	Improved Color Evaporation Model
IP	Interaction Point
L1	Level-1

L2	Level-2
L3	Level-3
LEIR	Low Energy Ion Ring
LEP	Large Electron-Positron collider
LHC	Large Hadron Collider
LHCb	Large Hadron Collider beauty
LDME	long-distance matrix element
LINAC	Linear Accelerator
LO	leading order
MB	Minimum Bias
MC	Monte Carlo
MiniAOD	Mini Analysis Object Data
NRQCD	Non-Relativistic Quantum Chromodynamics
NLO	next-to-leading order
OMS	Online Monitoring System
OMTF	Overlap Muon Track Finder
PDF	probability density function
PDG	Particle Data Group
PdmV	Physics data and Monte Carlo Validation
POG	Physics Object Group
PS	Proton Synchrotron
PU	Pileup
PX	perpendicular helicity
RECO	Reconstruction
RECO BS	Reconstructed Beamspot
RF	Radio Frequency
RPC	Resistive Plate Chamber
SF	scale factor
SIM	Simulation
SPS	Super Proton Synchrotron

SQ	Single Quality
TIB	Tracker Inner Barrel
TID	Tracker Inner Disks
TEC	Tracker Endcaps
TOB	Tracker Outer Barrel
QCD	Quantum Chromodynamics
QED	Quantum Electrodynamics
QGP	quark-gluon plasma
QRL	Quench Relief Line
VPT	vacuum phototriode
YETS	Year-End Technical Stop

List of Figures

List of Tables

<center>ABSTRACT</center>

$\Upsilon(1S)$ polarization measurement in PbPb collisions at $\sqrt{s_{NN}} = 5.02$ TeV using the CMS detector

The study of quarkonium polarization in heavy ion collisions provides crucial information about the quark-gluon plasma (QGP), a deconfined state of matter formed at extreme temperature and Energy density. In heavy ion collisions, the polarization of quarkonium states can be sensitive to extreme conditions in the QGP, such as strong electromagnetic and rotational fields, and may reflect screening effects and the degree of thermalization in the QGP. While quarkonium suppression in heavy ion collisions has been extensively studied as a QGP signature, measurements of quarkonium polarization remain relatively limited due to experimental challenges.

This thesis presents a measurement of the polarization of $\Upsilon(1S)$ mesons in lead-lead (Pb + Pb) collisions at a nucleon-nucleon center-of-mass energy of $\sqrt{s_{NN}} = 5.02$ TeV, using data collected by the Compact Muon Solenoid (CMS) experiment during the 2018 heavy ion run at the Large Hadron Collider (LHC). The analysis is performed in the dimuon decay channel as a function of transverse momentum (p_{T}) within the midrapidity region ($|y| < 2.4$). Polarization parameters (λ_θ, λ_φ, and $\lambda_{\theta\varphi}$) are extracted from the angular distributions of the decay muons in the Collins-Soper (CS) and helicity (HX) frames.

Acceptance and efficiency corrections are derived using fully simulated Monte Carlo (MC) samples, with generator-level and reconstructed-level corrections applied to the angular distributions. A frame-invariant parameter, $\tilde{\lambda}$, is also evaluated in order to facilitate a frame-independent interpretation. The results are compared to corresponding measurements in proton-proton ($p + p$) collisions to assess possible modifications due to QGP effects. This work provides new experimental input for theoretical models of quarkonium production and polarization in a QGP medium.

Chapter 1

Introduction

One of the fundamental questions in contemporary nuclear physics is how interacting matter behaves under extreme conditions. In the early universe, a few microseconds after the Big Bang, quarks and gluons existed in a deconfined state before combining into hadrons as the universe cooled. This deconfined phase of matter is known as the quark-gluon plasma (QGP). Understanding its properties provides insight into the dynamics of Quantum Chromodynamics (QCD) and the formation of matter [1, 2].

To recreate and study the QGP in the laboratory, experiments at the Large Hadron Collider (LHC) at CERN collide heavy nuclei at ultra-relativistic energies. These collisions produce Energy densities exceeding 1 GeV/fm^3 and temperatures on the order of 200 MeV [1, 3], well above the crossover temperature of about 155 MeV predicted by lattice QCD [4, 5]. Phenomenological models constrained by bottomonium suppression data also indicate that the initial temperatures in central LHC collisions can reach as high as ~ 600 MeV [6].

Among the various probes of the QGP, quarkonia (a bound state of a heavy quark and antiquark, $Q\overline{Q}$) play a unique role. Formed early in the collision and with a long lifetime when compared to the medium evolution, quarkonia traverse the full history of the plasma and are therefore excellent probes of its properties [7, 8]. While yield suppression has long

been studied as a key observable, polarization provides an additional observable that offers information on quarkonium production mechanisms and possible modifications induced by the QGP medium [9, 10].

This chapter is structured as follows: Sec. 1.1 introduces the properties of QCD matter and the QGP; Sec. 1.2 describes heavy ion collisions at the LHC; Sec. 1.3 motivates the use of quarkonia as a probe; Sec. 1.4 presents the physics motivation for quarkonium polarization measurements; Sec. 1.5 introduces the relevant observables and reference frames; and Sec. 1.6 outlines the scope of the present analysis.

1.1   QCD Matter and the QGP

QCD is the fundamental theory that describes the interactions of quarks and gluons via the exchange of color charges. Quarks are spin-1/2 fermions classified into six flavors: up (u), down (d), charm (c), strange (s), top (t), and bottom (b). They carry both color charge and fractional electric charge. Gluons are spin-1 bosons that mediate the strong interaction. Unlike photons in Quantum Electrodynamics (QED), gluons themselves carry color charge, which leads to gluon self-interactions. Fig. 1.1 illustrates the concept of color charge in QCD. Quarks must always combine to form color singlets ("white"), achieved either in the form of three-quark baryons or quark-antiquark mesons. This requirement underlines confinement and explains why free quarks are not observed.

Two unique features of QCD are asymptotic freedom and confinement. Asymptotic freedom implies the strong coupling constant $\alpha_s(Q^2)$ becomes small at asymptotically high values of the scale variable Q^2 [12, 13]. Here, Q^2 is defined as the negative of the squared four-momentum transfer q in a scattering process [14]:

$$Q^2 \equiv -q^2 = -(p_i - p_j)^2, \tag{1.1}$$
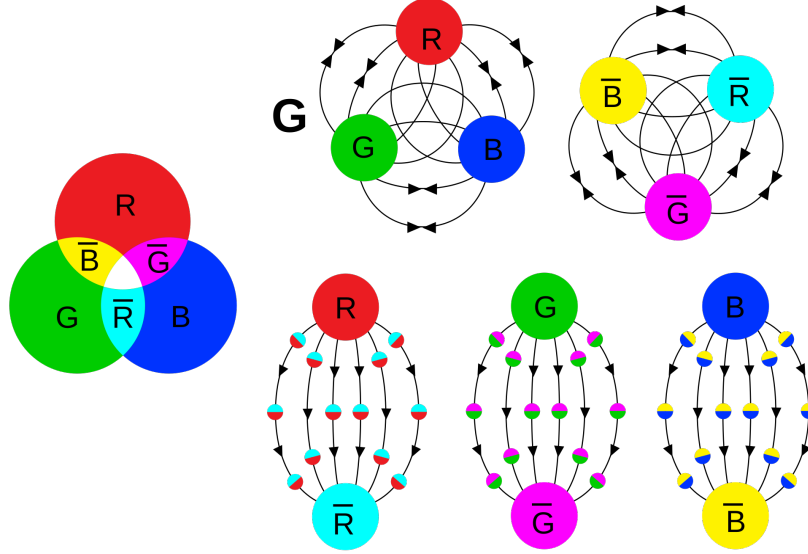
Figure 1.1: Illustration of color charges and gluon fields in QCD. The left diagram shows the three color charges and their anticolors. The right diagrams depict examples of color-neutral hadrons. The top diagram shows baryons. The bottom diagram shows mesons. Quarks are represented as large circles. Gluon fields are curved lines. Gluon color charges are small circles [11].

where p_i and p_j are the four-momenta before and after the interaction. Large Q^2 corresponds to short-distance and high-energy interactions, where quarks and gluons behave as nearly free particles. This behavior, shown in Fig. 1.2, makes perturbative calculations possible at high energies. Small Q^2 corresponds to long-distance and low-energy interactions. When this coupling increases, quarks and gluons are confined inside hadrons.

The scale dependence of $\alpha_s(Q^2)$ also implies that confinement can be overcome if the system is heated or compressed to extreme conditions. At sufficiently high temperatures or Energy densities, the average interaction strength decreases, and quarks and gluons are no longer bound into hadrons. The running of $\alpha_s(Q^2)$ therefore motivates the expectation of a transition between confined hadronic matter and deconfined QGP.

The temperature characterizing this transition at vanishing baryon chemical potential $(\mu_B = 0)$ is called the crossover (or pseudocritical) temperature T_c. Perturbative methods
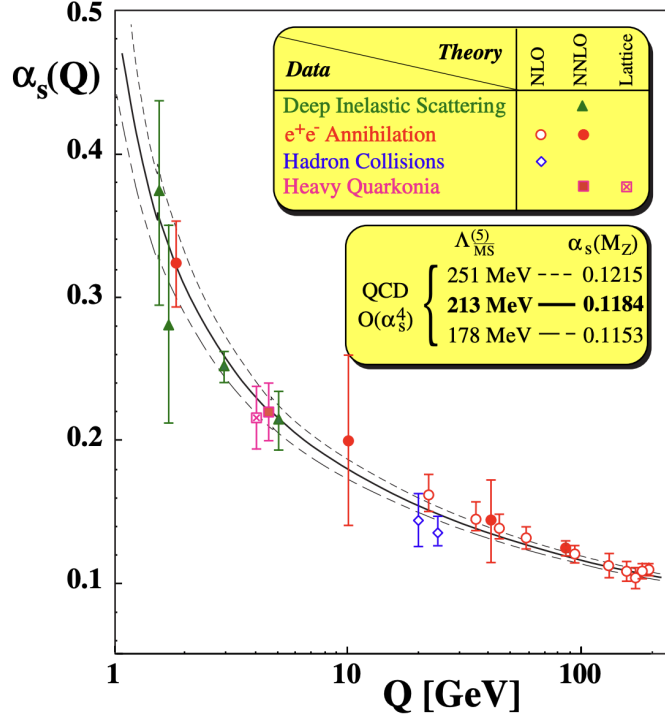
Figure 1.2: The running of the strong coupling constant $\alpha_s(Q^2)$ as a function of the momentum transfer Q. Experimental data from deep inelastic scattering, e^+e^- annihilation, hadron collision, and heavy quarkonia are compared with QCD predictions at next-to-leading order (NLO), next-to-next-to-leading order (NNLO), and lattice calculations. The logarithmic decrease of $\alpha_s(Q^2)$ with increasing Q^2 illustrates asymptotic freedom [15].

cannot reliably calculate T_c or the equation of state because α_s is large near the transition. Instead, lattice QCD provides a first-principles, non-perturbative approach. By discretizing space and time on a Euclidean grid, lattice QCD allows numerical calculations of strongly interacting matter. Lattice QCD calculates bulk properties of strongly interacting matter, providing access to thermodynamic observables such as pressure (p), Energy density (ϵ), and Entropy density (s).

These quantities rise rapidly near the crossover temperature ($T_c \sim 155$ MeV) [4, 5], as shown in Fig. 1.3. This rise indicates that quarks and gluons are no longer confined
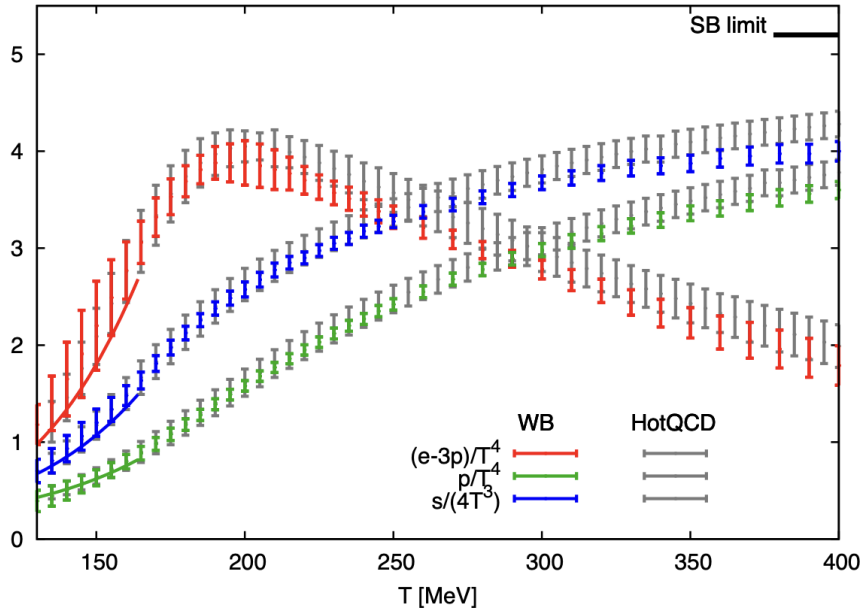
Figure 1.3: Lattice QCD results for bulk thermodynamic observables at vanishing baryon chemical potential ($\mu_B = 0$). The curves display the temperature dependence of the pressure (p), Energy density (ϵ), and Entropy density (s), normalized to the Stefan-Boltzmann (SB) limit of an ideal quark-gluon gas. Continuum-extrapolated results for the QCD equation of state have been provided by the Wuppertal–Budapest (WB) Collaboration and the HotQCD Collaboration. The two independent calculations show good agreement near and above the crossover temperature (T_c) [16].

within hadrons; instead they contribute directly to the medium. At very high temperatures ($T \gtrsim 3T_c \approx 500$ MeV), they approach but do not reach the Stefan-Boltzmann (SB) limit of an ideal quark-gluon gas. This deviation indicates that the QGP remains a strongly coupled medium [16]. The transition is a smooth crossover at vanishing baryon chemical potential ($\mu_B = 0$) [4, 5]. Baryon chemical potential (μ_B) is the change in free energy when one baryon is added to the system [17]. At finite baryon density, it is conjectured that this crossover turns into a first-order transition, terminating at a critical end point.

The QGP exhibits transport properties characteristic of a nearly perfect fluid with a shear viscosity to Entropy density ratio (η/s) near the theoretical lower bound [18]. Establishing
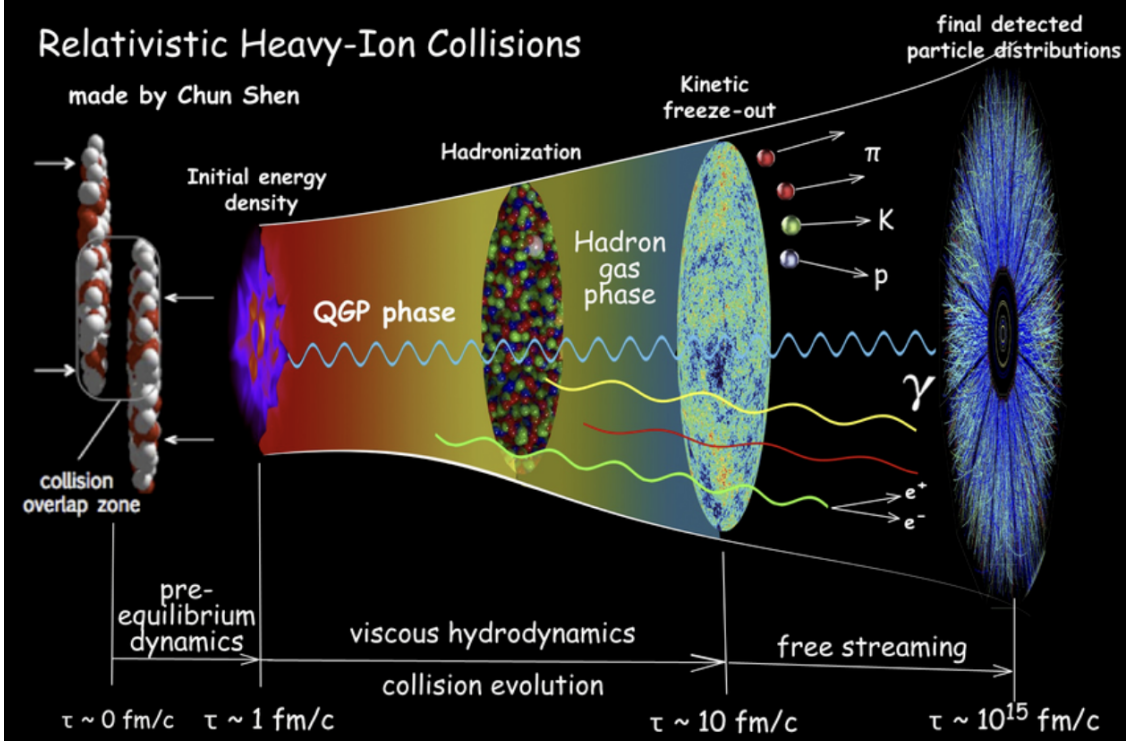
Figure 1.4: Schematic illustration of the space–time evolution of a relativistic heavy ion collision. Two lead nuclei collide at ultra-relativistic energies and form a hot, dense medium of deconfined quarks and gluons (QGP). The QGP subsequently expands, cools, and transitions into a hadron gas before freeze-out [20].

these properties experimentally in heavy ion collisions is a central goal of the LHC [3, 19].

1.2   Heavy Ion Collisions at the LHC

Relativistic heavy ion collisions provide a unique opportunity to study strongly interacting matter under extreme conditions of temperature and Energy density. When two lead nuclei collide at ultra-relativistic energies, the overlap region forms a hot and dense fireball. In this region, quarks and gluons are deconfined, creating the QGP [1].

Figure 1.4 schematically illustrates the evolution of relativistic heavy ion collisions [20]. The system evolves through several stages: an initial pre-equilibrium phase ($\tau \lesssim 1$ fm/c)

QGP formation and hydrodynamic expansion ($\tau \sim 1-10$ fm/c), and finally hadronization and freeze-out. Bottomonium states such as Υ are produced very early in the collision, during the initial hard scatterings ($\tau \sim 0$ fm/c). They then traverse the medium where they may be suppressed or modified before decaying into dileptons that escape without further interaction, providing direct information on the QGP.

The LHC at CERN operates the highest-energy heavy ion program worldwide. Pb + Pb collisions at $\sqrt{s_{NN}} = 2.76$ and 5.02 TeV have achieved initial Energy densities of several GeV per cubic femtometer, sufficient to sustain a deconfined QGP phase well beyond its initial formation [19, 21]. These unprecedented conditions make it possible to measure the thermodynamic and transport properties of the QGP with high precision.

A Large Ion Collider Experiment (ALICE), A Toroidal LHC Apparatus (ATLAS), Compact Muon Solenoid (CMS), and Large Hadron Collider beauty (LHCb) experiments provide complementary capabilities: ALICE specializes in comprehensive tracking and identified-particle measurements at low transverse momentum; ATLAS and CMS provide precise calorimetry and large-acceptance muon systems for high-p_{T} probes; and LHCb contributes to the heavy ion program with measurements at forward rapidities, particularly of charm and bottom production and fixed-target collisions [22, 23].

1.3 Quarkonia as a Probe of the QGP

Quarkonia, bound states of a heavy quark and its antiquark, have long been recognized as clean probes of the QGP [24]. The early formation and well-defined binding energies of quarkonia make them sensitive to medium effects such as color screening, which leads to the sequential suppression of different states depending on their binding strength [25]. In the case of bottomonium, the relevant reference scale is the open beauty threshold at $m_{B\bar{B}} \approx 10.56$ GeV (horizontal dotted line in Fig. 1.5). The binding energy of a given state
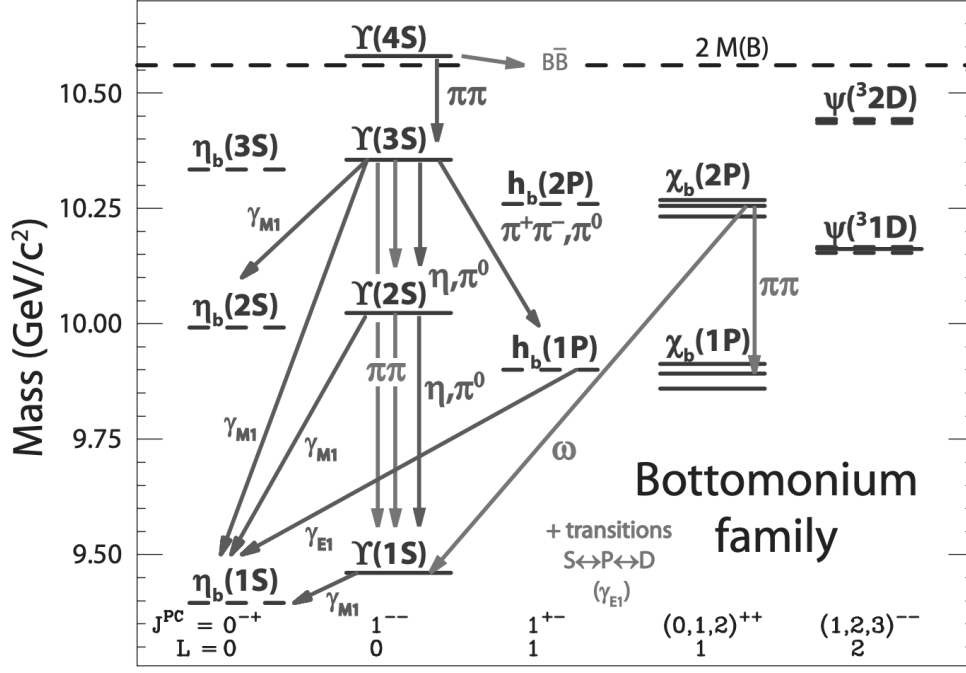
Figure 1.5: Bottomonium spectrum of bound $b\bar{b}$ states. Differences in binding energies **lead to** the observed sequential suppression pattern in heavy ion collisions [7].

is the difference between this threshold and the quarkonium mass. Thus, the tightly bound ground state $\Upsilon(1S)$, with

$$E_b \approx 10.56 - 9.46 \text{ GeV}$$
$$\simeq 1.1 \text{ GeV},$$

(1.2)

is expected to survive up to higher medium temperature, whereas the excited states are more weakly bound and therefore more easily suppressed.

The experimental study of bottomonium relies on the dilepton decay channels ($\mu^+ \mu^-$, $e^+ e^-$), which provide clean signatures and excellent mass resolution compared to hadronic decays. The overall Υ production cross section is much smaller than that of open bottom, reflecting the relatively low probability for a $b\bar{b}$ pair to evolve into a bound quarkonium state. The observed $\Upsilon(1S)$ signal includes not only direct production but also feed-down from

higher excited states such as $\Upsilon(2S)$, $\Upsilon(3S)$, and χ_b. This spectrum, illustrated in Fig. 1.5, is important because suppression and polarization patterns can differ between direct and feed-down contributions.

This sequential melting picture describes the role of the deconfined medium. In practice, however, the observed yields are shaped not only by QGP suppression but also by cold nuclear matter (CNM) effects present in the initial state. Proton-nucleus ($p + A$) collisions provide the control environment for disentangling these contributions, which must be taken into account when interpreting suppression in Pb + Pb [26].

Since the beginning of the heavy ion physics program at the LHC, the CMS Collaboration has played a leading role in the study of quarkonium dynamics in ultra-relativistic nucleus-nucleus ($A + A$) collisions. CMS has reported several key results in the bottomonium sector: the sequential suppression of Υ mesons [27–30]; one of the first investigations of bottomonium elliptic flow [31]; and the observation of the strongly-suppressed $\Upsilon(3S)$ production [32]. The systematic comparison of these results with the rich variety of model calculations demonstrates the importance of quarkonium observables in the investigation of the formation and interaction of bound states in the QGP. Ref. [8] provides a comprehensive summary of the existing approaches.

From a theoretical perspective, bottomonium plays a distinctive role in QCD. The large bottom-quark mass ($m_b(\mu = m_b) \approx 4.18$ GeV) ensures that the initial $b\bar{b}$ pair is produced perturbatively, at momentum scales where the strong coupling is small [33]. However, the subsequent binding into physical Υ states is inherently non-perturbative, governed by confinement. These complementary components make bottomonium a particularly valuable probe of the interplay between perturbative and non-perturbative QCD in the QGP. Beyond yield suppression, another key observable is polarization, which encodes spin alignment and may reveal QGP-induced modifications.

1.4 Quarkonium Polarization in Heavy Ion Collisions

While the suppression of quarkonium yields in $A + A$ collisions has been studied for more than four decades [24], much less is known about quarkonium polarization in the QGP. Polarization, which reflects the spin alignment of the produced quarkonium states, provides complementary information to yield measurements. It has been proposed that quarkonium polarization could be modified in a deconfined medium [9, 24], but experimental access to this observable in heavy ion collisions has only become possible in recent years.

Quarkonium production and polarization involve both perturbative and non-perturbative aspects of QCD. The heavy quark–antiquark pair is produced in a short-distance process, calculable using perturbative techniques. The subsequent hadronization into a bound state is non-perturbative and must be modeled. Several frameworks are used for this purpose: Non-Relativistic Quantum Chromodynamics (NRQCD) [34]; the Color Singlet Model (CSM) [35]; the Color Evaporation Model (CEM) [36, 37]; NRQCD with k_T factorization [38]; and the Improved Color Evaporation Model (ICEM) with k_T factorization [39]. While these approaches can reproduce quarkonium yields reasonably well, predicting polarization has proven significantly more challenging [40].

In addition to NRQCD, the color singlet model, and the traditional CEM, recent work has developed the ICEM [39]. The ICEM extends the CEM by incorporating the transverse momentum of the heavy quark pair via k_T-factorization, rather than relying on collinear parton distributions. This treatment modifies the mapping from the perturbatively produced $Q\overline{Q}$ pair to the physical quarkonium state, leading to different predictions for polarization relative to both CEM and NRQCD. Importantly, while NRQCD relied on long-distance matrix elements (LDMEs) that must be fitted from data, the ICEM introduces fewer nonperturbative parameters and offers direct predictions of quarkonium spin alignment. The comparison between ICEM predictions and experimental polarization measurements therefore provides

a critical test of this alternative framework.

Within the NRQCD framework, polarization predictions depend on the values of several LDMEs: the color-octet $^1S_0^{[8]}$, $^3S_1^{[8]}$, and $^3P_J^{[8]}$ components. These LDMEs cannot be computed from first principles and must be extracted from experimental data. However, past extractions have faced methodological limitations: inconsistent treatment of uncertainties; neglect of correlations; assumptions about polarization in the acceptance calculation; and the use of data outside the validity domain of the short-distance coefficients. As a result, different LDME fits lead to widely varying polarization predictions, making direct experimental input indispensable.

At leading order (LO) in NRQCD, quarkonium production at high transverse momentum ($p_T^{\mu\mu}$) predicts a sizable transverse polarization of the quarkonium states. However, measurements at the Tevatron and LHC revealed little to no polarization [41–47]. Next-to-leading order (NLO) calculations [48–52] showed that large cancellations among the various intermediate $Q\overline{Q}$ spin and angular momentum states can reproduce the small values observed in data. Similar approaches were needed for bottomonium studies, with the added complexity of significant feed-down contributions from excited states [53, 54].

The motivation for studying polarization in heavy ion collisions stems from the possibility that the QGP modifies the spin alignment of surviving quarkonium states. In the original argument of Ref. [9], screening of non-perturbative effects in the deconfined medium was expected to restore the applicability of LO perturbative predictions, leading to a nonzero polarization. Experimentally, ALICE has measured J/ψ polarization in both $p + p$ and Pb + Pb collisions and found no significant difference between the two systems [55]. However, bottomonium ($\Upsilon(1S)$, $\Upsilon(2S)$, $\Upsilon(3S)$) provides a cleaner probe: its higher mass and binding energies reduce the role of recombination and cold-nuclear-matter effects that complicate charmonium studies. A measurement of Υ polarization in Pb+Pb collisions therefore provides a sensitive test of whether the QGP induces modifications beyond those observed

in $p + p$. Alternatively, the measurement could provide a valuable null result that constrains theoretical models.

1.5   Polarization Observables and Reference Frames

The average polarization of any vector meson, and more specifically of quarkonia with quantum numbers $J^{PC} = 1^{--}$, such as Υ mesons decaying into lepton-antilepton pairs, can be experimentally determined by measuring the angular distribution of the decay particles [56]. The general form reads

$$W(\cos\theta, \varphi \mid \overrightarrow{\lambda}) = \frac{3/(4\pi)}{3 + \lambda_\theta}(1 + \lambda_\theta \cos^2\theta + \lambda_\varphi \sin^2\theta \cos 2\varphi + \lambda_{\theta\varphi} \sin 2\theta \cos\varphi), \qquad (1.3)$$

where θ and φ are, respectively, the polar and azimuthal angles of the positively-charged lepton (by convention) in the quarkonium's rest frame. The angles are defined with respect to a chosen polarization axis z and the production plane containing the colliding beam directions and the momentum of the parent Υ. The $\lambda_\theta, \lambda_\varphi, \lambda_{\theta\varphi}$ coefficients are referred to as the polarization parameters: λ_θ quantifies the polar anisotropy of the distribution (the dependence on $\cos^2\theta$); λ_φ describes the azimuthal anisotropy (the modulation in $\cos 2\varphi$); and $\lambda_{\theta\varphi}$ characterizes the correlation between polar and azimuthal angles (the $\sin 2\theta \cos\varphi$ term). Together, these parameters provide a complete characterization of the spin alignment of the vector meson.

A frame-invariant polarization parameter has the advantage of being independent of the chosen reference frame [10]. The frame-invariant polarization can be written, in terms of the measured parameters in any frame, as

$$\tilde{\lambda} \equiv \frac{\lambda_\theta + 3\lambda_\varphi}{1 - \lambda_\varphi}. \qquad (1.4)$$

There are several commonly used reference frames for polarization analysis, defined by different choices of the z-axis: helicity (HX), Collins-Soper (CS), perpendicular helicity (PX),
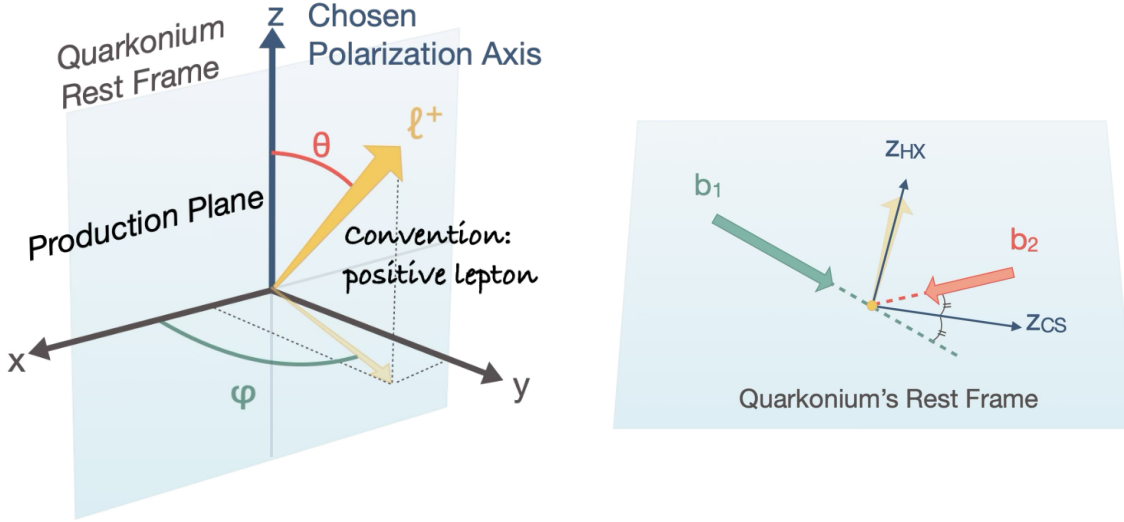
Figure 1.6: Reference frames used in quarkonium polarization analyses [56].

and Gottfried-Jackson (GJ) frames. In the HX frame, the z-axis is defined by adopting the momentum direction of the Υ meson from the center-of-mass frame of the colliding beams directly into the Υ meson's rest frame. The CS frame, on the other hand, uses the directions of the two colliding beams in the Υ meson's rest frame. The z-axis is defined by the bisector of the momentum direction of one beam and the opposite momentum direction of the other, representing the average of the two beams' momentum directions. In the PX frame, the z-axis is defined as perpendicular to the z-axis in the CS frame, while in the GJ frame, the z-axis is aligned with the momentum direction of one of the beams [56].

Previous analyses in various experiments have used 1-D fits to the angular distribution after integrating over $\cos\theta$ or φ. However, as discussed in Ref. [56], it is always preferable to use 2-D fits to extract the polarization, as the integration procedure can lead to systematic effects that can change the extracted polarization parameters when doing 1-D fits. Therefore, in this analysis, we focus on extracting the polarization parameters using 2-D fits to the angular distribution.

1.6   Scope and Structure of This Thesis

This analysis aims to extract the polarization parameters of $\Upsilon(1S)$ mesons in Pb + Pb collisions at $\sqrt{s_{NN}} = 5.02$ TeV using the 2018 CMS dataset, extending previous measurements by ALICE to mid-rapidity and covering finer $p_T^{\mu\mu}$ intervals.

Our analysis entails the following steps: (1) choice of polarization frame and kinematic binning, (2) signal yield extraction, (3) acceptance and efficiency correction, and (4) polarization parameter extraction. Two reference frames, CS and HX, are used to obtain the polarization parameters. To avoid amplifying background through acceptance and efficiency corrections, we first performed signal yield extraction from the raw data within a restricted $(\cos\theta, \varphi)$ region for a given $p_T^{\mu\mu}$ bin. After applying acceptance and efficiency corrections to the extracted yields, the polarization parameters λ_θ, λ_φ, and $\lambda_{\theta\varphi}$ were extracted in each $p_T^{\mu\mu}$ bin. Additionally, the invariant frame polarization parameter $\tilde{\lambda}$ was compared between the results obtained in the CS and HX frames.

The structure of this thesis is as follows: Chap. 2 describes the experimental facilities, Chap. 3 introduces the data and Monte Carlo (MC) samples used in this analysis and how they were obtained, Chap. 4 details the treatments applied to data and MC, Chap. 5 presents the signal extraction procedure used to isolate quarkonium yields from background, Chap. 6 discusses the acceptance and efficiency corrections, Chap. 7 explains the method of extracting polarization parameters, Chap. 8 provides closure tests to validate the analysis framework, Chap. 9 summarizes the systematic uncertainties, Chap. 10 presents the main results and their implications, and Chap. 11 concludes the thesis.

Chapter 2

Experimental Facilities

2.1 LHC Accelerator at CERN

The LHC is the world's largest particle accelerator, located at CERN[1] near Geneva on the border between Switzerland and France [22]. It collides beams of protons and heavy ions at nearly the speed of light, enabling the study of fundamental interactions at the smallest distance scales. This facility provides the high-energy heavy ion collisions that form the basis of the analysis in this thesis, particularly the study of quarkonium polarization in the QGP.

The LHC occupies a 26.7 km underground circular tunnel, originally constructed for the Large Electron-Positron collider (LEP) and upgraded extensively since 1998 to support high-energy hadron collisions [58]. The tunnel, situated approximately 100 m below the surface, houses two vacuum-insulated superconducting beam pipes. In these pipes, counter-rotating beams of protons or ions are accelerated to high energies. They are brought into collision at four dedicated Interaction Points (IPs): ATLAS, ALICE, CMS, and LHCb. Among these, the CMS experiment at IP5 plays a central role in this thesis, providing the dimuon datasets

---

[1]Although the acronym originates from its original French name, Conseil Européen pour la Recherche Nucléaire, it is now retained only for historical reasons.
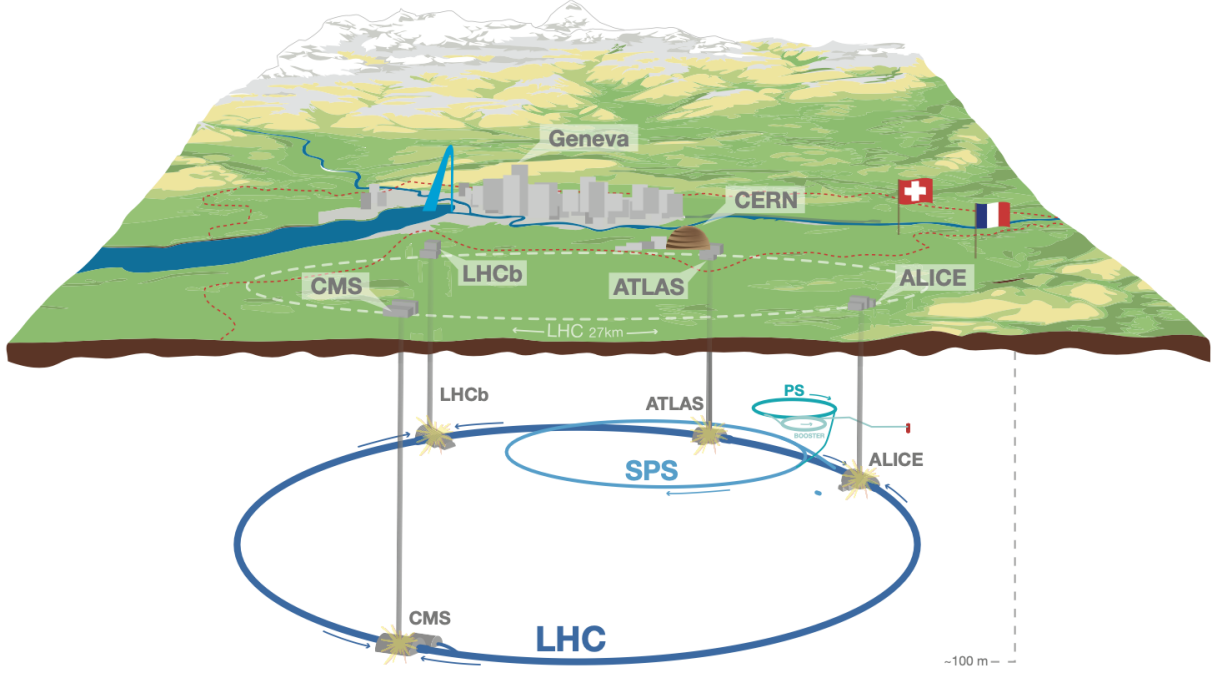
Figure 2.1: A schematic aerial view of the LHC [57]. The control rooms of the four experiments (ATLAS, ALICE, CMS, and LHCb) are positioned on the surface, while their underground caverns host the detectors. The LHC rings are situated 100 m below the surface and connected to CERN's accelerator complex.

used to reconstruct bottomonium states in Pb + Pb collisions. Figure 2.1 illustrates the layout and scale of the LHC.

The next sections introduce the following components of the LHC: Sec. 2.1.1, the key accelerator technologies; Sec. 2.1.2, collision systems; Sec. 2.1.3, interaction points including CMS at IP5; and Sec. 2.1.4, the injector chain that delivers pre-accelerated beams into the LHC. These elements provide the operational context for the measurements presented in this thesis.

2.1.1 LHC technologies

The LHC is designed to accelerate particles to energies of several tera-electron volts (TeV), requiring them to travel at nearly the speed of light. The maximum attainable energy in a circulating accelerator is determined by the balance between the Lorentz force and the relativistic centripetal force, expressed as:

$$F = qvB, \tag{2.1}$$

$$\gamma mv^2/R = qvB, \tag{2.2}$$

where F is the Lorentz force; q is the particle electric charge; v is its velocity; B is the magnitude of the magnetic field; m is the particle mass; and R is the radius of the accelerator. The resulting momentum p and energy E of a relativistic particle are:

$$p = qRB, \tag{2.3}$$

$$E \simeq pc \tag{2.4}$$

$$= qcRB \tag{2.5}$$

$$= qc\,\frac{Nl}{2\pi}\,B, \tag{2.6}$$

where N is the number of dipoles; l is the length of magnets; and B is the strength of the magnetic field. Here, R is approximated by $\frac{Nl}{2\pi}$, assuming the circular accelerator as a polygon with many (thousands) of linear segments. For protons ($q = e$), the attainable energy E in GeV is:

$$E\,[\,\mathrm{GeV}] \approx 0.3\,\frac{N}{2\pi}\,l\,[\mathrm{m}]\,B\,[\mathrm{T}]. \tag{2.7}$$

Using 1232 dipoles of 14.3 m length and an 8.3 T field (limited by Nb-Ti superconductivity), the maximum attainable E per proton in the lab frame is 7 TeV [22]. For Run 3, LHC operates the accelerator with 6.8 TeV per proton beam, corresponding to $\sqrt{s_{NN}} = 13.6$ TeV

17

for the proton beam. For ^{208}Pb beam with 82 protons in Pb, $\sqrt{s_{NN}}$ corresponds to 5.36 TeV:

$$\sqrt{s_{NN}} = 2 \, \frac{(E \text{ per proton in the lab frame}) \, (82 \text{ protons in } {}^{208}\text{Pb})}{(208 \text{ nucleons in } {}^{208}\text{Pb})} \tag{2.8}$$

$$= 2 \, \frac{6.8 \text{ TeV} \times 82}{208} \tag{2.9}$$

$$\approx 5.36 \text{ TeV}. \tag{2.10}$$

To accelerate particles close to the speed of light, the LHC uses advanced vacuum systems and superconducting magnets. These are crucial for minimizing energy loss and directly impact the maximum attainable energy of the accelerator. This high energy is essential for producing heavy quarkonia with sufficient transverse momentum to measure their polarization across a wide kinematic range. The following sections describe these key technologies.

2.1.1.1 Vacuum systems

The LHC employs three vacuum systems to preserve beam quality and luminosity: beam pipe, cryomagnets, and the helium distribution line (Quench Relief Line (QRL)) [61]. Figure 2.2 illustrates the tunnel with the cryogenic distribution line (left) and a cross section of the dipole magnet with its vacuum layers (right). The QRL is shown on the right-hand side of the left photograph; while the cross section on the right schematic drawing shows the beam pipe at the center, surrounded by the superconducting coils, thermal shields, and the outer vacuum vessel.

The vacuum inside the beam pipe is crucial for preventing a proton or a heavy ion from interacting with residual gas molecules, which would cause beam losses and reduce luminosity. Pressures as low as 10^{-14} atm are achieved during operation.

The surrounding vacuum vessel provides thermal insulation. At room temperature this vacuum reaches about 10^{-4} atm using standard mechanical pumps. When cooled to cryogenic temperatures, residual gas molecules condense on the cold surfaces, reducing the pressure below 10^{-9} atm and minimizing heat transfer to the 1.9 K cold mass.

LHC DIPOLE : STANDARD CROSS-SECTION
CERN AC/DI/MM - HE107 - 30 04 1999

ALIGNMENT TARGET

MAIN QUADRIPOLE BUS-BARS

HEAT EXCHANGER PIPE

SUPERINSULATION

SUPERCONDUCTING COILS

BEAM PIPE

VACUUM VESSEL

BEAM SCREEN

AUXILIARY BUS-BARS

SHRINKING CYLINDER / HE I-VESSEL

THERMAL SHIELD (55 to 75K)

NON-MAGNETIC COLLARS

IRON YOKE (COLD MASS, 1.9K)

DIPOLE BUS-BARS

SUPPORT POST
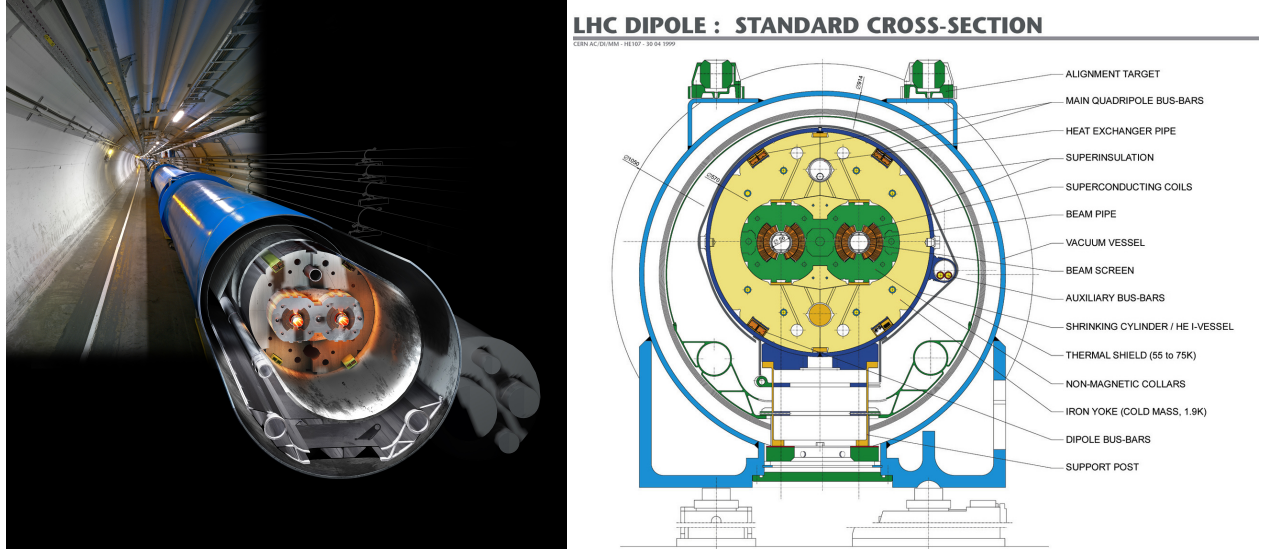
Figure 2.2: Left: Photograph of the LHC tunnel with the superconducting dipole magnets. The gray pipes outside of the blue cryostat on the right side of the photograph show the cryogenic distribution line (QRL). Right: A cross section diagram of the LHC dipole showing the beam pipes, superconducting coils, and surrounding cryostat layers [59, 60]

.

The QRL, which delivers superfluid helium to the magnets, is enclosed in its own independent insulation vacuum. It is maintained at 10^{-7}–10^{-9} atm to reduce heat inleak to the helium. The QRL connects to the cryostat via jumper modules that allow helium flow while keeping the vacuum separate.

These vacuum systems are essential for maintaining the cryogenic environment required for the superconducting magnets, discussed next.

2.1.1.2 Superconductivity

The LHC uses superconducting magnets to bend and focus particle beams along the 27 km ring. These magnets are based on Nb-Ti superconducting cables that operate at 1.9 K in a superfluid helium bath. The superconducting state eliminates electrical resistance, allowing
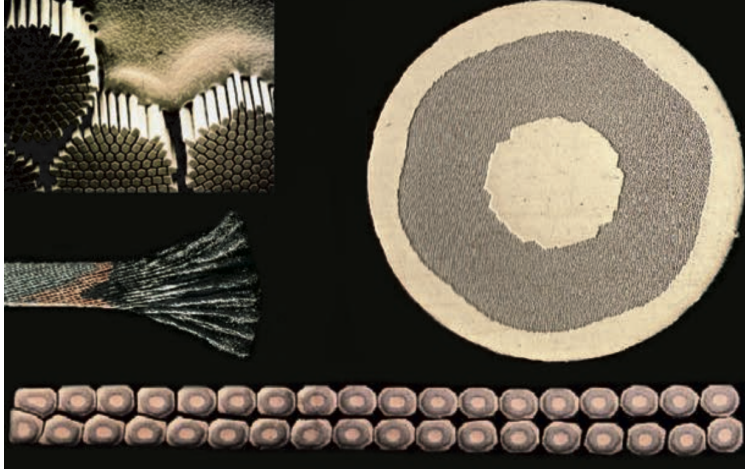
Figure 2.3: Structure of the LHC superconducting cables [62]. The top-right image shows a cross section of a single wire, with Nb-Ti filaments (dark region) surrounded by copper (white regions). The top-left image shows a bundle of many such wires before cabling. The middle-left image is a side view of multiple wires twisted together to form a Rutherford cable. The bottom row shows Rutherford cables after being flattened into their final shape, ready to be wound into the coils of dipole and quadrupole magnets.

very high currents (up to ~ 11.8 kA in dipoles) without energy loss [63].

Each wire is about 1 mm in diameter and contains thousands of fine Nb-Ti filaments (about one-third of the cross section), stabilized by copper (about two-thirds). The copper provides thermal and electrical stability, allowing the magnet to safely transition in the event of a quench (a sudden return to the normal-conducting state). Figure 2.3 illustrates the microscopic structure of a single wire, the bundle of wires forming a Rutherford-type cable, and the complete cable used in the LHC magnets.

Two main types of superconducting magnets are used: dipole and quadrupole magnets. Dipole magnets generate a uniform magnetic field of 8.33 T and bend the beams along the circular trajectory. Quadrupole magnets provide a field gradient and focus the beams transversely, maintaining a small beam size and thereby maximizing luminosity.

2.1.2 Particle species

The LHC's physics program relies on a variety of collision systems in order to explore both fundamental particle interactions and the properties of nuclear matter.

Proton-proton $(p + p)$ collisions constitute the primary operating mode. Protons are accelerated and collided at center-of-mass energies up to 14 TeV, enabling precision tests of the Standard Model and searches for new phenomena beyond it.

Heavy ion runs use fully stripped lead nuclei (Pb+Pb) at nucleon-nucleon center-of-mass energies of several TeV to create and study the QGP.

Proton-lead $(p + \text{Pb})$ collisions are performed to investigate cold nuclear matter effects and provide essential baselines for interpreting $\text{Pb} + \text{Pb}$ data. Additional collision systems, such as proton-proton $(p+p)$ reference runs at the same energies as $\text{Pb}+\text{Pb}$, and lighter-ion collisions $(p + \text{O}, \text{O} + \text{O}, \text{Ne} + \text{Ne})$, have been introduced to explore initial-state effects, and expand the physics reach of the LHC [64, 65].

The annual schedule typically consists of $p+p$ operation from April to October, followed by a heavy ion run in the latter part of the year, usually in November. The remaining months are reserved for the Year-End Technical Stop (YETS) for maintenance and upgrades of the accelerator and detector systems [66].

2.1.3 IPs of the LHC

The LHC contains eight long straight sections, known as IPs, distributed around its 27 km circumference (see Fig. 2.4). Four of them host the large physics experiments: ATLAS (IP1), ALICE (IP2), CMS (IP5), and LHCb (IP8). ATLAS at IP1 and CMS at IP5 are general-purpose detectors designed to explore a wide range of phenomena, including Higgs boson properties and searches for new physics. ALICE at IP2 focuses on heavy ion collisions to study the QGP, while LHCb at IP8 investigates heavy-flavor physics and Charge-Parity (CP)
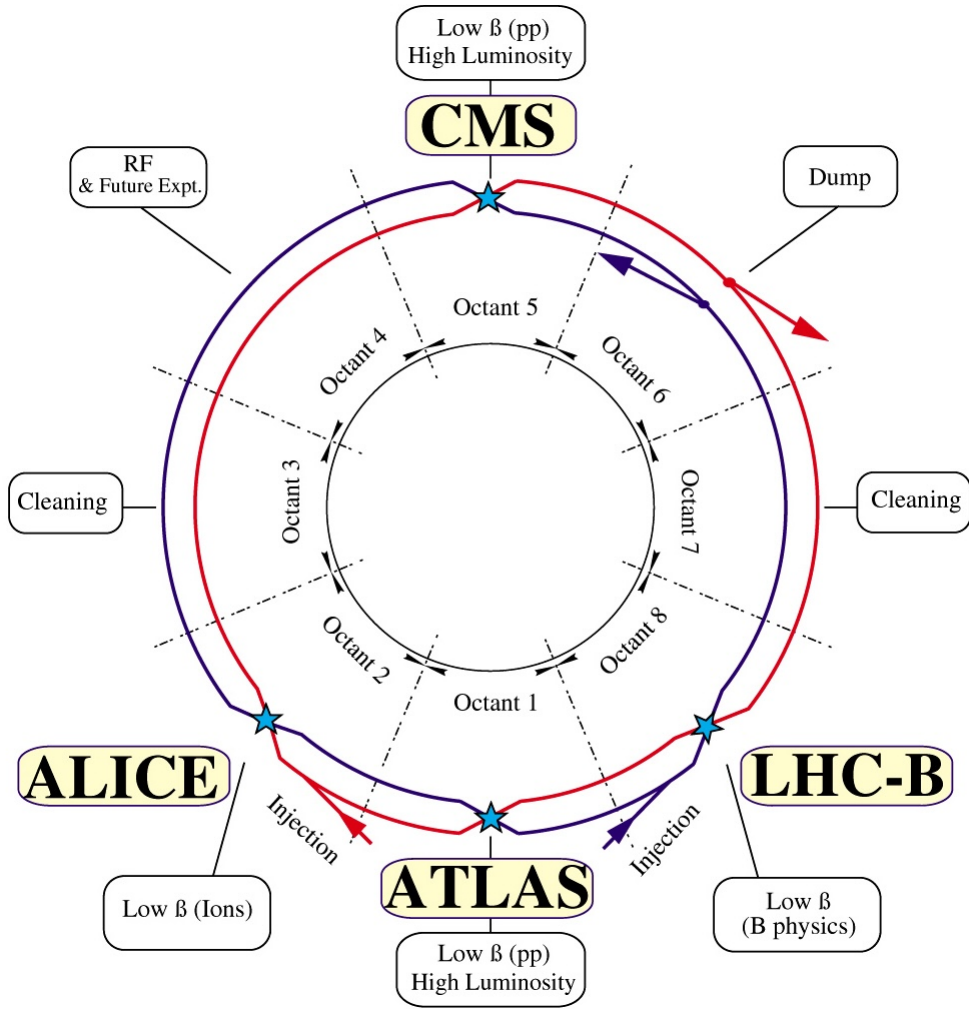
Figure 2.4: Schematic layout of the LHC showing the eight IPs, their primary functions, and the locations of the four main experiments [67].

violation in the *b*- and *c*-quark sectors. CMS at IP5 is used for this thesis due to its high-performance muon detection system and large acceptance for quarkonium reconstruction in Pb + Pb collisions.

The remaining IPs are dedicated to essential accelerator systems: collimation (IP3 and IP7), Radio Frequency (RF) acceleration (IP4), and the beam dump system (IP6). The collimation systems clean the beam halo that consists of particles outside of the core of the nominal beam envelope in transverse or longitudinal phase space. The 400 MHz RF cavities maintain and accelerate the beams. These superconducting cavities compensate for energy losses each circular turn and keep protons and ions tightly grouped into bunches. The beam dump system is used to safely extract and dispose of the circulating beams at the end of a run. In an emergency, the beam dump system uses graphite absorbers that gradually dissipate the energy [58]. Together, these eight IPs provide the infrastructure necessary for both high-precision experiments and safe, reliable operation of the LHC [62].

2.1.4 The LHC injection chain

The LHC does not accelerate particles directly from rest to TeV-scale energies. Instead, beams are prepared and pre-accelerated in a chain of machines that progressively increase the beam energy and improve beam quality and intensity [69]. Figure 2.5 shows a schematic drawing of the European Organization for Nuclear Research (CERN) accelerator complex.

In the case of proton beams, hydrogen gas is ionized in a duoplasmatron source to produce H^- ions. These beams are accelerated in the Linear Accelerator (LINAC) 4. This accelerator is 35 m long and accelerates beams to 160 MeV and then injects them into the Booster. The Booster is a four-ring synchrotron with a 157 m circumference. It accelerates protons to 2 GeV. The beam then enters the Proton Synchrotron (PS). This accelerator has 628 m circumference and reaches 26 GeV before transfer to the Super Proton Synchrotron (SPS).

The CERN accelerator complex
Complexe des accélérateurs du CERN
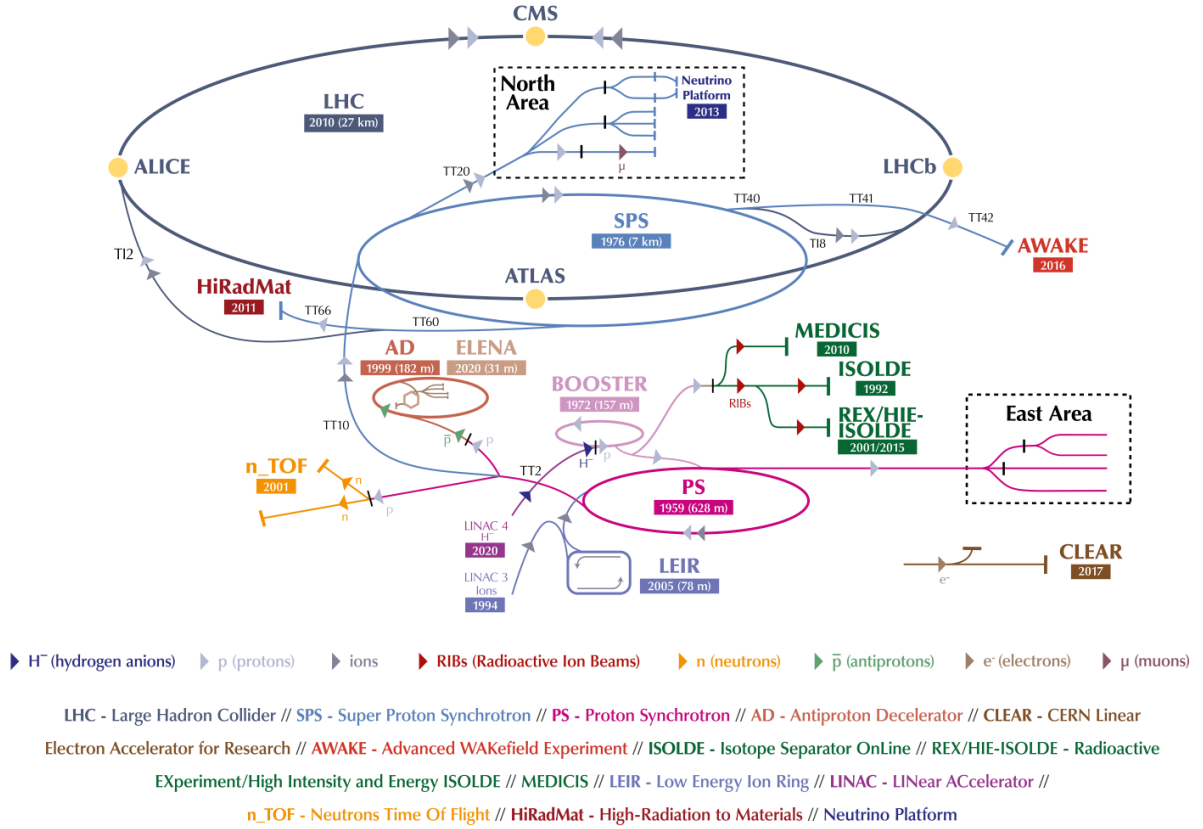
Figure 2.5: The CERN accelerator complex showing the chain of pre-accelerators supplying protons and heavy ions to the LHC. Protons are accelerated via LINAC 4 → Booster → PS → SPS, while lead ions follow LINAC 3 → LEIR → PS → SPS [68].

The SPS has 6.9 km circumference and accelerates it to the LHC injection energy of 450 GeV. The beams are then injected into the LHC, where they are ramped up to the nominal collision energy of 6.8 TeV.

To produce heavy ion beams, fully stripped $^{208}\mathrm{Pb}^{82+}$ ions are generated in an Electron Cyclotron Resonance (ECR) source and pre-accelerated in LINAC 3. They are then accumulated and cooled in the Low Energy Ion Ring (LEIR) before being sent through the PS and SPS, and finally injected into the LHC.

The chain delivers the high-intensity, low-emittance beams that enable the luminosity and event statistics necessary for the quarkonium polarization analysis in this work.

2.2 CMS Detector

The CMS detector is built around its collision point with a series of concentric cylindrical subdetectors that include a silicon tracker, an Electromagnetic Calorimeter (ECAL), a Hadron Calorimeter (HCAL), a superconducting solenoid, and muon chambers. Figure 2.6 shows a cross section photograph of the CMS detector, annotated with subdetector names and example particle trajectories. The following sections describe each of these subdetectors in detail, beginning with its coordinate system.

2.2.1 Coordinate system

Figure 2.7 illustrates the CMS coordinate system. CMS employs a right-handed coordinate system that is optimized for collider physics analyses. The origin is defined at the nominal interaction point, which corresponds to the design center of the detector. Geometrically, this point approximately coincides with the barycentre of the Barrel Pixel Detector (BPIX). In practice, the true luminous region is displaced from this nominal point, and these deviations are measured and corrected for in beam spot calibration and alignment. The z-axis is aligned

25
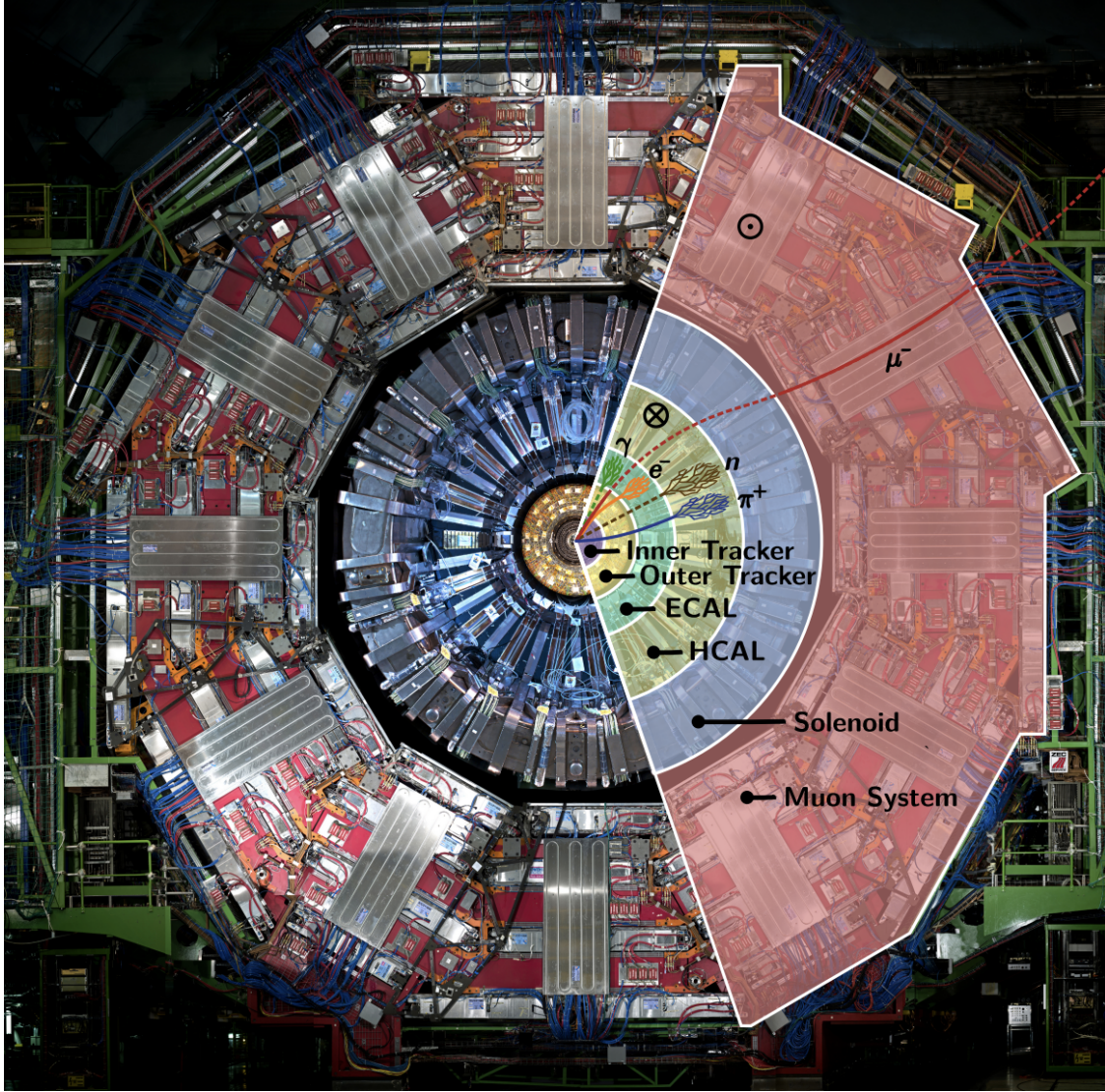
Figure 2.6: Cross section photograph of the CMS detector with schematic overlays indicating the main subdetectors and typical particle interactions. Starting from the interaction point at the center: charged particles are reconstructed in the silicon Inner and Outer Tracker; photons and electrons deposit energy in the electromagnetic calorimeter (ECAL); hadrons are measured in the hadron calorimeter (HCAL); and muons are identified in the outer Muon System after traversing the superconducting solenoid. The colored lines illustrate the paths of representative particles (γ, e^-, n, π^+, μ^-). Symbols indicate the magnetic field direction: $\otimes$ denote magnetic field lines going into the page, and $\odot$ denotes field lines coming out of the page. The annotated version is adapted from Ref. [70], based on the original photograph from Ref. [71].
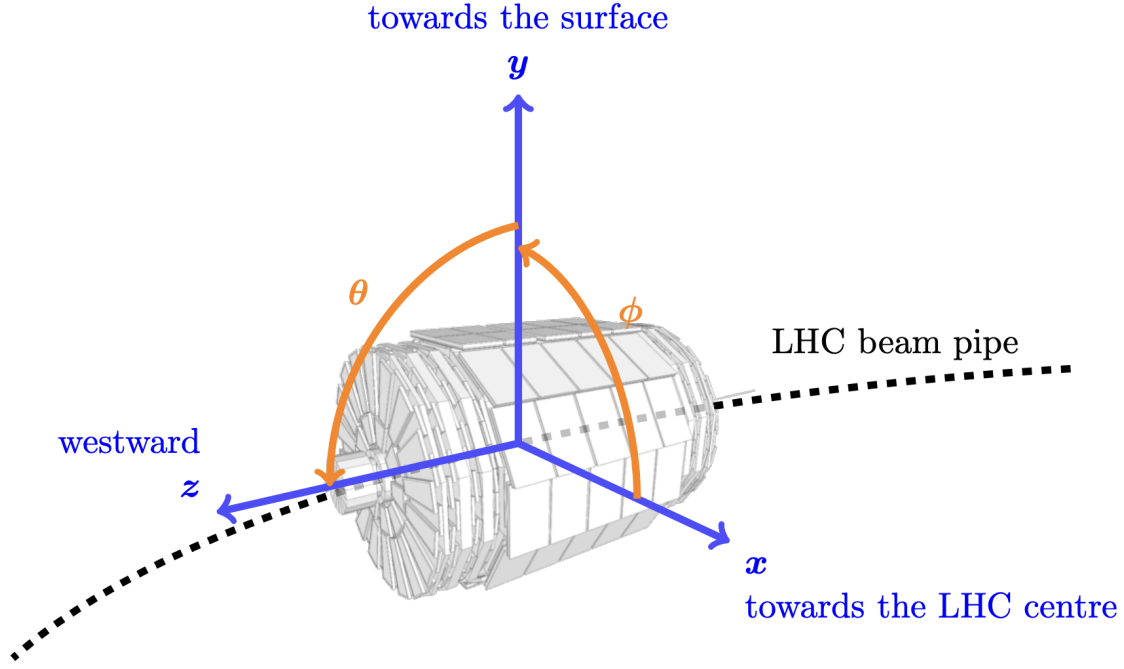
Figure 2.7: CMS coordinate system: z-axis along the beam pipe, x-axis toward the LHC ring center, and y-axis upward. In cylindrical coordinates (r, φ, z), r is the radial distance from the beamline, θ is the polar angle with respect to the z-axis, and φ is the azimuthal angle around the beam axis (denoted as ϕ in the figure) [72].

with the beam direction, the x-axis points radially toward the LHC ring center, and the y-axis is directed vertically upwards. The azimuthal angle φ is measured in the x-y plane around the z-axis and the polar angle θ denotes the angle between the particle momentum and the z-axis. Pseudorapidity, η, is used to describe angular coverage as it remains approximately invariant under Lorentz boosts along the beam direction. Since it depends only on θ, it provides an alternative way of expressing that angle, and is defined as:

$$\eta = -\ln\left[\tan\left(\frac{\theta}{2}\right)\right]. \tag{2.11}$$
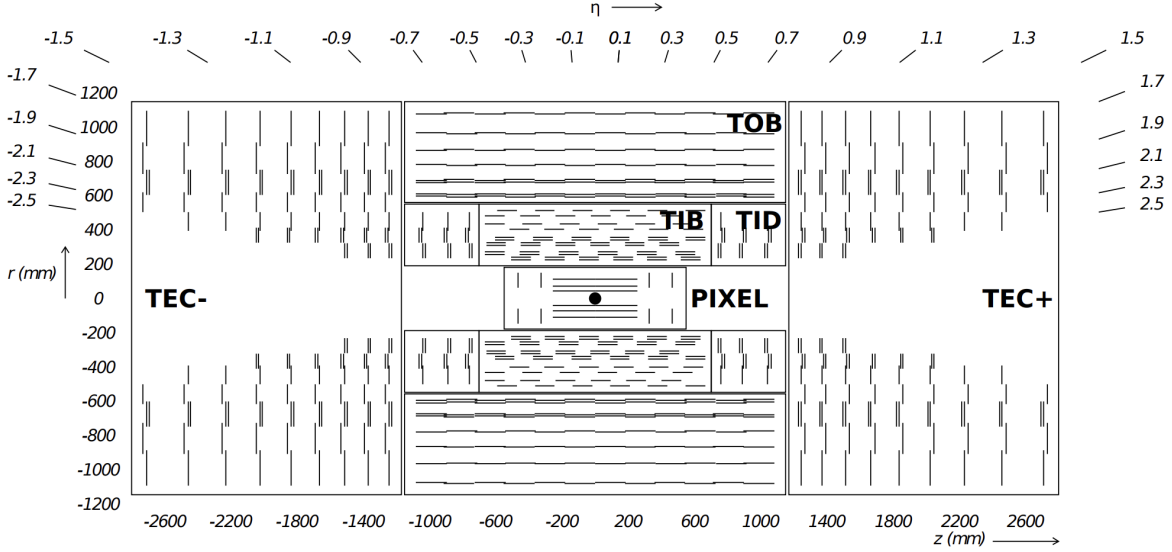
Figure 2.8: Schematic cross section of the CMS tracker in y–z plane. Each line represents a detector module: the barrel pixel (BPIX) and forward pixel (FPIX) detectors in the innermost layers. The pixel detectors are surrounded by the silicon strip detectors of the Tracker Inner Barrel (TIB), Tracker Outer Barrel (TOB), Tracker Inner Disks (TID), and Tracker Endcaps (TEC). Double lines indicate double-sided modules which deliver stereo hits [73]. The black dot at the center denotes the origin of the detector geometry (interaction point). The radial direction extends outward from the origin and the z-axis is along the beam pipe. The slanted lines annotated with numbers indicate lines of constant pseudorapidity η, with positive η defined along the $+z$ direction.

2.2.2 Silicon tracker

The silicon tracker is responsible for reconstructing charged-particle trajectories and interaction vertices with high precision. It consists of two subsystems: the pixel detector in the innermost layers, and the silicon strip detectors in the outer regions. Both operate on the same fundamental principle: when a charged particle traverses a silicon sensor, it ionizes the material, creating electron-hole pairs along its path. Under an applied electric field, these charges drift to the electrodes, producing a current pulse that is amplified and digitized by the readout electronics. This solid-state technology provides excellent spatial resolution, fast response times, and high rate capability, making silicon an ideal choice for the LHC envi-

ronment. These properties enable the silicon tracker to surpass traditional gaseous trackers in spatial precision, rate handling, and operational stability, all of which are indispensable for the high-luminosity LHC.

The tracker layout in the longitudinal (y-z) plane is shown in Fig. 2.8 (corresponding to the coordinates in Fig. 2.7). The innermost pixel detector provides three-dimensional space points close to the interaction region, with three concentric barrel layers (BPIX) and two forward disks (Forward Pixel Detector (FPIX)) on each endcap. The silicon strip detectors surround it, which extend the tracking coverage up to $|\eta| < 2.5$. The Tracker Inner Barrel (TIB) and Tracker Outer Barrel (TOB) are in the barrel, and the Tracker Inner Disks (TID) and Tracker Endcaps (TEC) are in the endcaps.

Pixel detectors provide the high granularity required for pattern recognition and vertexing in the innermost region, while strip detectors give precise momentum measurements over the full tracker volume in a cost effective way. The following sections describe each in detail.

2.2.2.1 Silicon pixel detectors

Silicon pixel detectors (Fig. 2.9) are positioned closest to the interaction point, where the particle flux is highest. Each sensor is segmented into small two-dimensional pixels, typically measuring $100 \times 150 \ \mu\text{m}^2$. The fine segmentation allows each traversing particle to produce a distinct, localized charge signal, yielding a three-dimensional space point from a single hit. This enables unambiguous pattern recognition in the dense environment near the beamline. Pixels are crucial for track seeding and vertex reconstruction, providing micrometer-level precision for locating primary and secondary vertices, a process that is essential for heavy-flavor tagging and quarkonium analyses. Their design integrates readout electronics directly behind each pixel cell, allowing fast, zero-suppressed data acquisition at rates of several hundred hits per square centimeter per bunch crossing. This capability comes at the cost of increased complexity, power consumption, and manufacturing expense [65, 76].
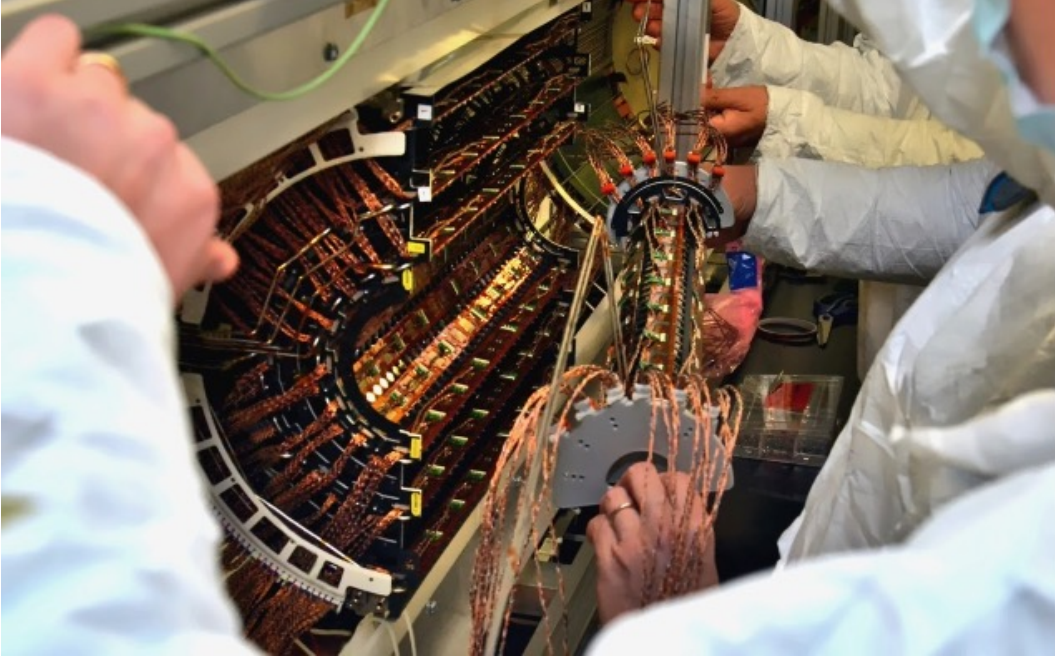
Figure 2.9: Mechanical insertion of the innermost silicon tracker support structure. The outer cylindrical part shown corresponds to one half of the new 3-layer pixel detector module [74, 75].

2.2.2.2 Silicon strip detectors

Silicon strip detectors (Fig. 2.10) cover the outer tracker volume where hit rates are lower, but a long lever arm is needed for precise momentum measurements. Each strip sensor consists of long, narrow strips, typically several centimeters in length and 80–200 μm in width, providing a one-dimensional measurement perpendicular to the strip orientation. When a charged particle traverses the sensor, it ionizes the silicon along its path. The resulting charge is collected on the intersected strips, yielding a spatial hit coordinate. To obtain full three-dimensional space points, multiple layers are used. Some layers employ double-sided modules with two sensors mounted back-to-back. Their strips are rotated relative to each other by a small stereo angle of about 100 mrad in CMS. This configuration provides two independent measurements at each module, improving spatial resolution and enabling robust
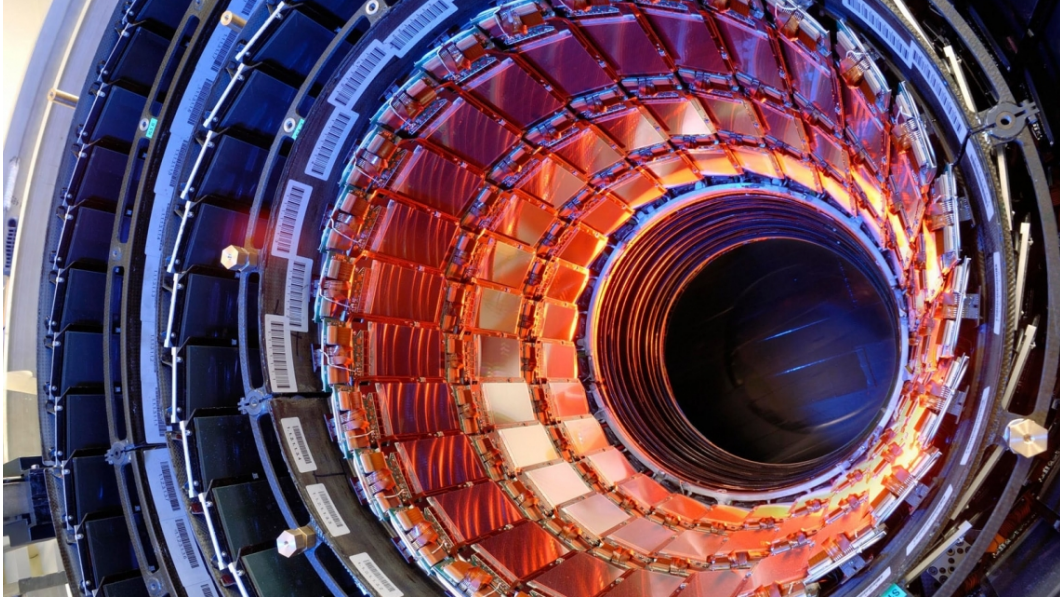
Figure 2.10: CMS tracker showing silicon strip detectors in the barrel module [77].

pattern recognition while keeping the number of readout channels manageable [75].

2.2.3 Electromagnetic calorimeter

The ECAL (Fig. 2.11) consists of the ECAL Barrel (EB), ECAL Endcap (EE), and ECAL Preshower (ES). This subdetector measures the energies of electrons and photons by fully absorbing them in dense scintillating crystals and reconstructing the electromagnetic showers they produce. High-energy electrons entering the absorber material lose energy via bremsstrahlung as they interact with atomic nuclei; high-energy photons initiate showers through pair production, generating electron-positron pairs. These secondary electrons and positrons undergo further bremsstrahlung and pair creation, resulting in a cascade of charged particles that deposit their energy in the crystals.

The ECAL in CMS is made of 75,848 lead tungstate ($PbWO_4$) crystals [80]. Lead tungstate was chosen for its high density (8.3 g/cm^3), short radiation length ($X_0 = 0.89$ cm),
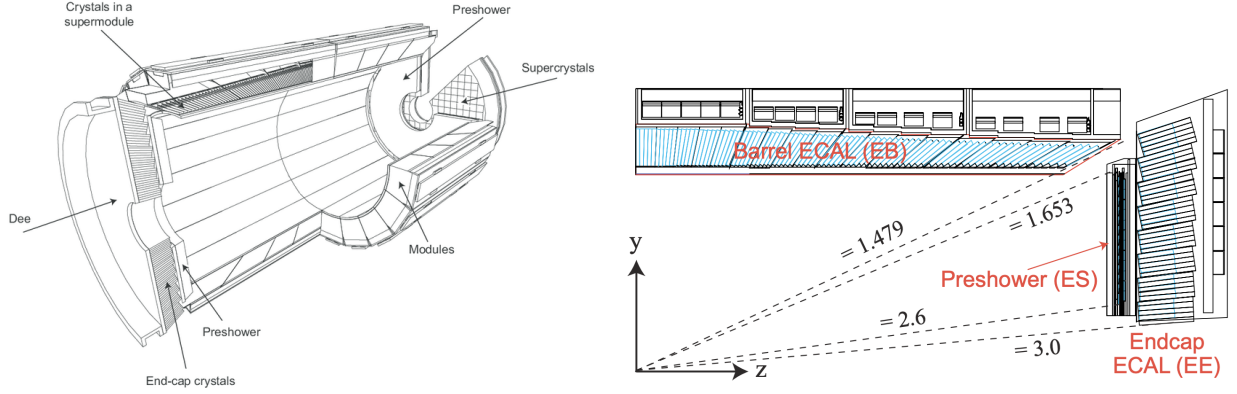
Figure 2.11: Layout of the ECAL. Left: barrel supermodules, the two endcaps and the preshower detectors [78]. Right: quadrant view of the ECAL in the y-z plane, including EB, EE, and ES [79].

and fast scintillation response (~ 10 ns), which enable excellent spatial and timing resolution in the high-luminosity LHC environment. Each crystal functions as an independent calorimeter cell: when traversed by shower particles, the crystal emits scintillation light proportional to the deposited energy. This light is detected by avalanche photodiodes (APDs) in the barrel [81] and vacuum phototriodes (VPTs) in the endcaps [82]. The light is then digitized by the front-end electronics.

The ECAL achieves a stochastic energy resolution of roughly

$$\frac{\sigma_E}{E} \approx \frac{2.8\%}{\sqrt{(E/1 \text{ GeV})}} \oplus 0.3\%, \tag{2.12}$$

where the first term is the stochastic contribution (dominated by photon statistics in the crystals) and the second term is the constant arising from calibration and detector uniformity. This performance is essential for precision measurements such as $H \to \gamma\gamma$ and $Z \to e^+e^-$, as well as electromagnetic probes of the QGP in heavy ion collisions [65, 80]. Figure 2.12 shows the installation of the last ECAL barrel supermodule, illustrating the engineering scale of the detector.
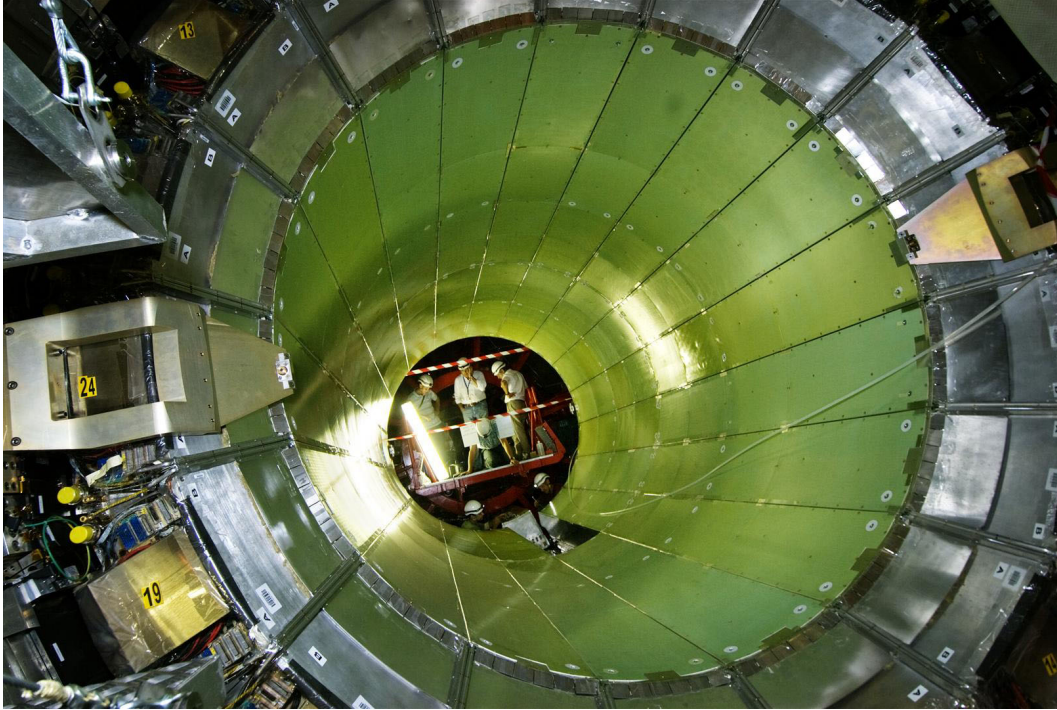
Figure 2.12: Insertion of the last CMS ECAL supermodules in the EB+ [83].

2.2.4 Hadron calorimeter

The HCAL measures the energy of hadrons (such as pions, kaons, and neutrons) by fully containing the hadronic showers they produce when interacting with dense absorber material. It is a sampling calorimeter, consisting of alternating layers of passive absorbers and active scintillator. The absorbers, made of thick brass plates, are dense enough to induce nuclear interactions of incoming hadrons and generate cascades of secondary particles. Even neutral hadrons such as neutrons are detected indirectly, as their strong interactions produce secondary charged particles that ionize the scintillator. The scintillator layers, placed between the absorber plates, act as the active medium: when charged shower particles traverse the scintillator layers, the scintillator emits light pulses. These signals are collected by wavelength-shifting fibers, transmitted to hybrid photodiodes, and digitized by the front-end
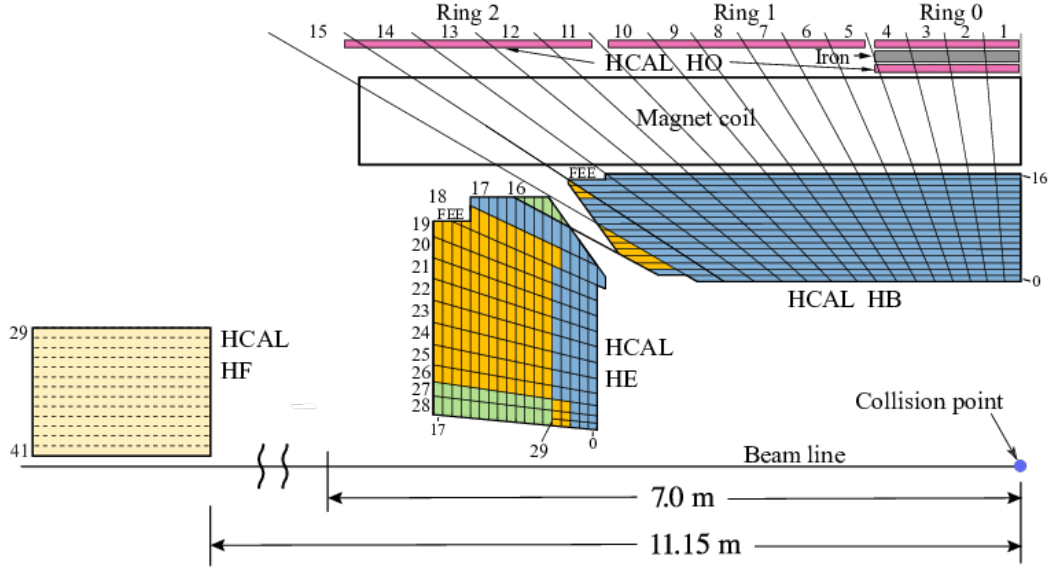
Figure 2.13: A schematic view of the quadrant HCAL detectors in the *y-z* plane [84].

electronics [65, 85].

Because hadronic showers have a large invisible energy component (for example, nuclear binding energy losses, neutrons, and low-energy particles below detection thresholds) and show larger fluctuations than electromagnetic showers, the HCAL resolution is limited on its own. It is therefore combined with the ECAL to provide accurate jet-energy and missing transverse energy ($E_{\mathrm{T}}^{\mathrm{miss}}$) measurements.

The HCAL consists of four subsystems, as shown in Fig. 2.13: the barrel (Hadron Barrel (HB)), two endcaps (Hadron Endcap (HE)), outer calorimeter (Hadron Outer (HO)) located outside the solenoid to catch leakage, and the forward calorimeter (Hadron Forward (HF)) extending coverage to $|\eta| < 5$. Together, they ensure nearly hermetic calorimetry, essential for reconstructing energy balance in $p + p$ and heavy ion collisions. The unique forward coverage of HF is also used for minimum-bias triggering and centrality determination in heavy ion runs.

34

2.2.5 Superconducting solenoid

The silicon tracker, ECAL, and HCAL are enclosed within a superconducting solenoid generating a 3.8 T magnetic field [65, 86]. The field bends charged-particle trajectories, allowing their momenta to be measured precisely when combined with the silicon tracker.

The solenoid is 6 m in diameter and 13 m in length, making it the largest superconducting magnet ever built. Surrounding the solenoid is a massive steel return yoke, which both confines the magnetic flux and provides structural support.

The solenoid is located inside the muon system because extending it to the muon chambers would require a prohibitively large magnet, which would be technically challenging and unnecessary. Muons can already be efficiently identified and measured using detectors embedded in the return yoke that provides the additional bending power.

2.2.6 Muon chambers

The muon system measures muon momentum and provides a robust trigger over a wide pseudorapidity range ($|\eta| < 2.4$). Muons traverse the calorimeters, solenoid, and return yoke with minimal energy loss. Their momentum is therefore measured from the curvature of their tracks in the 3.8 T solenoidal magnetic field, using gas-ionization detectors embedded in the steel return yoke. The system also generates fast-trigger signals for muon identification and timing [65, 87]. It comprises four layers of muon stations in the barrel and endcaps, using four complementary technologies: Drift Tube (DT), Resistive Plate Chamber (RPC), Cathode Strip Chamber (CSC), and Gas Electron Multiplier (GEM) (fig. 2.14).

2.2.6.1 DTs

Drift Tubes (DTs) are large rectangular drift cells filled with a gas mixture located in the barrel region ($|\eta| < 1.2$). A traversing muon ionizes the gas and the released electrons drift
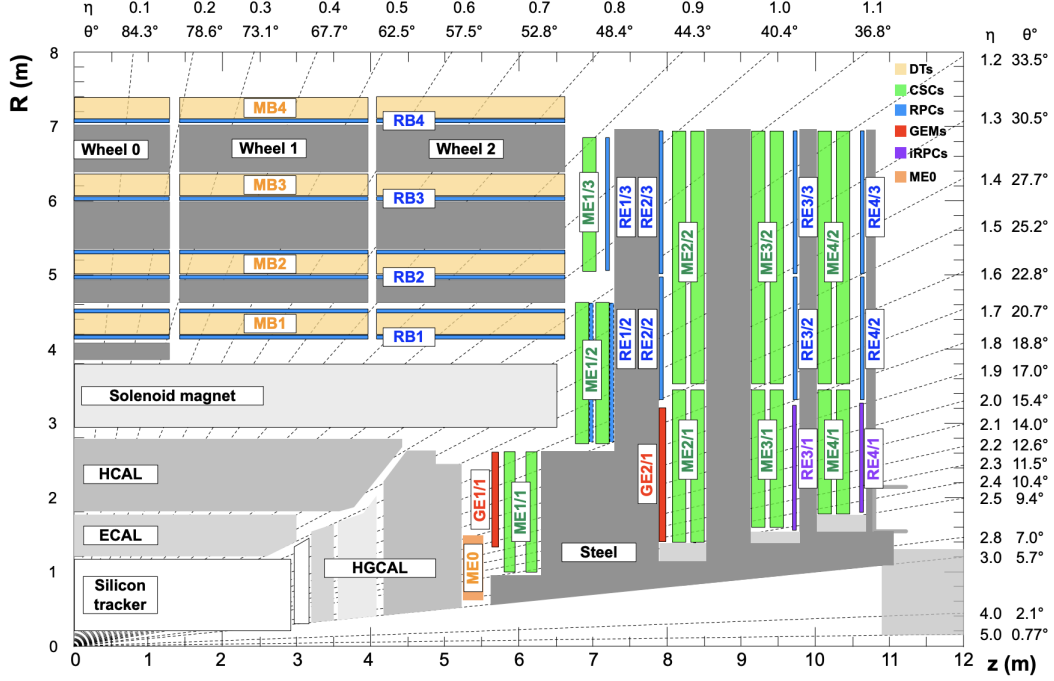
Figure 2.14: A cross section of a quadrant of the CMS detector in the R-z plane showing the various muon stations (colored boxes) and the steel flux-return disks (dark-gray areas). The DT stations in the barrel are labeled MB. The CSCs in the endcaps are labeled ME. RPCs are mounted in both the barrel and endcaps of CMS and labeled RB and RE, respectively. GEM, introduced in the forward region, are labeled GE. The vertical axis indicates the radial distance R from the beamline, and the horizontal axis shows the longitudinal distance z along the beamline. The numbers along the top and right edges denotes pseudorapidity (η) values together with the corresponding polar angle θ (see Eq.(2.11)) [87].

toward an anode wire under an electric field. The drift time is used to reconstruct the muon position with a spatial resolution of 100–200 μm. DTs provide precise position measurements in the low-background central region [88].

2.2.6.2   RPCs

Resistive Plate Chambers (RPCs) are parallel-plate gaseous detectors with excellent time resolution ($\sim$1–2 ns), installed in both the barrel ($|\eta| < 1.2$) and endcap ($|\eta| < 2.1$) regions.

They consist of resistive plates with a uniform electric field. When a muon passes between the plates, it triggers an avalanche in the gas gap, generating a fast electrical signal. RPCs are primarily used for triggering because of their fast timing response. They provide an independent confirmation of muon identification alongside DTs and CSCs [89].

2.2.6.3 CSCs

Cathode Strip Chamber (CSCs) are multiwire proportional chambers located in the endcap region ($0.9 < |\eta| < 2.4$). Each chamber consists of a gas volume bounded by cathode panels, with layers of wires running through it. When a muon traverses a CSC, it loses energy by ionizing the chamber gas. The freed electrons drift toward the anode wires, where gas amplification produces detectable signals. The induced charge on the cathode strips provides precise two-dimensional position measurements in the plane perpendicular to the wires. The timing of the signals on the anode wires ("wire timing") adds information along the beam direction. CSCs are specifically designed to cope with the high hit rates and background levels in the endcaps, making them the principal tracking and triggering detectors in this region [90].

2.2.6.4 GEMs

Gas Electron Multiplier (GEM) detectors, added in the Phase-1 upgrade of CMS, cover the very forward region ($1.6 < |\eta| < 2.4$). They consist of thin perforated foils that amplify electrons as they drift through successive stages. GEMs provide high spatial resolution, excellent rate capability (exceeding MHz/cm^2), and fast timing. These features enhance muon triggering and tracking in the very forward regions, which are the most challenging regions of the detector [91, 92].
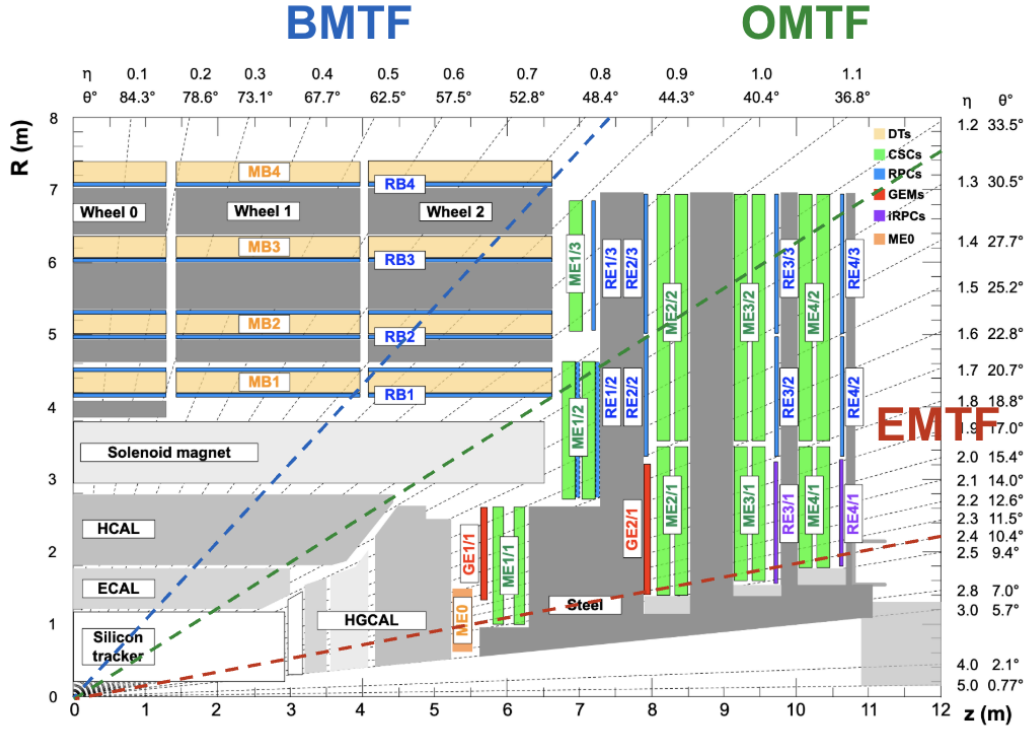
Figure 2.15: L1 muon track finders (BMTF, OMTF, and EMTF) used in the CMS trigger system to identify muon candidates, based on data from the DT, CSC, and RPC detectors. This figure is the same cross sectional view of the CMS detector as in Fig. 2.14, but now with the regions used by the three muon track finders overlaid. The diagram illustrates the parts of the detector where the track segments are reconstructed in the barrel, endcap, and barrel-endcap transition regions [87, 93].

2.2.7   Trigger system

The CMS trigger system reduces the raw LHC bunch-crossing rate of 40 MHz to a manageable output of about 1 kHz for permanent storage, while maintaining high efficiency for physics signals of interest. It operates in two stages: the hardware-based Level-1 (L1) trigger and the software-based High-Level Trigger (HLT) [65, 87].
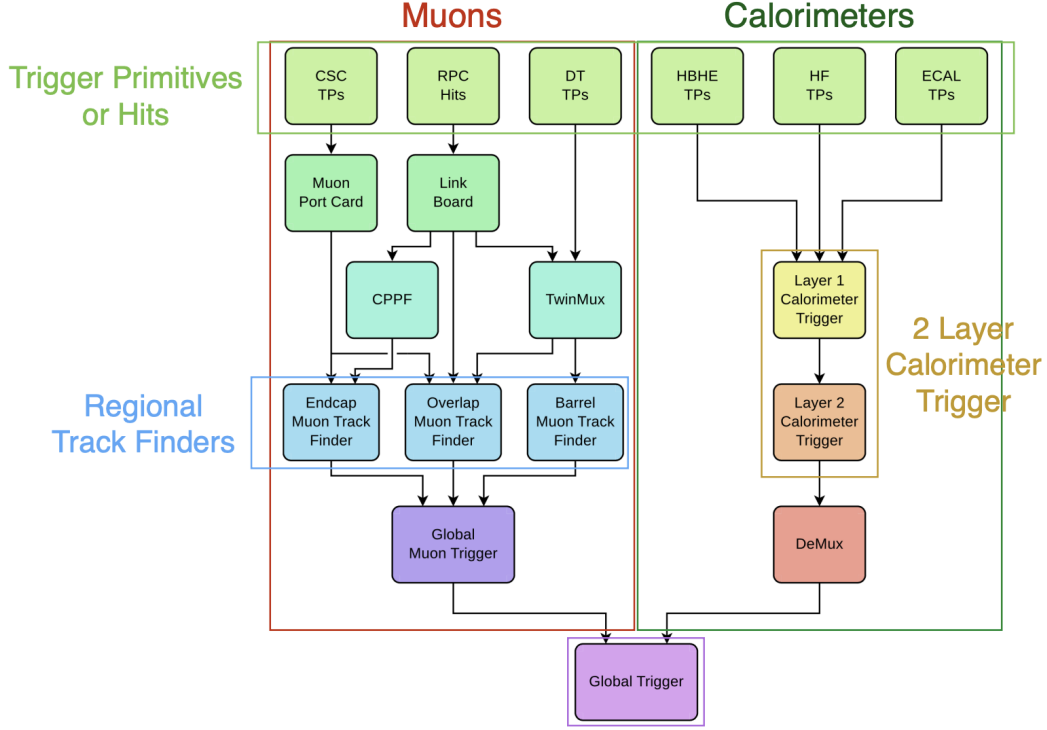
Figure 2.16: Schematic of the L1 trigger architecture showing the components involved in event selection, including the calorimeters (ECAL, HCAL), the muon system (DT, CSC, RPC), and the hardware-based processing units that perform real-time event selection [87, 93].

2.2.7.1 L1 trigger

The L1 trigger is implemented in dedicated hardware processors based on custom electronic boards. It performs real-time event selection within a fixed latency of about 4 μs. It also reduces the input rate of 40 MHz bunch crossings to about 100–120 kHz, which can then be handled by the software-based HLT. The L1 trigger uses information from the calorimeters (ECAL, HCAL) and the muon system (DT, CSC, RPC) to identify missing transverse energy and high-p_T objects such as muons, electrons, photons, and jets. Although the L1 trigger reconstructs several types of objects, the discussion here focuses on the muon trigger, which provides the key observables for the Υ polarization measurements presented in this thesis.

39

To measure muons, three dedicated regional track finders (see Fig. 2.15) reconstruct local track segments in different parts of the detector [87, 93]:

- Barrel Muon Track Finder (BMTF) uses DTs and RPCs in the barrel ($|\eta| < 0.83$).

- Overlap Muon Track Finder (OMTF) combines DT, CSC, and RPC data in the barrel-endcap transition ($0.83 < |\eta| < 1.24$).

- Endcap Muon Track Finder (EMTF) reconstructs muons using CSCs (and RPCs) in the endcaps ($1.24 < |\eta| < 2.4$).

Each of these regional triggers assigns a quality code to its muon candidates to quantify the reliability of the reconstruction. The definitions vary by subsystem:

- In the BMTF, the code reflects the number and pattern of DT and RPC stations contributing to the track. Four-station tracks are assigned the highest quality (7). Candidates reconstructed with fewer stations receive lower values.

- In the OMTF, the muon quality corresponds to the number of detector layers with valid hits, reflecting the complexity of the barrel-endcap overlap region.

- In the EMTF, the muon quality is encoded as a bit-mask specifying which CSC (and RPC/GEM) stations contributed. For example, code 12 (binary 1100) denotes a candidate formed from stations 1 and 2. By construction, at least two stations must be present.

In the case of the BMTF and OMTF, certain code values are reserved for special cases: for example, code 1 corresponds to beam-halo muons while codes 2–4 are typically suppressed in trigger menus. A summary of the BMTF/OMTF codes, together with the EMTF station-bitmask, is given in Table 2.1 [94].

Subsystem	Regional code	Meaning
BMTF/OMTF	0	Empty candidate
	1	Halo muon (CSC-only)
	2–4	Very low quality (poor patterns)
	5	RPC-only (unmatched)
	6	DT- or CSC-only (unmatched)
	7	Matched DT/RPC or CSC/RPC (highest)
EMTF	0–15	Station bitmask (e.g. 1001 = stations 1+4)

Table 2.1: Regional quality codes for L1 muons. The BMTF and OMTF use a 3-bit regional quality (0–7), while the EMTF uses a 4-bit code (0–15) corresponding to station hit patterns.

All regional muon candidates are forwarded to the Global Muon Trigger (GMT)[2], which merges inputs from the BMTF, OMTF, and EMTF (see Fig. 2.16). The GMT suppresses duplicates from subsystem overlaps and remaps the regional quality codes into a standardized global scale represented by a 4-bit code ranging from 0 to 15. This mapping is summarized in Table 2.2. In practice, the muon trigger menus apply two quality categories: Double Quality (DQ) and Single Quality (SQ). DQ is defined as global codes 8–15, and SQ is defined as global codes 12–15. The GMT then selects the highest quality muons (up to four per event) and forwards them to the HLT [94].

2.2.7.2 HLT

The HLT is responsible for further filtering events after the L1 trigger. It reduces the event rate from ~ 100 kHz (from the L1 output) to ~ 1 kHz using a software-based system running on commercial Central Processing Units (CPUs). The HLT performs full event reconstruction in order to identify physics signals and efficiently reduce the dataset for offline storage and analysis [95].

---

[2]In the Phase-1 upgrade, the hardware implementation of the GMT was replaced by the μGMT, but its logical function remains the same. In this thesis, the term GMT is used generically.

Global code	Meaning	Quality category
0	Empty candidate	–
1	Beam-halo muon (CSC-only)	–
2–4	Very low quality (partial patterns)	Suppressed
5–6	Single-subsystem track (RPC, DT, or CSC only)	–
7	Matched DT/RPC or CSC/RPC candidate	–
8–11	Multi-station candidate (good quality)	DQ
12–15	High-quality multi-station candidate	SQ, DQ

Table 2.2: Global muon quality codes assigned by the GMT. The 4-bit code (0–15) is derived from the number and pattern of muon stations contributing to the candidate.

Muon HLT reconstruction proceeds in two stages:

- Level-2 (L2): "Standalone" muons are reconstructed using information only from the seeds from muon chambers (e.g., DT, CSC, RPC). This step uses segment fitting from the muon detectors and performs outside-in track fitting. At this stage, early selections (including p_T, invariant mass, and calorimeter-based isolation) are applied to reduce the event rate.

- Level-3 (L3): Surviving L2 muons are matched to tracks reconstructed in the silicon tracker, using regional tracking around the muon trajectory. This step provides the "global" muon reconstruction, combining the tracker and muon chamber data to achieve full momentum resolution. Final selections are made at this stage by applying refined criteria: p_T, invariant mass, impact parameter, track quality, and tracker-based isolation.

This two-stage process ensures high muon efficiency, even in the high-occupancy environment of Pb + Pb collisions. The process is also effectively reduced the event rate to manageable levels for offline storage and analysis [96].

Chapter 3

Data and MC Samples

This chapter provides detailed information on the data and MC samples used in the analysis. The data serve as the basis for extracting polarization observables, while the MC samples are used to constrain signal-shape parameters in the signal extraction procedure and to model detector effects such as acceptance and efficiency corrections.

3.1   Sample Overview and Configuration

This analysis is based on the PbPb collision data recorded in 2018 at a nucleon-nucleon center-of-mass energy of $\sqrt{s_{NN}} = 5.02$ TeV. Both data and official MC samples were analyzed in the Mini Analysis Object Data (MiniAOD) [97] data tier, a CMS-defined processing level optimized for analysis-level workflow and were reconstructed using the CMS Software Framework (CMSSW) version `11_2_X`.

This analysis utilizes three types of samples: (i) the 2018 PbPb collision data collected with dimuon triggers (discussed in Sec. 3.2.1); (ii) a PYTHIA-embedded HYDJET MC sample generated with PYTHIA 8 and embedded into a heavy ion background, which includes full detector simulation and is used for signal modeling and efficiency studies; and (iii) a ded-

icated, private, generator-level PYTHIA 8 sample produced under CMSSW version `14_1_8` and used exclusively for acceptance calculations in order to avoid potential biases from the embedded sample.

Label	Sample Type	Dataset Path	Global Tag (GT)	Number of Events
(i)	Data	DAS Path[1]	112X_dataRun2_PromptLike_HI_v7	69M
(ii)	$\Upsilon(1S)$ PYTHIA -embedded Hydjet MC	DAS Path[2]	112X_upgrade2018_realistic_HI_v9	10M
(iii)	$\Upsilon(1S)$ PYTHIA MC	DAS Path[3]	141X_mcRun3_2024_realistic_ppRef5TeV_v7	50M

Table 3.1: Summary of the dataset paths, Global Tags (GTs), and event statistics for data and MC samples used in this analysis. Dataset paths are provided in footnotes.

As listed in Table 3.1, the analysis uses one data sample and two MC samples, with their corresponding Global Tags (GTs) and event statistics. A GT defines a CMS-specific configuration that bundles together a consistent set of versioned conditions for a given data-taking or simulation scenario (e.g., a specific data-taking year or MC campaign). Each condition is stored under a tag, representing a record in the CMS Condition Database (CondDB). The GT provides a snapshot of all relevant tags required for a consistent reconstruction or simulation within CMSSW.

Although the private MC sample was generated using CMSSW version `141X`, neither the CMSSW version nor the GT affect the polarization analysis. This is because the acceptance calculation relies exclusively on generator-level kinematics, such as the transverse momentum and pseudorapidity of individual muons, without applying any vertex position cuts or modeling reconstruction and detector response.

---

[1] `/HIDoubleMuon/HIRun2018A-PbPb18_MiniAODv1-v1/MINIAOD`

[2] `/Upsilon1S_pThat-2_TuneCP5_HydjetDrumMB_FixCalo_5p02TeV_pythia8/HINPbPbSpring21MiniAOD-FixL1Cal oGT_112X_upgrade2018_realistic_HI_v9-v1/MINIAODSIM`

[3] `/Upsilon1S_pTHatMin2GeV_nopTHatBias_5p02TeV_TuneCP5_/fdamas-GEN_11June2025-a3898be0d6fb7085f390 daa3dbe4d15f/USER`

3.2 Data Samples

The 2018 heavy ion data-taking period at the LHC spanned runs 325530 to 327802, as recorded in the Online Monitoring System (OMS) [98]. This analysis uses only the subset of data recorded during the "stable beams" period, corresponding to runs 326381–327564. Stable beam status was declared by the LHC when the beam conditions are suitable for physics-quality data-taking.

To ensure that only high-quality data are used, the CMS Data Quality Monitoring (DQM) team checked detector performance both in real time and during offline certification. Only periods in which all detector systems functioned properly are certified as "good for physics." These certified intervals are listed in a JSON file,[4] where each unit of time is referred to as a *luminosity section*, lasting approximately 23.3 seconds.[5]

The data used in this analysis come from the `DoubleMuon` primary dataset, which includes events containing two muons that pass a specific trigger, described in Sec. 3.2.1. In CMS terminology, a dataset refers to a group of events selected by related trigger paths designed for a particular physics purpose, such as dimuon-from-quarkonium decays.

After applying the initial selection criteria, the total dataset corresponds to an integrated luminosity of $1.61\,\mathrm{nb}^{-1}$, computed using the standard CMS luminosity tool, `brilcalc`, with the recommended calibration file.[6] This value is quoted only to indicate the size of the analyzed dataset; the polarization measurement itself does not depend on the absolute luminosity value.

The selection of events for this analysis proceeds in two stages. First, during data-taking, the CMS trigger system, including the hardware-based L1 and software-based HLT, selects

---

[4]Available at: `https://cms-service-dqmdc.web.cern.ch/CAF/certification/Collisions18/HI/PromptReco/Cert_326381-327564_HI_PromptReco_Collisions18_JSON_MuonPhys.txt`.

[5]This duration is defined by convention, based on the time it takes for the beams to complete 2^{18} revolutions around the LHC ring.

[6]`/cvmfs/cms-bril.cern.ch/cms-lumi-pog/Normtags/normtag_BRIL.json`, which is accessible under the CERN LXPLUS system.

events that are likely to contain two muons. This significantly reduces the dataset size by keeping only events that may contain interesting physics signals.

In the second stage, during the offline analysis, these pre-selected events are further filtered to identify high-quality Υ candidates. This procedure involves applying kinematics and quality criteria to the reconstructed muon pairs in order to isolate signal events from the background. Further details are provided in the following subsections.

3.2.1 Event selection
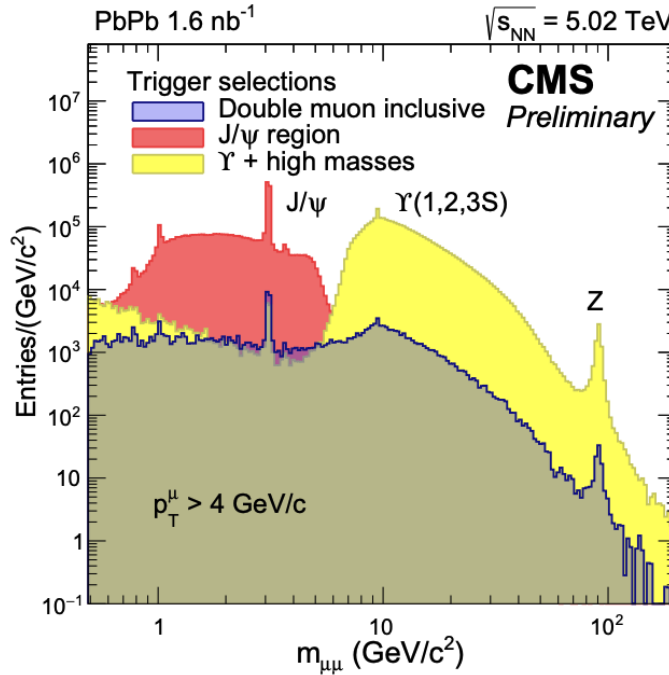
Figure 3.1: Invariant mass distributions of dimuons after applying different trigger selections in 2018 PbPb data. The purple histogram corresponds to the inclusive double-muon trigger, the red histogram to the J/ψ trigger region, and the yellow histogram to the Υ trigger region [99].

Events containing muons from possible Υ decays are identified using a dedicated trigger path `HLT_HIL3Mu2p5NHitQ10_L2Mu2_M7toinf_v1`, in the CMS detector's HLT system,

46

designed to select events with two muon candidates. In each selected event, both muons must be reconstructed at the L2 of the HLT with $p_T > 2$ GeV/c. In addition, at least one of the two muons must be matched to a track reconstructed in the silicon tracker at the L3, with $p_T > 2.5$ GeV/c. The L2 muons are reconstructed using only the muon chambers, whereas the L3 muons are reconstructed with a combined fit including both the tracker and muon chambers, resulting in a much better p_T resolution. To ensure reconstruction quality, the track must include at least ten *high-quality* hits in the inner tracker. The track quality imposes additional requirements on the number of 3-D hits, the χ^2/ndf of the fit, and the significance of the impact parameters [100]. Events are selected if they contain at least one L2 muon and one L3 muon, forming a pair with an invariant mass greater than 7 GeV/c^2. Figure 3.1 shows the invariant mass distributions of dimuons for the different trigger selections, with the yellow histogram corresponding to events passing the Υ trigger.

Following trigger selection, offline event filters at the analysis stage are applied to suppress background events originating from beam-gas collisions, electromagnetic interactions between the colliding nuclei, etc. Each event must have at least one reconstructed primary vertex based on at least two tracks.[7] The shape of the clusters in the silicon pixel detectors must also be consistent with the direction of the tracks, pointing to the reconstructed primary vertex.

Additionally, to ensure the event comes from a hadronic interaction, events are selected by requiring at least three towers in each half of the HF calorimeters, with an energy greater than 4 GeV per tower. This condition introduces inefficiency in the most peripheral events; therefore, the analysis focuses on the 0–90% most central collision events, where the event selection is fully efficient.

---

[7]The average number of primary vertices for the 2018 Pb + Pb dataset is 1.007.

3.2.2 Υ candidate selection

Once the relevant events are identified, the next step is to select the muons that come from Υ decays. The performance of reconstructed muon object (i.e., muons defined within the CMS reconstruction framework) for the 2018 Pb + Pb data has been studied in detail in a CMS analysis note (AN-2018/316) and reported in a dedicated paper [96]. In this section, the quality criteria used in this analysis are described, along with the motivations for each choice.

Muons are required to pass the *hybrid-soft Identification (ID)* criteria [96], which is a version of the *soft muon ID* optimized for hadronic Pb + Pb events. These criteria include:

- The muon must be reconstructed as both a tracker and a global muon (see Sec. 2.2.7.2) to reduce the high fake rate of the tracker-muon reconstruction, particularly for central collisions at low p_T.

- The muon track must include hits in at least one pixel layer and five tracker layers to ensure an accurate momentum measurement.

- The Distance of Closest Approach (DCA), defined as the shortest distance between the extrapolated trajectory of the muon track and the reconstructed primary vertex, must be less than $0.3\,\mathrm{cm}$ in the transverse plane (xy) and less than $20\,\mathrm{cm}$ along the beam axis (z direction).

In addition, a specific matching requirement is applied between offline muons (reconstructed after data-taking and identified using the *hybrid-soft ID* described above) and online muons (selected by the HLT system, including both L2 and L3 muons). The separation is defined in the direction of the momentum vector as $\Delta R = \sqrt{(\Delta\eta)^2 + (\Delta\phi)^2}$, where the differences in η and ϕ are taken between the online and offline muon momentum variables. The requirement is $\Delta R < 0.3$ for the L2 muons and $\Delta R < 0.1$ for the L3 muons.

A further selection is applied to the muon kinematics, which is particularly important in this analysis, as it directly impacts the polarization measurement. Since the definition of the reference frames is based on the Υ decay kinematics, the choice of the muon phase space also determines the angular coverage within each frame. The first constraint is on the muon $(\eta^{\mu}, p_{T}^{\mu})$ phase space, where efficiency corrections can be reliably estimated. Figure 3.2 shows the distribution of the single-muon total efficiency for MC events, together with the boundaries of the muon kinematics agreed on for the 2018 Pb + Pb data analyses:

- $p_{T}^{\mu} > 3.5 \, \text{GeV}/c$ for $0.0 < |\eta^{\mu}| < 1.2$

- $p_{T}^{\mu} > (5.47 - 1.89 * |\eta^{\mu}|) \, \text{GeV}/c$ for $1.2 < |\eta^{\mu}| < 1.57$

- $p_{T}^{\mu} > 2.5 \, \text{GeV}/c$ for $1.57 < |\eta^{\mu}| < 2.4$

The $p_{T}^{\mu} > 2.5 \, \text{GeV}/c$ is applied in the region where $|\eta^{\mu}|$ is greater than 1.57, in order to reflect the threshold of the L3 trigger, as described in Sec. 3.2.1. The same acceptance criteria for single muons are applied throughout the analysis. For simplicity, the p_{T}^{μ} limit on the plots is denoted as "$p_{T}^{\mu} > \text{thresholds}(\eta)$" to reflect the fact that the value of the threshold depends on the value of η^{μ}.

Each muon passing the aforementioned selection criteria is paired with all the other selected muons with opposite electrical charges in the same event. We set a cut on the probability that the paired muons originate from a common vertex. Cutting at a probability of 1% reduces the combinatorial background, defined as random pairing of muons coming from uncorrelated processes, without affecting the significance of $\Upsilon \to \mu^{+}\mu^{-}$ yields.
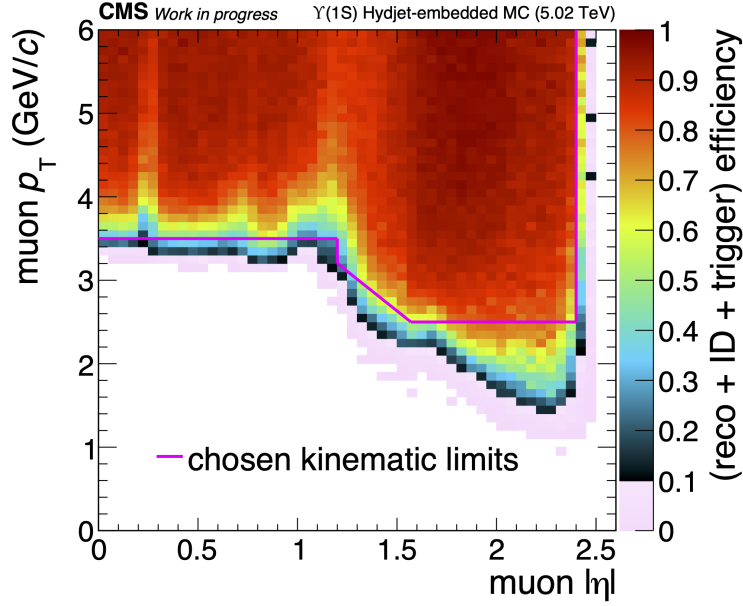
Figure 3.2: Muon reconstruction, ID, and trigger efficiency as a function of pseudora-pidity and transverse momentum. The pink line delimits the muon kinematic region used for this analysis.

3.3 MC Samples

The $\Upsilon(1S)$ signal is generated using PYTHIA 8.2 tune CMS Physics tune 5 (CP5) [101], assuming unpolarized production as a baseline. The intrinsic angular anisotropy introduced by polarized decays, referred to here as underlying polarization effects, is accounted for by generator-level reweighting applied at a later stage, as detailed in Chapter 6. The decay is restricted to oppositely-charged muon pairs, with final-state QED radiation modeled via the PHOTOS package.

To realistically model background conditions in heavy ion collisions, underlying-event effects from the PbPb collision environment are emulated by embedding a subset of the generated events into Minimum Bias (MB) PbPb backgrounds. These events are simulated with HYDJET version 1.9, tune Drum5F [102]. These samples undergo a full detector simulation

using the GEANT4 transport code [103], which provides a realistic modeling of the CMS detector response. The embedded samples are reconstructed and serve as input for signal shape modeling and reconstruction-level efficiency studies.

As mentioned in Sec. 3.1, private generator-level samples are used for acceptance evaluation. These samples, produced without detector simulation or trigger filtering, provide an unbiased reference for mapping angular acceptance in the CS and HX frames.

3.4 Data and MC Processing Workflow

This section is intended for readers less familiar with the CMS computing model or CMS data formats. It provides a self-contained overview of how both data and MC samples are processed into analyzable formats, highlighting practical steps that are often passed down informally among collaborators.

3.4.1 Data processing workflow

For data, this analysis starts from the MiniAOD data tier, which is centrally produced by CMS from raw detector output following the HLT selection. The Tier-0 prompt reconstruction workflow, operated at the central computing facility at CERN, converts RAW data into Reconstruction (RECO) and subsequently into MiniAOD. This data tier contains high-level reconstructed objects such as muons, primary vertices, and trigger information, serving as the standard input for most physics analyses.

MiniAOD samples were retrieved using the Data Aggregation System (DAS) [104] and processed with a custom CMSSW analyzer in order to apply event and muon selection, extract kinematic variables, and perform HLT-trigger matching. Specifically, the OniaTree Analyzer was used for this analysis. Setup instructions are available on the TWiki [105], and the configuration used was stored in the following Git repository [106].

The resulting flat ntuples (ROOT-based data structures containing simplified, event-level variables) were used for signal selection, angular variable computation, and polarization studies described in subsequent chapters.

3.4.2 MC processing workflow

Prior to MC production, the detector conditions and simulation parameters, such as alignment, calibration constants, and vertex smearing settings, must be determined. These are provided via the GT, as described in Sec. 3.1.
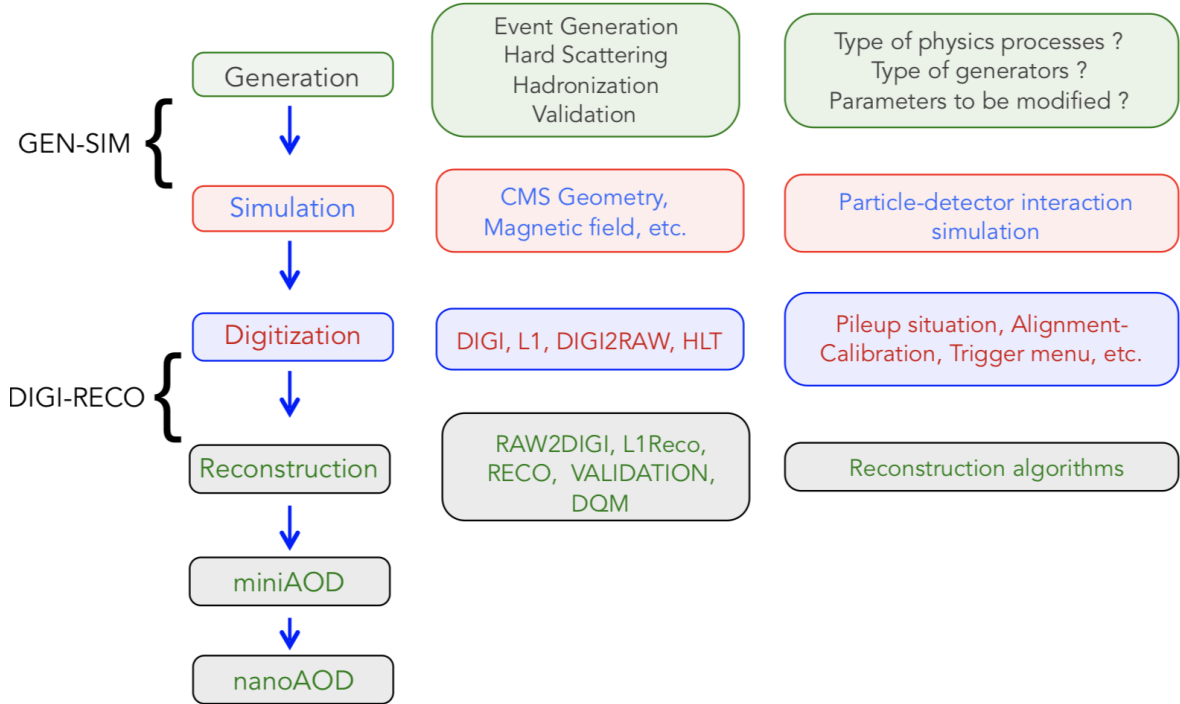
Figure 3.3: Schematic illustration of the CMS MC production workflow, including GEN, SIM, DIGI, and RECO steps [107].

The MC production workflow consists of four main steps: GEN, Simulation (SIM), Digitization (DIGI) (often referred to as `DIGI-RAW`), and RECO. A schematic overview of this workflow is shown in Fig. 3.3.

In the GEN step, high-energy physics events are produced at the particle level, using dedicated event generators such as PYTHIA, or MADGRAPH, depending on the physics process of interest. The configuration of this step is typically defined in a fragment file,[8] which specifies the generator settings, particle species, decay channels, and any relevant physical assumptions such as polarization, energy spectrum, or production mechanisms.

During this step, the primary vertex position is simulated using the vertex-smearing parameters provided via the GT. Specifically, the smearing parameters are stored in a tag associated with the `SimBeamSpotObjectsRcd` record. These parameters include the beam spot (BS) positions (x, y, z), transverse and longitudinal widths $(\sigma_x, \sigma_y, \sigma_z)$, the beam optics parameter β^*, and emittance [23, 100]. The emittance quantifies the beam spread in transverse phase space and determines its intrinsic focusability. This configuration reproduces the spatial distribution of generated collision vertices observed in real data, by producing particles around a realistically smeared BS.

The SIM step uses a GEANT-based simulation to propagate the generated particles through a detailed model of the CMS detector, starting from the smeared primary vertex. In this step, particles are tracked through all layers of the CMS detector geometry, taking into account the magnetic field, material composition, and detector response. Then, various interactions between the particles and detector material are simulated, including ionization, bremsstrahlung, multiple scattering, hadronic interactions, and electromagnetic showers. The locations where particles deposit energy are recorded as simulated hits, which are the input for the next step.

The DIGI step emulates the detector's electronic response, converting energy deposits into digitized signals that resemble real data readout. During this stage, electronic noise is introduced, and additional Pileup (PU) interactions are simulated by overlaying MB events.

---

[8]An example of the fragment file used in this analysis to produce the HYDJET MC samples is available at https://github.com/CMS-HIN-dilepton/MCRequest/blob/master/2019/Ups1SMM/Ups1SMM_5p02TeV_TuneCP5_nofilter_cfi.py.

For example, in this analysis, PYTHIA-generated signal events are embedded in HYDJET-simulated backgrounds to reproduce the underlying event activity of Pb + Pb collisions. Furthermore, L1 and HLT emulations are performed at this stage to simulate the real-time trigger decisions used in data-taking. The output is stored in RAW format, which emulates the data structure recorded by the CMS detector during real collisions.

Finally, the RECO step reconstructs physical objects, such as tracks, vertices, muons, jets, and calorimeter clusters, from the digitized detector signals. The output is a high-level reconstructed dataset in standardized CMS data tiers suitable for physics analysis. This process involves sophisticated algorithms for pattern recognition, track fitting, and vertex reconstruction. The Reconstructed Beamspot (RECO BS), which represents the average collision vertex position and spatial spread determined from the distribution of reconstructed primary vertices in a given run or luminosity section, is a key component for the reconstruction. The RECO BS is used as a constraint in primary vertex finding and track fitting, helping improve resolution and suppress false vertices, particularly in high-multiplicity environments such as heavy ion collisions. The output of this step is stored in a RECO data tier, which contains both low-level detector information and high-level physics objects. This tier is further processed into condensed CMS data tiers such as Analysis Object Data (AOD) and MiniAOD, which contain the derived physics objects used in most analyses.

The general introduction and instruction on CMS MC production workflow is presented in the webpage managed by CMS Physics data and Monte Carlo Validation (PdmV) group [108].

Chapter 4

Reference Frame Transformation and MC Event Reweighting

After preparing the data and the MC samples in the OniaTree format for analysis, as described in Chapter 3, three key preprocessing steps are performed on the data and MC samples: (i) reference frame transformations from the laboratory frame to the CS and HX frames (Sec. 4.1); (ii) centrality weighting of MC events to reproduce the centrality distribution in data (Sec. 4.2); and (iii) $p_\mathrm{T}^{\mu\mu}$ reweighting of the MC to match the $p_\mathrm{T}^{\mu\mu}$ distribution in data (Sec. 4.3).

4.1 Reference Frame Transformations

As described in Sec. 1.5, the angular variables used in this analysis are computed in both the CS and HX frames, whose definitions are given there. This section outlines the procedure used to transform the kinematic variables into these reference frames (See Fig. 1.6 for a schematic illustration).

The variables $\cos\theta_\mathrm{HX}$ and φ_HX, which characterize the angular distribution of the μ^+

in the HX frame, are computed by first boosting the four-momentum of each μ^+ by the Υ laboratory-frame momentum. After the boost, the muon momentum vector is actively rotated to align the coordinate system with the HX frame. This rotation involves two successive active rotations: a rotation about the z-axis by $-\varphi_{\mathrm{Lab}}$, followed by a rotation about the y-axis by $-\theta_{\mathrm{Lab}}$, where φ_{Lab} and θ_{Lab} are the azimuthal and polar angles of the Υ in the laboratory frame. This sequence aligns the z-axis of the new coordinate system with the Υ momentum direction in the nucleon-nucleon center-of-mass frame, following a standard Euler rotation convention [10]. The angular variables $\cos\theta_{\mathrm{HX}}$ and φ_{HX} are then calculated from the rotated μ^+ momentum vector in this frame.

The CS frame is constructed relative to the HX frame. After boosting the μ^+ into the Υ rest frame, its momentum is rotated by the angle between the z-axes of the HX and CS frames. This rotation is determined by first boosting the four-momenta of the two colliding $\mathrm{Pb} + \mathrm{Pb}$ beams into the Υ rest frame and calculating the angle between the resulting beam bisector and the z-axis of the HX frame. The two colliding beams in the laboratory frame are assumed to align back-to-back, with four-momenta $(0, 0, \pm p_z, E)$ that correspond to the nominal center-of-mass energy per nucleon pair. The angular variables $\cos\theta_{\mathrm{CS}}$ and φ_{CS} are then computed from the rotated μ^+ momentum vector in the CS frame.

4.2   Centrality Calibration of MC Events

Centrality in heavy ion collisions is a relative experimental measure of the overlap geometry between the two colliding nuclei. It is experimentally estimated from observables related to collision activity [17]. In this analysis, centrality is estimated using the total E_{T} deposited in both the forward (HF+) and backward (HF−) calorimeters. Only HF towers with digitized signals above a threshold of 15 ADC counts are included in the sum in order to suppress noise while retaining sensitivity to hadronic activity.

MB events passing quality selections are sorted by the summed HF E_{T} from the lowest to the highest value. The resulting distribution is then divided into percentile intervals, each corresponding to a fixed fraction of the total inelastic Pb + Pb cross section. For example, 0–10% centrality corresponds to the most head-on (central) collisions, while 90–100% corresponds to the most peripheral collisions. This centrality determination procedure was implemented centrally by the CMS Heavy Ion (HIN) Global Observable (GO) group, as detailed in the CMS analysis note from Ref. [109].

The obtained centrality values are stored in the OniaTree and applied to the Υ-triggered data sample. The event distribution as a function of centrality is not uniform, due to trigger bias. The underlying HYDJET events are generated in minimum-bias mode, corresponding to uniform sampling in impact parameter space. However, the centrality distribution derived from the simulated events does not exactly reproduce the one observed in data. After trigger and reconstruction selections, the resulting Υ sample shows a strongly non-uniform centrality distribution, as illustrated in Fig. 4.1. Since quarkonium production is expected to scale with the number of binary nucleon–nucleon collisions (N_{coll}), the MB MC events are reweighted using an N_{coll} estimate from a Glauber model. This correction improves the agreement between data and simulation.

A centrality-dependent weight that is proportional to N_{coll} is applied to the MC events. This correction accounts for the expected centrality scaling of quarkonium production. Figure 4.1 compares the number of Υ(1S) candidates in data and in MC, before and after applying N_{coll}-based weights. The blue histogram represents the Υ(1S) candidates in data prior to event selection. The red histogram shows the unweighted PYTHIA-embedded HYD-JET MC distribution, while the yellow histogram corresponds to the same MC sample after applying the N_{coll} weights. After weighting, the data and MC distributions show improved agreement. The ratio between data and MC is shown in the bottom panel to highlight the remaining differences. A residual mismatch, particularly in the peripheral region, is observed.
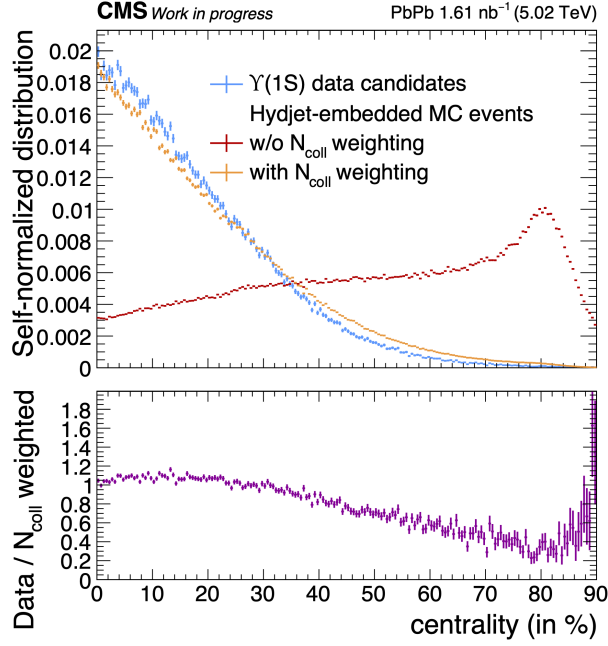
Figure 4.1: Centrality distribution of events containing at least one $\Upsilon(1S)$ candidate. The centrality variable has an estimated resolution of 0.5%, and the distribution is therefore sampled in bins of this width. Events in the 90-100% (ultra-peripheral) range are excluded.

Such differences are typically included in the systematic uncertainty evaluation.

4.3 p_{T} Reweighting of MC Events

Accurate modeling of the $p_{\mathrm{T}}^{\mu\mu}$ distribution is crucial for the polarization analysis. Acceptance and efficiency corrections are computed separately for different $p_{\mathrm{T}}^{\mu\mu}$ intervals, each with a distinct correction map in the $\cos\theta$–φ space. If the MC $p_{\mathrm{T}}^{\mu\mu}$ distribution does not match that of the data, the averaged corrections may be incorrectly applied to the wrong kinematic regions, introducing bias. Furthermore, polarization parameters (such as λ_θ, λ_φ, $\lambda_{\theta\varphi}$) are sensitive to the shape of the underlying $p_{\mathrm{T}}^{\mu\mu}$ distribution, and mismatches can distort the extracted polarization results.

Reweighting at the GEN level corrects the event shape independently of detector-related effects. This also facilitates clearer separation of systematic uncertainties and improves statistical stability in efficiency estimation across the $p_T^{\mu\mu}$ spectrum.

However, the true $p_T^{\mu\mu}$ distribution at the GEN level cannot be directly extracted from the data, which are available only at the RECO level. Unfolding the RECO data to the GEN level requires acceptance and efficiency corrections, which themselves depend on the unknown $p_T^{\mu\mu}$ distribution. This interdependence gives a self-consistent unfolding procedure that cannot be accomplished without prior knowledge of the true $p_T^{\mu\mu}$ spectrum. Therefore, the published CMS measurement [110], which provides a corrected $p_T^{\mu\mu}$ spectrum at the GEN level, was used as a reliable reference. This distribution has already been corrected for detector effects, making it suitable for deriving reweighting factors.
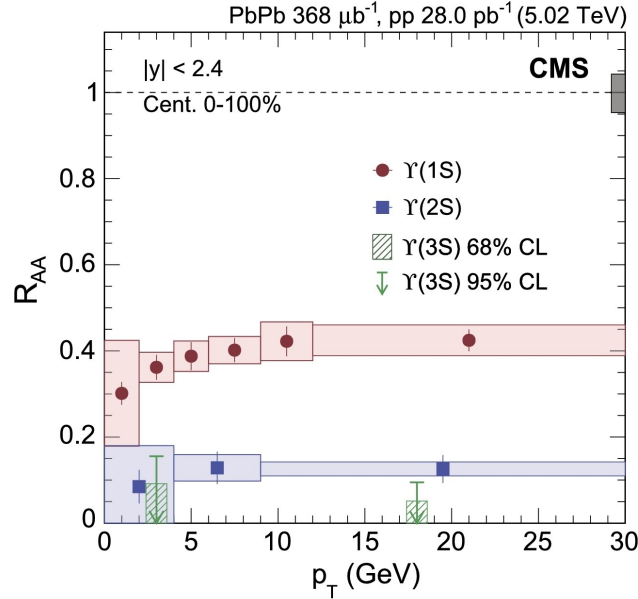
Figure 4.2: R_{AA} as a function of $p_T^{\mu\mu}$ for $\Upsilon(1\mathrm{S})$, $\Upsilon(2\mathrm{S})$, and $\Upsilon(3\mathrm{S})$ in Pb + Pb collisions at $\sqrt{s_{NN}} = 5.02$ TeV, for $|y| < 2.4$ and 0-100% centrality. The figure is from Ref. [110].

In this analysis, the reweighting is based on the $p_T^{\mu\mu}$ distribution measured in $p + p$ collisions at $\sqrt{s_{NN}} = 5.02$ TeV. This choice is motivated by the structure of the MC samples

used in the analysis, where the quarkonium signal is generated using PYTHIA in a $p + p$ framework. Since the $p_{\mathrm{T}}^{\mu\mu}$ spectrum of the generated signal follows the $p+p$ production kinematics, applying weights derived from the $p+p$ measurement ensures consistency. Moreover, as shown in Fig. 4.2, the R_{AA} measurements reported in Ref. [110], indicate that the $p + p$ and Pb + Pb spectra have similar shapes without significant $p_{\mathrm{T}}^{\mu\mu}$ dependence. Given that the $p + p$ data points are much more precise and the Pb + Pb spectrum includes nuclear modifications not fully modeled in the signal generation, the $p+p$ spectrum serves as a more reliable reference for reweighting.
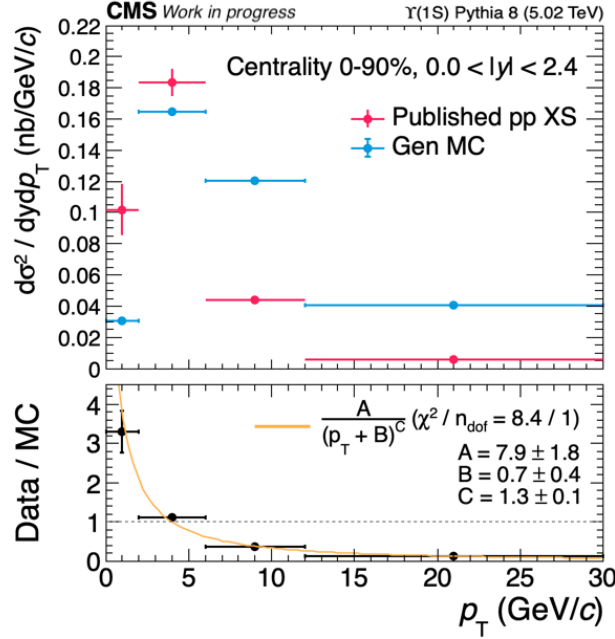
Figure 4.3: GEN-level $p_{\mathrm{T}}^{\mu\mu}$ distributions of $\varUpsilon(1S)$ candidates for centrality 0-100% and rapidity $|y| < 2.4$. The top panel compares the published $p + p$ cross section from Ref. [110] (red histogram) with the PYTHIA MC events (blue histogram), scaled by the integrated $p + p$ cross section. The bottom panel shows the ratio of data to MC distributions along with the fit function used for reweighting. Vertical error bars represent the statistical uncertainties only.

Figure 4.3 compares the published $p + p$ cross section (blue) and the PYTHIA GEN MC

60

$p_\text{T}^{\mu\mu}$ distribution (red), scaled to match the integrated cross section of the published data, for $\varUpsilon(1S)$ candidates as a function of $p_\text{T}^{\mu\mu}$. The binning was constrained by that of the published $p+p$ cross section, which led to adopting a wider binning. The bottom panel shows the ratio of the data to the MC distributions. This ratio is fitted with the following function:

$$f(p_\text{T}^{\mu\mu}) = \frac{A}{(p_\text{T}^{\mu\mu} + B)^C} \tag{4.1}$$

that is then used to weight the MC $\varUpsilon(1S)$ events according to their $p_\text{T}^{\mu\mu}$ in order to match the measured $\varUpsilon(1S)$ $p_\text{T}^{\mu\mu}$ distribution. This function was chosen because power-law shapes naturally describe heavy quarkonium p_T spectra, with the parameter B providing flexibility at the low p_T. It is important to note that the reduced χ^2 value of the fit is 8.4, which is significantly greater than 1 due to the large MC statistics (50M events). This discrepancy can be accounted for within the systematic uncertainties; e.g. using a different weighting function and quantifying the difference it makes in the polarization parameters.

The obtained weight factors are applied at the GEN level during the acceptance and efficiency calculation by weighting MC events according to their generated $p_\text{T}^{\mu\mu}$ values. This procedure ensures that the acceptance and efficiency corrections accurately reflect the $p_\text{T}^{\mu\mu}$ spectrum observed in data, reducing bias in the polarization extraction.

Chapter 5

Signal Extraction

The data contain background that must be removed in order to accurately obtain the $\Upsilon(1S)$ signals. This is to determine the number of μ^+ within a specific $(p_T^{\mu\mu}, \cos\theta, \varphi)$ bin in a chosen reference frame. Since Υ decays into μ^+ and μ^-, the Υ count directly corresponds to the number of μ^+. This extraction is performed by fitting the Υ invariant mass $(m^{\mu\mu})$ distribution with signal and background models. While the fits also provide yields for the $\Upsilon(2S)$ and $\Upsilon(3S)$ states, the analysis focuses on the $\Upsilon(1S)$; after splitting the data into $(p_T^{\mu\mu}, \cos\theta, \varphi)$ bins, the statistics are insufficient to extract reliable measurements of the excited states.

Details on the fitting procedure are given in Sec. 5.1, with the binning scheme summarized in Sec. 5.2. The signal and background models are described in Secs. 5.3 and 5.4, respectively, and the combined fit approach is explained in Sec. 5.5.

5.1 Procedure

The signal extraction follows these steps:

1. Mass window selection: The $m^{\mu\mu}$ of dimuon candidates is restricted to the range 7-11.5 GeV/c^2 to include the $\Upsilon(1S)$, $\Upsilon(2S)$, and $\Upsilon(3S)$ resonances.

2. Binning: The selected dimuon candidates are categorized into bins based on their $(p_T^{\mu\mu}$, $\cos\theta$, $\varphi)$ in the chosen reference frame. This binning allows measurement of polarization parameters as a function of kinematics.

3. Model construction: The invariant mass distribution in each bin is modeled as a sum of signal and background components. The signal is described by a Double-sided Crystal Ball (DSCB) function whose shape parameters are constrained based on MC simulations. The background is modeled by an exponential function modulated by an error function to account for kinematic selection effects.

4. Fitting: For each bin, an extended unbinned maximum likelihood fit is performed on the $m^{\mu\mu}$ distribution. The fit determines the yields of the $\Upsilon(1S)$, $\Upsilon(2S)$, and $\Upsilon(3S)$ signals, as well as background parameters.

5. Yield extraction: The fitted signal yields in each bin serve as the basis for subsequent analysis of polarization parameters.

5.2   Binning Selection

The binning of $p_T^{\mu\mu}$, $\cos\theta$, and φ used to extract the polarization parameters of the $\Upsilon(1S)$ signal in both the HX and CS frames is specified as follows: for $\cos\theta$, due to the low acceptance when $|\cos\theta| > 0.7$ (as shown in Fig. 6.1), signal extraction is performed within the region $|\cos\theta| \leq 0.7$; in addition, to improve the statistical precision of the signal yield and enable more reliable fits, the φ-axis was folded at 0 to exploit its symmetry (validated in Sec. 6.3).

- For $p_T^{\mu\mu}$ (3 bins, in GeV/c): $2 < p_T^{\mu\mu} < 6$, $6 < p_T^{\mu\mu} < 12$, $12 < p_T^{\mu\mu} < 20$

- For $\cos\theta$ (5 bins): $-0.70 < \cos\theta < -0.42$, $-0.42 < \cos\theta < -0.14$,

$$-0.14 < \cos\theta < 0.14, \ 0.14 < \cos\theta < 0.42, \ 0.42 < \cos\theta < 0.70$$

- For $|\varphi|$ (3 bins, in degrees): $0 < |\varphi| < 60$, $60 < |\varphi| < 120$, $120 < |\varphi| < 180$

5.3 Nominal Model of the $\Upsilon \to \mu^+ \mu^-$ Signal Shape

For the nominal signal shape to describe the Υ resonances in the muon channel, a DSCB
PDF with a symmetric Gaussian core and power-law tails extending to high and low masses
was selected for each Υ resonance. The equation for the DSCB PDF is defined as:

$$\mathrm{DSCB}(m; \mu, \sigma, \alpha_L, n_L, \alpha_H, n_H) = \begin{cases} e^{-t^2/2} & \text{if } \alpha_L < t < \alpha_H \\ e^{-\alpha_L^2/2} \left[\frac{\alpha_L}{n_L} \left(\frac{n_L}{\alpha_L} - \alpha_L - t \right) \right]^{-n_L} & \text{if } t \leq -\alpha_L \\ e^{-\alpha_H^2/2} \left[\frac{\alpha_H}{n_H} \left(\frac{n_H}{\alpha_H} - \alpha_H - t \right) \right]^{-n_H} & \text{if } t \geq \alpha_H, \end{cases} \quad (5.1)$$

where $t \equiv (m - \mu)/\sigma$. Here μ and σ are the mean and width of the Gaussian core; $\alpha_{L,H}$
are the transition points (in units of σ) to the low/high-mass power-law tails; and $n_{L,H}$ are
corresponding tail exponents.

The full signal model S is the weighted sum of three DSCB functions, one for each Υ
state:

$$S = N_{\Upsilon(1S)} \ \mathrm{DSCB}_{\Upsilon(1S)}(m; \mu_{1S}, \sigma_{1S}, \alpha_L, n_L, \alpha_H, n_H)$$
$$+ N_{\Upsilon(2S)} \ \mathrm{DSCB}_{\Upsilon(2S)}(m; \mu_{2S}, \sigma_{2S}, \alpha_L, n_L, \alpha_H, n_H) \quad (5.2)$$
$$+ N_{\Upsilon(3S)} \ \mathrm{DSCB}_{\Upsilon(3S)}(m; \mu_{3S}, \sigma_{3S}, \alpha_L, n_L, \alpha_H, n_H),$$

where $N_{\Upsilon(1S)}$, $N_{\Upsilon(2S)}$, and $N_{\Upsilon(3S)}$ represent the number of signal events for each Υ resonance.

The yields ($N_{\Upsilon(1S)}$, $N_{\Upsilon(2S)}$, $N_{\Upsilon(3S)}$) and $\Upsilon(1S)$ mean (μ_{1S}) and standard deviation (σ_{1S})
are free parameters in the fit. Constraints were applied to the means (μ_{2S}, μ_{3S}), standard
deviations (σ_{2S}, σ_{3S}), and tail parameters (α_L, α_R, n_L, n_R) in the fit. The $\Upsilon(2S)$ and

$\Upsilon(3S)$ Gaussian means and widths are tied to those of $\Upsilon(1S)$ through the Particle Data Group (PDG) mass ratios [33]:

$$\mu_{2S,3S} \propto \mu_{1S},$$
$$\sigma_{2S,3S} \propto \sigma_{1S}, \tag{5.3}$$

i.e., μ and σ for the excited states are scaled relative to the 1S values by the known $m_{2S,3S}/m_{1S}$ factors. To reduce degeneracy and stabilize the fits, the three Υ functions share the same tail parameters:

$$\alpha_L^{(1S)} = \alpha_L^{(2S)} = \alpha_L^{(3S)}, \quad \alpha_H^{(1S)} = \alpha_H^{(2S)} = \alpha_H^{(3S)},$$
$$n_L^{(1S)} = n_L^{(2S)} = n_L^{(3S)}, \quad n_H^{(1S)} = n_H^{(2S)} = n_H^{(3S)}. \tag{5.4}$$

When fitting the data, Gaussian constraints (penalty terms) are applied to the shape parameters: the $\Upsilon(1S)$ width (σ_{1S}) and the tail parameters (α_L, α_R, n_L, n_R) are constrained by Gaussians with widths set by the MC statistical uncertainties. This procedure is discussed in more detail in Sec. 5.5.

5.4   Nominal Model of the Background Shape

An exponential multiplied by an error function was selected as a nominal model of the background shape. The error function is used to describe the effect of kinematic selections that produce a peak in the background distribution. These selections arise from both the trigger requirement and from the specific kinematic range that defines a particular ($p_T^{\mu\mu}$, $\cos\theta$, φ) range for the bin being analyzed. The exponential is used to model the phase space of the combinatorial background, which is the dominant contribution to the background in this mass range. The full background model PDF B is defined as:

$$B(m^{\mu\mu}; \lambda, \mu_{\text{err}}, \sigma_{\text{err}}, N_{\text{bkg}}) = N_{\text{bkg}} \ \exp(-\frac{m^{\mu\mu}}{\lambda}) \ \frac{1 + \text{Erf}(\frac{m^{\mu\mu} - \mu_{\text{err}}}{\sqrt{2}\sigma_{\text{err}}})}{2}, \tag{5.5}$$

where λ is the exponent of the exponential function, μ_{err} is the mean, and σ_{err} is the standard deviation of the error function.

5.5 Fits

The signal extraction fits were performed using the function F, defined as:

$$F = S + B. \tag{5.6}$$

To perform the signal-extraction fits, the MIGRAD algorithm in MINUIT was first applied, followed by the calculation of the HESSE method [111]. In addition, the extended log-likelihood function was applied.

The fits to the MC sample were performed in the invariant mass range of 8.8 to 10.2 GeV/c^2. The DSCB function for $\Upsilon(1S)$ was used for the fit without constraints, except for the upper and lower limits of the parameters.

The tail parameters (α_L, n_L, α_H, n_H) and the standard deviation (σ_{1S}) of the DSCB function in the signal model were extracted from the RECO MC sample listed in Table 3.1 for each bin of ($p_{\mathrm{T}}^{\mu\mu}$, $\cos\theta$, φ) in both the CS and HX frames individually. Figure 5.1 (left) shows an example in the HX frame of the fit to the MC $m^{\mu\mu}$ spectrum for the bin in the kinematic range $2 < p_{\mathrm{T}}^{\mu\mu} < 6$ GeV/c, $-0.42 < \cos\theta_{\mathrm{HX}} < -0.14$, and $60 < |\varphi_{\mathrm{HX}}| < 120°$. This figure illustrates the extracted signal-shape parameters. These parameters except for $m^{\mu\mu}$ were then used to constrain the fit during the signal extraction process.

Figure 5.1 (right) shows the fits to the $m^{\mu\mu}$ distributions in Pb + Pb data using the nominal model function F from Eq. (5.6). It is done for the same kinematic bin as the left plot of the figure. The bottom panels in both plots in the figure display the corresponding pull distributions, defined as

$$\mathrm{pull}_i = \frac{N_{i,\mathrm{data}} - N_{j,\mathrm{fit}}}{\sqrt{\sigma_{i,\mathrm{data}}^2 + \sigma_{j,\mathrm{fit}}^2}}, \tag{5.7}$$

66
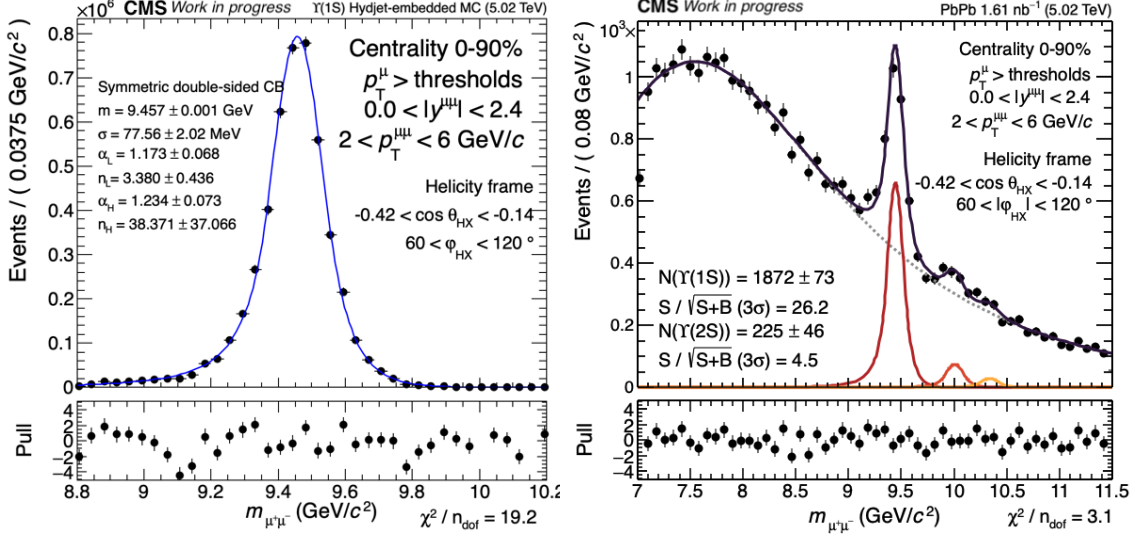
Figure 5.1: Parameter extraction fit from MC (left) and signal extraction fit from data (right) in the bin range $2 < p_T^{\mu\mu} < 6$ GeV/c, $-0.42 < \cos\theta_{HX} < -0.14$, and $60 < |\varphi_{HX}| < 120°$ in the HX frame. The bottom panel of each plot shows the pull distributions of the fits, along with the chi-square value (χ^2) divided by the number of degrees of freedom as a measure of goodness-of-fit.

where $N_{i,\text{data}}$ and $N_{j,\text{fit}}$ denote the fit value and data, and $\sigma_{i,\text{data}}$ and $\sigma_{j,\text{data}}$ are their statistical uncertainties. The black circles in both plots are the binned histograms of the invariant mass distribution. In the left plot, the blue line corresponds to the fit using the DSCB function for $\Upsilon(1S)$. In the right plot, the total fit F is depicted as the dark purple line, with the signal components $\Upsilon(1S)$, $\Upsilon(2S)$, and $\Upsilon(3S)$ shown in red, orange, and yellow, and the background component represented by the dotted gray line. The statistical significance of the extracted $\Upsilon(1S)$ signal is quantified using the ratio

$$\frac{S}{\sqrt{S+B}}, \tag{5.8}$$

where S and B denote the number of signal and background events, respectively, within a mass window of $\pm 3\sigma$ around the fitted $\Upsilon(1S)$ peak.

The parameters extracted from the MC sample for the bin shown in Fig. 5.1 (left) are:

$\sigma_{1S} = 77.56 \pm 2.02$ MeV, $\alpha_L = 1.173 \pm 0.068$, $n_L = 3.380 \pm 0.436$, $\alpha_H = 1.234 \pm 0.073$, and

$n_H = 38.371 \pm 37.066$. In the fit to the Pb+Pb data, these 4 tail parameters, $\alpha_L, n_L, \alpha_H, n_H$, were constrained based on the MC fit results. The σ_{1S} parameter was constrained via a Gaussian constraint, where the value of the σ_{1S} parameter of the MC fit in a given bin was used to set the mean of the Gaussian constraint, and the uncertainty in the σ_{1S} parameter was used to set the sigma of the Gaussian constraint. This procedure reduces the number of free parameters in the invariant-mass fits of the Υ resonances and mitigates biases in the signal yield estimation due to limited acceptance in certain analysis bins (see Fig. 6.1). The final extracted signal yield of $\Upsilon(1S)$ in this bin is 1872 ± 73, as shown in Fig. 5.1 (right).

Note that the extracted $\Upsilon(1S)$ yields within the same $p_T^{\mu\mu}$ interval are consistent between the HX and CS frames when integrated over the $(\cos\theta, \varphi)$ bins, within statistical uncertainties. This confirms that the choice of polarization frame does not bias the total extracted yield; the apparent frame dependence only arises at the level of the angular binning, as expected from frame-dependent acceptance distributions.

Each $(p_T^{\mu\mu}, \cos\theta, \varphi)$ bin of the analysis has its own set of signal shape parameters obtained from the MC sample that are used to set the Gaussian constraints for that bin during the fit to extract the signal. In total, this corresponds to $3\,p_T^{\mu\mu} \times 5\,\cos\theta \times 3\,\varphi$ bins $= 45$ independent sets of signal extractions. The complete results are presented in Appendices A for MC and B for data.

In bins where the acceptance is high and there is a good signal-to-background ratio, the σ_{1S} parameter is left free (the tail parameters are fixed). For example, the acceptance is $A \approx 0.89$ in the bin presented in Fig. 5.1. A comparison of the signal extraction with/without the Gaussian constraint is shown in Fig. 5.2, where the left plot shows the fit with the Gaussian constraint, and the right plot shows the fit with the sigma parameter left free. The extracted $\Upsilon(1S)$ yield remains consistent within the uncertainty range. In this case, the $\Upsilon(1S)$ yield with a fixed σ_{1S} is 1872 ± 73, while the yield with the free σ_{1S} is 2012 ± 98. This
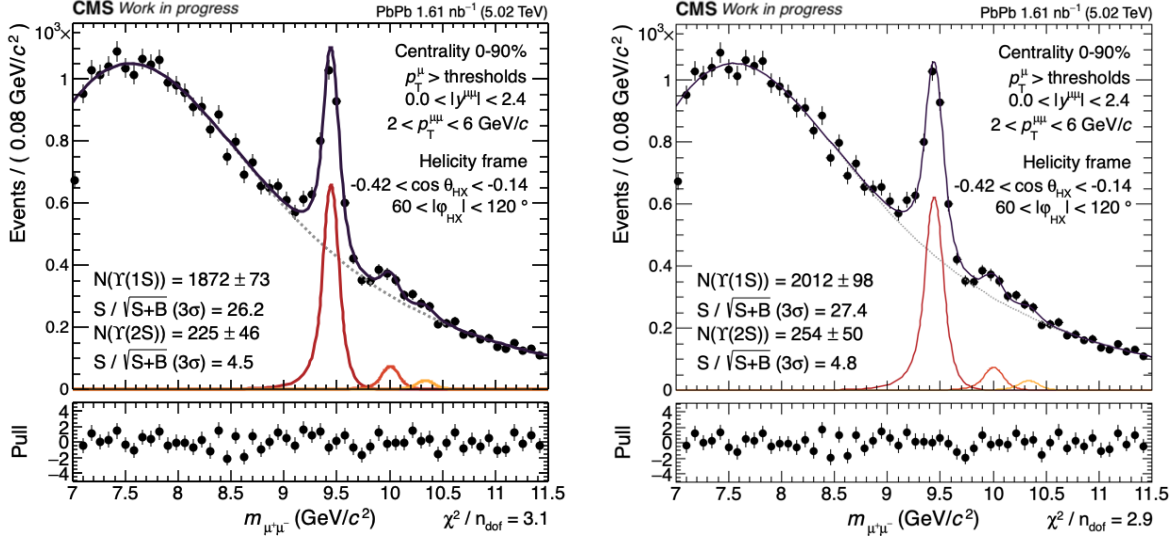
Figure 5.2: Signal extraction fits from data with a constrained σ_{1S} (left) and with a free σ_{1S} (right) in the bin range $2 < p_T^{\mu\mu} < 6$ GeV/c, $-0.42 < \cos\theta_{CS} < -0.14$, and $60 < |\varphi_{CS}| < 120°$ in the HX frame (same analysis bin as in Fig. 5.1). The bottom panel also includes the pull distribution and (χ^2), as mentioned in the previous plot.

demonstrates that utilizing the σ_{1S} obtained from the MC simulation for signal extraction does not compromise the accuracy of the extracted $\Upsilon(1S)$ yield.

Figure 5.3 presents an example in the CS frame of signal extraction fits for the $m^{\mu\mu}$ using the nominal model function F from Eq. (5.6), within the bin range $2 < p_T^{\mu\mu} < 6$ GeV/c, $-0.70 < \cos\theta_{CS} < -0.42$, and $0 < |\varphi_{CS}| < 60°$. The acceptance in this bin is A ≈ 0.17. Due to the low acceptance, and low signal-to-background ratio, background fluctuations become more dominant, making the Υ resonance peaks less prominent and the determination of σ_{1S} more challenging.

The plot on the left shows the invariant mass fit with σ_{1S} constrained via the Gaussian constraint, while the plot on the right presents the fit with a free σ_{1S} parameter. The obtained σ_{1S} value from the right plot is ~ 360.39 MeV, which exceeds the typical detector resolution, leading to an overestimation of the signal yield (1040 ± 233) compared to the yield

69
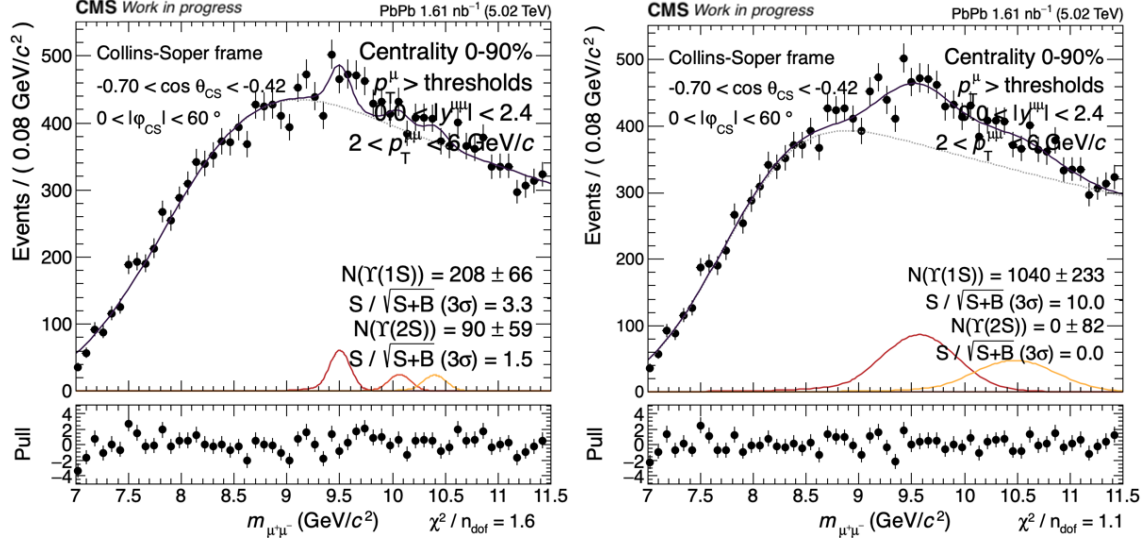
Figure 5.3: Signal extraction fits from data with σ_{1S} fixed using the value obtained from MC (left) and with free σ_{1S} (right) in the bin range $2 < p_T^{\mu\mu} < 6$ GeV/c, $-0.70 < \cos\theta_{CS} < -0.42$, and $0 < |\varphi_{CS}| < 60°$ in the CS frame. Each bottom panel also includes the pull distribution and (χ^2), as mentioned in the previous plot.

obtained using the σ_{1S} from the MC simulation (208 ± 66). For this reason, we concluded that adopting Gaussian constraints was the best procedure for obtaining the nominal yield results and the nominal polarization parameters.

Chapter 6

Acceptance and Efficiency Corrections

Not all muons from Υ decays produced in the collisions are detected and reconstructed by the detector. Detector acceptance and efficiency corrections are therefore required to recover the true angular distribution from the raw $\Upsilon(1S)$ yields described in Chapter 5. In polarization analyses, these corrections are especially important because variations across the $\cos\theta$–φ phase space can distort the angular distribution and bias the extracted polarization parameters.

In this chapter, the definitions of acceptance and efficiency are presented in Secs. 6.1 and 6.2, respectively. Sec. 6.3 describes the symmetrization of acceptance and efficiency, where the φ-axis is folded to effectively increase the available signal statistics for signal extraction fits.

6.1   Acceptance Corrections and Analysis Phase Space

Acceptance is the fraction of generated particles within the detector's geometric and kinematic coverage that are successfully detected and reconstructed. In this analysis, it refers to the fraction of generated muon pairs that satisfy the analysis kinematic cuts (see Fig. 3.2).

71

This is quantified as the ratio of the number of generated muon pairs passing the kinematic cuts to the total number within a given fiducial range, i.e.,

$$A = \frac{N_{\text{GEN}}^{\mu\mu}\left[|y^{\mu\mu}| < 2.4,\, p_{\text{T}}^{\mu} > \text{thresholds}(\eta),\, |\eta^{\mu}| < 2.4\right]}{N_{\text{GEN}}^{\mu\mu}\left[|y^{\mu\mu}| < 2.4\right]}, \tag{6.1}$$

where the fiducial range $|y^{\mu\mu}| < 2.4$ ensures that the acceptance is evaluated consistently within the detector's reliable coverage region. The p_{T}^{μ} thresholds(η) are defined in Sec. 3.2.2. The acceptance is computed from the GEN-level PYTHIA MC sample (Table 3.1) after applying the $p_{\text{T}}^{\mu\mu}$-dependent reweighting factors described in Sec. 4.3 to all events, applied identically to both numerator and denominator. The statistical uncertainties of the acceptance are evaluated using the 'kFNormal' option of the 'TEfficency' package, which provides asymmetric confidence intervals [112, 113].
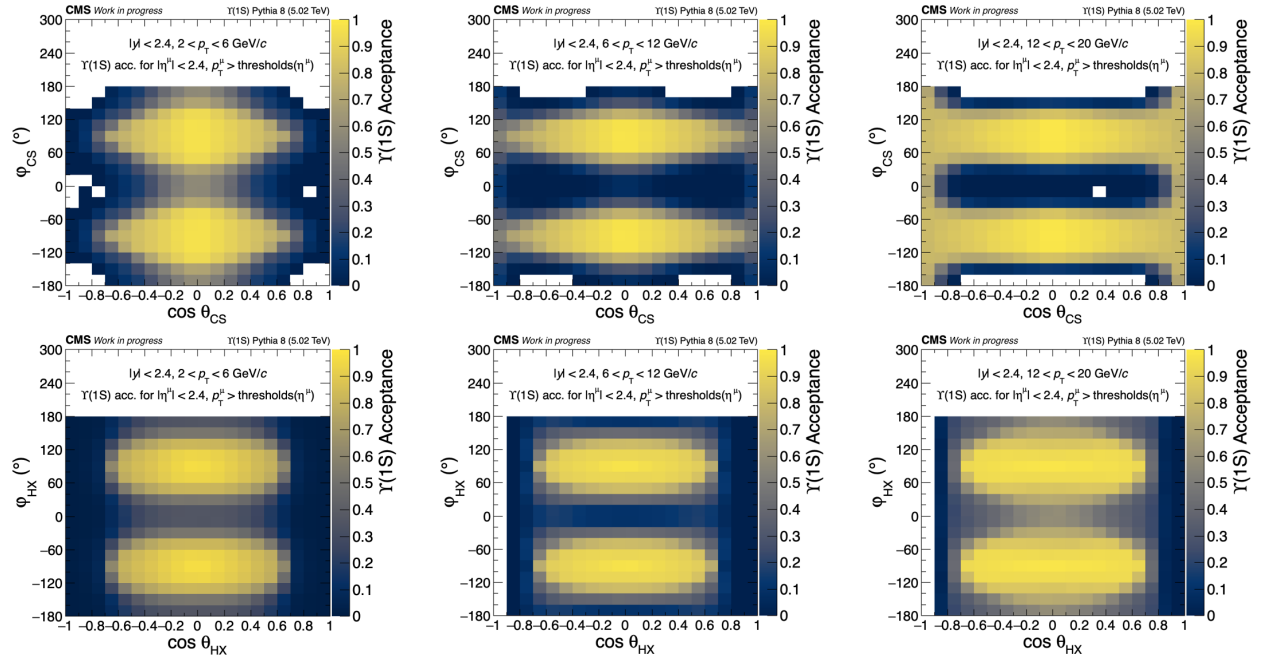
Figure 6.1: Acceptance maps generated with the zero polarization assumption for the CS (top row) and HX (bottom row) frames in the 2-D $\cos\theta$–φ plane, depending on the selected $p_{\text{T}}^{\mu\mu}$ regions.

Figure 6.1 shows the acceptance maps for the CS and HX frames in the $\cos\theta$–φ plane for the $p_{\rm T}^{\mu\mu}$ ranges defined in Sec. 5.2. Regions of vanishing acceptance are observed near $\varphi \approx 0°$ and $180°$. The $\cos\theta$ coverage broadens with increasing $p_{\rm T}^{\mu\mu}$, reflecting the higher average decay $p_{\rm T}^{\mu}$ at larger $p_{\rm T}^{\mu\mu}$. Measurements are restricted to $|\cos\theta| \leq 0.7$ to avoid regions where acceptance varies rapidly and becomes unreliable.

The angular decay distribution is symmetric about the φ-axis (cf. Eq. (1.3)). This property is used to mitigate discontinuities from acceptance gaps and to increase the statistical precision of the signal extraction through folding. The acceptance and efficiency must also be symmetric for this approach to be **valid and this** requirement is examined in Sec. 6.3.

6.2 Efficiency Corrections

The total dimuon efficiency ($\epsilon_{tot}^{\mu\mu}$) quantifies the effectiveness of the detector in reconstructing and identifying muon pairs that satisfy the analysis selections, including reconstruction, identification, and trigger requirements. It is defined within the fiducial kinematic region, after applying the acceptance requirement.

The $\epsilon_{tot}^{\mu\mu}$ is determined from MC simulations as the ratio of reconstructed dimuon candidates to generated dimuon candidates within the acceptance region. In the reconstructed sample, candidates are required to satisfy the reconstruction, trigger, and muon identification criteria, as well as the dimuon selection described in Sec. 3.2.2. The single-muon scale factors (SFs) are applied in order to correct for discrepancies between data and MC, obtained using the tag-and-probe method [96].

The efficiency is defined as:

$$\epsilon^{\mu\mu} = \frac{N_{\rm RECO}^{\mu\mu}\left[|y^{\mu\mu}| < 2.4,\, p_{\rm T}^{\mu} > \text{thresholds},\, |\eta^{\mu}| < 2.4,\, \text{selection}\right]}{N_{\rm GEN}^{\mu\mu}\left[|y^{\mu\mu}| < 2.4,\, p_{\rm T}^{\mu} > \text{thresholds},\, |\eta^{\mu}| < 2.4\right]}$$
$$\otimes \left[\text{SF}(p_{\rm T}^{\mu^-},\, \eta^{\mu^-}) \times \text{SF}(p_{\rm T}^{\mu^+},\, \eta^{\mu^+})\right],$$
(6.2)

where the single-muon SF is given by:

$$\text{SF}(p_{\text{T}}^{\mu}, \eta^{\mu}) = \frac{\epsilon_{\text{data}}^{\mu}(p_{\text{T}}^{\mu}, \eta^{\mu})}{\epsilon_{\text{MC}}^{\mu}(p_{\text{T}}^{\mu}, \eta^{\mu})}. \tag{6.3}$$

The symbol $\otimes$ indicates that the SF was applied individually to the μ^- and μ^+ according to their p_{T}^{μ} and η^{μ}. In this analysis, three types of SFs are considered in the efficiency estimation: muon identification, tracking, and trigger. These are centrally provided by the HIN muon Physics Object Group (POG), with details in the analysis note [114]. However, the analysis note has not been updated since 2018, whereas the underlying efficiency corrections were subsequently revised. The implementation actually used in this analysis is distributed as a header file in the official Github repository [115]. This file contains the final scale factor values as a function of muon kinematics, but does not include the underlying efficiencies in data and MC or their statistical uncertainties. Therefore, the SF curves shown in Appendix C were reconstructed directly from the header file, and represent the most up-to-date values available, though without the corresponding error decomposition.

The statistical uncertainties of the efficiency are also evaluated with the 'kFNormal' option of 'TEfficiency', consistent with the procedure applied for the acceptance. The efficiency maps in the $\cos\theta$–φ phase space are shown in Fig. 6.2 for each selected $p_{\text{T}}^{\mu\mu}$ range in both the CS and HX frames.

6.3 Symmetry of the Acceptance and Efficiency in the $\cos\theta$–φ Space

The folding procedure used in the extraction of the polarization parameters relies on the assumption that the acceptance and efficiency corrections are symmetric with respect to the φ-axis. This symmetry originates from the properties of the angular decay distribution (Eq. (1.3)) and is exploited to reduce the statistical uncertainty by combining mirrored bins
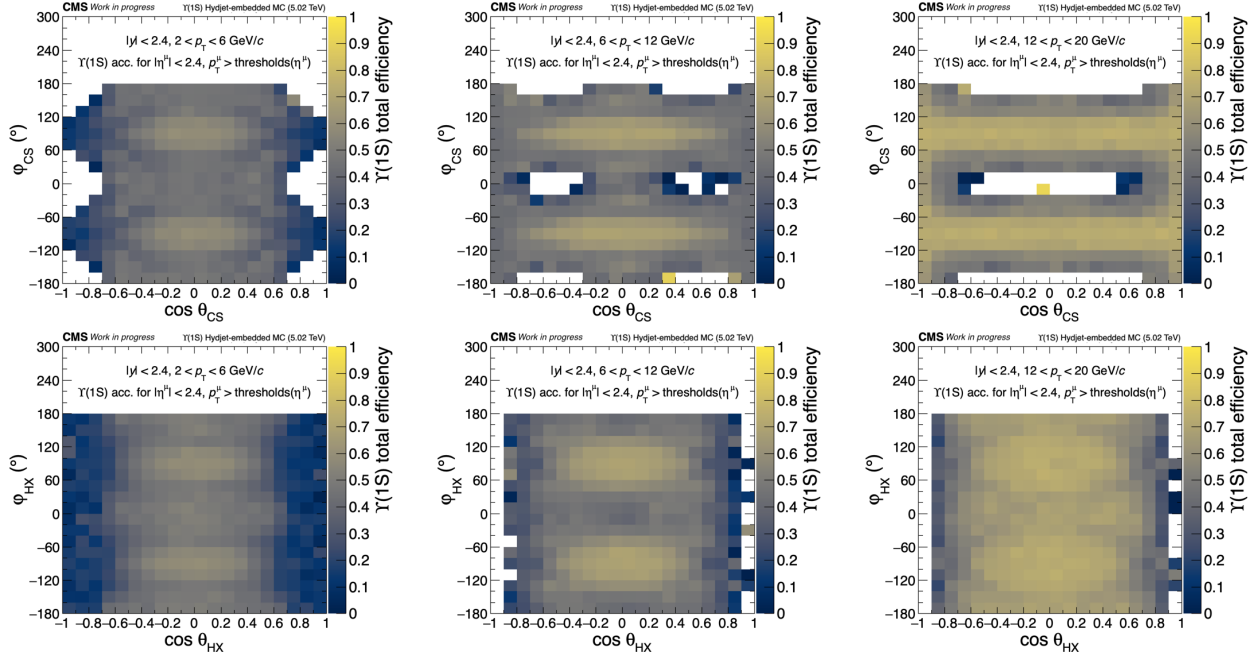
Figure 6.2: Efficiency maps for the CS (top row) and HX (bottom row) frames in the 2-D $\cos\theta$–φ plane, depending on the selected $p_T^{\mu\mu}$ regions.

in φ. Any significant asymmetry in the corrections could bias the extracted polarization parameters, so this assumption must be validated.

Acceptance × efficiency maps (the inverse of the full correction factor) are calculated for each $p_T^{\mu\mu}$ interval in both the CS and HX frames, using the defined binning shown in Fig. 6.3. For each map, mirrored bins across the φ or $\cos\theta$ axes are compared via 1-D projections displayed in Figs. 6.4 – 6.9. The difference between mirrored bins is quantified using the pull. For symmetric statistical uncertainties, the pull value is defined as:

$$\text{pull} = \frac{v_i - v_j}{\sqrt{\sigma_i^2 + \sigma_j^2}}, \tag{6.4}$$

where v_i and v_j are the measured acceptance × efficiency values in the mirrored bins, and σ_i and σ_j are their statistical uncertainties. Because our acceptance and efficiency have asymmetric uncertainties, the upper error is used for the bin with the larger value and the
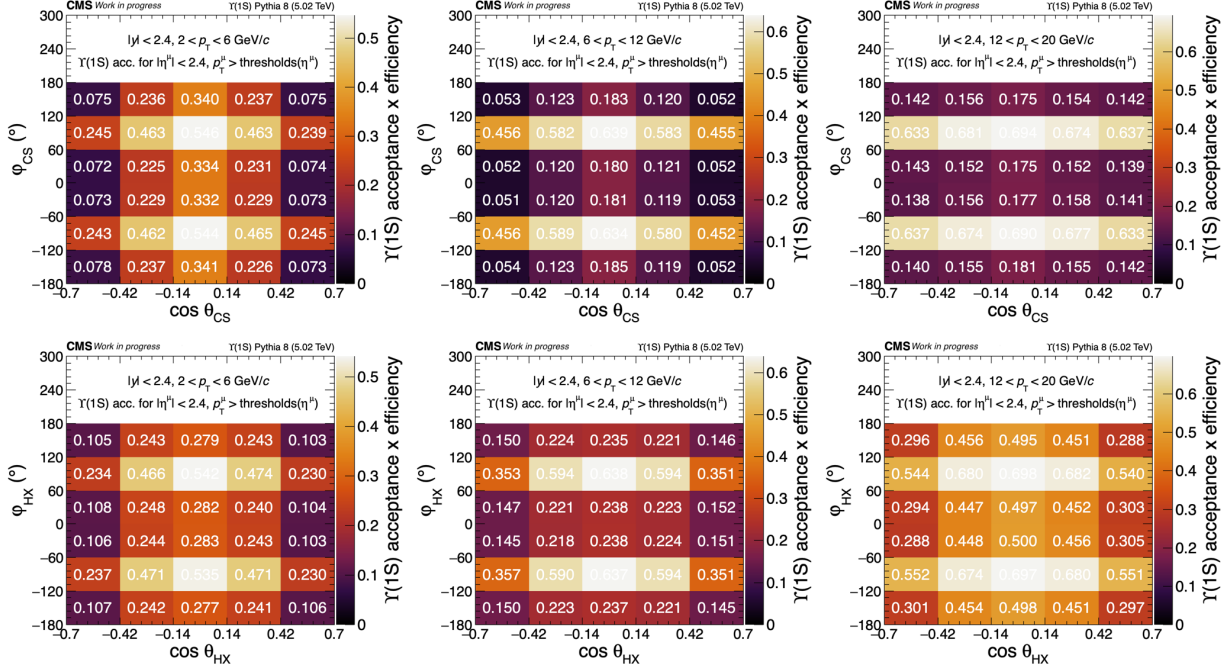
Figure 6.3: Acceptance × efficiency maps for the null polarization parameters in the CS (top row) and HX (bottom row) frames in the 2-D $\cos\theta$–φ plane, shown for different $p_T^{\mu\mu}$ intervals. The values of acceptance × efficiency are displayed on each $(\cos\theta, \varphi)$ bin, with the background color representing the corresponding values.

lower error for the bin with the smaller value.

These 1-D projections present the acceptance × efficiency values for the corresponding positive and negative bins, with the lower panels showing the pull distributions. This provides a direct visual check of the symmetry assumption used in the folding procedure.

Each figure set follows the same format:

- Top left panel: the 2-D acceptance × efficiency map in the $(\cos\theta, \varphi)$ plane. The color scale encodes the numerical value in each bin, while numbers above the bins indicate the asymmetric uncertainties.

- Top middle and right panels: 1-D projections along φ for fixed $|\cos\theta|$ slices. Purple points correspond to bins on the positive $\cos\theta$ side; blue points to the mirrored bins

on the negative side.

- Bottom panels: analogous 1-D projections along $\cos\theta$ for fixed $|\varphi|$ slices, comparing positive (purple) and negative (blue) sides.

The pull distributions defined in Eq. (6.4) are shown at the bottom of each 1-D plot. Pull values close to zero indicate good agreement between mirrored bins, while significant deviations would reveal asymmetries in the corrections that could bias the folding procedure.

Across all $p_T^{\mu\mu}$ intervals and both polarization frames, the pull distributions are centered near zero with fluctuations consistent with statistical uncertainties. Note that the large deviations sometimes occur because the statistical uncertainties of the acceptance and efficiency map are very small, which result from the large statistics of the MC sample used for the calculations. No significant asymmetries are observed in the acceptance $\times$ efficiency along the φ-axis, confirming that the symmetry assumption used in the folding procedure is valid. For completeness, Appendices D and E present the symmetrization of acceptance and efficiency separately.
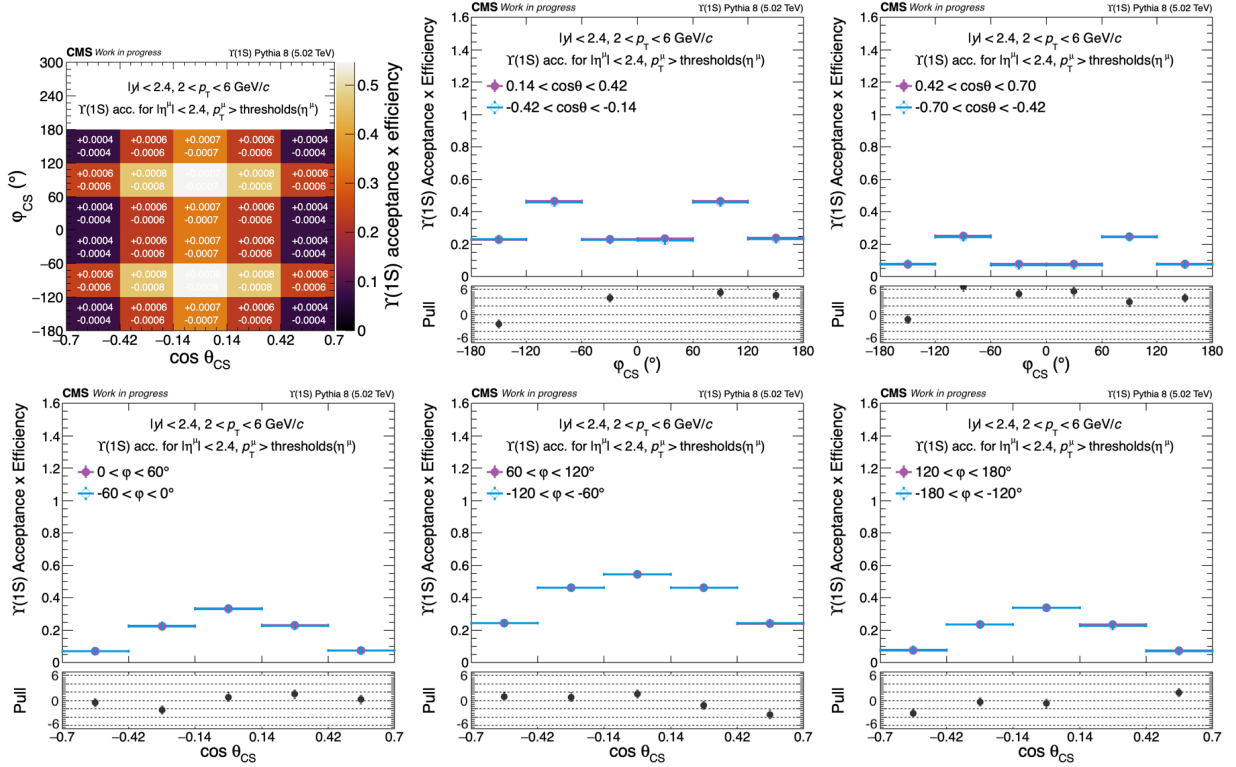
Figure 6.4: Acceptance × efficiency distributions in 1-D along the φ axis (top) and $\cos\theta$ axis (bottom) in the CS frame for $2 < p_T^{\mu\mu} < 6$ GeV/c. The 2-D plot at the top left is identical to the one in Fig. 6.3, but it displays asymmetric uncertainty values above each bin. Each of the other plots refers to the top left panel. Each 1-D plot compares a column (top) or row (bottom) on the positive side of $\cos\theta$ or φ values (purple) with the corresponding column or row on the negative side (blue). The bottom panel of each 1-D plot presents the pull distribution for each bin.
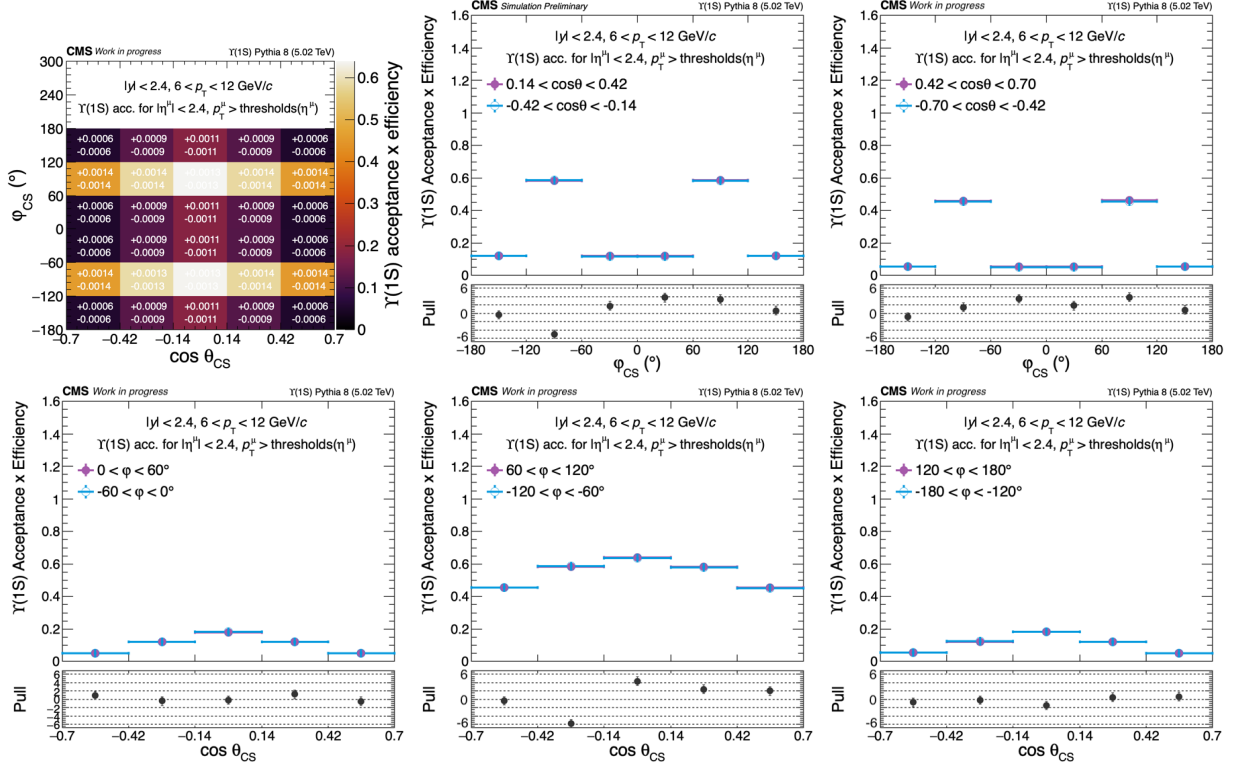
Figure 6.5: Acceptance × efficiency plots in 1-D along the φ axis (top) and $\cos\theta$ axis (bottom) in the CS frame for $6 < p_T^{\mu\mu} < 12$ GeV/c. The 2-D plot in the top left is identical to the one in Fig. 6.3, but it displays asymmetric uncertainty values above each bin. Each 1-D plot compares a column (top) or row (bottom) on the positive side of $\cos\theta$ or φ values (purple) with the corresponding column or row on the negative side (blue). The bottom panel of each 1-D plot presents the pull distribution for each bin.
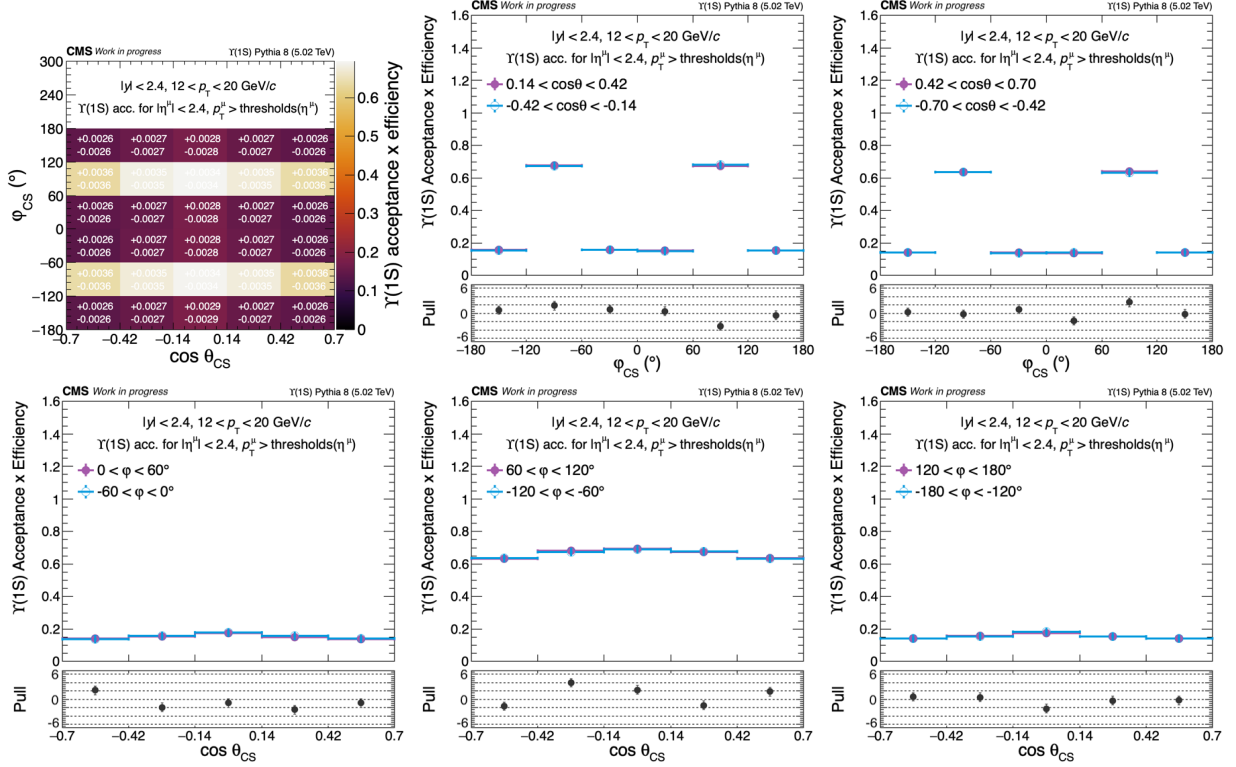
Figure 6.6: Acceptance × efficiency plots in 1-D along the φ axis (top) and $\cos\theta$ axis (bottom) in the CS frame for $12 < p_{\mathrm{T}}^{\mu\mu} < 20$ GeV/c. The 2-D plot in the top left is identical to the one in Fig. 6.3, but it displays asymmetric uncertainty values above each bin. Each 1-D plot compares a column (top) or row (bottom) on the positive side of $\cos\theta$ or φ values (purple) with the corresponding column or row on the negative side (blue). The bottom panel of each 1-D plot presents the pull distribution for each bin.
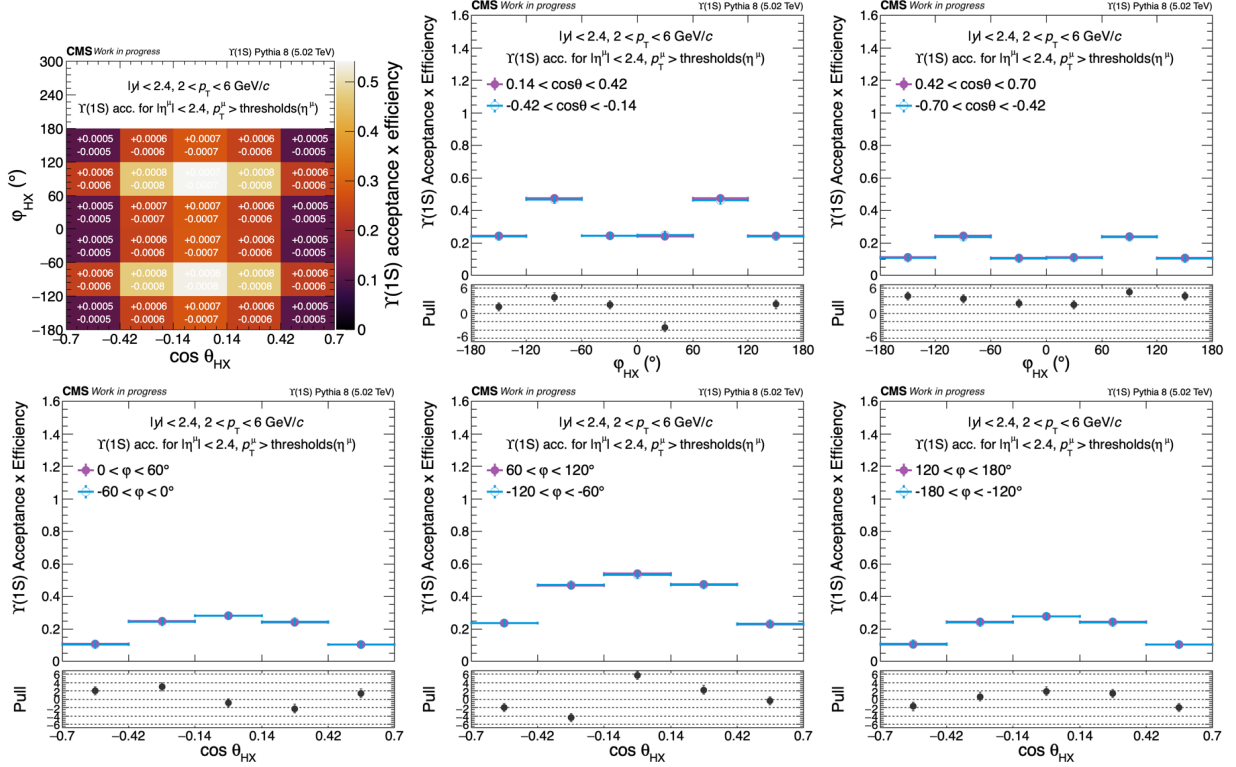
Figure 6.7: Acceptance × efficiency plots in 1-D along the φ axis (top) and $\cos\theta$ axis (bottom) in the HX frame for $2 < p_T^{\mu\mu} < 6$ GeV/c. The 2-D plot in the top left is identical to the one in Fig. 6.3, but it displays asymmetric uncertainty values above each bin. Each 1-D plot compares a column (top) or row (bottom) on the positive side of $\cos\theta$ or φ values (purple) with the corresponding column or row on the negative side (blue). The bottom panel of each 1-D plot presents the pull distribution for each bin.
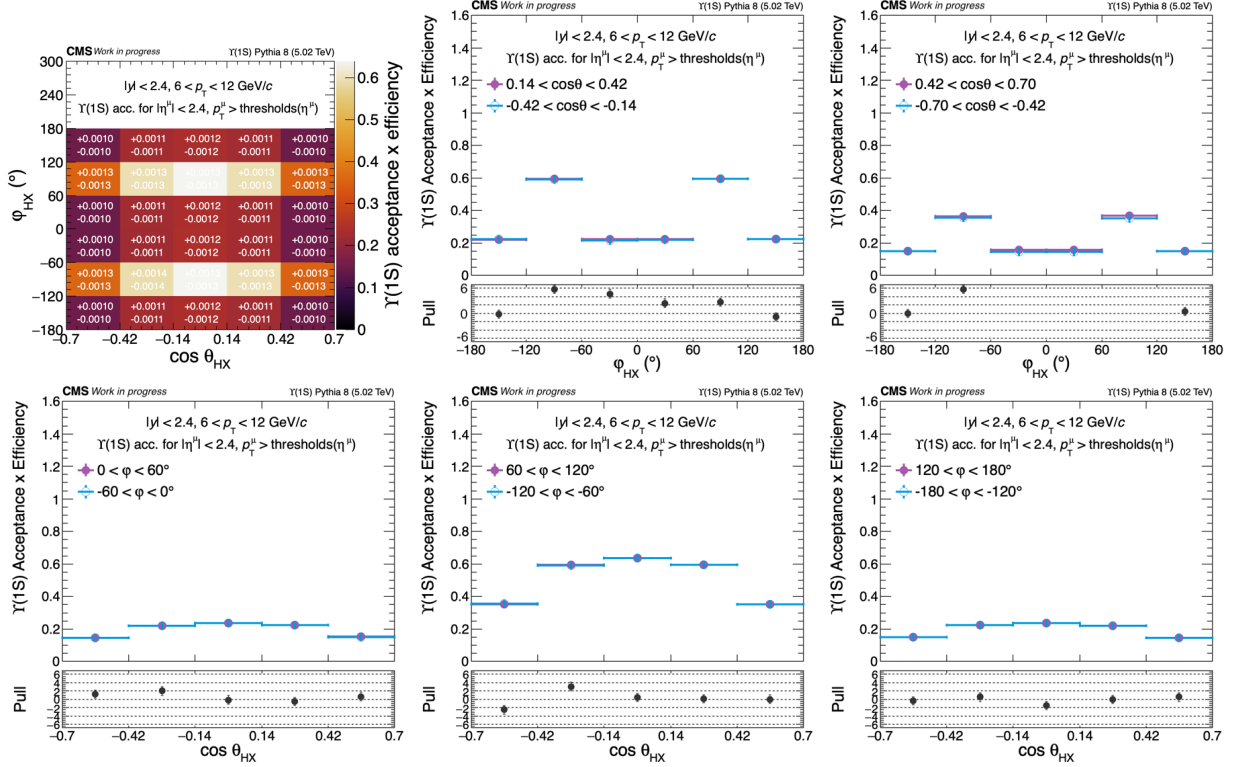
Figure 6.8: Acceptance × efficiency plots in 1-D along the φ axis (top) and $\cos\theta$ axis (bottom) in the HX frame for $6 < p_T^{\mu\mu} < 12$ GeV/c. The 2-D plot in the top left is identical to the one in Fig. 6.3, but it displays asymmetric uncertainty values above each bin. Each 1-D plot compares a column (top) or row (bottom) on the positive side of $\cos\theta$ or φ values (purple) with the corresponding column or row on the negative side (blue). The bottom panel of each 1-D plot presents the pull distribution for each bin.
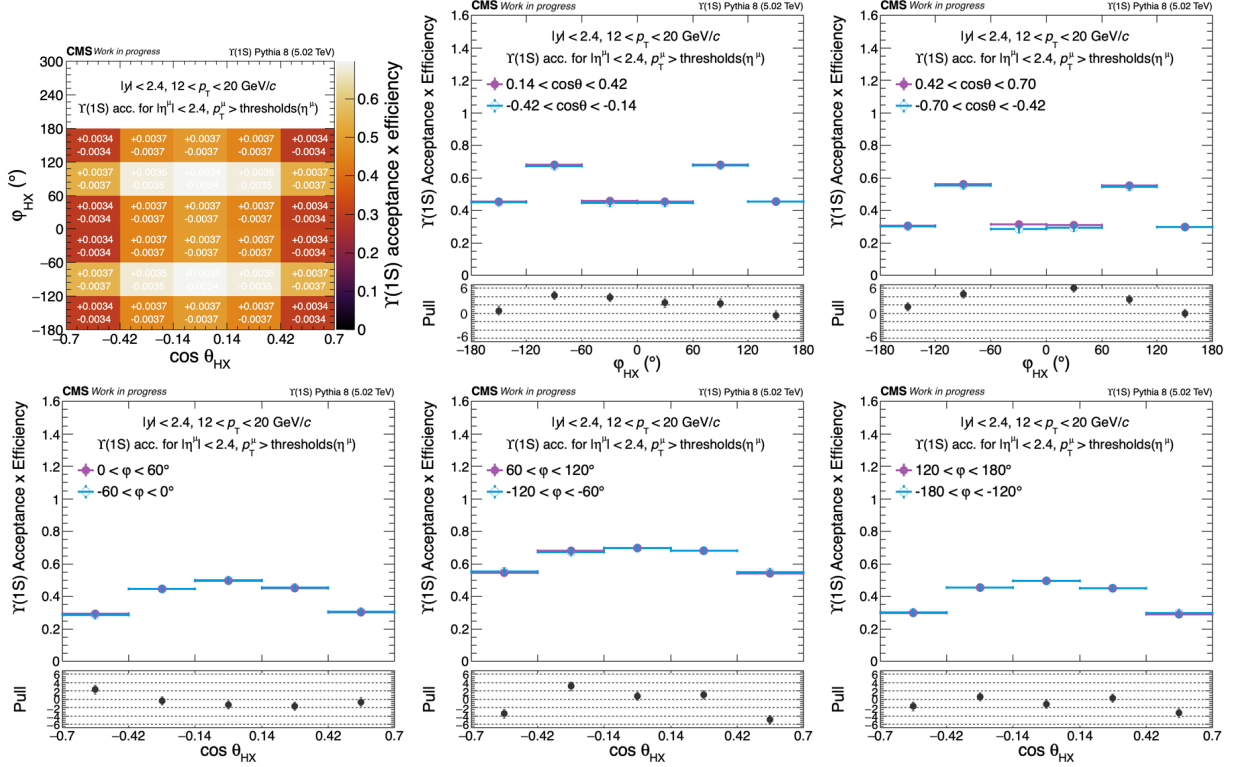
Figure 6.9: Acceptance × efficiency distributions in 1-D along the φ axis (top) and $\cos\theta$ axis (bottom) in the HX frame for $12 < p_T^{\mu\mu} < 20$ GeV/c. The 2-D plot in the top left is identical to the one in Fig. 6.3, but it displays asymmetric uncertainty values above each bin. Each 1-D plot compares a column (top) or row (bottom) on the positive side of $\cos\theta$ or φ values (purple) with the corresponding column or row on the negative side (blue). The bottom panel of each 1-D plot presents the pull distribution for each bin.

Chapter 7

Polarization Parameter Extraction

The extraction of polarization parameters in a given $p_T^{\mu\mu}$ bin requires correcting the $\Upsilon(1S)$ signal yield with the weight w defined below, applied bin by bin in the $\cos\theta$–φ phase space, to compensate for the effects of detector acceptance and efficiency:

$$w(p_T^{\mu\mu}, \cos\theta, \varphi) = \frac{1}{A(p_T^{\mu\mu}, \cos\theta, \varphi) \cdot \epsilon(p_T^{\mu\mu}, \cos\theta, \varphi)}, \tag{7.1}$$

where A and ϵ represent the acceptance and the efficiency, respectively, as obtained in Secs. 6.1 and 6.2. The corresponding acceptance $\times$ efficiency maps for the selected analysis bins, as defined in Sec. 5.2, are provided in Fig. 6.3.

Fits to extract polarization parameters are performed using a binned χ^2 minimization over the $\cos\theta$–φ phase space in each $p_T^{\mu\mu}$ bin with Eq. (1.3) as a fitting function. The fitting function is integrated over the bin ranges rather than evaluated at bin centers. Parameter uncertainties are obtained with Minos, together with the IMPROVE algorithm of TMinuit. After extracting λ_θ, λ_φ, and $\lambda_{\theta\varphi}$, the frame-invariant polarization parameter $\tilde{\lambda}$ is calculated using Eq. (1.4), which provides a frame-independent consistency check. For these fits, only the statistical uncertainties on the $\Upsilon(1S)$ signal yields were propagated. The statistical uncertainties of the acceptance and efficiency maps are separately accounted for as systematic

uncertainties (see Sec. 9.5).

The fit quality was evaluated using the reduced χ^2 and the corresponding p-value [116], which were typically found in the ranges $0.5 < \chi^2 < 1.9$ and $0.03 < p < 0.88$, indicating good agreement between the corrected $\Upsilon(1S)$ yields and the fitting function.

Figure 7.1 shows corrected $\Upsilon(1S)$ yields with uncertainties (left) and polarization parameter extraction fits with results (right) for two selected $p_T^{\mu\mu}$ bins: $2 < p_T^{\mu\mu} < 6\,\mathrm{GeV}/c$ (top) and $12 < p_T^{\mu\mu} < 20\,\mathrm{GeV}/c$ (bottom) in the HX frame. In the left plot, the corrected $\Upsilon(1S)$ yields are color-mapped with percentage uncertainties displayed for each bin. The right plot presents them as 3-D lego plots, overlaid with a red mesh representing the fit. The extracted polarization parameters are:

- $2 < p_T^{\mu\mu} < 6\,\mathrm{GeV}/c$, HX: $\lambda_\theta = 0.31 \pm 0.17$, $\lambda_\varphi = 0.00 \pm 0.03$, $\lambda_{\theta\varphi} = 0.05 \pm 0.07$, and $\tilde{\lambda} = 0.32 \pm 0.08$

- $12 < p_T^{\mu\mu} < 20\,\mathrm{GeV}/c$, HX: $\lambda_\theta = 0.10 \pm 0.23$, $\lambda_\varphi = -0.02 \pm 0.05$, $\lambda_{\theta\varphi} = -0.03 \pm 0.08$, and $\tilde{\lambda} = 0.04 \pm 0.16$

The results shown here were obtained with unpolarized acceptance and efficiency maps. The corresponding plots for the other $p_T^{\mu\mu}$ bins and for the CS frame are provided in Appendix F. An iterative procedure is performed in which the acceptance and efficiency are reweighted using the extracted polarization parameters in order to obtain the final results presented in Chapter 8.
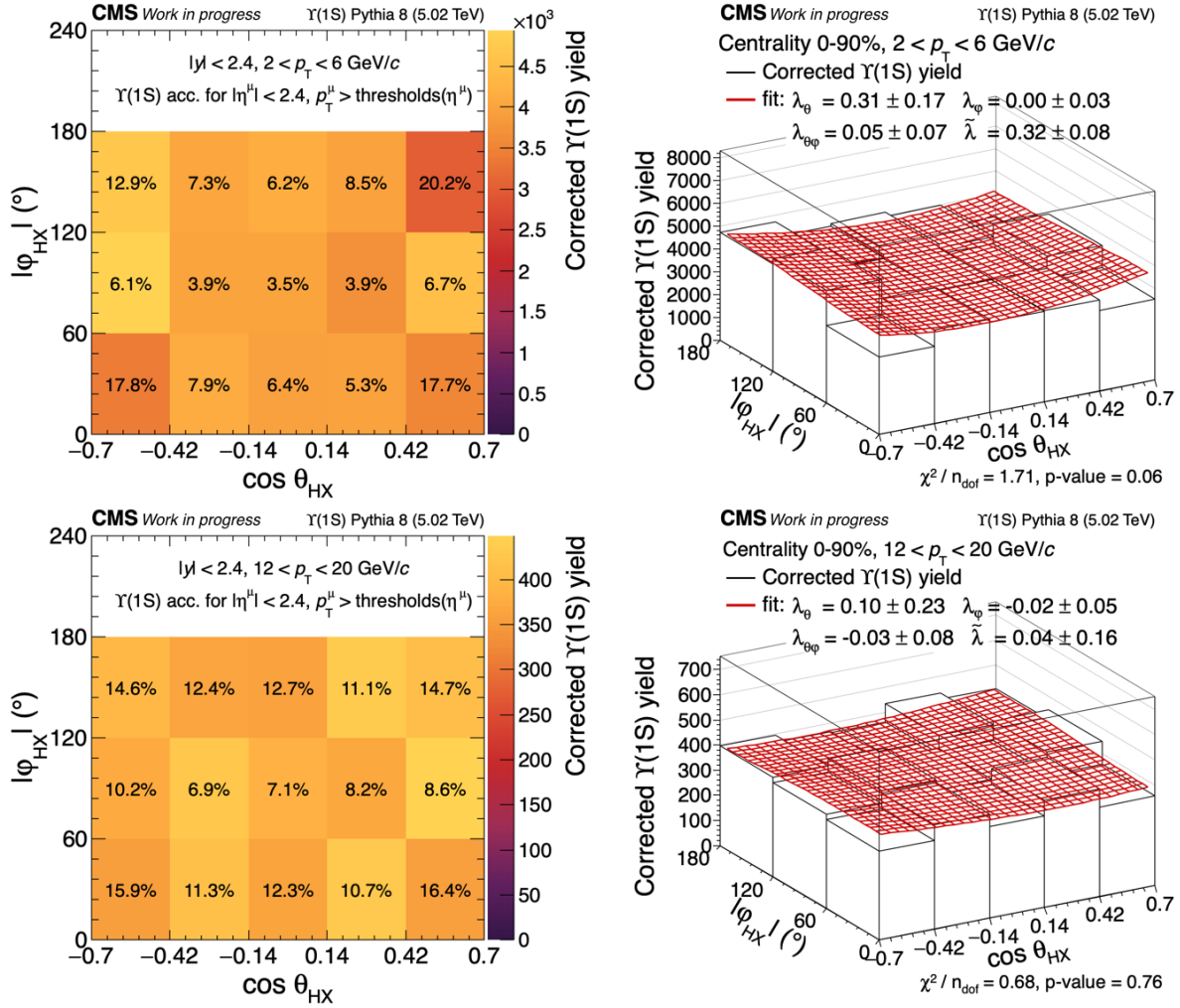
Figure 7.1: Examples of polarization parameter extraction fits: (top right) $2 < p_{\mathrm{T}}^{\mu\mu} < 6\,\mathrm{GeV}/c$ and (bottom right) $12 < p_{\mathrm{T}}^{\mu\mu} < 20\,\mathrm{GeV}/c$ in the HX frame. The left 2-D plots next to each 3-D fit show percentage uncertainty values over color-mapped corrected $\Upsilon(1S)$ yields.

Chapter 8

Closure Test

The analysis procedure, which includes acceptance and efficiency corrections as well as polarization parameter extraction, was validated using closure tests. Predetermined input polarization parameters were applied to the unpolarized MC samples. The extracted parameters were compared to the input parameters. Closure tests were performed independently for the two MC samples: the $\Upsilon(1S)$ PYTHIA MC and the $\Upsilon(1S)$ PYTHIA-embedded HYDJET MC, listed as (iii) and (ii) in Table 3.1. These were used to validate the acceptance-only correction to the GEN events and the combined acceptance and efficiency corrections to the RECO events, respectively.

The general steps of the closure test procedure are as follows:

1. Apply the input polarization parameters $(\lambda_\theta^{\text{in}}, \lambda_\varphi^{\text{in}}, \lambda_{\theta\varphi}^{\text{in}})$ to the MC sample at the GEN level on a dimuon-by-dimuon basis, using the general form of the angular distribution of the decay particles defined in Eq. (1.3).

2. Correct the polarized MC sample using correction factors derived under the null-polarization assumption $(\lambda_\theta, \lambda_\varphi, \lambda_{\theta\varphi}) = (0, 0, 0)$, applied bin-by-bin in the $(\cos\theta, \varphi)$ angular distribution plane. In the case of the $\Upsilon(1S)$ PYTHIA MC, only the ac-

87

ceptance map was applied; in the PYTHIA-embedded HYDJET sample, the combined acceptance and efficiency map was used.

3. Extract polarization parameters by fitting the corrected MC distributions. Compare the results to the input parameters in order to assess closure within the statistical uncertainties.

A closure test using an iterative procedure, which improves the closure test result, is discussed in Sec. 8.3.

All multi-panel figures referenced in this section share a unified style: In each 2-D plot, z-axis values are color-coded and displayed on top of each bin. In the 3-D plot, the red mesh indicates the fit. The extracted parameters with their uncertainties are shown in the legend.

8.1 Closure Test Using $\Upsilon(1S)$ PYTHIA MC with Acceptance Correction

Figures 8.1 and 8.2 show closure test results for two representative input polarization scenarios in the HX frame for the region $2 < p_{\mathrm{T}}^{\mu\mu} < 6\,\mathrm{GeV}$; $(\lambda_\theta^{\mathrm{in}}, \lambda_\varphi^{\mathrm{in}}, \lambda_{\theta\varphi}^{\mathrm{in}}) = (0, 0, 0)$ and $(1, 0, 0)$. Each figure includes four panels that illustrate the closure test procedure.

The top-left panel shows the angular distribution of generated $\Upsilon(1S)$ events in which both muons fall within the acceptance region shown in Fig. 3.2, based on the GEN-level MC sample without any kinematic filters. The top-right panel displays the corresponding acceptance map, obtained according to the definition in Eq. (6.1) under the assumption of null polarization. The bottom-left panel presents the generated $\Upsilon(1S)$ events in the angular distribution plane after applying acceptance corrections on a bin-by-bin basis. The bottom-right panel shows the polarization parameters extracted from the corrected distribution.

Figure 8.1: Closure test with input polarization parameters $(\lambda_\theta^{in}, \lambda_\varphi^{in}, \lambda_{\theta\varphi}^{in}) = (0, 0, 0)$ in the HX frame for the region $2 < p_T^{\mu\mu} < 6$ GeV. Top-left: angular distribution of generated $\Upsilon(1S)$ events within the acceptance region. Top-right: acceptance map computed under the null polarization assumption. Bottom-left: angular distribution after acceptance correction. Bottom-right: fit to the corrected distribution and extracted polarization parameters.

In the unpolarized case $(\lambda_\theta^{in}, \lambda_\varphi^{in}, \lambda_{\theta\varphi}^{in}) = (0, 0, 0)$, the extracted values are consistent with the input parameters. When the input $(\lambda_\theta^{in}, \lambda_\varphi^{in}, \lambda_{\theta\varphi}^{in}) = (1, 0, 0)$, a non-negligible deviation $(0.93 \pm 0.02, -0.00 \pm 0.01, 0.00 \pm 0.01)$ is observed, indicating that the acceptance correction does not fully recover the polarization in non-zero polarization cases.

Figure 8.2: Closure test with input polarization parameters $(\lambda_\theta^{\text{in}}, \lambda_\varphi^{\text{in}}, \lambda_{\theta\varphi}^{\text{in}}) = (1, 0, 0)$ in the HX frame for the region $2 < p_\text{T}^{\mu\mu} < 6\,\text{GeV}$. Top-left: angular distribution of generated $\Upsilon(1S)$ events within the acceptance region. Top-right: acceptance map computed under the null polarization assumption. Bottom-left: angular distribution after acceptance correction. Bottom-right: fit to the corrected distribution and extracted polarization parameters.

The discrepancy between the input and extracted polarization parameters arises from averaging the polarization weights when mapping the dimuon-based acceptance. This mismatch can be mitigated by applying finer binning in $\cos\theta$ and φ, or by performing an iterative procedure, which will be discussed in Sec. 8.3. Figure 8.3 demonstrates that finer binning

recovers the input polarization parameters, within uncertainties. However, the choice of analysis bins is constrained by the available Υ statistics in the signal extraction step. In this analysis, the iterative procedure described in Sec. 8.3 was adopted.
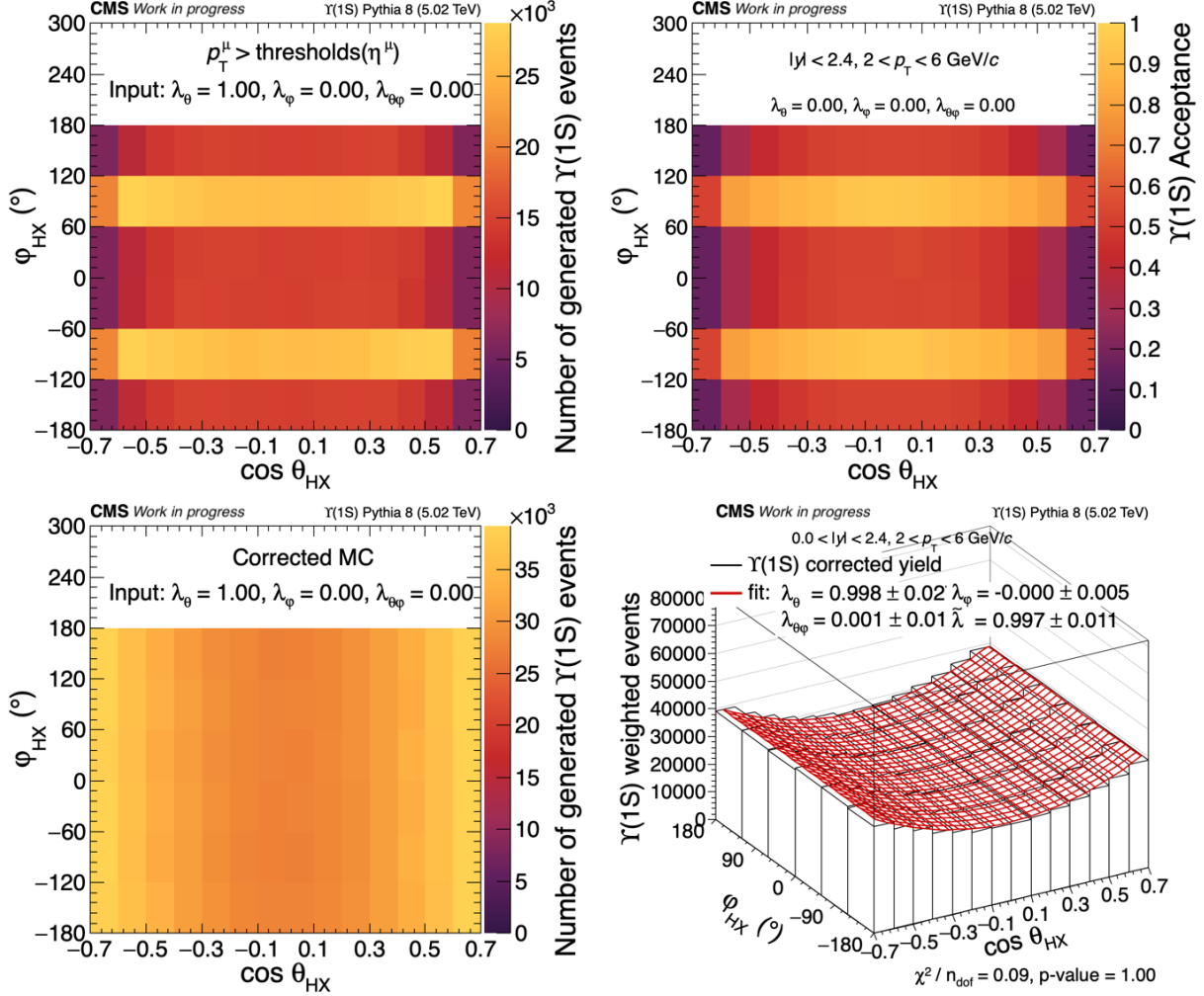
Figure 8.3: Closure test with input polarization parameters $(\lambda_\theta^{\text{in}}, \lambda_\varphi^{\text{in}}, \lambda_{\theta\varphi}^{\text{in}}) = (1, 0, 0)$ in the HX frame for $2 < p_{\text{T}}^{\mu\mu} < 6$ GeV, using finer binning along the $\cos\theta$-axis $(5 \to 14$ bins). Top-left: angular distribution of generated $\Upsilon(1\text{S})$ events within the acceptance region. Top-right: acceptance map computed under the null polarization assumption. Bottom-left: angular distribution after acceptance correction. Bottom-right: fit to the corrected distribution and extracted polarization parameters.

8.2 Closure Test Using PYTHIA-embedded HYDJET MC with Acceptance and Efficiency Corrections

Another closure test was performed using the reconstructed PYTHIA-embedded HYDJET $\Upsilon(1S)$ sample to validate the analysis procedure including acceptance and efficiency corrections. The same procedure as described in Sec. 8.1 was followed, but this time both acceptance and efficiency corrections were applied at the RECO level.

Important details about this procedure:

- SFs were not applied in the efficiency calculation since SFs are meant to compensate for discrepancies between data and MC. In this test, only MC is used.

- Because acceptance and efficiency were computed from two different MC samples, a small residual arises from the correction factor. By definition (see Eqs. (6.1), (6.2), and (7.1)), the acceptance numerator should be identical to the efficiency denominator. The only reason they are not is that the two quantities come from different MC samples, which contain a large number of events and can therefore introduce small but statistically significant fluctuations in the corrected distribution. The residual weight correction ensures that these fluctuations are removed. The residual weight, $w_{res}(p_T^{\mu\mu}, \cos\theta, \varphi)$, is defined as the ratio of the acceptance numerator to the efficiency denominator:

$$w_{res}(p_T^{\mu\mu}, \cos\theta, \varphi) = \frac{\text{acceptance numerator}}{\text{efficiency denominator}}. \tag{8.1}$$

- This residual factor is calculated for every iterative procedure and multiplied into the nominal correction weight to cancel the mismatch and avoid polarization bias.

Figures. 8.4 and 8.5 show representative cases for two input polarization scenarios in the HX frame for the region $2 < p_T^{\mu\mu} < 6\,\text{GeV}$; $(\lambda_\theta^{in}, \lambda_\varphi^{in}, \lambda_{\theta\varphi}^{in}) = (0, 0, 0)$ and $(1, 0, 0)$. Each

figure includes five panels: reconstructed angular distribution, acceptance map, efficiency map, corrected distribution, and final 2-D fit with extracted polarization parameters.

In the unpolarized input case $(\lambda_\theta^{\text{in}}, \lambda_\varphi^{\text{in}}, \lambda_{\theta\varphi}^{\text{in}}) = (0, 0, 0)$, the fitted parameters are consistent with zero, within the uncertainties. This test with null polarization confirms that the procedure does not generate polarization bias. When the input parameters $(\lambda_\theta^{\text{in}}, \lambda_\varphi^{\text{in}}, \lambda_{\theta\varphi}^{\text{in}})$ = (1, 0, 0) were applied, the input values were not fully recovered (extracted polarization parameters $(\lambda_\theta, \lambda_\varphi, \lambda_{\theta\varphi}) = (0.86 \pm 0.03, -0.00 \pm 0.01, 0.00 \pm 0.01)$). This deviation reflects the same polarization weight averaging effect observed in the GEN-level test in Sec. 8.1, indicating the need for finer binning or an iterative procedure in the analysis.

Figure 8.6 shows the extracted polarization parameters for the $(\lambda_\theta^{\text{in}}, \lambda_\varphi^{\text{in}}, \lambda_{\theta\varphi}^{\text{in}}) = (1, 0, 0)$ case in the HX frame for the region $2 < p_{\text{T}}^{\mu\mu} < 6\,\text{GeV}$, when the number of bins along the $\cos\theta$-axis was increased from 5 to 14. The extracted parameters $(\lambda_\theta, \lambda_\varphi, \lambda_{\theta\varphi}) = (0.99 \pm 0.03, 0.00 \pm 0.01, 0.00 \pm 0.01)$ demonstrate that the input parameters are recovered within the uncertainties. However, as already noted in the previous section, the choice of analysis binning is constrained by available statistics. For this case, an iterative procedure was adopted, as discussed in Sec. 8.3.

8.3 Iterative Procedure

The closure tests demonstrated that acceptance and efficiency maps derived under the null polarization assumption can bias the extraction of polarization parameters when the true polarization is nonzero. To mitigate this effect, an iterative procedure was implemented.

The iterative steps are as follows:

1. Apply corrections with acceptance and efficiency maps constructed under the null polarization assumption.

2. Extract the polarization parameters from the corrected distribution. Use these parameters to reweight the underlying polarization in the MC samples, from which new acceptance and efficiency maps are derived.

3. Recalculate the corrected distribution using the updated acceptance and efficiency maps

4. Repeat steps 2–4 until convergence (i.e., the parameter changes between successive iterations are smaller than their statistical uncertainties).

In this way, the acceptance and efficiency corrections are made consistent with the actual underlying polarization.

Figures 8.7 and 8.8 show the iterative procedure for two representative input polarization scenarios: $(\lambda_\theta^{\mathrm{in}}, \lambda_\varphi^{\mathrm{in}}, \lambda_{\theta\varphi}^{\mathrm{in}}) = (1, 0, 0)$ and $(0.88, -0.8, 0.2)$. The bottom-right plot in each figure displays the evolution of the extracted polarization parameters over successive iterations. In both cases, the input values are recovered within statistical uncertainties after approximately two to four iterations, demonstrating the rapid convergence of the iterative correction method.
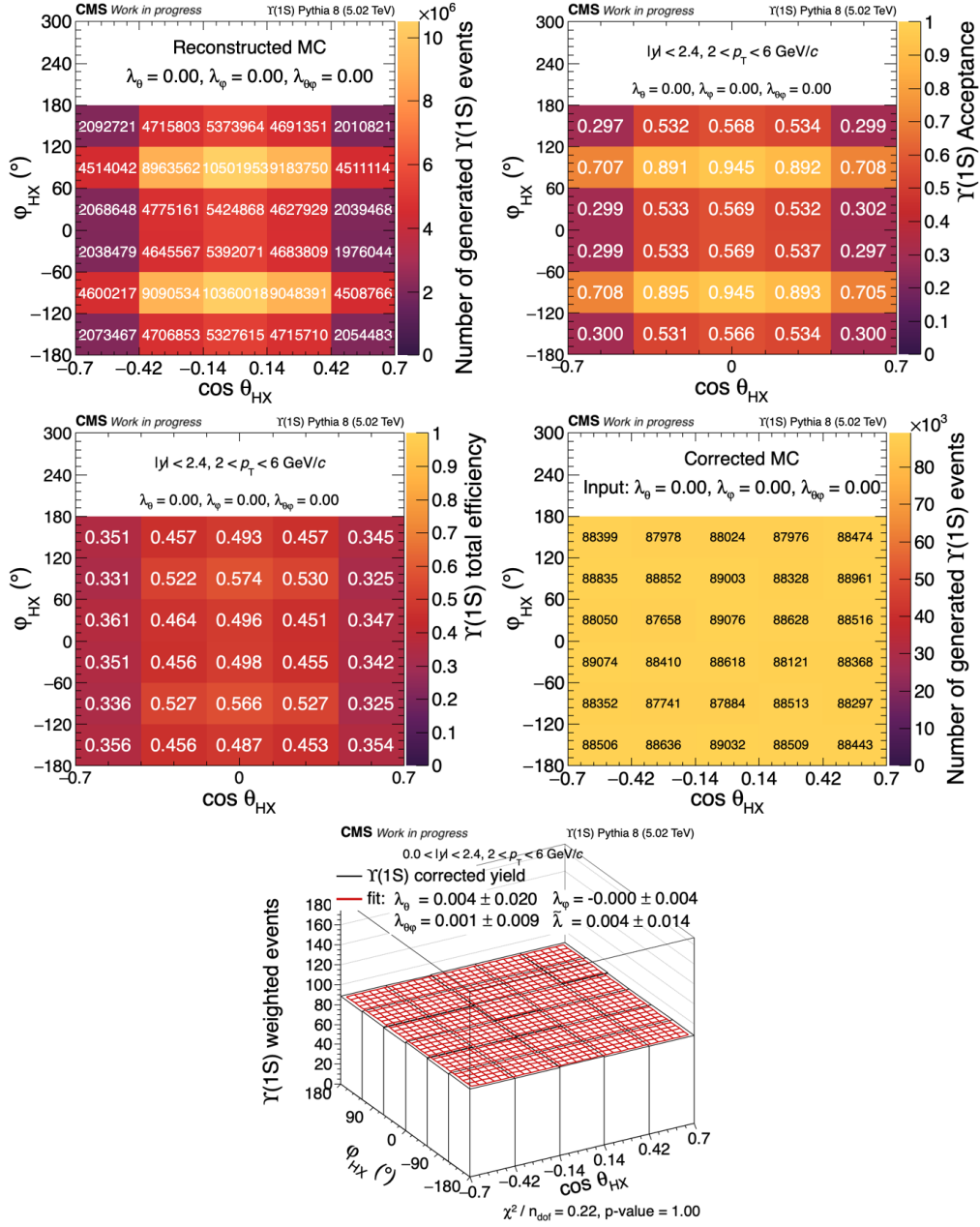
Figure 8.4: Closure test with input polarization parameters $(\lambda_\theta^{\mathrm{in}}, \lambda_\varphi^{\mathrm{in}}, \lambda_{\theta\varphi}^{\mathrm{in}}) = (0, 0, 0)$ in the HX frame for the region $2 < p_\mathrm{T}^{\mu\mu} < 6\,\mathrm{GeV}$. Top-left: angular distribution of reconstructed $\Upsilon(1S)$ events. Top-right: acceptance map computed under the null polarization assumption. Middle-left: total efficiency map computed under the null polarization assumption. Middle-right: angular distribution after Acceptance × efficiency correction. Bottom: fit to the corrected distribution and extracted polarization parameters.
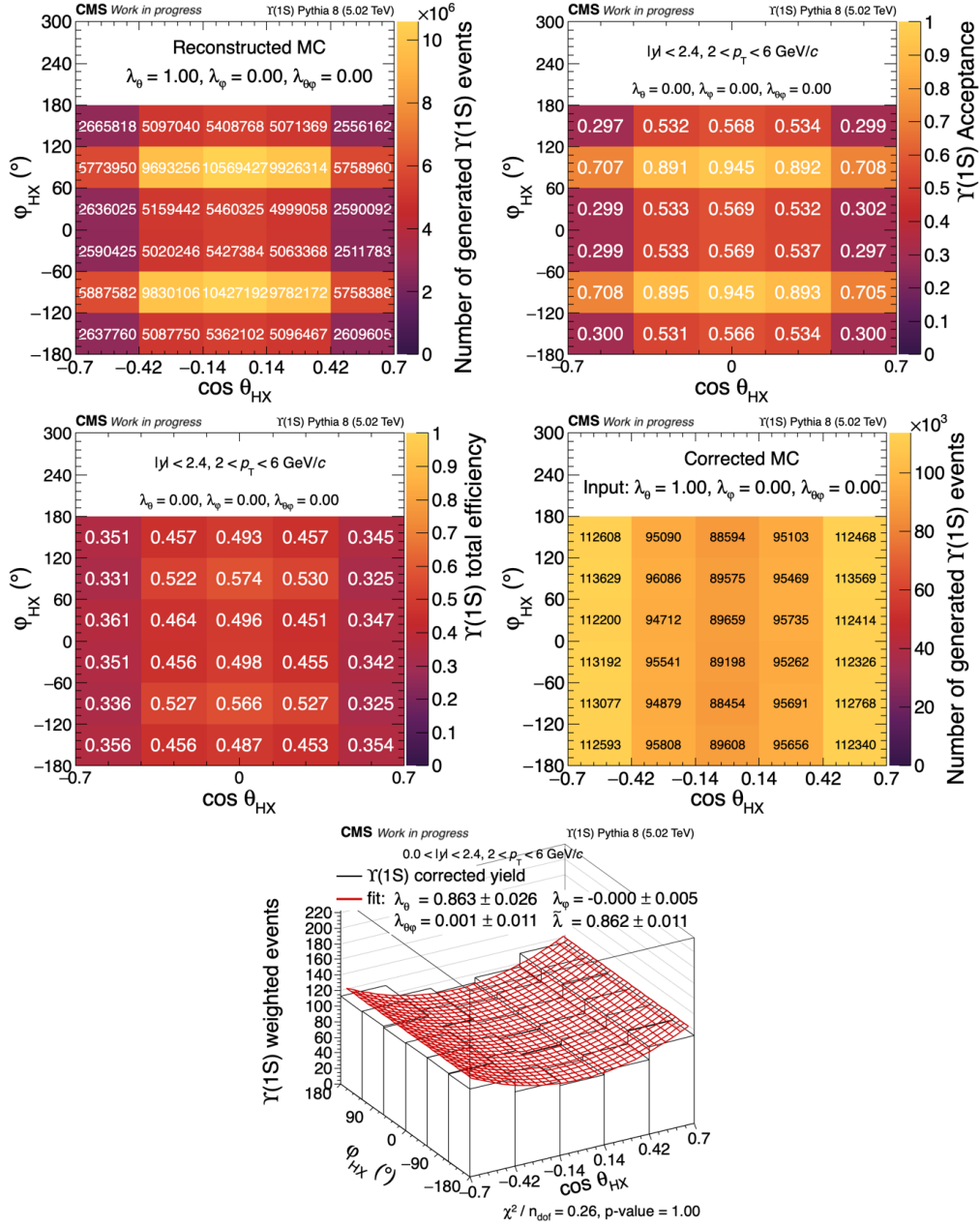
Figure 8.5: Closure test with input polarization parameters $(\lambda_\theta^{\text{in}}, \lambda_\varphi^{\text{in}}, \lambda_{\theta\varphi}^{\text{in}}) = (1, 0, 0)$ in the HX frame for the region $2 < p_T^{\mu\mu} < 6$ GeV. Top-left: angular distribution of reconstructed $\Upsilon(1S)$ events. Top-right: acceptance map computed under the null polarization assumption. Middle-left: total efficiency map computed under the null polarization assumption. Middle-right: angular distribution after Acceptance × efficiency correction. Bottom: fit to the corrected distribution and extracted polarization parameters.
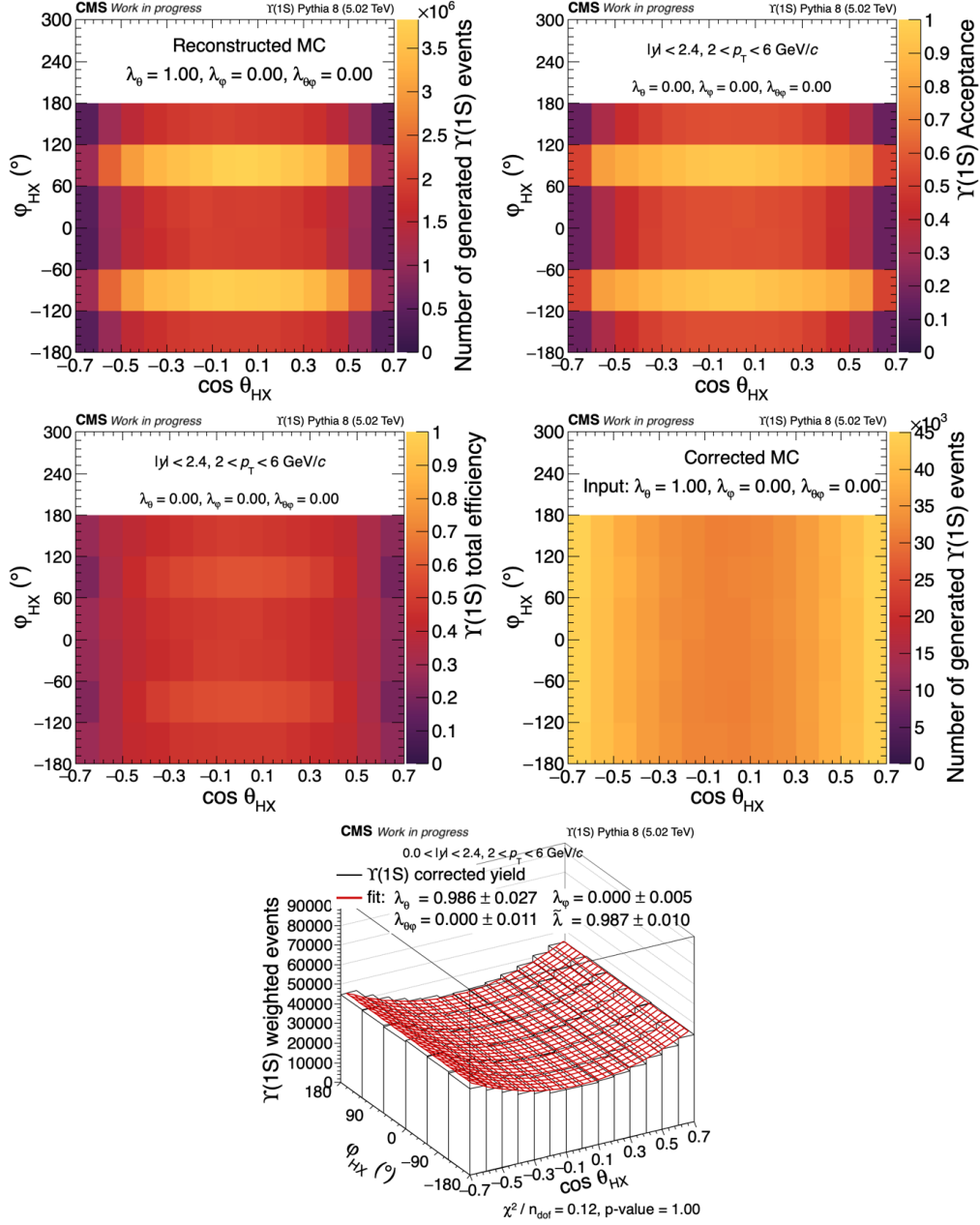
Figure 8.6: Closure test with input polarization parameters $(\lambda_\theta^{\mathrm{in}}, \lambda_\varphi^{\mathrm{in}}, \lambda_{\theta\varphi}^{\mathrm{in}}) = (1, 0, 0)$ in the HX frame for the region $2 < p_{\mathrm{T}}^{\mu\mu} < 6\,\mathrm{GeV}$, using finer binning along the $\cos\theta$-axis ($5 \to 14$ bins). Top-left: angular distribution of reconstructed $\Upsilon(1S)$ events. Top-right: acceptance map computed under the null polarization assumption. Middle-left: total efficiency map computed under the null polarization assumption. Middle-right: angular distribution after Acceptance × efficiency correction. Bottom: fit to the corrected distribution and extracted polarization parameters.
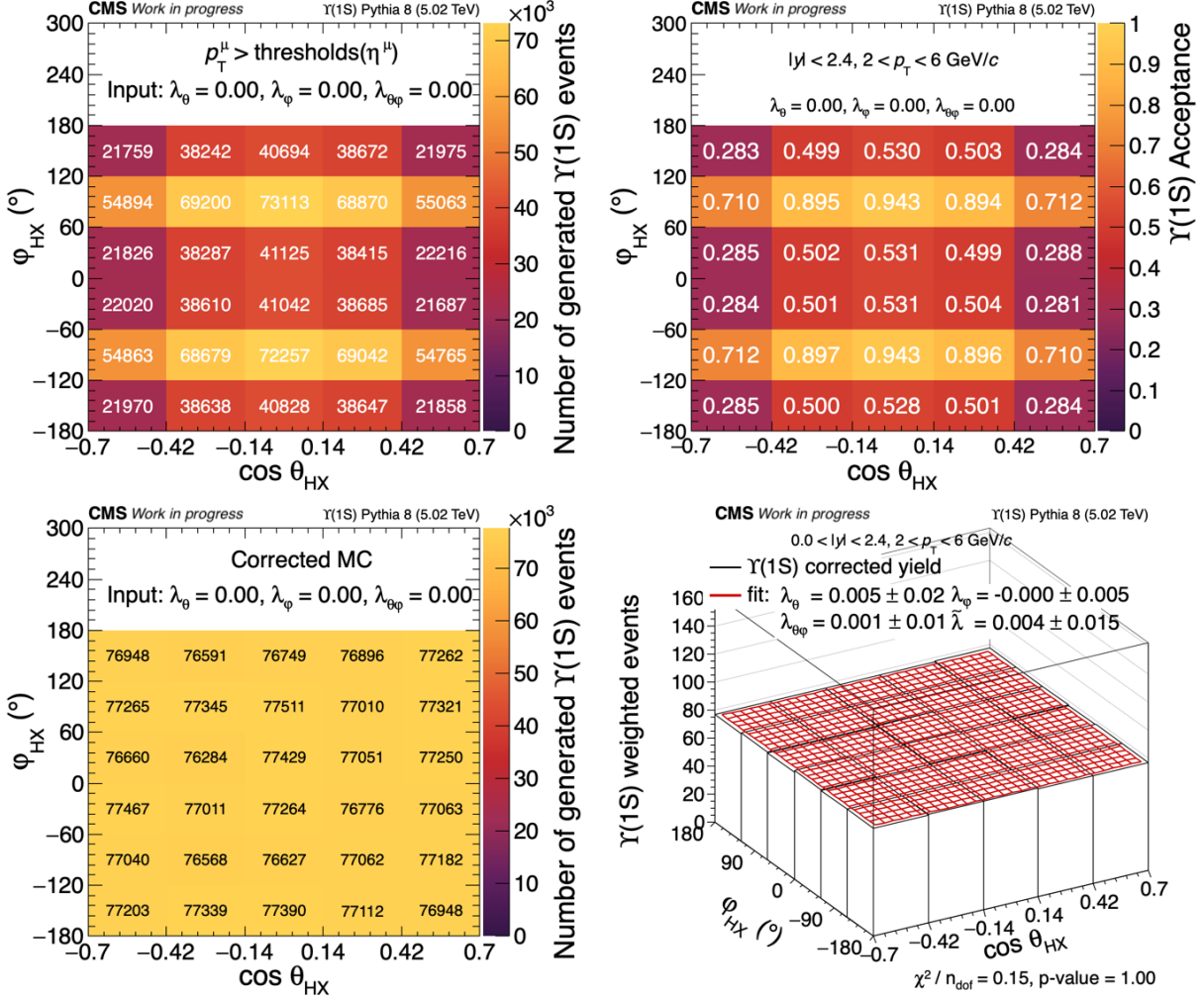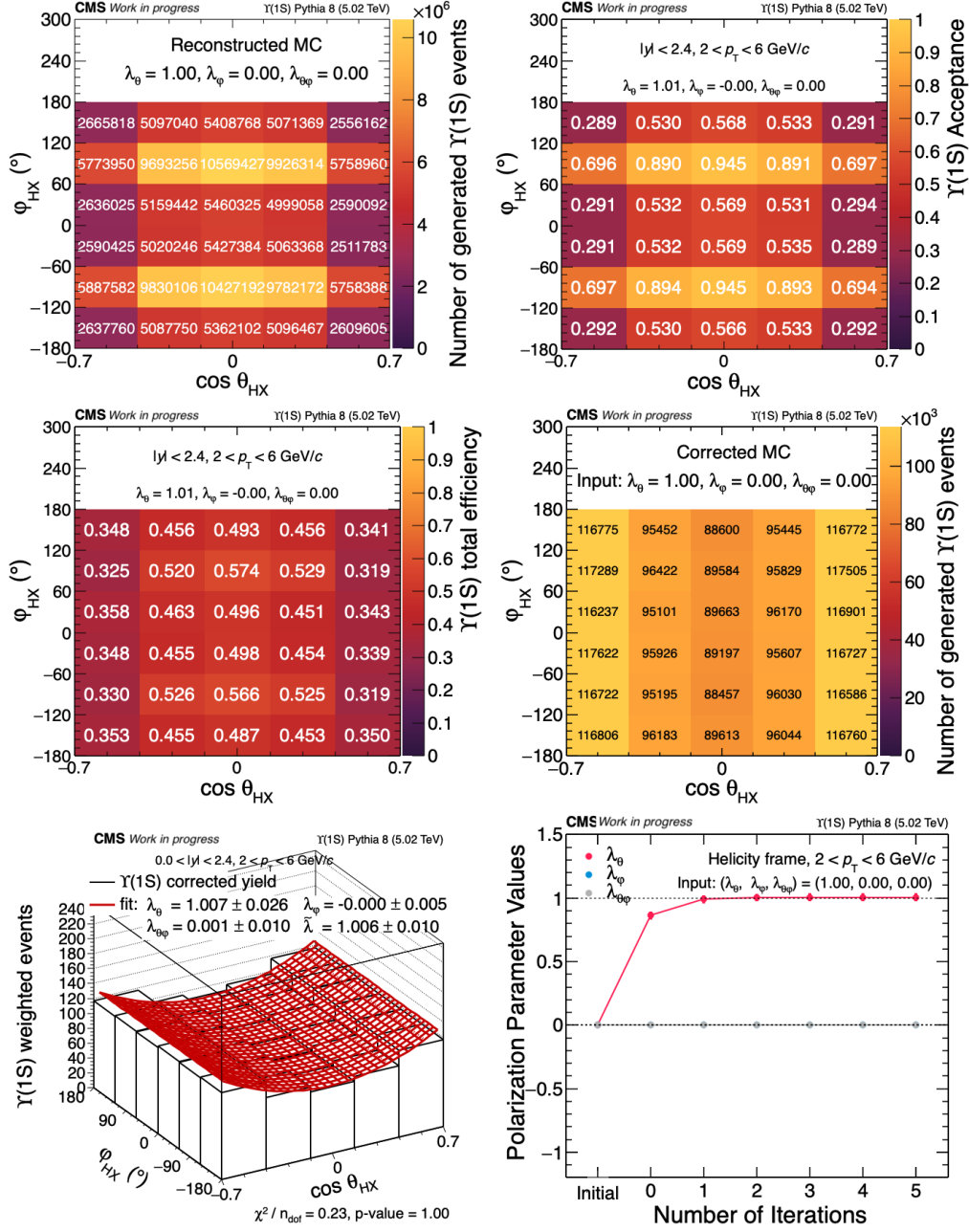
Figure 8.7: Iterative closure test with input polarization parameters $(\lambda_\theta^{\mathrm{in}}, \lambda_\varphi^{\mathrm{in}}, \lambda_{\theta\varphi}^{\mathrm{in}}) = (1, 0, 0)$ in the HX frame for the region $2 < p_{\mathrm{T}}^{\mu\mu} < 6\,\mathrm{GeV}$. Top-left: angular distribution of reconstructed $\Upsilon(1S)$ events. Top-right: acceptance map (iteration 5). Middle-left: efficiency map (iteration 5). Middle-right: angular distribution after acceptance × efficiency correction (iteration 5). Bottom-left: fit to the corrected distribution with extracted polarization parameters (iteration 5). Bottom-right: evolution of the extracted parameters versus the number of iterations.
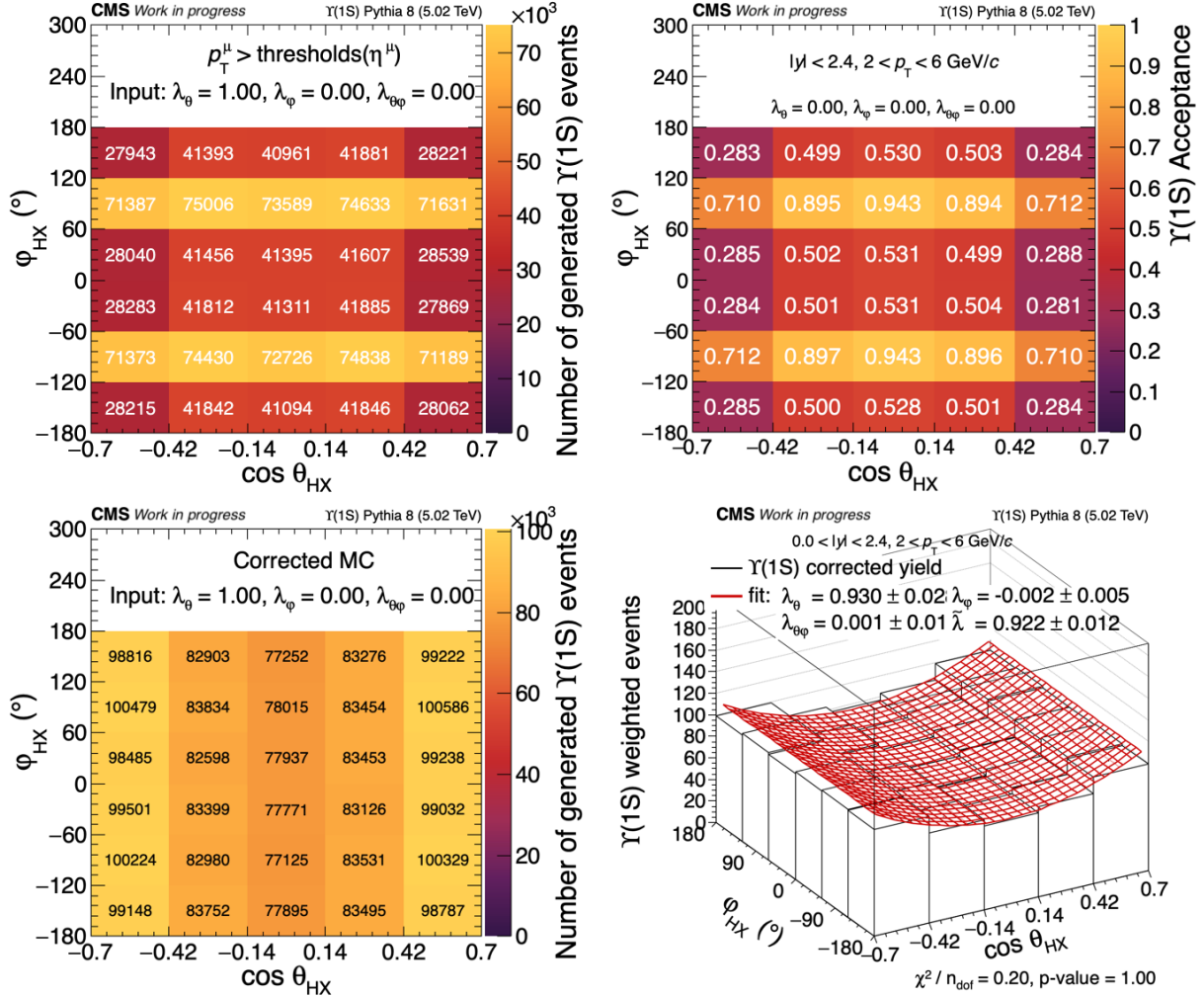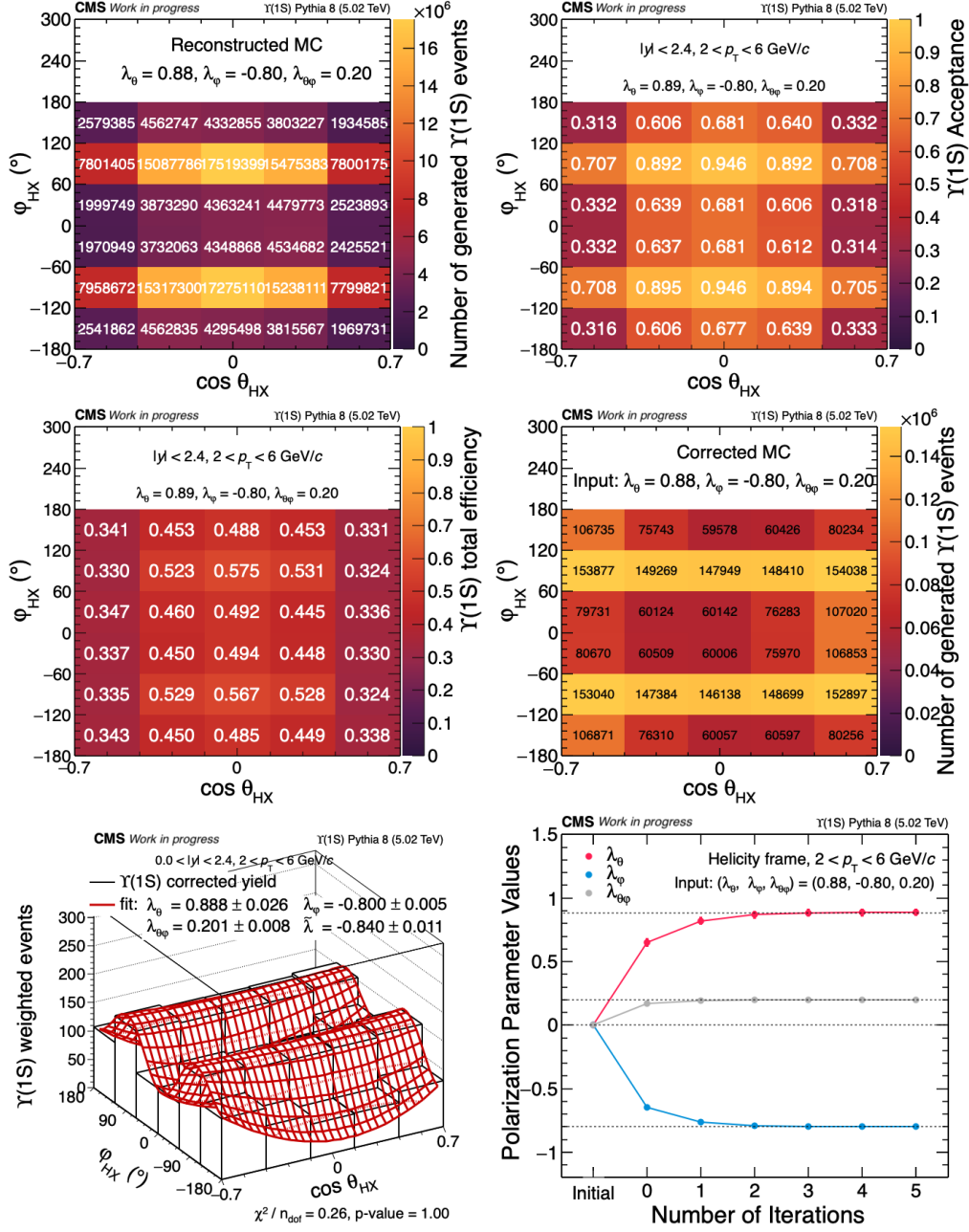
Figure 8.8: Iterative closure test with input polarization parameters $(\lambda_\theta^{\text{in}}, \lambda_\varphi^{\text{in}}, \lambda_{\theta\varphi}^{\text{in}}) = (0.88, -0.80, 0.20)$ in the HX frame for the region $2 < p_T^{\mu\mu} < 6\,\text{GeV}$. Top-left: angular distribution of reconstructed $\Upsilon(1S)$ events. Top-right: acceptance map (iteration 5). Middle-left: efficiency map (iteration 5). Middle-right: angular distribution after acceptance $\times$ efficiency correction (iteration 5). Bottom-left: fit to the corrected distribution with extracted polarization parameters (iteration 5). Bottom-right: evolution of the extracted parameters versus the number of iterations.

Chapter 9

Systematic Uncertainties

Systematic uncertainties were evaluated from muon efficiency SFs and from alternative signal/background fit models. The systematic uncertainties in the polarization parameters from various sources were determined by first calculating the systematic uncertainties on the $\Upsilon(1S)$ yields in each $(p_{\mathrm{T}}^{\mu\mu}, \cos\theta, \varphi)$ bin. The polarization parameters were then re-extracted, using the newly obtained $\Upsilon(1S)$ yields to derive the final systematic uncertainty.

The potential bias of the fit models was assessed through pseudo-experiments, accounting for fluctuations in the data. The procedure for the pseudo-experiments is outlined as follows:

1. Generate the PDF using the fit results from $\Upsilon(1S)$ yield extraction in each $(p_{\mathrm{T}}^{\mu\mu}, \cos\theta, \varphi)$ bin.

2. Sample from the PDF to reproduce the same number of entries as the sum of signal and background in the original PDF.

3. Fit the generated pseudo-data with an alternative fit model.

4. Repeat the pseudo-data generation and fitting process 10,000 times.

5. Calculate the mean value of the difference between the input yield used to generate the PDF and the yield obtained from the pseudo-data fits.

6. Extract the polarization parameters from the new yields.

9.1 Signal Shape Modeling

As an alternative signal model, Johnson's PDF was utilized, defined as follows:

$$J(m^{\mu\mu}; \gamma, \delta, \mu, \lambda) = \frac{\delta}{\lambda\sqrt{2\pi}} \frac{1}{\sqrt{1 + (\frac{m^{\mu\mu}-\mu}{\lambda})^2}} \exp\left(-\frac{1}{2}\left(\gamma + \delta \sinh^{-1}\left(\frac{m^{\mu\mu}-\mu}{\lambda}\right)\right)^2\right), \quad (9.1)$$

where γ and δ are shape parameters, μ is a location parameter, and λ is a scale parameter [117, 118].

The DSCB signal model for each resonance state Υ in Eq. (5.2) was replaced with J from Eq. (9.1). The three Υ resonance states shared the same values for the parameters γ, δ, and λ, which were extracted from the MC sample corresponding to each $(p_T^{\mu\mu}, \cos\theta, \varphi)$ bin. For the signal extraction procedure, these parameters were constrained using Gaussian constraints. Pseudo-experiments were then performed in each $(p_T^{\mu\mu}, \cos\theta, \varphi)$ bin for both the CS and HX frames, following the aforementioned procedure.

Figure 9.1 presents an example of pseudo-experiment results for the alternative signal model in the HX frame within the kinematic range $2 < p_T^{\mu\mu} < 6$ GeV/c, $-0.42 < \cos\theta < -0.14$, and $60 < |\varphi| < 120°$. The plot on the left shows the fit using J as an alternative signal model for the data in the same bin. The plot on the right illustrates the distribution of the yield difference between the nominal fit to the data using DSCB as the signal model and the fit with J to the same pseudo-data, after 10,000 pseudo-experiments. Fits were excluded from the distribution if they failed or if the reduced χ^2 value exceeded 5. For this bin, the $\Upsilon(1S)$ yield with J is estimated to be, on average, ~ 9 events lower than the nominal fit.

The complete set of pseudo-experiment results across all $(p_{\mathrm{T}}^{\mu\mu}, \cos\theta, \varphi)$ bins can be found in Appendix G.
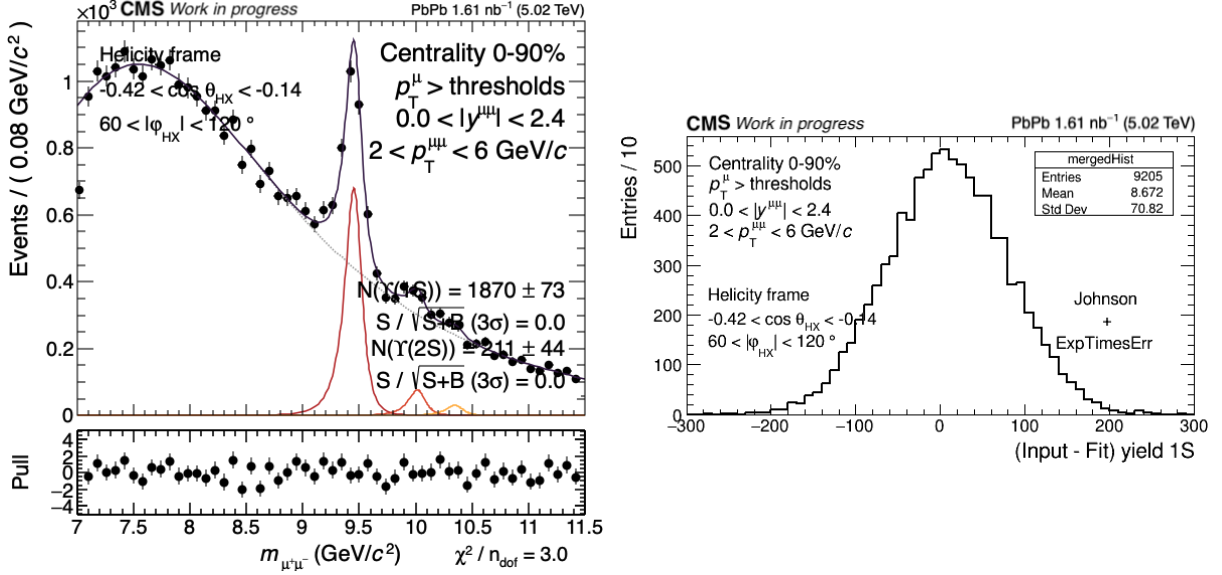
Figure 9.1: An example of pseudo-experiment results with an alternative signal model: Johnson's PDF in the range $2 < p_{\mathrm{T}}^{\mu\mu} < 6$ GeV/c, $-0.42 < \cos\theta < -0.14$, and $60 < |\varphi| < 120°$ in the HX frame. The plot on the left shows a fit to the data with this alternative signal model, with the pull distribution displayed in the bottom panel. The plot on the right shows the pseudo-experiment results after repeating the procedure 10,000 times. The $\Upsilon(1S)$ yield difference was defined as alternative fit to pseudo-data minus nominal fit to data. The average difference in $\Upsilon(1S)$ yield was ~ 9 counts.

9.2 Background Shape Modeling

As an alternative background fit model, third-order Chebyshev polynomials of the first kind were selected [119, 120]. The Chebyshev polynomials of the first kind are defined as:

$$T_n(x) = \cos(n \cos^{-1} x), \tag{9.2}$$

with the recurrence relation:

$$T_0(x) = 1, \quad T_1(x) = x, \quad T_{n+1}(x) = 2xT_n(x) - T_{n-1}(x).$$

102

Following this recurrence relation, the third-order polynomial is given by

$$T_3(x) = 4x^3 - 3x. \tag{9.3}$$

The polynomial was evaluated in a rescaled variable $x \in [-1, 1]$, obtained from the invariant mass m through

$$x = \frac{2\,(m - m_{\mathrm{min}})}{m_{\mathrm{max}} - m_{\mathrm{min}}} - 1, \tag{9.4}$$

where m_{min} and m_{max} are the edges of the fit mass window. For the pseudo-experiments, the background model B in Eq. (5.6) was replaced with a third-order Chebyshev polynomial.

Figure 9.2 shows an example of the pseudo-experiment using the alternative background model in $2 < p_{\mathrm{T}}^{\mu\mu} < 6$ GeV/c, $-0.42 < \cos\theta < -0.14$, and $60 < |\varphi| < 120°$ in the HX frame. The plot on the left shows the fit to the data using the alternative background model. The plot on the right shows the pseudo-experiment results for the same bin. After repeating 10,000 pseudo-experiments, a shift in the $\Upsilon(1\mathrm{S})$ yield was observed, with 12 more events than estimated by the nominal model.

The complete set of pseudo-experiment results across all $p_{\mathrm{T}}^{\mu\mu}$, $\cos\theta$, and φ bins is presented in Appendix G.

9.3 Ambiguity of Signal and Background

In addition, in some bins of the analysis, the particular selection of $(p_{\mathrm{T}}^{\mu\mu}, \cos\theta, \varphi)$ produced a kinematic peak in the underlying background near the location of the Υ mass. In these bins, the fit procedure could incorrectly assess the yield of Υ mesons. To assess the effect of the uncertainty arising from the cases where the background peak is near the signal peak, the pseudo-experiment was fitted with the same signal and background PDF that was used to generate the pseudo-data.
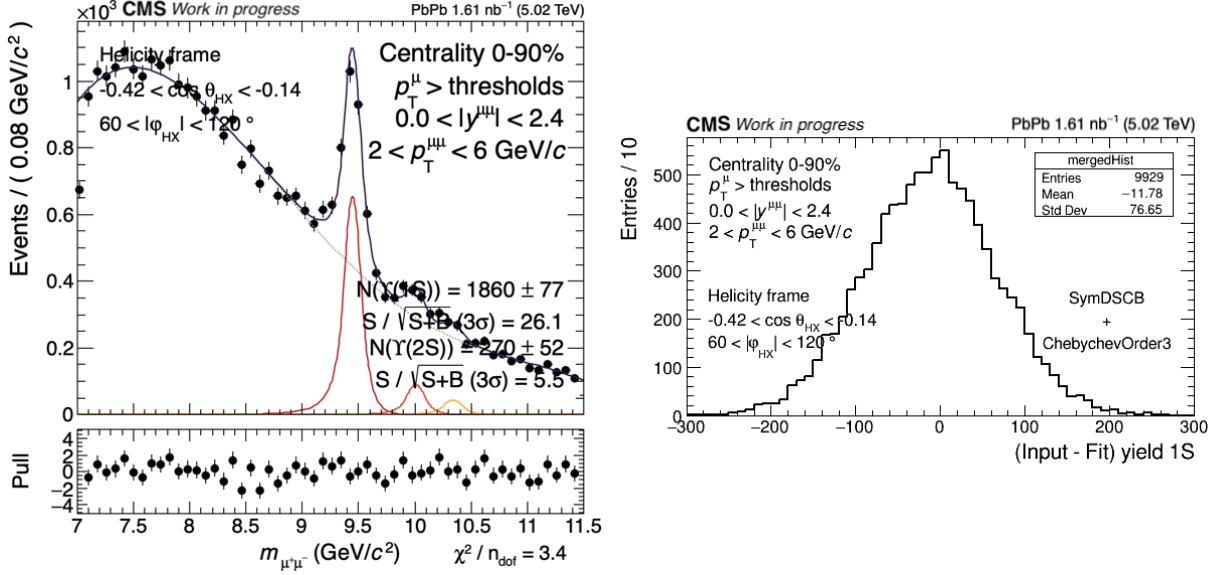
Figure 9.2: An example of pseudo-experiment results with an alternative background model, third-order Chebyshev polynomials in the range $2 < p_T^{\mu\mu} < 6$ GeV/c, $-0.42 < \cos\theta < -0.14$, and $60 < |\varphi| < 120°$ in the HX frame. The plot on the left shows a fit to the data with this alternative background model, with the pull distribution displayed in the bottom panel. The plot on the right shows the pseudo-experiment results after repeating the procedure 10,000 times. The Υ(1S) yield difference between the nominal fit model fitted to the data and the alternative model fitted to the pseudo-data was $\sim$ -12 events, on average.

In a given ($p_T^{\mu\mu}$, $\cos\theta$, φ) region, when the background peak did not fall under the signal peak, the yield that was extracted from the fit matched the input yield, leading to no change in the yield for that bin. However, other ($\cos\theta$, φ) bins within the same $p_T^{\mu\mu}$ region that have a background peak that did fall under the signal peak showed systematic shifts in the extracted yield relative to the input yield. Taking this uncertainty into account, i.e. the fact that the yield could shift more in some ($\cos\theta$, φ) bins than in others, led to a modification of the shape of the angular distribution in a given $p_T^{\mu\mu}$ range. This effect was one of the largest sources of uncertainty in the polarization parameters. This background under signal ambiguity is already counted by the alternative background PDF pseudo experiments. The dedicated

104

pseudo-experiments with the nominal PDF were used only to verify the mechanism, and no additional separate uncertainty was assigned so as to avoid double counting.

Figure 9.3 shows an example of the pseudo-experiment results. In this case, the signal and background PDF are identical to the nominal PDF. Here, the background peak was below the signal peak. This example corresponds to the bin range $2 < p_{\mathrm{T}}^{\mu\mu} < 6$ GeV/c, $-0.70 < \cos\theta < -0.42$, and $60 < |\varphi| < 120$. The mean value of the difference between the input from the nominal results and the fitted yield in the pseudo-experiment was expected to be close to 0. However, the obtained mean value is $\sim -16 \pm 71$, as shown in the figure on the right. This result indicates the ambiguity of signal and background when the background peak is located near or beneath the signal peak.

The complete set of pseudo-experiment results across all $(p_{\mathrm{T}}^{\mu\mu}, \cos\theta, \varphi)$ bins is presented in Appendix G.

9.4   Muon Efficiency Scale Factors

The systematic uncertainties in the polarization parameters that arise from the systematic uncertainties of the SFs, were determined by recalculating the SFs at their upper and lower systematic uncertainty limits. The uncertainties for each SF are detailed in Ref. [114]. The total SFs, $\mathrm{SF}_{\mathrm{total}}^{\mathrm{syst+}}$ and $\mathrm{SF}_{\mathrm{total}}^{\mathrm{syst-}}$, corresponding to the upper and lower limits of the systematic uncertainties, are expressed as:

$$
\mathrm{SF}_{\mathrm{total}}^{\mathrm{syst+}} = (\mathrm{SF}_{\mathrm{trk}}^{\mathrm{syst+},\mu^+} \times \mathrm{SF}_{\mathrm{trk}}^{\mathrm{syst+},\mu^-}) \cdot (\mathrm{SF}_{\mathrm{MuID}}^{\mathrm{syst+},\mu^+} \times \mathrm{SF}_{\mathrm{MuID}}^{\mathrm{syst+},\mu^-}) \cdot (\mathrm{SF}_{\mathrm{trg}}^{\mathrm{syst+},\mu^+} \times \mathrm{SF}_{\mathrm{trg}}^{\mathrm{syst+},\mu^-}),
$$
$$
\mathrm{SF}_{\mathrm{total}}^{\mathrm{syst-}} = (\mathrm{SF}_{\mathrm{trk}}^{\mathrm{syst-},\mu^+} \times \mathrm{SF}_{\mathrm{trk}}^{\mathrm{syst-},\mu^-}) \cdot (\mathrm{SF}_{\mathrm{MuID}}^{\mathrm{syst-},\mu^+} \times \mathrm{SF}_{\mathrm{MuID}}^{\mathrm{syst-},\mu^-}) \cdot (\mathrm{SF}_{\mathrm{trg}}^{\mathrm{syst-},\mu^+} \times \mathrm{SF}_{\mathrm{trg}}^{\mathrm{syst-},\mu^-}),
$$
$$(9.5)$$

where $\mathrm{SF}_{\mathrm{trk}}$, $\mathrm{SF}_{\mathrm{MuID}}$, and $\mathrm{SF}_{\mathrm{trg}}$ represent the SFs for tracking, muon identification, and trigger, respectively.
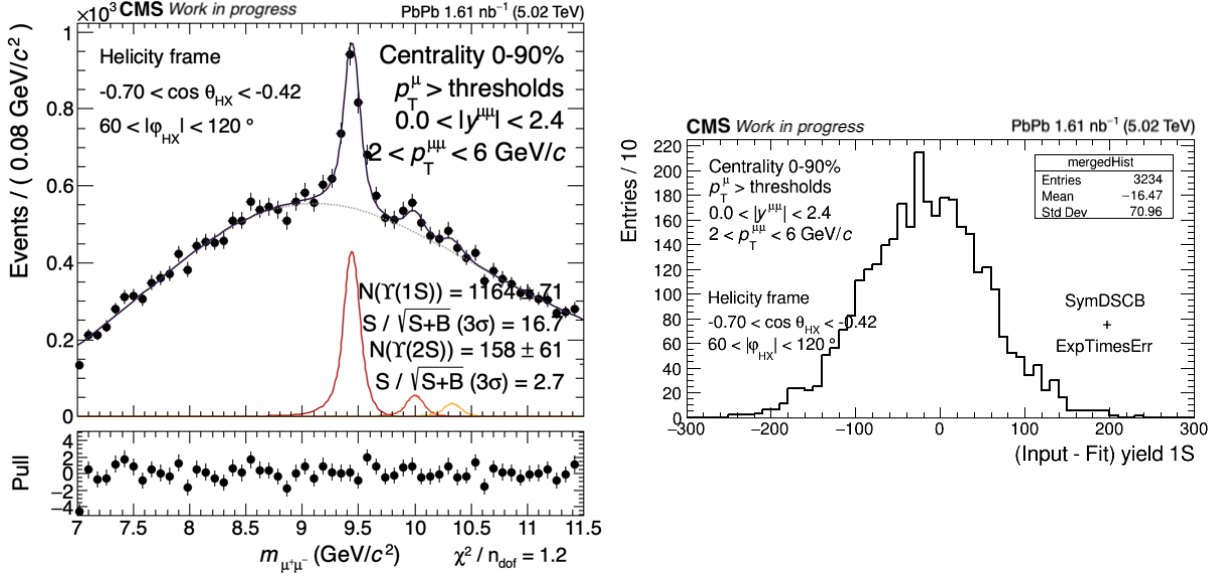
Figure 9.3: An example of the pseudo-experiment results when the background peak falls beneath the signal peak. The bin range corresponds to $2 < p_{\mathrm{T}}^{\mu\mu} < 6$ GeV/c, $-0.70 < \cos\theta < -0.42$, and $60 < |\varphi| < 120°$ in the HX frame. The plot on the left shows the signal extraction from the Υ candidates invariant mass distribution using the nominal fit model, with the pull distribution at the bottom. The plot on the right shows the pseudo-experiment results using the same PDF model as the nominal fit model.

By incorporating these recalculated SFs into the efficiency definition in Eq. (6.2), the modified efficiencies $\epsilon_{\mathrm{total}}^{\mathrm{syst}+,\mu\mu}$ and $\epsilon_{\mathrm{total}}^{\mathrm{syst}-,\mu\mu}$ are derived.

The polarization parameters were re-extracted by applying modified weights to the nominal signal extraction results in each $p_{\mathrm{T}}^{\mu\mu}$, $\cos\theta$, and φ bin in both the CS and HX frames. These weights were obtained by replacing the nominal efficiency in Eq. (7.1) with the modified efficiencies from Eq. 9.5. The resulting changes in each polarization parameter, $\Delta\lambda_\theta$, $\Delta\lambda_\varphi$, and $\Delta\lambda_{\theta\varphi}$, are presented in Table 9.1. The systematic uncertainties from the muon SFs are less than 0.01 in most $p_{\mathrm{T}}^{\mu\mu}$ bins, which is an insignificant contribution to the total systematic uncertainty. Given that these uncertainties were basically based on the stat uncertainty of the efficiencies, which is very small, we opted to include a larger variation that better reflects the systematic uncertainty in the efficiency scale factors, so we increased the

uncertainty by a factor of 5 so that it would be of order 1–2%.

9.5 Summary of Systematic Uncertainties

The polarization parameters were re-extracted using the newly obtained $\Upsilon(1S)$ yields to evaluate the final systematic uncertainty. Variations in the polarization parameters in both CS and HX frames, associated with the previously discussed uncertainty sources, are summarized in Table 9.1. These results were obtained via the pseudo-experiments done with the alternative signal PDF (first row) and the alternative background PDF (second row). Within each row, the three sub-rows pertain to the three $p_T^{\mu\mu}$ bins of this analysis. The uncertainties are reported by noting the change in the three polarization parameters, e.g. $\Delta\lambda_\theta \equiv \lambda_\theta^{\mathrm{nominal}} - \lambda_\theta^{\mathrm{alternative}}$. The eight uncertainties were combined in quadrature. An exception is the uncertainty due to the background peak underlying the signal peak as the estimate for the total systematic uncertainty, given in the last row of Table 9.1.

Uncertainty source	$p_{\mathrm{T}}^{\mu\mu}$ (GeV/c)	CS frame			HX frame		
		$\Delta\lambda_\theta$	$\Delta\lambda_\varphi$	$\Delta\lambda_{\theta\varphi}$	$\Delta\lambda_\theta$	$\Delta\lambda_\varphi$	$\Delta\lambda_{\theta\varphi}$
Alternative signal shape	2-6	-0.078	0.000	0.002	-0.036	0.005	-0.002
	6-12	0.027	-0.026	-0.002	-0.046	-0.003	-0.008
	12-20	-0.031	-0.006	0.000	-0.009	-0.004	-0.008
Alternative background shape	2-6	0.164	0.022	-0.002	0.160	0.001	-0.002
	6-12	0.010	-0.015	-0.025	0.132	-0.053	-0.031
	12-20	0.030	-0.025	0.002	0.040	-0.009	-0.001
Background peak under signal peak	2-6	-0.090	0.000	0.005	-0.021	0.000	0.000
	6-12	0.018	-0.026	0.002	-0.038	-0.009	-0.007
	12-20	-0.029	-0.010	0.008	-0.012	-0.007	-0.005
Muon scale factor systematic up	2-6	0.005	0.000	0.000	0.004	0.000	0.000
	6-12	-0.001	0.001	0.000	0.002	0.000	0.000
	12-20	0.000	0.001	0.000	0.001	0.000	0.000
Muon scale factor systematic down	2-6	-0.005	0.000	0.000	-0.004	0.000	0.000
	6-12	0.001	-0.001	0.000	-0.002	0.000	0.000
	12-20	0.000	-0.001	0.000	-0.001	0.000	0.000
Acceptance statistical up	2-6	0.008	0.002	0.000	0.005	0.002	0.000
	6-12	0.002	0.007	0.001	0.003	0.004	0.000
	12-20	-0.003	0.012	0.000	0.007	0.005	0.000
Acceptance statistical down	2-6	-0.008	-0.002	0.000	-0.005	-0.002	0.000
	6-12	-0.001	-0.007	-0.001	-0.002	-0.004	0.000
	12-20	0.003	-0.012	0.000	-0.007	-0.005	0.000
Efficiency statistical up	2-6	0.000	0.000	0.000	0.000	0.000	0.000
	6-12	0.000	0.000	0.000	0.000	0.000	0.000
	12-20	0.000	0.000	0.000	0.001	0.000	0.000
Efficiency statistical down	2-6	0.000	0.000	0.000	0.000	0.000	0.000
	6-12	0.000	0.000	0.000	0.000	0.000	0.000
	12-20	0.000	0.000	0.000	-0.001	0.000	0.000
Total systematic uncertainty	2-6	0.183	0.023	0.003	0.165	0.006	0.003
	6-12	0.029	0.031	0.025	0.140	0.053	0.032
	12-20	0.043	0.031	0.002	0.043	0.012	0.008

Table 9.1: Summary of the systematic uncertainties.

Chapter 10

Results and Discussion

Figure 10.1 shows the polarization parameters λ_θ (top), λ_φ (middle), and $\lambda_{\theta\varphi}$ (bottom), extracted in three $p_{\mathrm{T}}^{\mu\mu}$ intervals for both the CS (left) and HX (right) reference frames. In the CS frame, the $\Upsilon(1S)$ polarization parameters are close to zero except in the region $2 < p_{\mathrm{T}}^{\mu\mu} < 6$ and $6 < p_{\mathrm{T}}^{\mu\mu} < 12$ GeV/c, where λ_θ reaches values up to about 0.56. In the HX frame, the polarization parameters are consistent with zero within uncertainties. λ_θ also shows deviations from zero in the same $p_{\mathrm{T}}^{\mu\mu}$ intervals. The deviations in the HX frame are about 0.2, which is smaller than those observed in the CS frame. Table 10.1 lists the numerical values of the polarization parameters, with statistical and systematic uncertainties quoted separately.

When compared to the $p + p$ baseline from Ref. [44], the Pb + Pb results are consistent within uncertainties, indicating that no significant modification of $\Upsilon(1S)$ polarization was observed in heavy ion collisions for $p_{\mathrm{T}}^{\mu\mu} > 10$ GeV/c.

The results are also compared with the Improved Color Evaporation Model (ICEM) predictions provided by V. Cheung and R. Vogt (personal communication). These predictions were calculated specifically for the kinematic conditions of this analysis ($\sqrt{s_{NN}} = 5.02$ TeV, $|y^{\mu\mu}| < 2.4$, and $2 < p_{\mathrm{T}}^{\mu\mu} < 20$ GeV/c) in the CS and HX frames, using the methodology
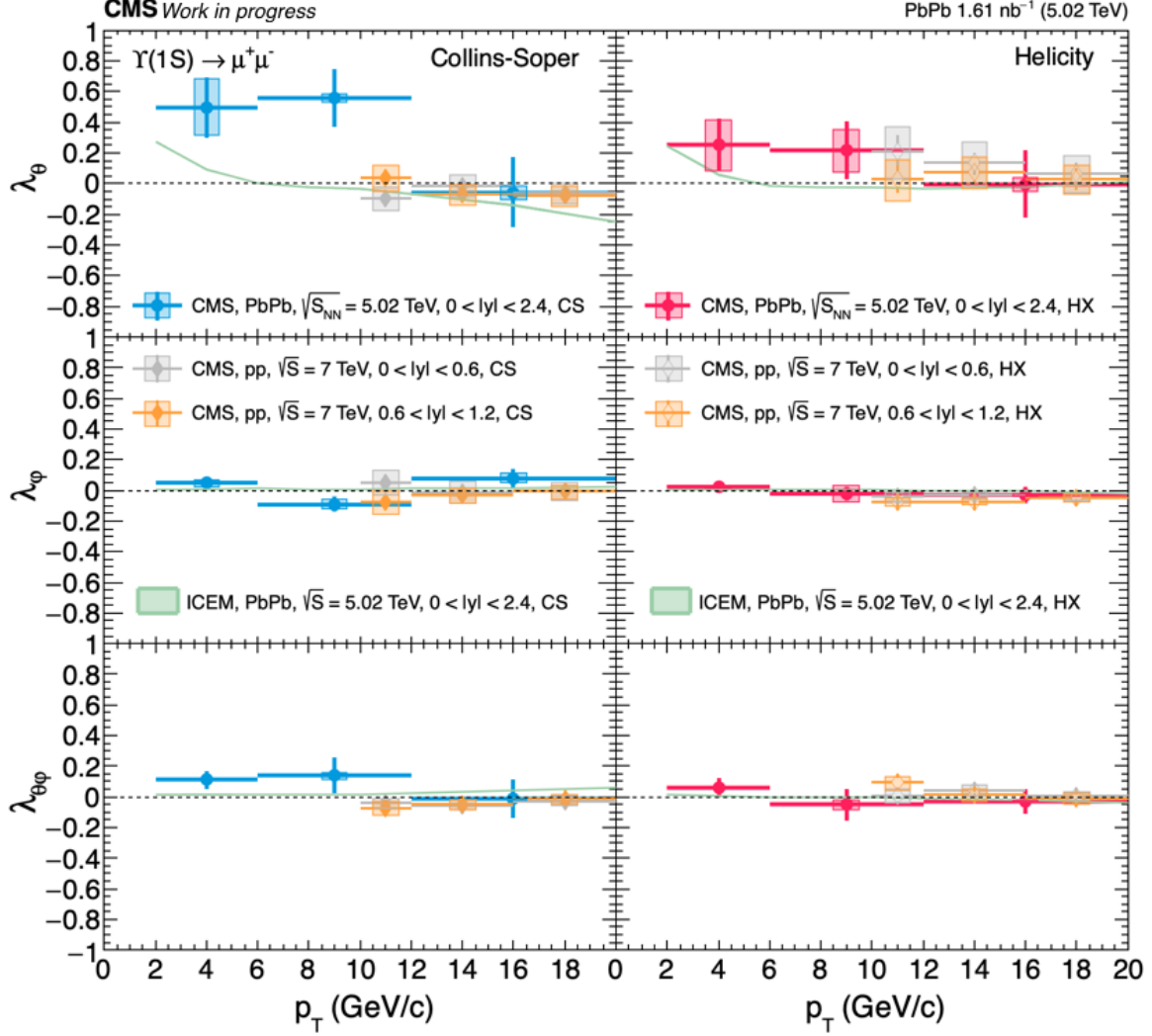
Figure 10.1: Polarization parameters λ_θ (top), λ_φ (middle), and $\lambda_{\theta\varphi}$ (bottom) parameters for the $\Upsilon(1S)$ as a function of $p_T^{\mu\mu}$ in Pb + Pb collisions at $\sqrt{s_{NN}} = 5.02$ TeV (blue: CS frame, red: HX frame). Results are compared with CMS polarization measurements in $p + p$ collisions at $\sqrt{s_{NN}} = 7$ TeV (gray: $0 < |y^{\mu\mu}| < 0.6$, Orange: $0.6 < |y^{\mu\mu}| < 1.2$). Preliminary ICEM predictions from V. Cheung and R. Vogt are shown (green band). Error bars represent statistical uncertainties. Shaded boxes represent systematic uncertainties.

described in Ref. [121]. The ICEM results presented here are preliminary, and the theoretical uncertainty reflects only variations of the bottom-quark mass. Within uncertainties, the $\mathrm{Pb} + \mathrm{Pb}$ measurements are consistent with both the $p + p$ data and the ICEM predictions, suggesting no measurable QGP-induced modification of $\Upsilon(1S)$ polarization at mid-rapidity.

	$p_{\mathrm{T}}^{\mu\mu}$ (GeV/c)	Collins-Soper	Helicity
λ_θ	$2 < p_{\mathrm{T}} < 6$	$0.497 \pm 0.196 \pm 0.183$	$0.252 \pm 0.170 \pm 0.165$
	$6 < p_{\mathrm{T}} < 12$	$0.557 \pm 0.188 \pm 0.029$	$0.215 \pm 0.188 \pm 0.140$
	$12 < p_{\mathrm{T}} < 20$	$-0.057 \pm 0.229 \pm 0.043$	$-0.004 \pm 0.218 \pm 0.043$
λ_φ	$2 < p_{\mathrm{T}} < 6$	$0.048 \pm 0.026 \pm 0.023$	$0.023 \pm 0.029 \pm 0.006$
	$6 < p_{\mathrm{T}} < 12$	$-0.091 \pm 0.048 \pm 0.031$	$-0.023 \pm 0.046 \pm 0.053$
	$12 < p_{\mathrm{T}} < 20$	$0.081 \pm 0.063 \pm 0.031$	$-0.029 \pm 0.051 \pm 0.012$
$\lambda_{\theta\varphi}$	$2 < p_{\mathrm{T}} < 6$	$0.109 \pm 0.061 \pm 0.003$	$0.057 \pm 0.065 \pm 0.003$
	$6 < p_{\mathrm{T}} < 12$	$0.136 \pm 0.117 \pm 0.025$	$-0.051 \pm 0.105 \pm 0.032$
	$12 < p_{\mathrm{T}} < 20$	$-0.015 \pm 0.125 \pm 0.002$	$-0.032 \pm 0.079 \pm 0.008$

Table 10.1: Polarization parameters measured for each $p_{\mathrm{T}}^{\mu\mu}$ region for the CS and HX frames. In each column, the first uncertainty is statistical uncertainty (from the fits); the second is systematic uncertainty.

After obtaining the polarization parameters (λ_θ, λ_φ, and $\lambda_{\theta\varphi}$) in each of the reference frames of the analysis, the frame-invariant polarization parameter, $\tilde{\lambda}$, was calculated based on Eq. (1.4) for the CS and HX frames. The results are displayed in Fig 10.2. The results from the two methods are consistent with each other in the region $p_{\mathrm{T}}^{\mu\mu} > 6\,\mathrm{GeV}/c$. For the $2 < p_{\mathrm{T}}^{\mu\mu} < 6\,\mathrm{GeV}/c$ interval, the larger systematic uncertainties are the main source of the difference observed in the $\tilde{\lambda}$ parameter. This discrepancy arises chiefly from the signal-to-background ambiguity when the background peak is under the signal peak, as discussed in Sec. 9.3. The non-perturbative effects predicted in Ref. [9] are expected to be most significant at low $p_{\mathrm{T}}^{\mu\mu}$. While it is possible that the polarization in this region could be similar to those predictions, the systematic uncertainties in the low-$p_{\mathrm{T}}^{\mu\mu}$ region currently preclude a firm conclusion.
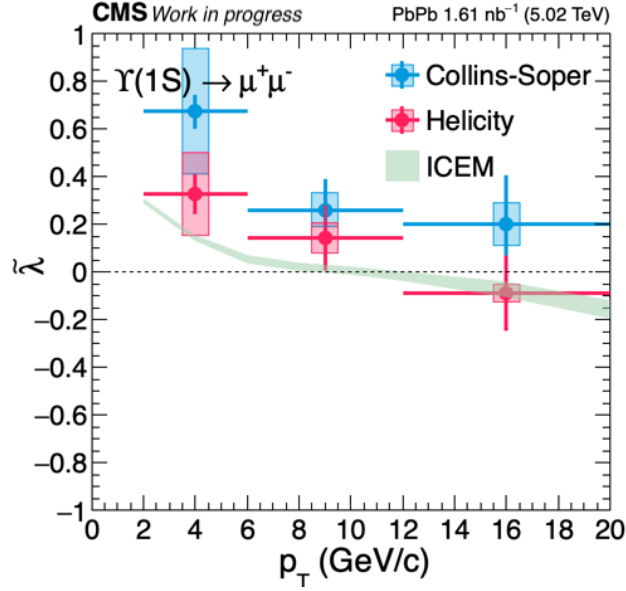
Figure 10.2: Frame-invariant polarization parameters $\tilde{\lambda}$ for $\Upsilon(1S)$ as a function of $p_{\mathrm{T}}^{\mu\mu}$ in Pb + Pb collisions at $\sqrt{s_{NN}} = 5.02$ TeV(blue: CS frame, red: HX frame). Results are compared with preliminary ICEM predictions from V. Cheung and R. Vogt (green band). Error bars represent statistical uncertainties. Shaded boxes represent systematic uncertainties.

Overall, the polarization measurements in Pb + Pb collisions are consistent with those obtained in $p + p$ collisions and with ICEM predictions, indicating that the QGP does not significantly modify $\Upsilon(1S)$ polarization within the present experimental limitations. These results provide an important constraint on theoretical models predicting medium-induced quarkonium polarization.

Chapter 11

Conclusion

We studied the polarization of the Υ(1S) meson in Pb+Pb collisions at $\sqrt{s_{NN}} = 5.02$ TeV, using the full rapidity coverage of the CMS detector ($|y^{\mu\mu}| < 2.4$). Polarization parameters λ_θ, λ_φ, and $\lambda_{\theta\varphi}$ were extracted in both the CS and HX reference frames. The frame-independent parameter $\tilde{\lambda}$ was evaluated in both frames.

The measurements show that the Υ(1S) polarization is consistent with zero in most of the measured $p_T^{\mu\mu}$ regions. A positive deviation from zero in λ_θ is observed in the $2 < p_T^{\mu\mu} < 12$ GeV/c region, but within the uncertainties the results remain compatible with no significant polarization. At higher $p_T^{\mu\mu}$ (> 10 GeV/c), the polarization parameters are consistent with zero, in agreement with CMS $p + p$ measurements at $\sqrt{s_{NN}} = 7$ TeV in a comparable rapidity ($|y^{\mu\mu}| < 1.2$). This indicates that the Υ(1S) mesons surviving the hot and dense medium retain the same polarization as those produced in $p + p$ collisions, providing no evidence of QGP-induced polarization effects.

The results have also been compared with theoretical predictions from the ICEM provided to us by V. Cheung and R. Vogt. Preliminary ICEM calculations, obtained in the same kinematic conditions, are consistent with the data within uncertainties.

This work represents the first mid-rapidity study of Υ(1S) polarization in heavy ion

collisions. The null result provides an important constraint on models that predict medium-induced polarization of quarkonia. Together with previous measurements of quarkonium suppression and flow, these results add to the comprehensive picture of quarkonium behavior in the QGP.

Future measurements with larger datasets (Run 3) and improved precision will allow for finer $p_{\mathrm{T}}^{\mu\mu}$ binning and separation of centrality classes, potentially revealing more subtle medium effects. Complementary studies of excited bottomonium states and comparisons across collision energies will also provide further insight. Improved model calculations by theorists, including full uncertainty estimates (such as feed-down effects and scale variation) will contribute to clear understanding of polarization phenomena.

Appendix A

MC Fits for Parameter Extractions

Figures A.1 to A.6 show MC dimuon invariant mass fits, along with the obtained fit parameters and pull distributions, for both the CS frame and the HX frame corresponding to different p_T ranges. Each figure contains plots in a grid where rows correspond to different $\cos\theta$ ranges, and columns correspond to different $|\varphi|$ ranges. The rows are as follows (top to bottom): $0.42 < \cos\theta < 0.70$, $0.14 < \cos\theta < 0.42$, $-0.14 < \cos\theta < 0.14$, $-0.42 < \cos\theta < -0.14$, $-0.70 < \cos\theta < -0.42$. The columns are as follows (left to right): $0 < |\varphi| < 60°$, $60 < |\varphi| < 120°$, $120 < |\varphi| < 180°$.

Figure A.1: MC dimuon invariant mass fits in the CS frame for $2 < p_T^{\mu\mu} < 6\,\text{GeV}/c$.

Figure A.2: MC dimuon invariant mass fits in the CS frame for $6 < p_T^{\mu\mu} < 12\,\mathrm{GeV}/c$.
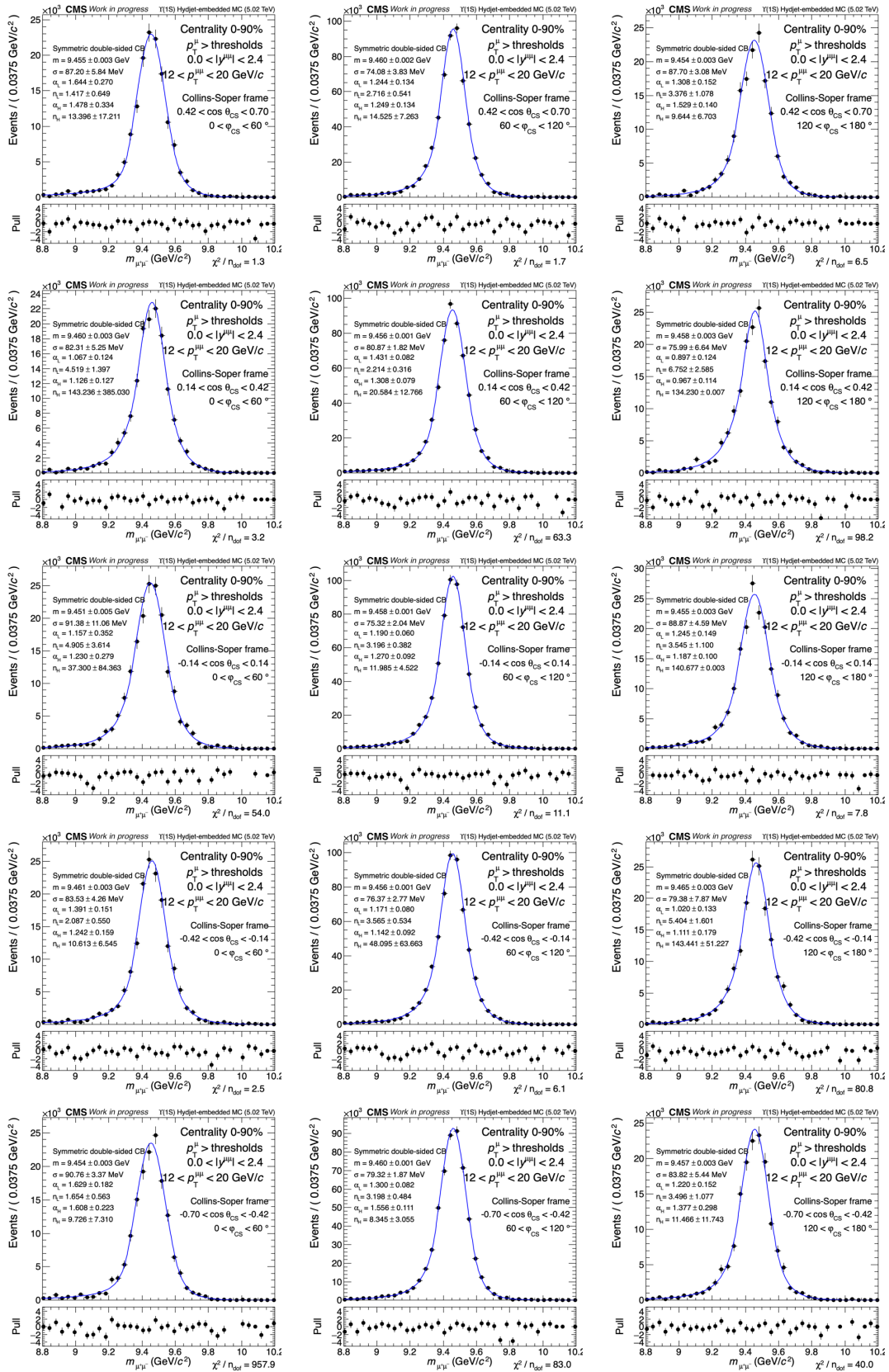
Figure A.3: MC dimuon invariant mass fits in the CS frame for $12 < p_T^{\mu\mu} < 20\,\mathrm{GeV}/c$.
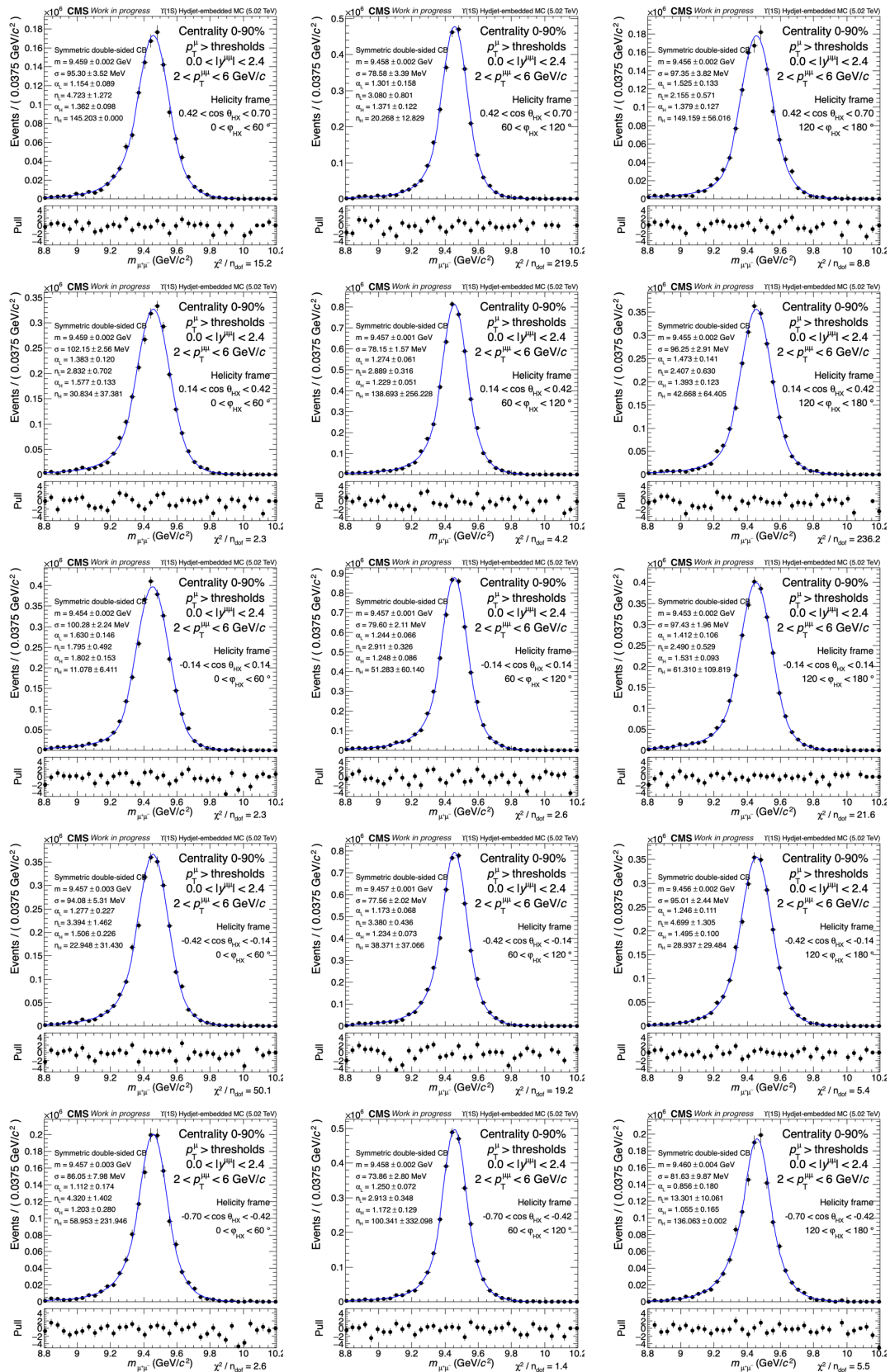
Figure A.4: MC dimuon invariant mass fits in the HX frame for $2 < p_T^{\mu\mu} < 6 \, \mathrm{GeV}/c$.
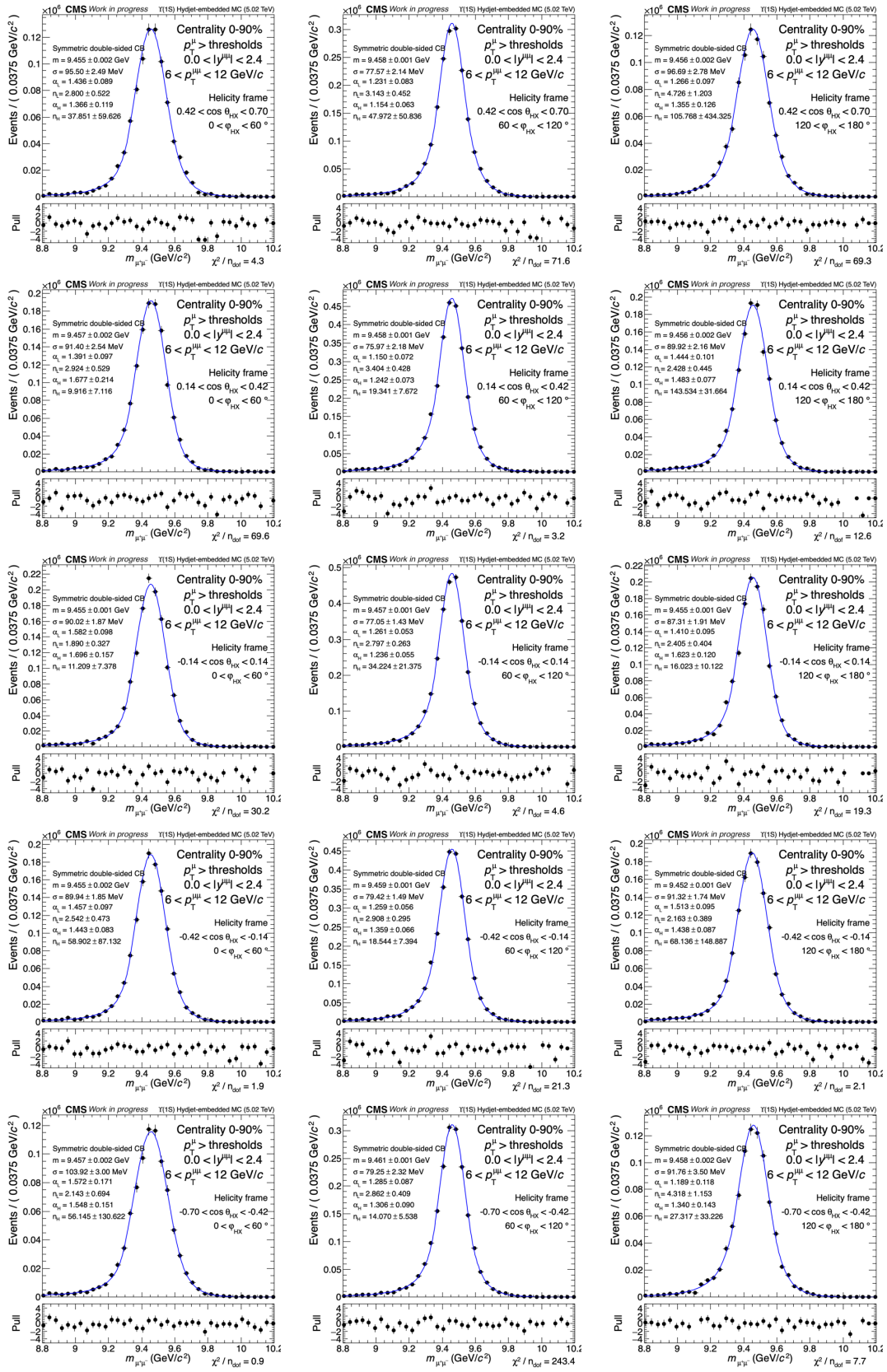
Figure A.5: MC dimuon invariant mass fits in the HX frame for $6 < p_T^{\mu\mu} < 12\,\mathrm{GeV}/c$.
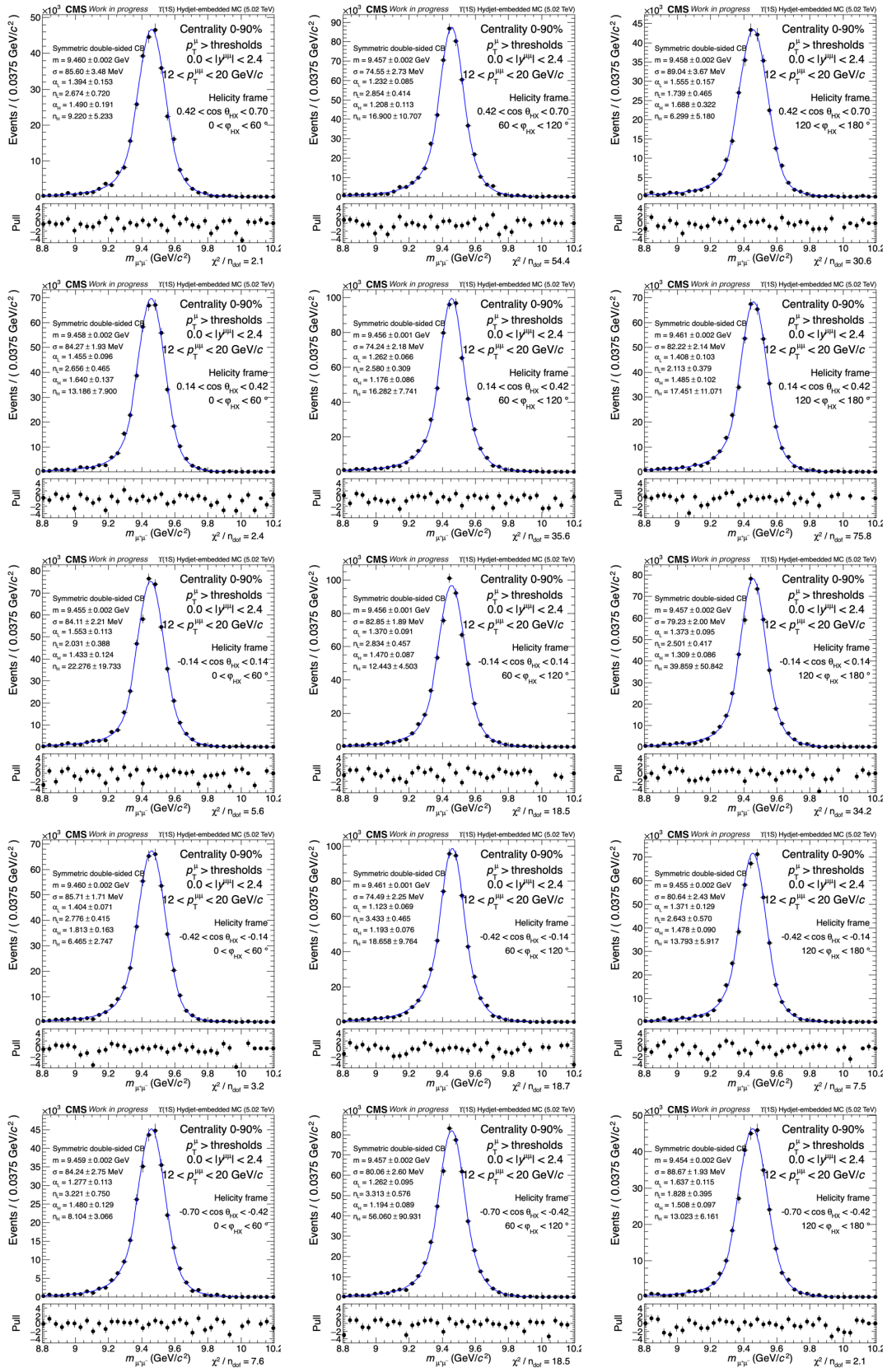
Figure A.6: MC dimuon invariant mass fits in the HX frame for $12 < p_T^{\mu\mu} < 20\,\text{GeV}/c$.

Appendix B

Data Fits for Signal Extraction with the Nominal Model

The figures from B.1 to B.6 present data dimuon-invariant mass fits, including the extracted $\Upsilon(1S)$ yield and pull distributions, for both the CS and HX frames across different $p_{\mathrm{T}}^{\mu\mu}$ ranges. Each figure consists of a grid of plots, consistent with the MC fits described in the Appendix A. The rows correspond to the following $\cos\theta$ ranges (top to bottom): $0.42 < \cos\theta < 0.70$, $0.14 < \cos\theta < 0.42$, $-0.14 < \cos\theta < 0.14$, $-0.42 < \cos\theta < -0.14$, and $-0.70 < \cos\theta < -0.42$. The columns correspond to the following $|\varphi|$ ranges (left to right): $0 < |\varphi| < 60\,°$, $60 < |\varphi| < 120\,°$, and $120 < |\varphi| < 180\,°$.
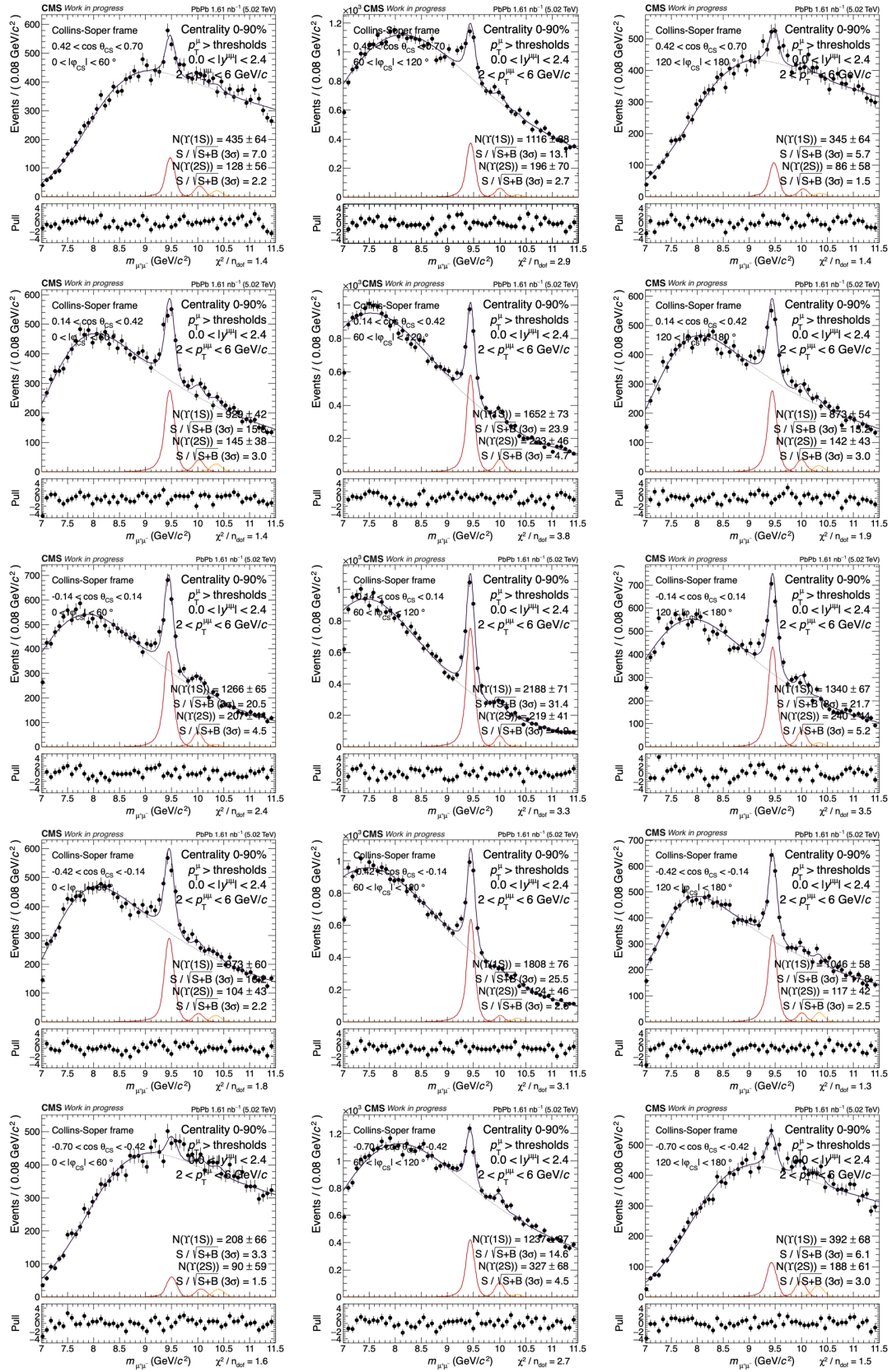
Figure B.1: The dimuon invariant mass fits with signal extraction results and the pulls in the CS frame for $2 < p_T^{\mu\mu} < 6\,\mathrm{GeV}/c$.
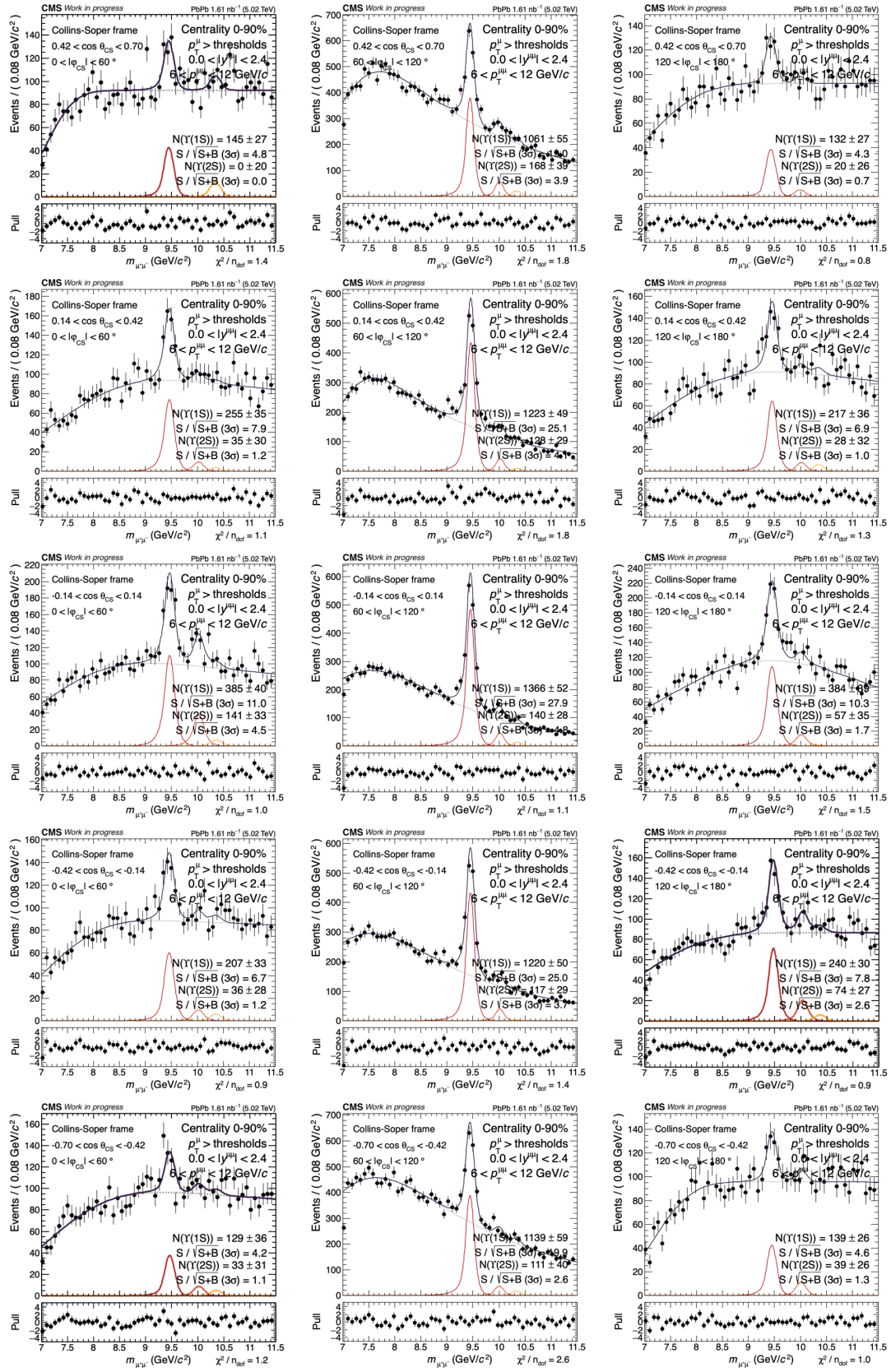
Figure B.2: The dimuon invariant mass fits with signal extraction results and the pulls in the CS frame for $6 < p_{\mathrm{T}}^{\mu\mu} < 12\,\mathrm{GeV}/c$.

124
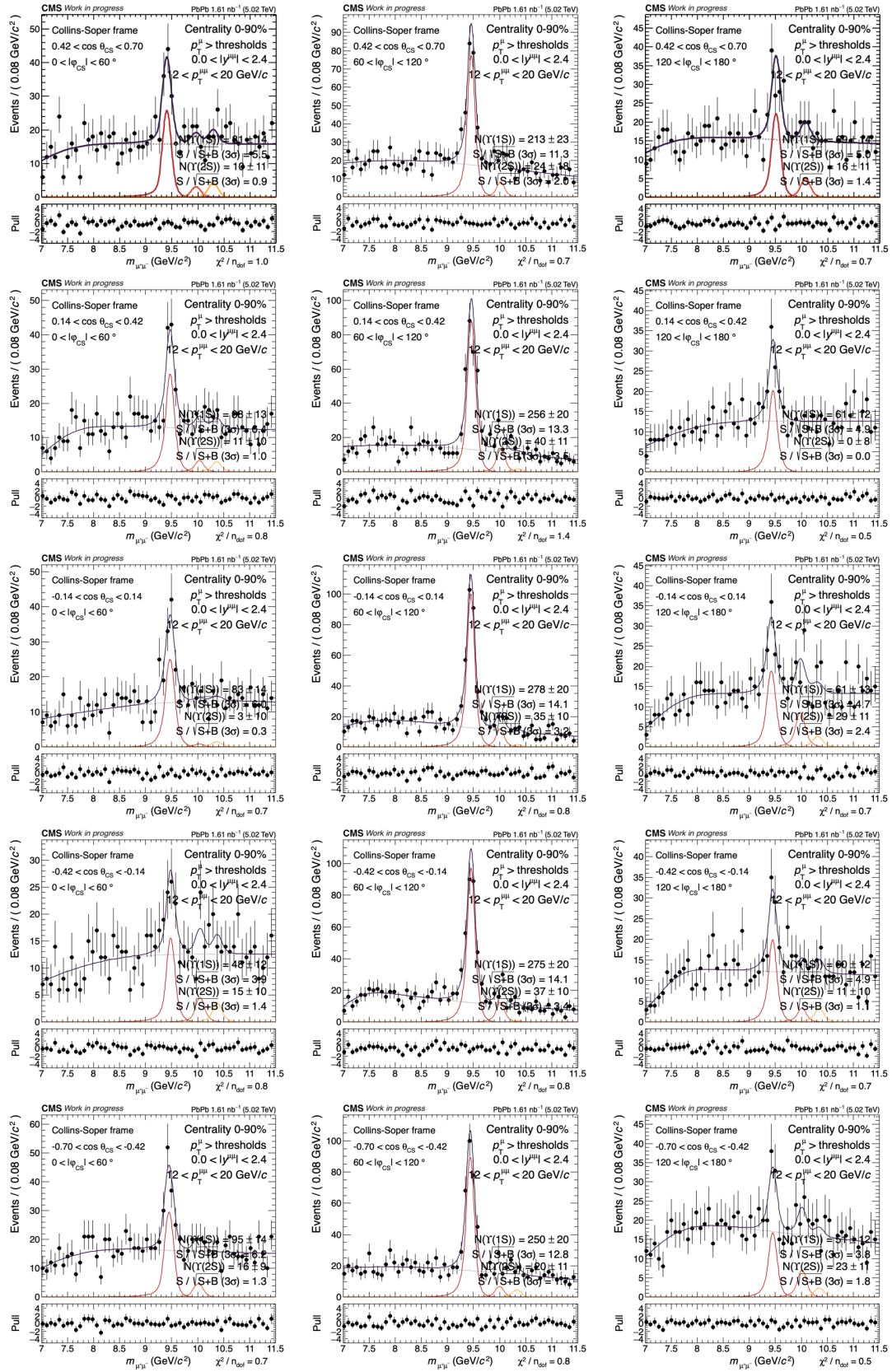
Figure B.3: The dimuon invariant mass fits with signal extraction results and the pulls in the CS frame for $12 < p_{\mathrm{T}}^{\mu\mu} < 20\,\mathrm{GeV}/c$.
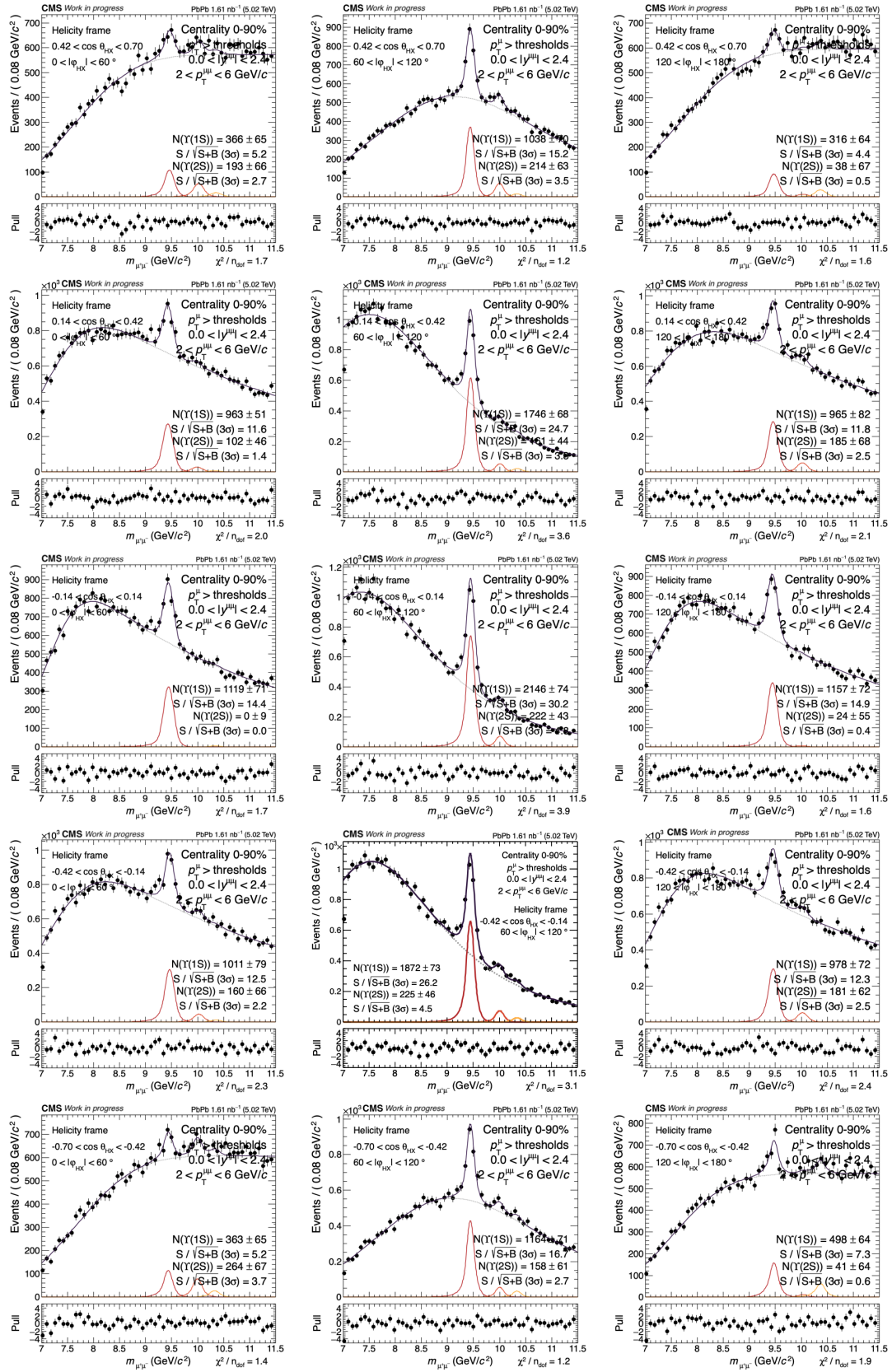
Figure B.4: The dimuon invariant mass fits with signal extraction results and the pulls in the HX frame for $2 < p_{\mathrm{T}}^{\mu\mu} < 6\,\mathrm{GeV}/c$.
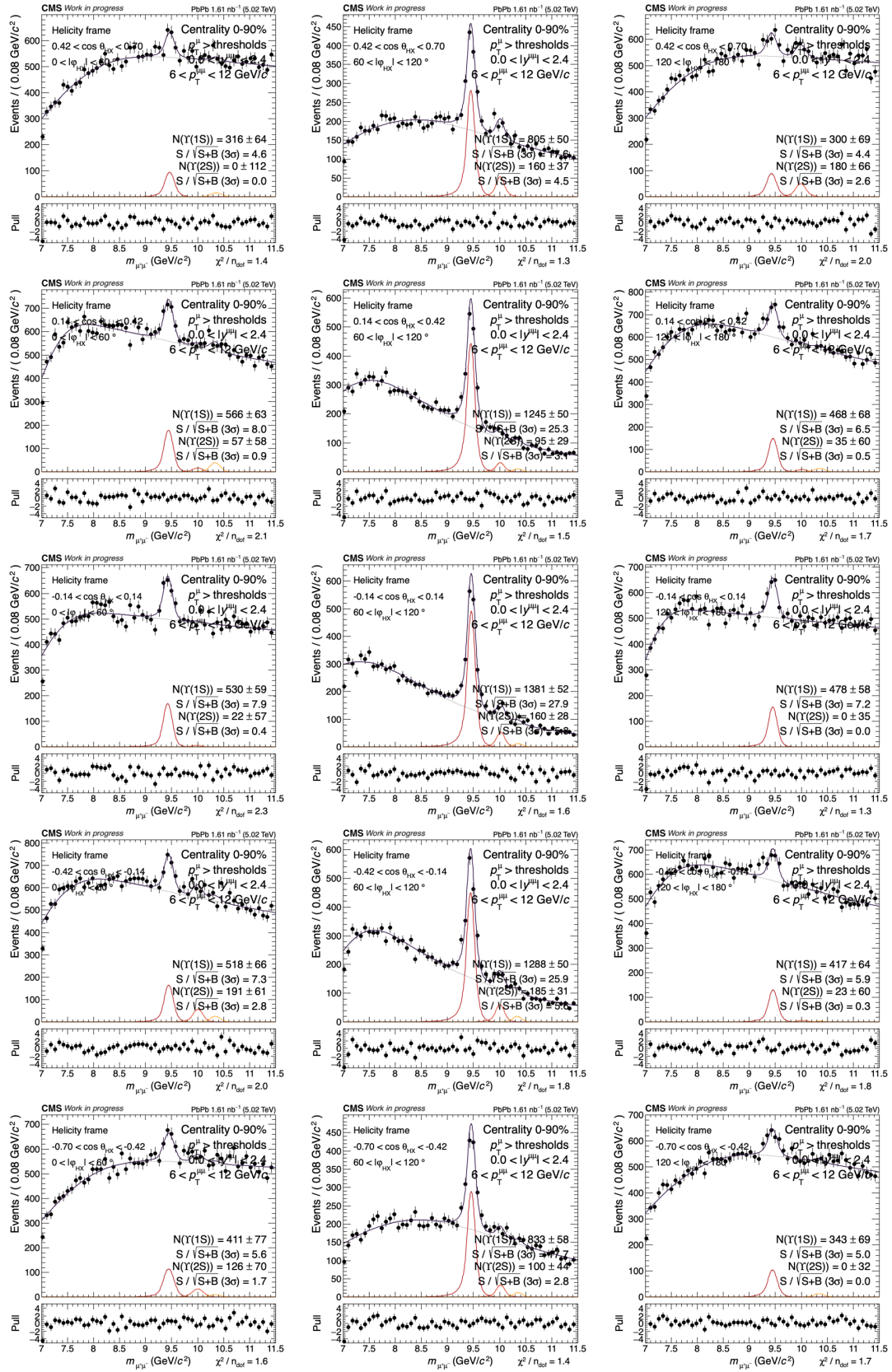
Figure B.5: The dimuon invariant mass fits with signal extraction results and the pulls in the HX frame for $6 < p_T^{\mu\mu} < 12\,\mathrm{GeV}/c$.
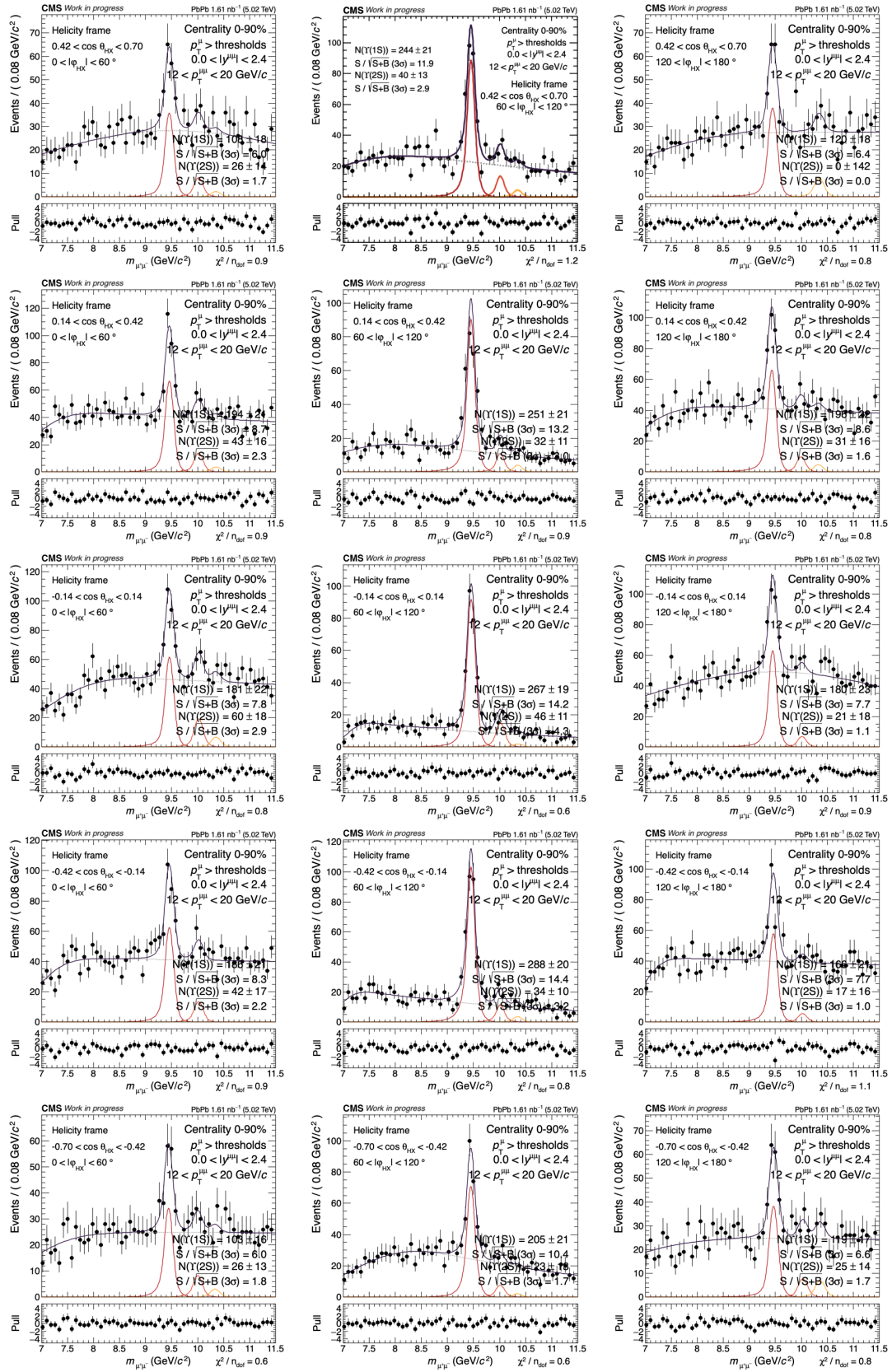
Figure B.6: The dimuon invariant mass fits with signal extraction results and the pulls in the HX frame for $12 < p_T^{\mu\mu} < 20\,\mathrm{GeV}/c$.

Appendix C

TnP Efficiency and SF

In this analysis, three types of SFs were considered in the efficiency estimation: muon identification, tracking, and trigger. These were centrally provided by the HIN muon POG, with details in the analysis note [114]. However, the analysis note has not been updated since 2018, whereas the underlying efficiency corrections were subsequently revised. The implementation actually used in this analysis is distributed as a header file in the official Github repository [115]. This file contains the final scale factor values as a function of muon kinematics, but does not include the underlying efficiencies in data and MC or their statistical uncertainties. The SF curves shown in Fig. C.1 through Fig. C.8 were reconstructed directly from the header file, and represent the most up-to-date values available, though without the corresponding error decomposition. Figures C.9–C.12 show the bin-averaged SFs in each $(p_T^{\mu\mu}, \cos\theta, \varphi)$ bin, representing the effective SF values applied in this analysis.
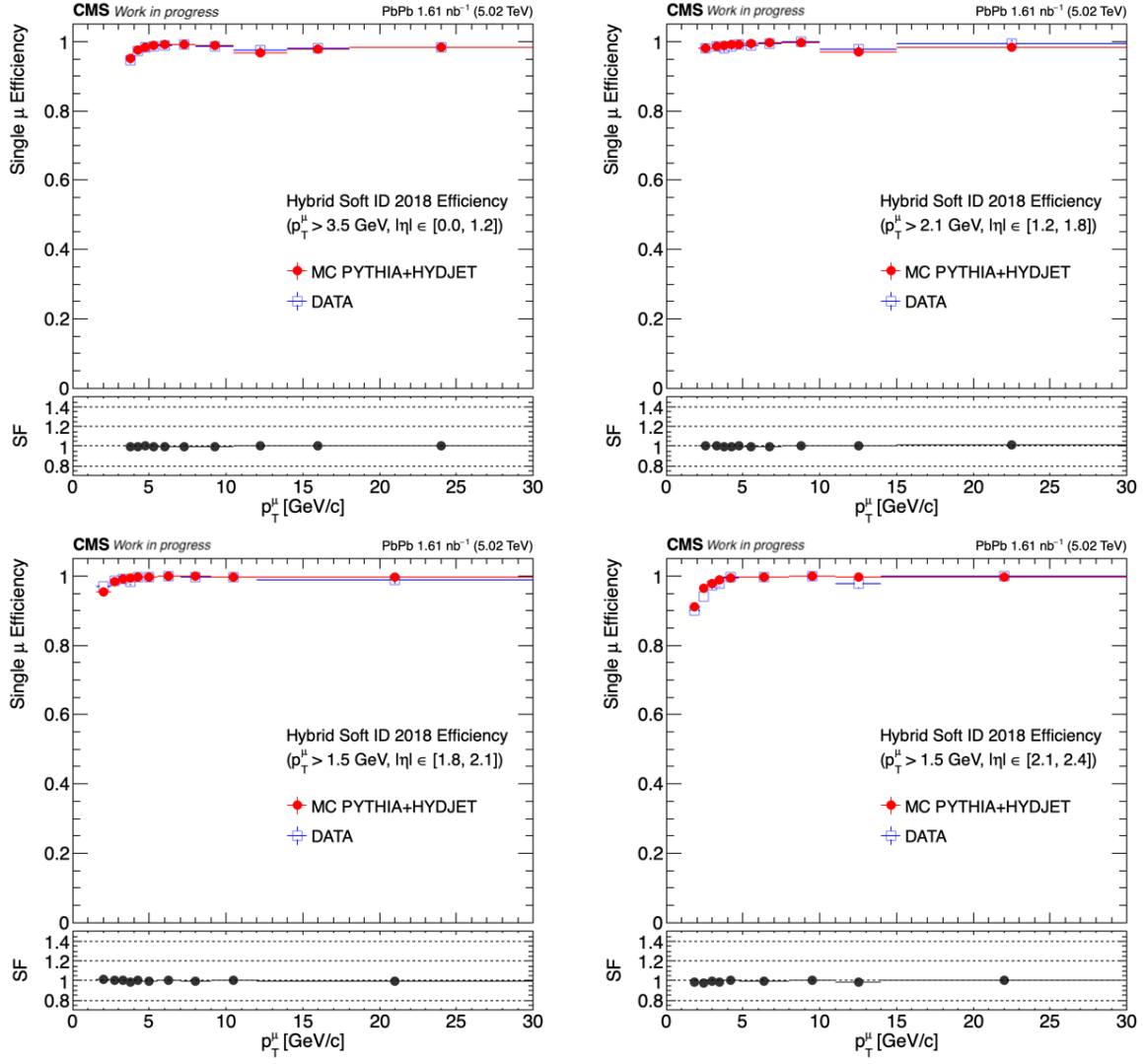
Figure C.1: Tag and probe SF muon identification.
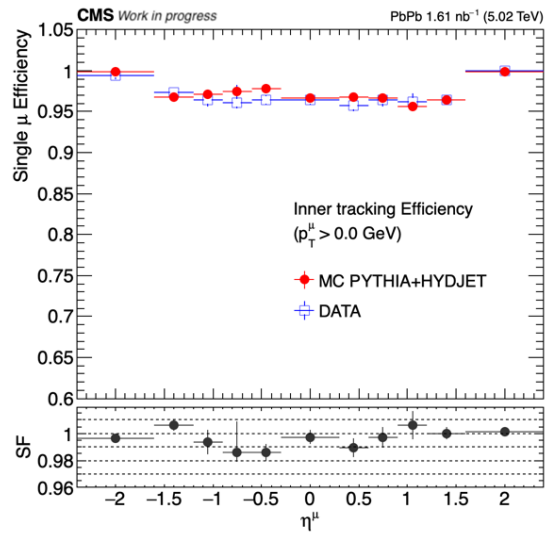
Figure C.2: Tag and probe SF tracking.
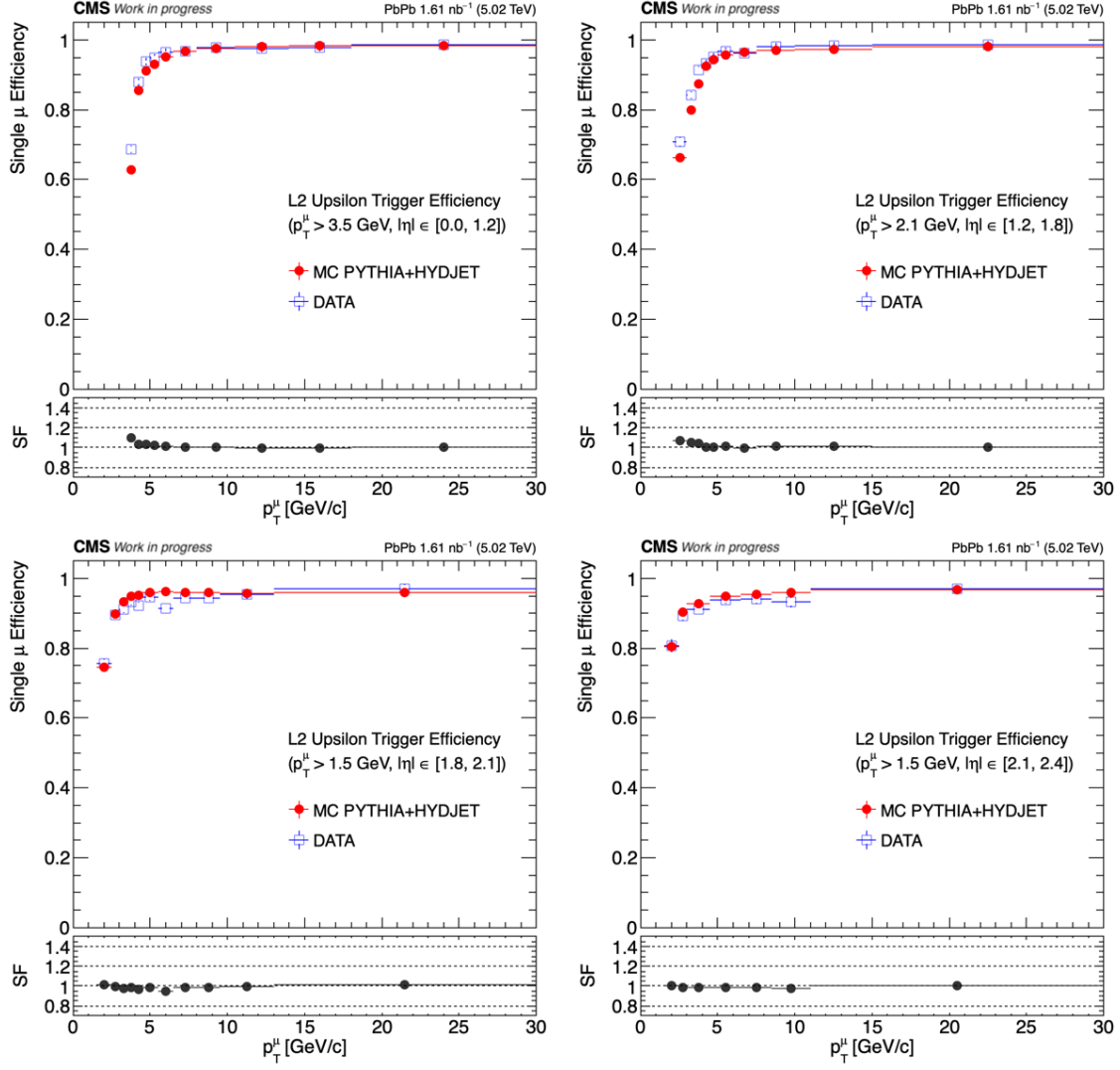
Figure C.3: Tag and probe SF trigger Upsilon L2.
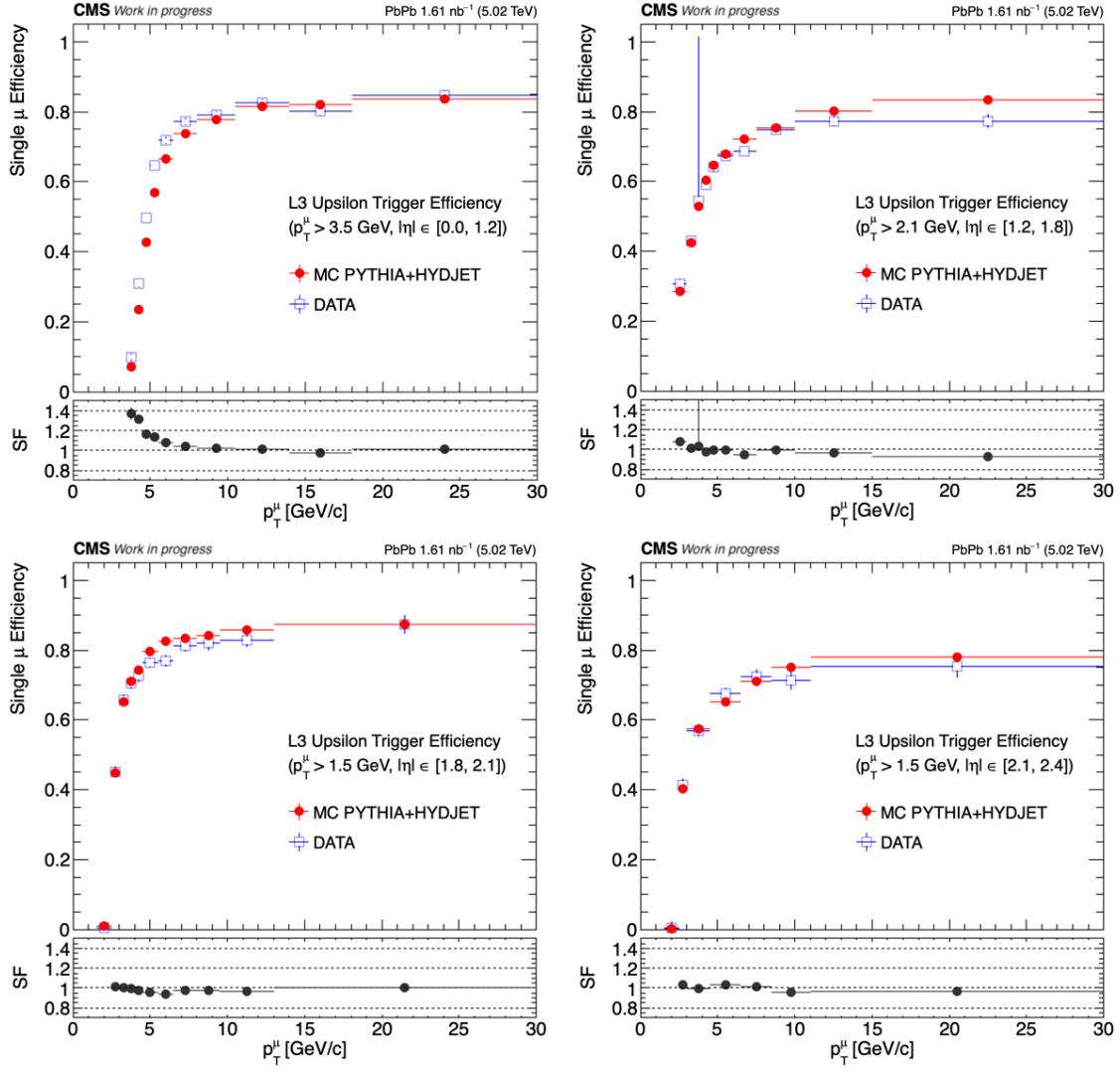
Figure C.4: Tag and probe SF trigger Upsilon L3.

133
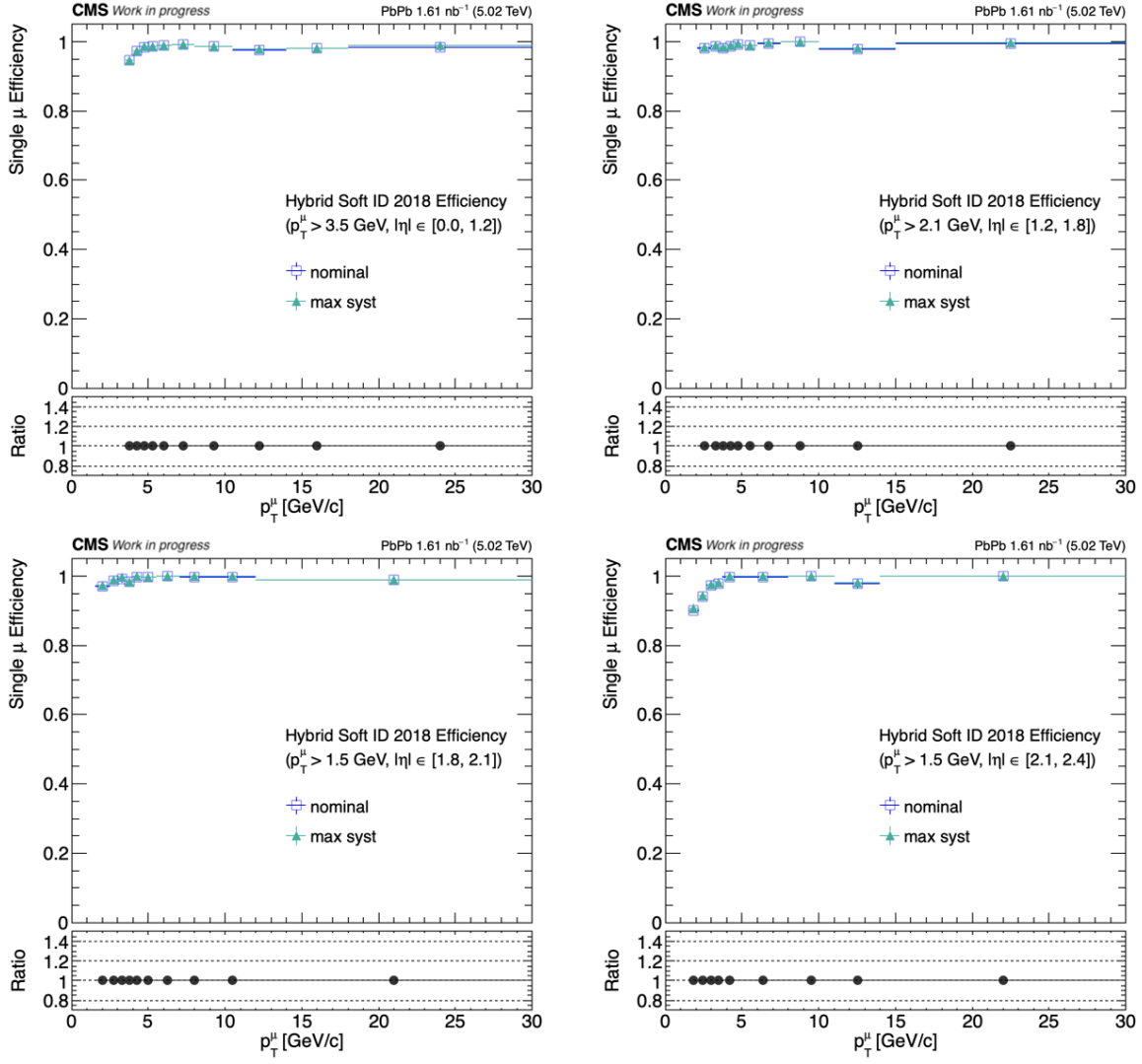
Figure C.5: Tag and probe SF muon identification systematic variation.
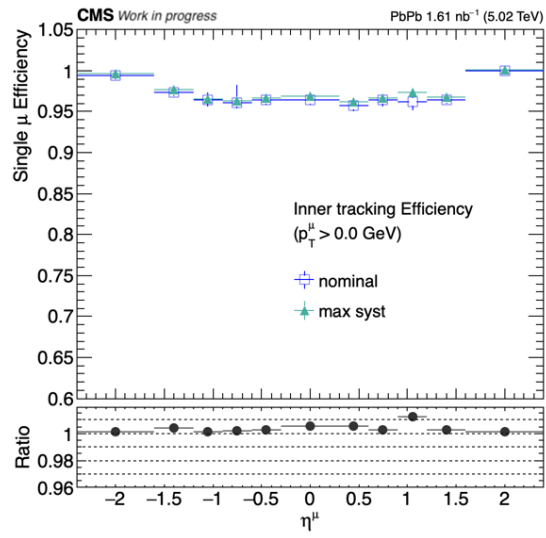
Figure C.6: Tag and probe SF tracking systematic variation.
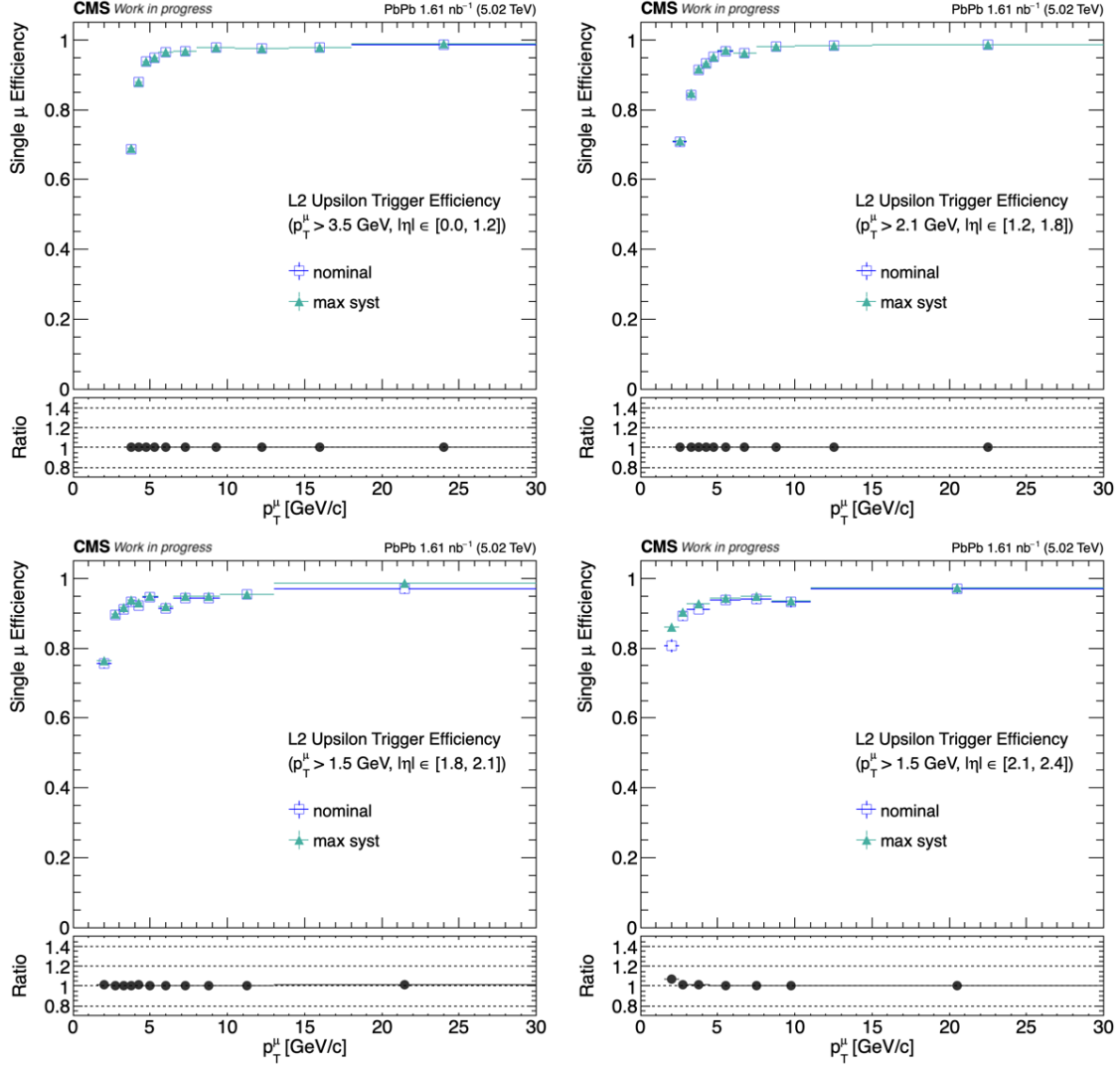
Figure C.7: Tag and probe SF trigger Upsilon L2 systematic variation.
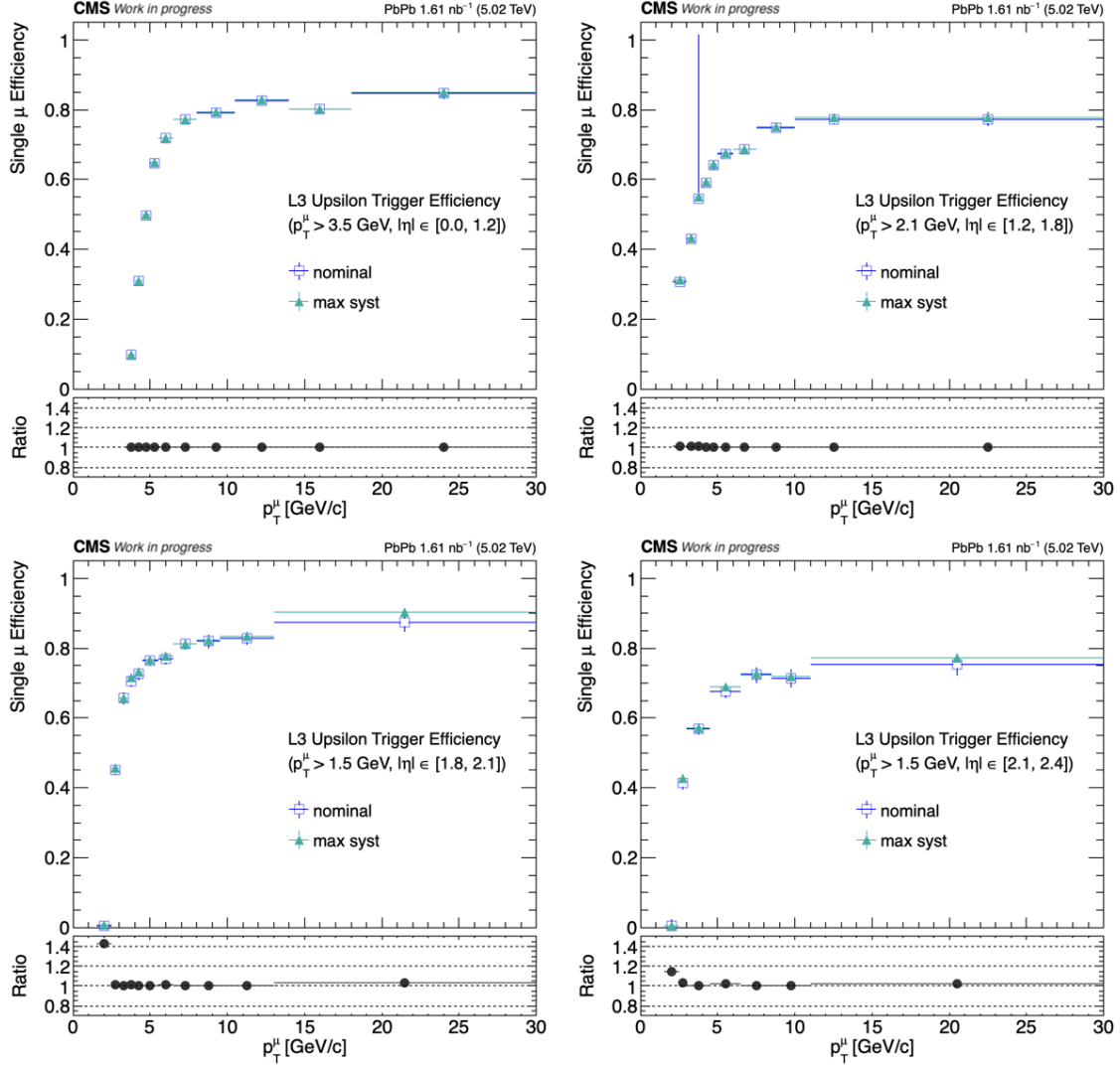
Figure C.8: Tag and probe SF trigger Upsilon L3 systematic variation.
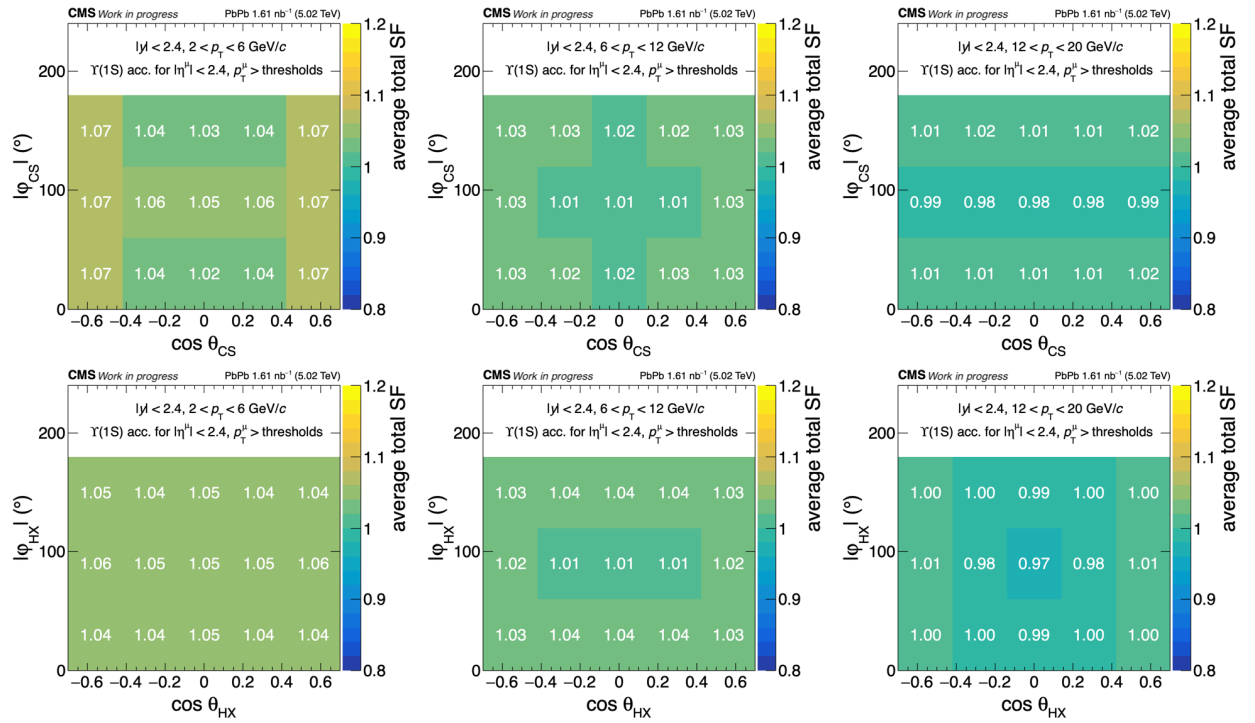
Figure C.9: Average total SF within the analysis bins in the CS (top row) and HX (bottom) frames.
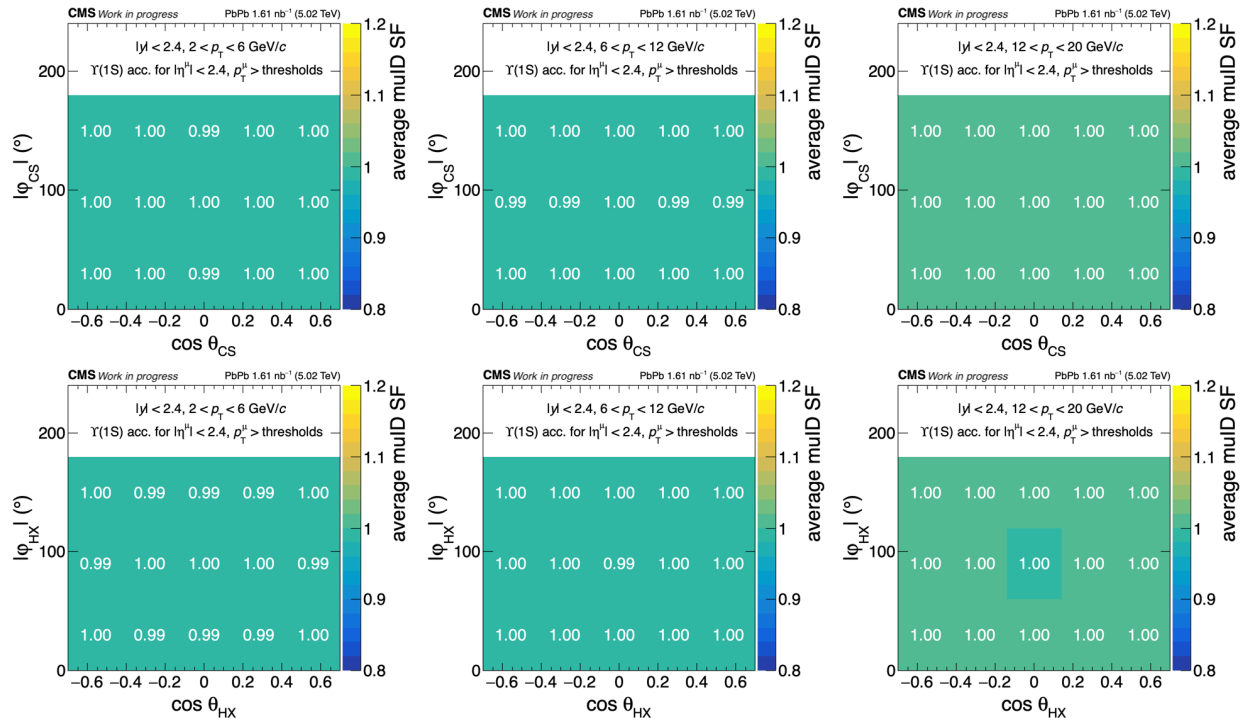
Figure C.10: Average muon identification SF within the analysis bins in the CS (top row) and HX (bottom) frames.
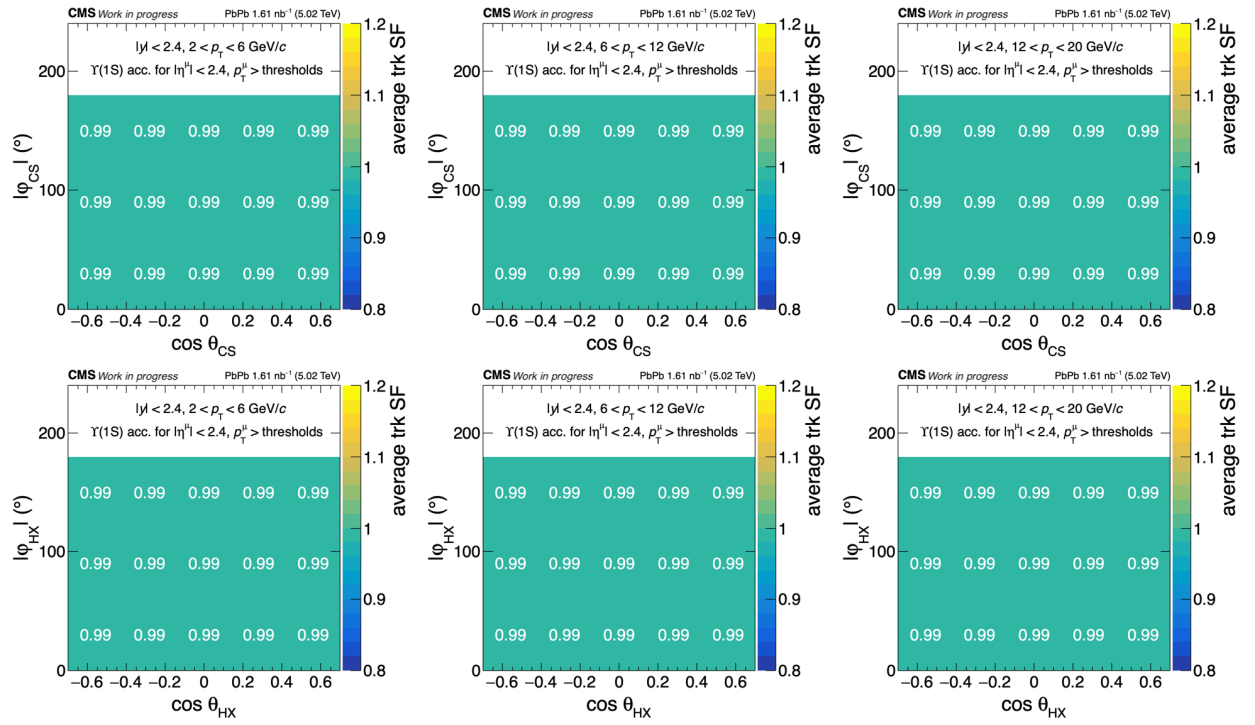
Figure C.11: Average tracking SF within the analysis bins in the CS (top row) and HX (bottom) frames.
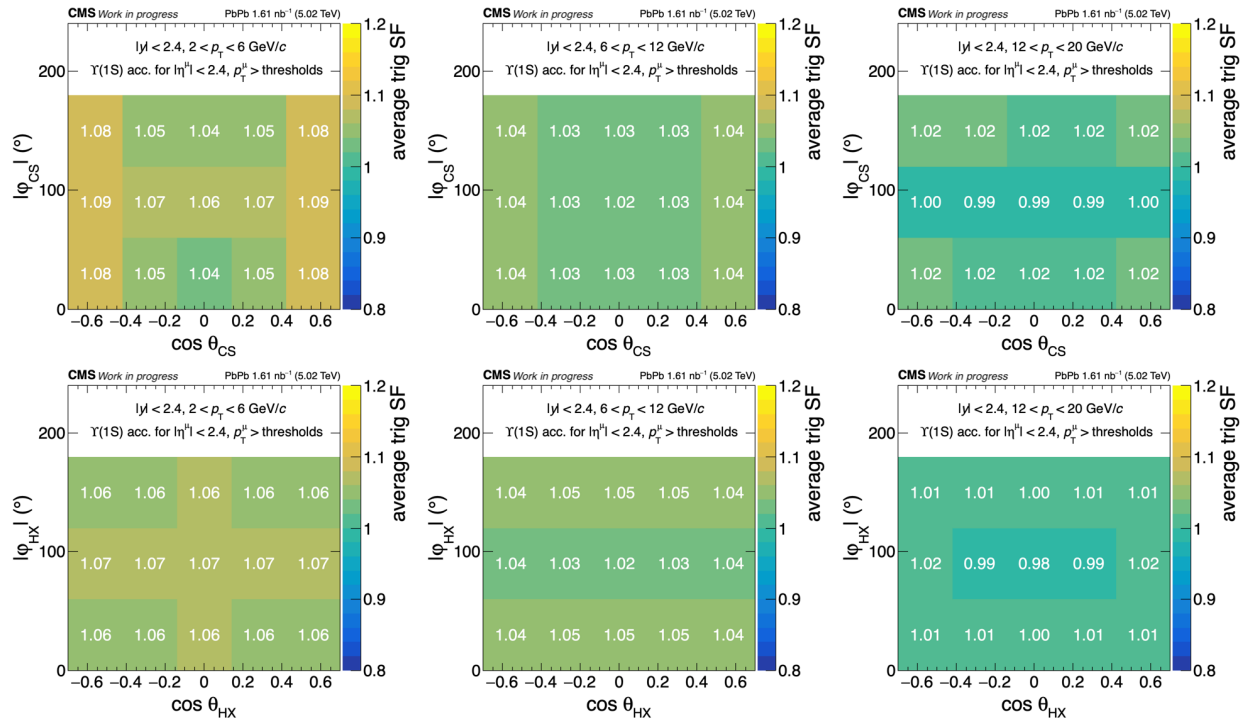
Figure C.12: Average trigger SF within the analysis bins in the CS (top row) and HX (bottom) frames.

Appendix D

Symmetry of Acceptance in the $\cos\theta$-φ Space

The folding procedure used in the extraction of the polarization parameters relies on the assumption that the acceptance and efficiency corrections are symmetric with respect to the φ-axis. This symmetry originates from the properties of the angular decay distribution (Eq. (1.3)) and is exploited to reduce the statistical uncertainty by combining mirrored bins in φ. Any significant asymmetry in the corrections could bias the extracted polarization parameters, so this assumption must be validated.

In the Sec. 6.3, the symmetry of Acceptance $\times$ Efficiency was verified. Figures D.1–D.6 show the corresponding acceptance maps and their 1D projections along the $\cos\theta$ and φ-axes.

Figure D.1: Acceptance distribution as a function of φ (top) and $\cos\theta$ (bottom) in the CS frame for $2 < p_{\mathrm{T}} < 6$ GeV/c. The 2D plot in the top left is identical to the one in Fig. 6.3, but it displays asymmetric uncertainty values above each bin. Each 1D plot compares a column (top) or row (bottom) on the positive side of $\cos\theta$ or φ values (purple) with the corresponding column or row on the negative side (blue). The bottom panel of each 1D plot presents the pull distribution for each bin.

Figure D.2: Acceptance distribution as a function of φ (top) and $\cos\theta$ (bottom) in the CS frame for $6 < p_T < 12$ GeV/c. The 2D plot in the top left is identical to the one in Fig. 6.3, but it displays asymmetric uncertainty values above each bin. Each 1D plot compares a column (top) or row (bottom) on the positive side of $\cos\theta$ or φ values (purple) with the corresponding column or row on the negative side (blue). The bottom panel of each 1D plot presents the pull distribution for each bin.

Figure D.3: Acceptance distribution as a function of φ (top) and $\cos\theta$ (bottom) in the CS frame for $12 < p_{\mathrm{T}} < 20$ $GeVc$. The 2D plot in the top left is identical to the one in Fig. 6.3, but it displays asymmetric uncertainty values above each bin. Each 1D plot compares a column (top) or row (bottom) on the positive side of $\cos\theta$ or φ values (purple) with the corresponding column or row on the negative side (blue). The bottom panel of each 1D plot presents the pull distribution for each bin.

Figure D.4: Acceptance distribution as a function of φ (top) and $\cos\theta$ (bottom) in the HX frame for $2 < p_T < 6$ GeV/c. The 2D plot in the top left is identical to the one in Fig. 6.3, but it displays asymmetric uncertainty values above each bin. Each 1D plot compares a column (top) or row (bottom) on the positive side of $\cos\theta$ or φ values (purple) with the corresponding column or row on the negative side (blue). The bottom panel of each 1D plot presents the pull distribution for each bin.

Figure D.5: Acceptance distribution as a function of φ (top) and $\cos\theta$ (bottom) in the HX frame for $6 < p_T < 12$ GeV/c. The 2D plot in the top left is identical to the one in Fig. 6.3, but it displays asymmetric uncertainty values above each bin. Each 1D plot compares a column (top) or row (bottom) on the positive side of $\cos\theta$ or φ values (purple) with the corresponding column or row on the negative side (blue). The bottom panel of each 1D plot presents the pull distribution for each bin.

Figure D.6: Acceptance distribution as a function of φ (top) and $\cos\theta$ (bottom) in the HX frame for $12 < p_\mathrm{T} < 20$ GeV/c. The 2D plot in the top left is identical to the one in Fig. 6.3, but it displays asymmetric uncertainty values above each bin. Each 1D plot compares a column (top) or row (bottom) on the positive side of $\cos\theta$ or φ values (purple) with the corresponding column or row on the negative side (blue). The bottom panel of each 1D plot presents the pull distribution for each bin.

Appendix E

Symmetry of Efficiency in the $\cos\theta$-φ Space

The folding procedure used in the extraction of the polarization parameters relies on the assumption that the acceptance and efficiency corrections are symmetric with respect to the φ-axis. This symmetry originates from the properties of the angular decay distribution (Eq. (1.3)) and is exploited to reduce the statistical uncertainty by combining mirrored bins in φ. Any significant asymmetry in the corrections could bias the extracted polarization parameters, so this assumption must be validated.

In the Sec. 6.3, the symmetry of Acceptance $\times$ Efficiency was verified. Figures E.1–E.6 show the corresponding efficiency maps and their 1D projections along the $\cos\theta$ and φ-axes.
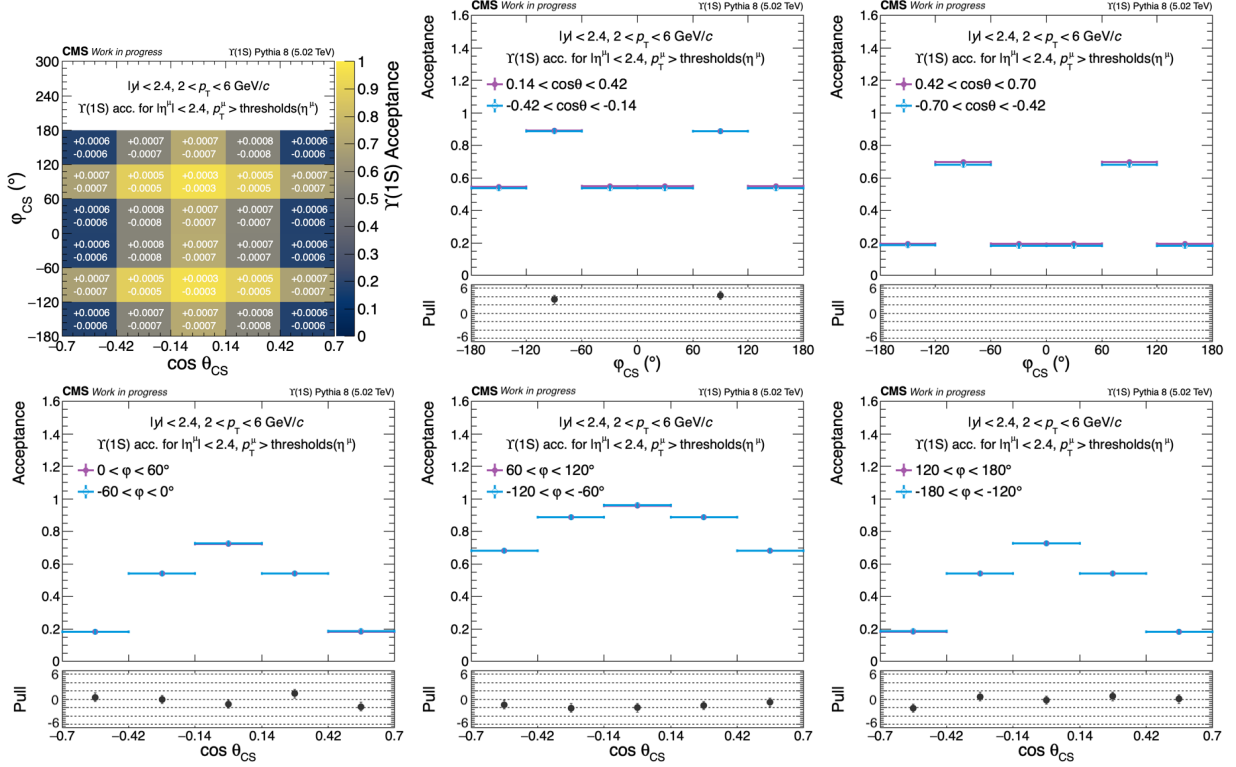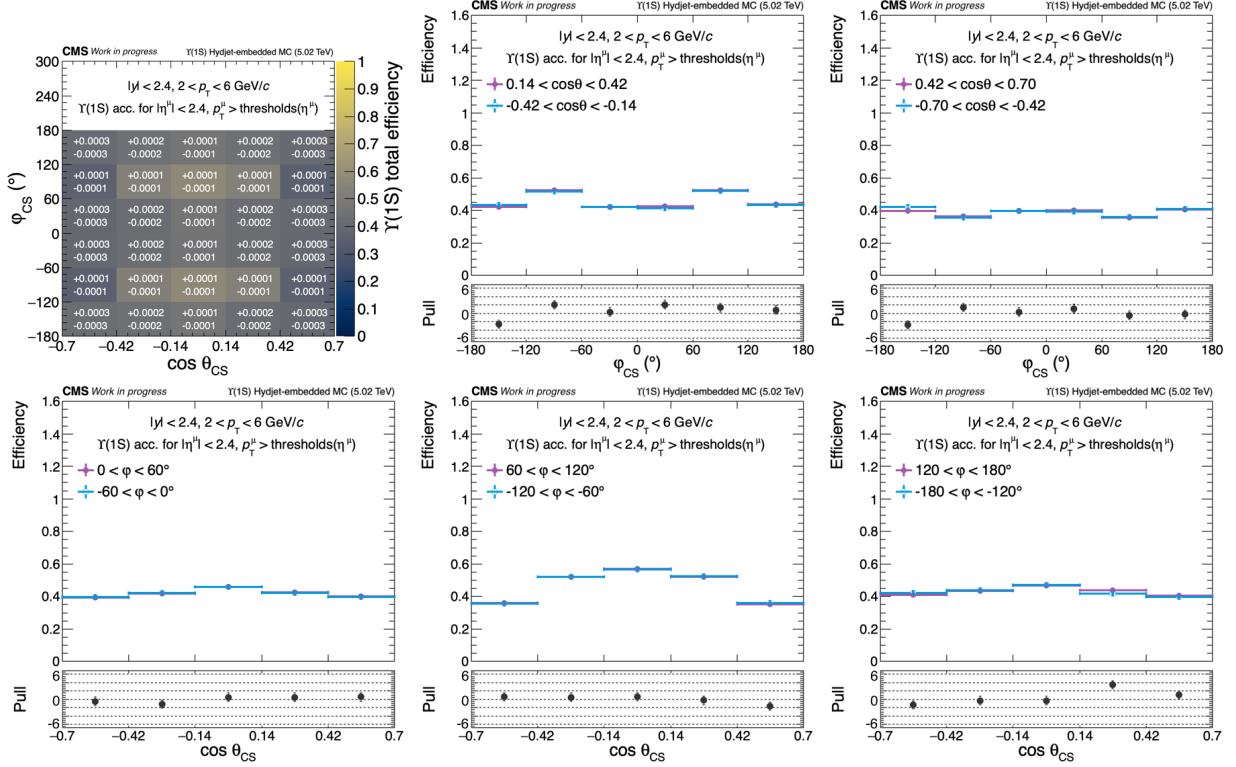
Figure E.1: Efficiency distribution as a function of φ (top) and $\cos\theta$ (bottom) in the CS frame for $2 < p_{\mathrm{T}} < 6$ GeV/c. The 2D plot in the top left is identical to the one in Fig. 6.3, but it displays asymmetric uncertainty values above each bin. Each 1D plot compares a column (top) or row (bottom) on the positive side of $\cos\theta$ or φ values (purple) with the corresponding column or row on the negative side (blue). The bottom panel of each 1D plot presents the pull distribution for each bin.
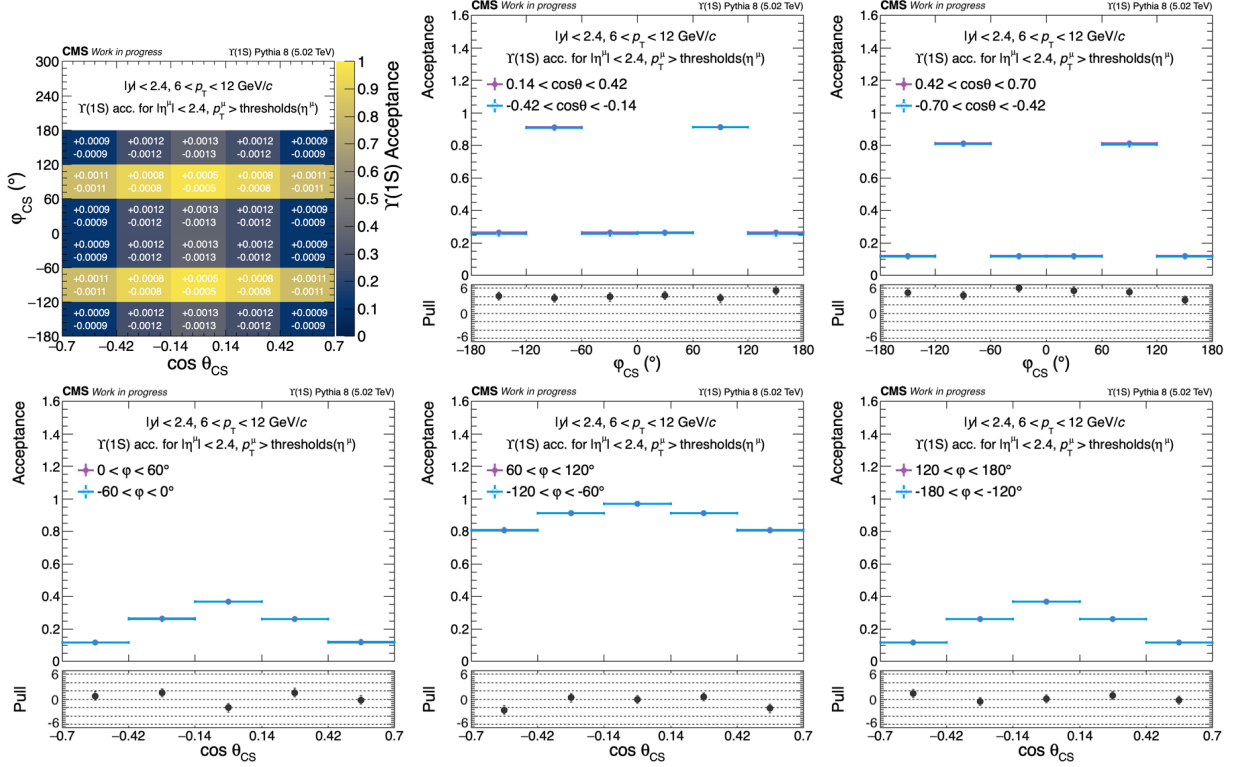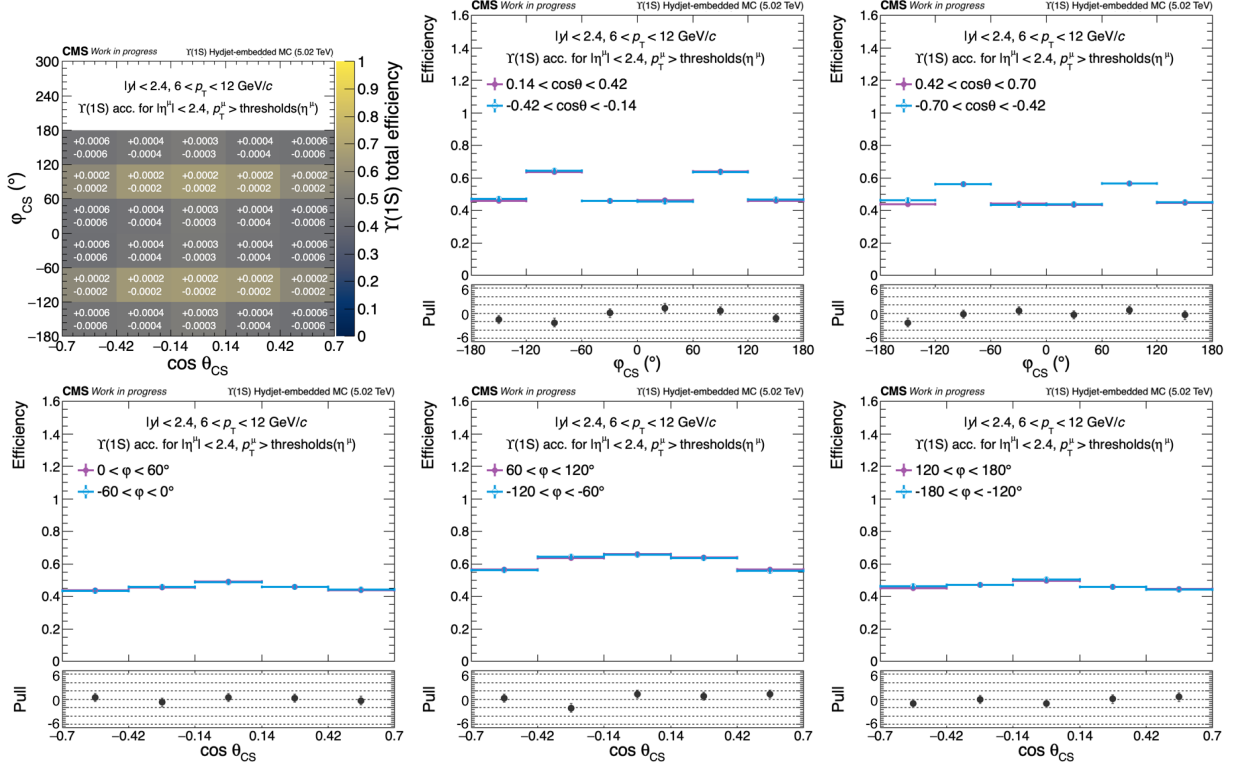
Figure E.2: Efficiency distribution as a function of φ (top) and $\cos\theta$ (bottom) in the CS frame for $6 < p_{\mathrm{T}} < 12$ GeV/c. The 2D plot in the top left is identical to the one in Fig. 6.3, but it displays asymmetric uncertainty values above each bin. Each 1D plot compares a column (top) or row (bottom) on the positive side of $\cos\theta$ or φ values (purple) with the corresponding column or row on the negative side (blue). The bottom panel of each 1D plot presents the pull distribution for each bin.
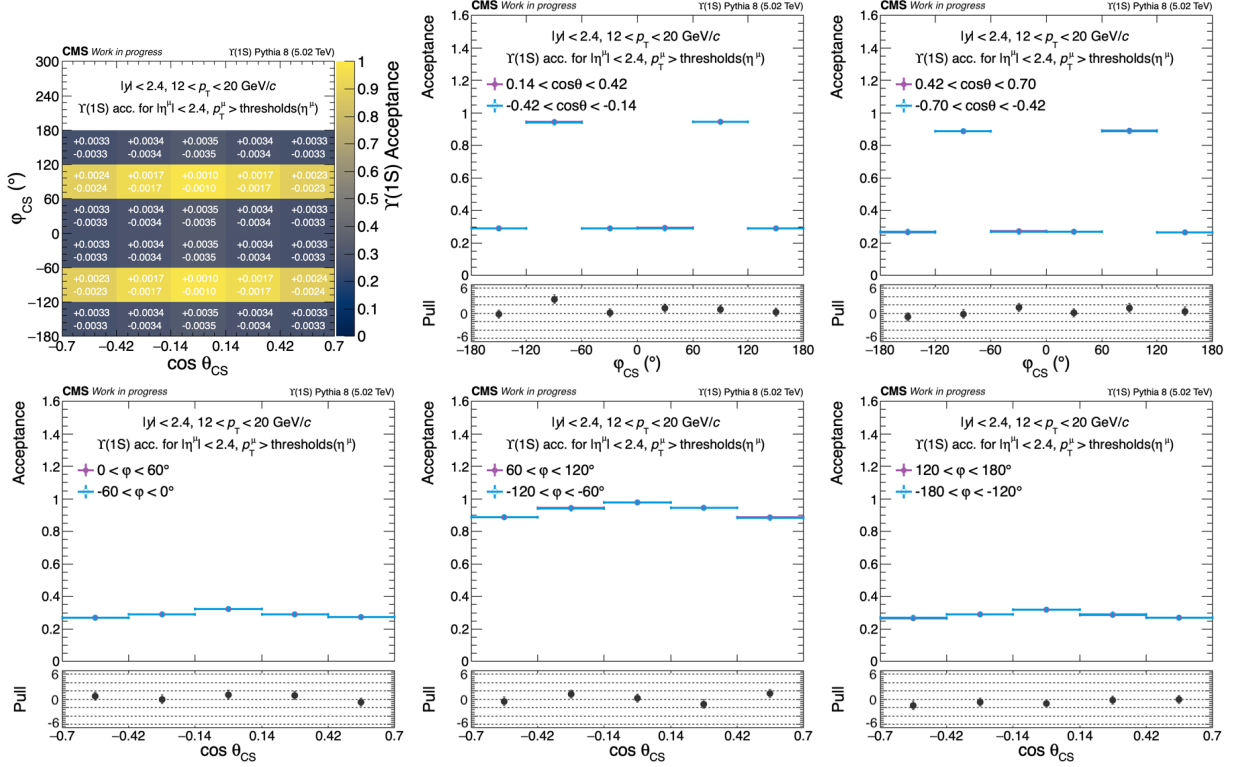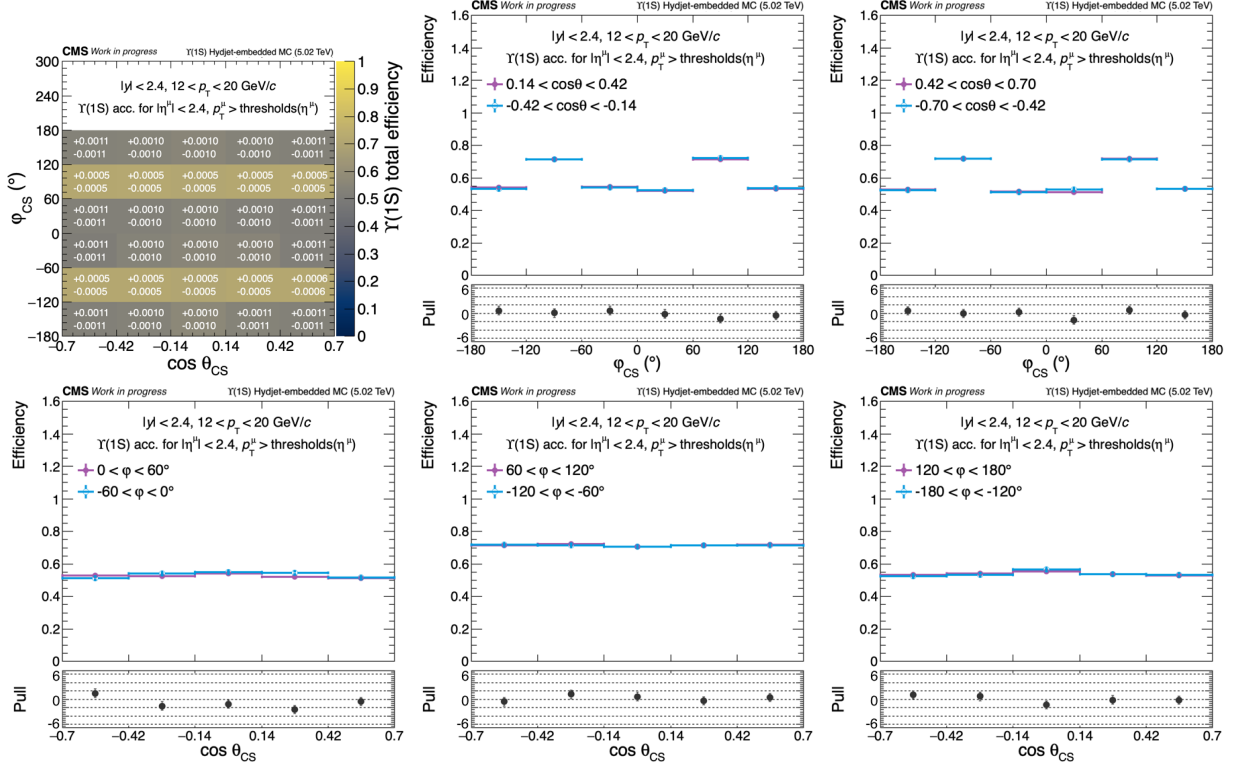
Figure E.3: Efficiency distribution as a function of φ (top) and $\cos\theta$ (bottom) in the CS frame for $12 < p_{\mathrm{T}} < 20 \ GeV c$. The 2D plot in the top left is identical to the one in Fig. 6.3, but it displays asymmetric uncertainty values above each bin. Each 1D plot compares a column (top) or row (bottom) on the positive side of $\cos\theta$ or φ values (purple) with the corresponding column or row on the negative side (blue). The bottom panel of each 1D plot presents the pull distribution for each bin.
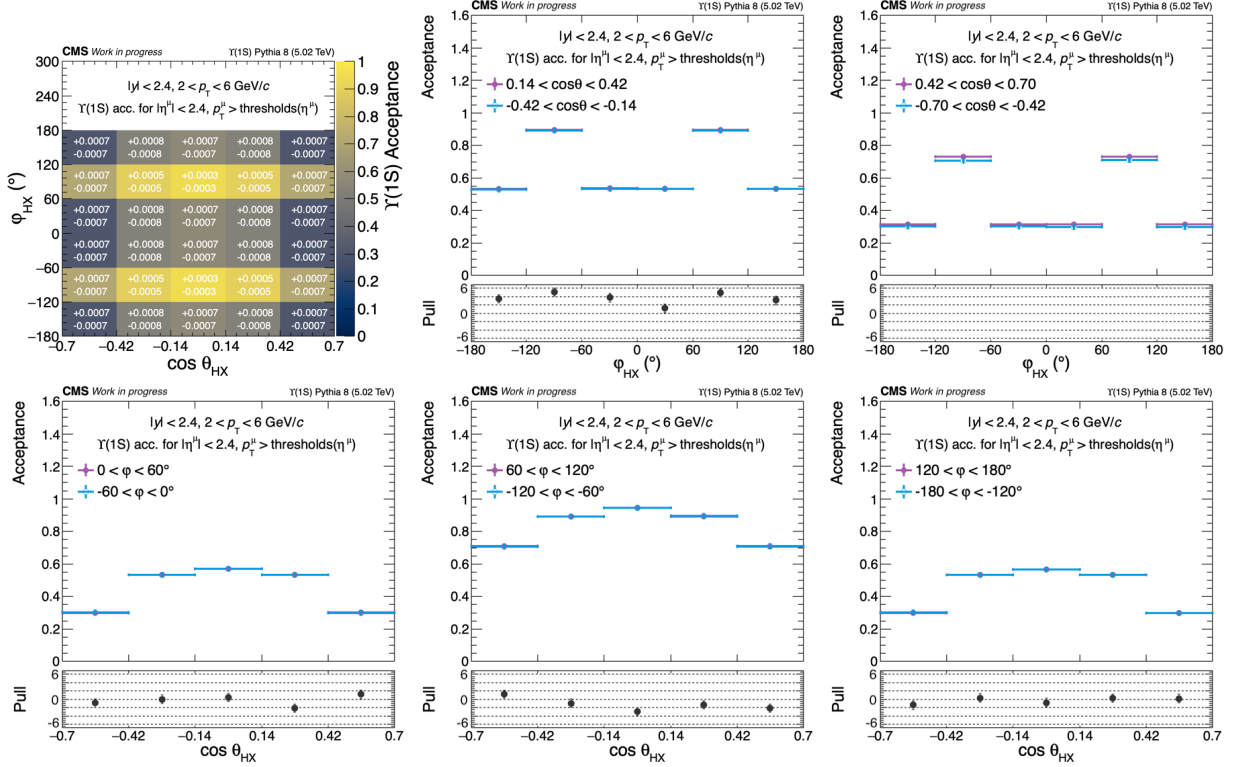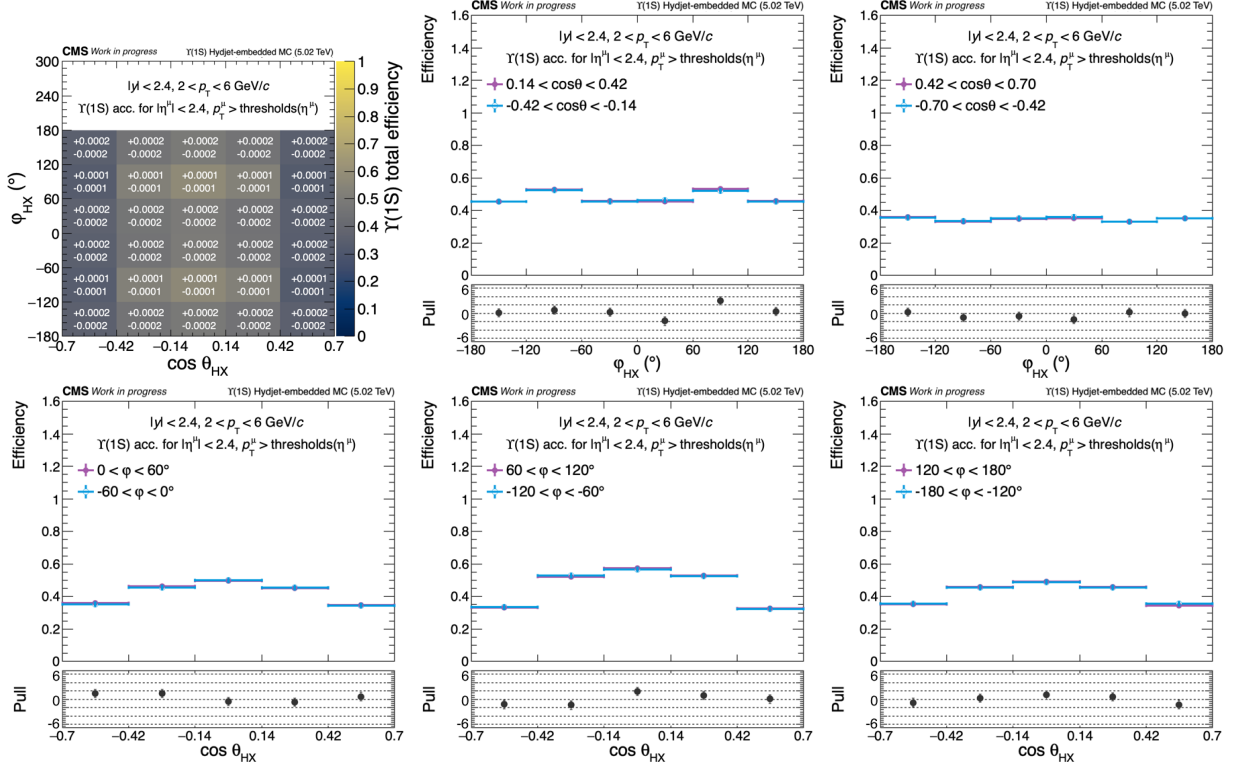
Figure E.4: Efficiency distribution as a function of φ (top) and $\cos\theta$ (bottom) in the HX frame for $2 < p_{\mathrm{T}} < 6$ GeV/c. The 2D plot in the top left is identical to the one in Fig. 6.3, but it displays asymmetric uncertainty values above each bin. Each 1D plot compares a column (top) or row (bottom) on the positive side of $\cos\theta$ or φ values (purple) with the corresponding column or row on the negative side (blue). The bottom panel of each 1D plot presents the pull distribution for each bin.
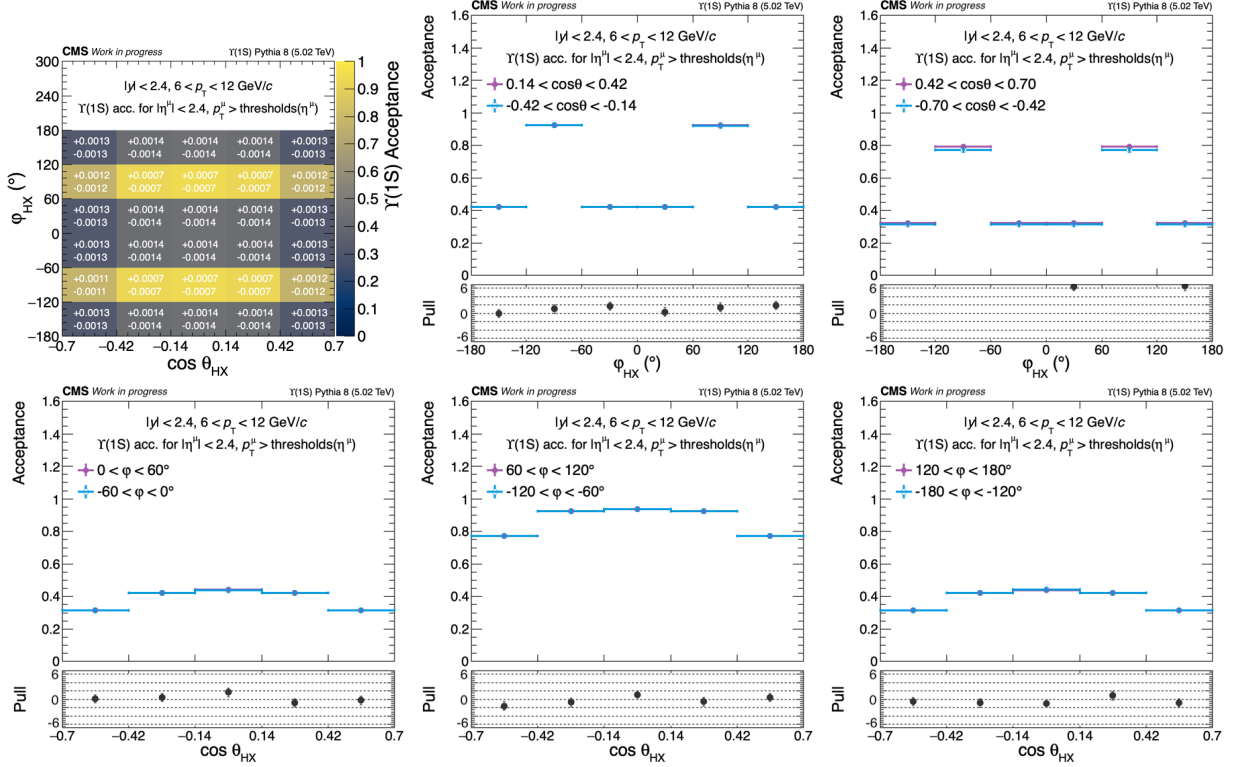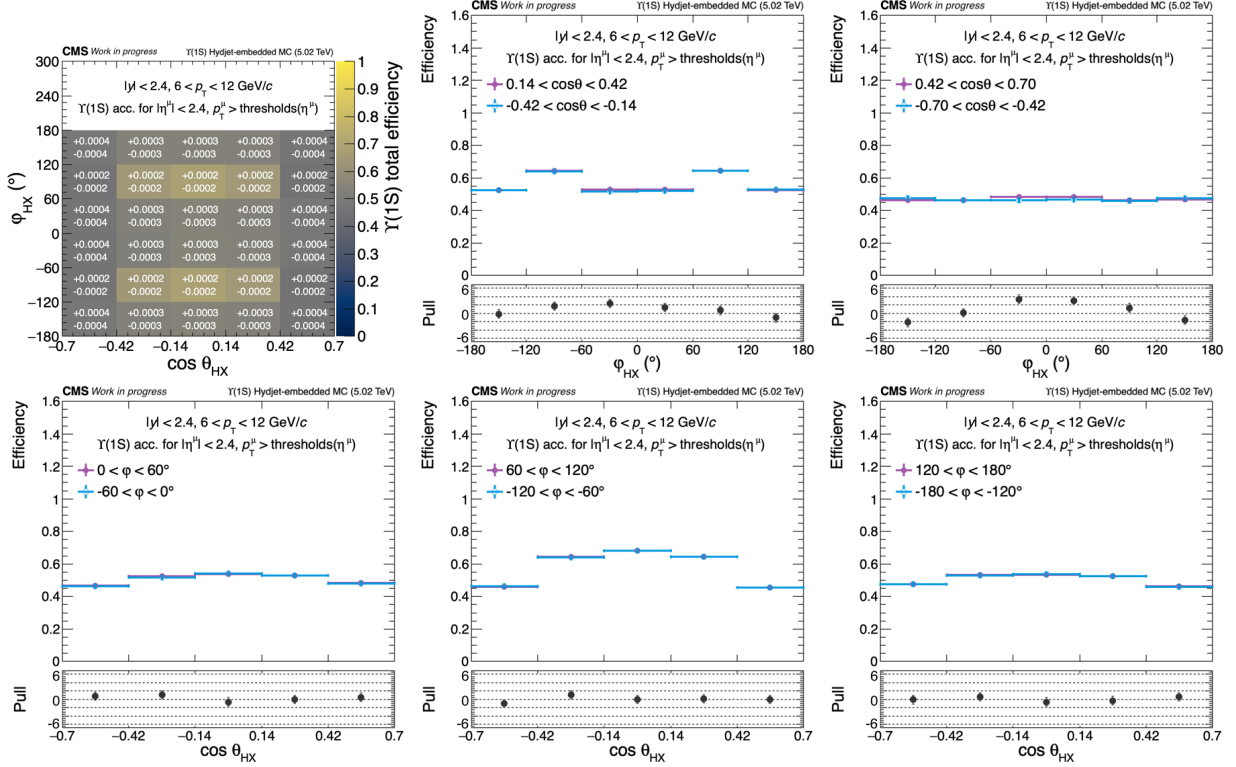
Figure E.5: Efficiency distribution as a function of φ (top) and $\cos\theta$ (bottom) in the HX frame for $6 < p_T < 12$ GeV/c. The 2D plot in the top left is identical to the one in Fig. 6.3, but it displays asymmetric uncertainty values above each bin. Each 1D plot compares a column (top) or row (bottom) on the positive side of $\cos\theta$ or φ values (purple) with the corresponding column or row on the negative side (blue). The bottom panel of each 1D plot presents the pull distribution for each bin.
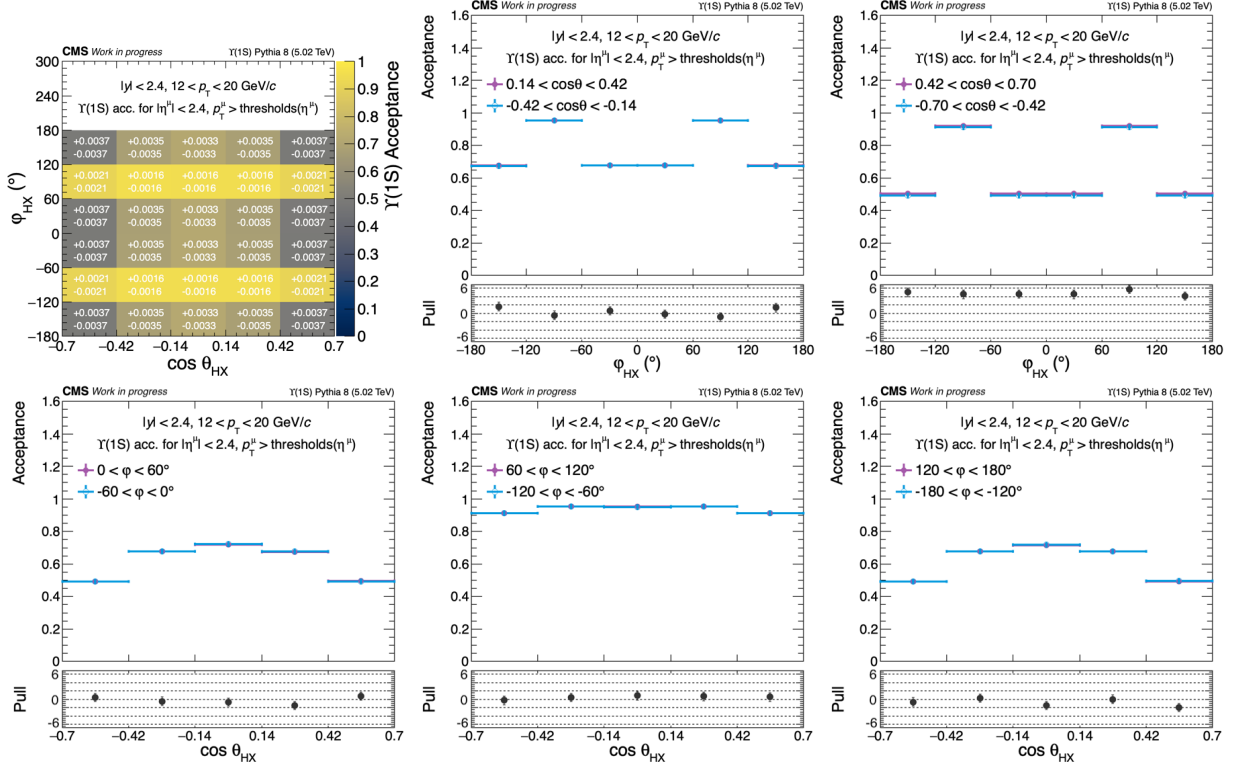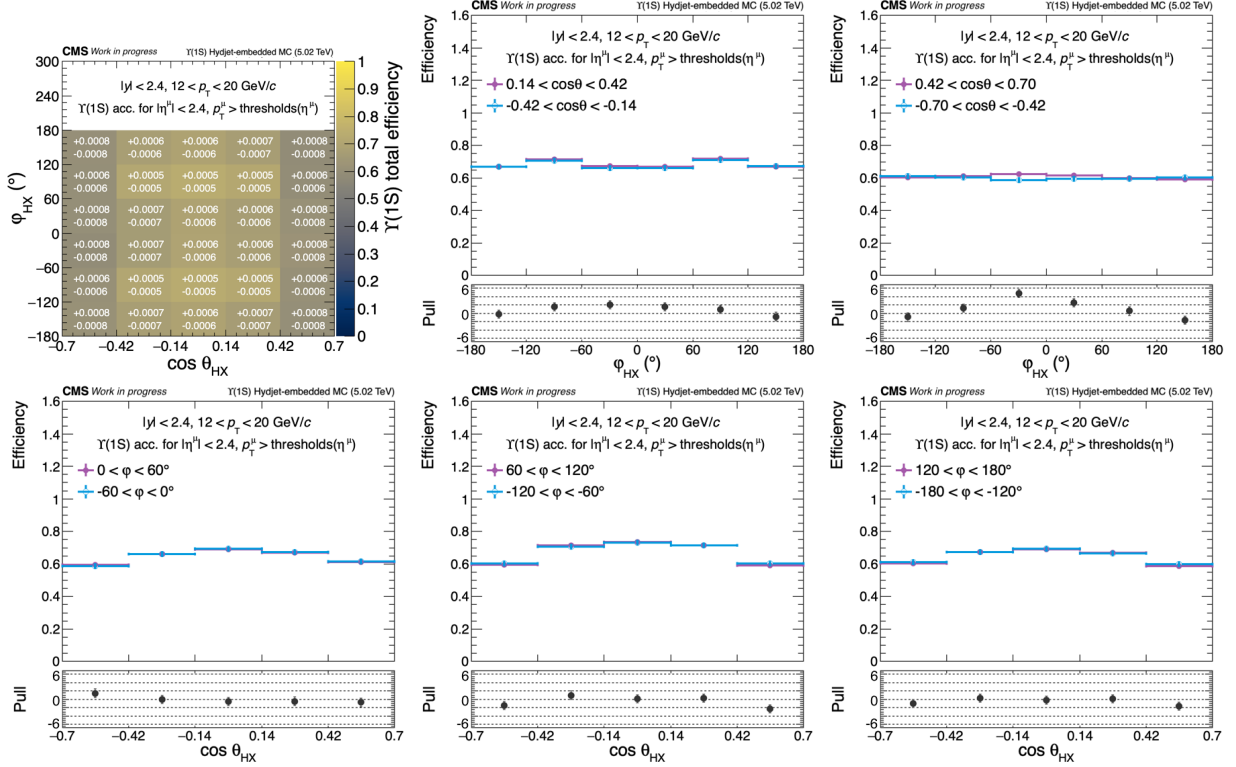
Figure E.6: Efficiency distribution as a function of φ (top) and $\cos\theta$ (bottom) in the HX frame for $12 < p_T < 20$ GeV/c. The 2D plot in the top left is identical to the one in Fig. 6.3, but it displays asymmetric uncertainty values above each bin. Each 1D plot compares a column (top) or row (bottom) on the positive side of $\cos\theta$ or φ values (purple) with the corresponding column or row on the negative side (blue). The bottom panel of each 1D plot presents the pull distribution for each bin.

Appendix F

Polarization Parameter Extraction Fits

Figures F.1 and F.2 show the complete set of corrected $\Upsilon(1S)$ yields with uncertainties and the corresponding polarization parameter extraction fits with results. The corrected $\Upsilon(1S)$ yields in Fig. F.1 are color-mapped with percentage uncertainties displayed for each bin. Figure F.2 presents them as 3D lego plots, overlaid with a red mesh representing the fit.

The results shown here were obtained with unpolarized acceptance and efficiency maps. An iterative procedure is performed in which the acceptance and efficiency are reweighted using the extracted polarization parameters in order to obtain the final results presented in Chapter 8.
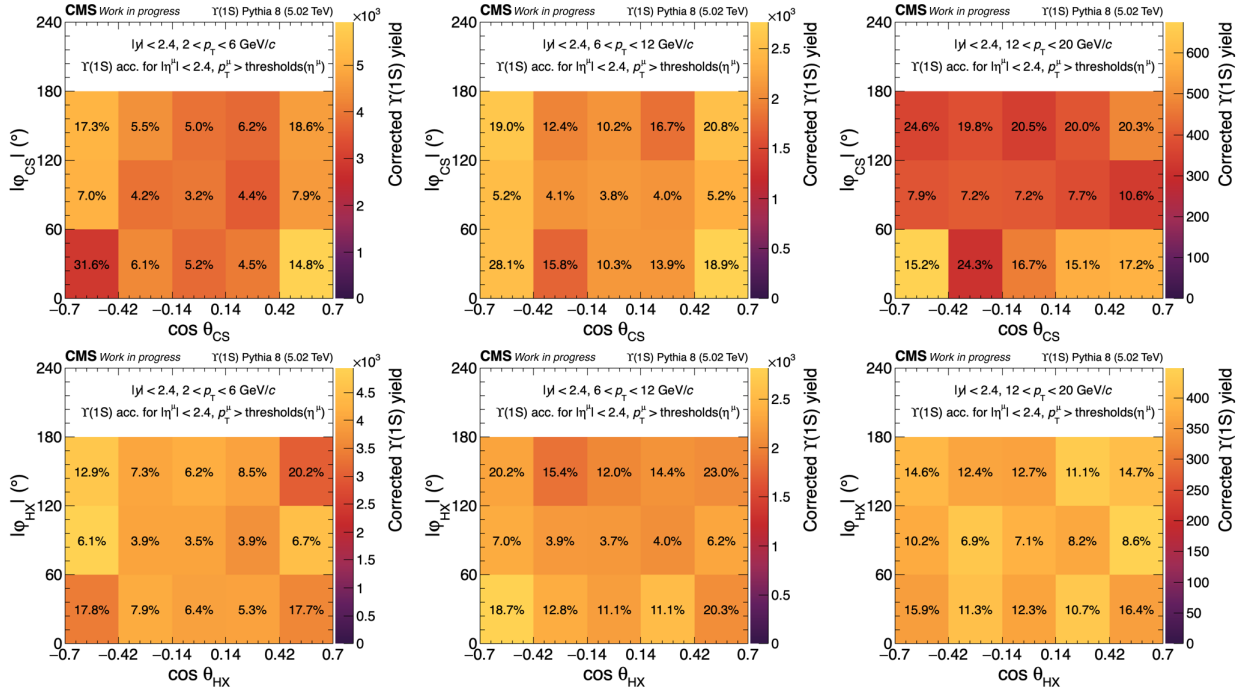
Figure F.1: $\Upsilon(1S)$ yields, corrected using correction factors, in the 2D phase space of $\cos\theta - |\varphi|$ for the CS (top row) and HX (bottom row) frames. Each column corresponds to a different p_T analysis bin: (left) $2 < p_T^{\mu\mu} < 6\,\mathrm{GeV}/c$, (middle) $6 < p_T^{\mu\mu} < 12\,\mathrm{GeV}/c$, and (right) $12 < p_T^{\mu\mu} < 20\,\mathrm{GeV}/c$. The $\Upsilon(1S)$ yields in each $(p_T, \cos\theta, \varphi)$ bin are represented by a color scale, with percentage uncertainties displayed on each cell. The uncertainties account for signal extraction likelihood uncertainties in the $\Upsilon(1S)$ yields.
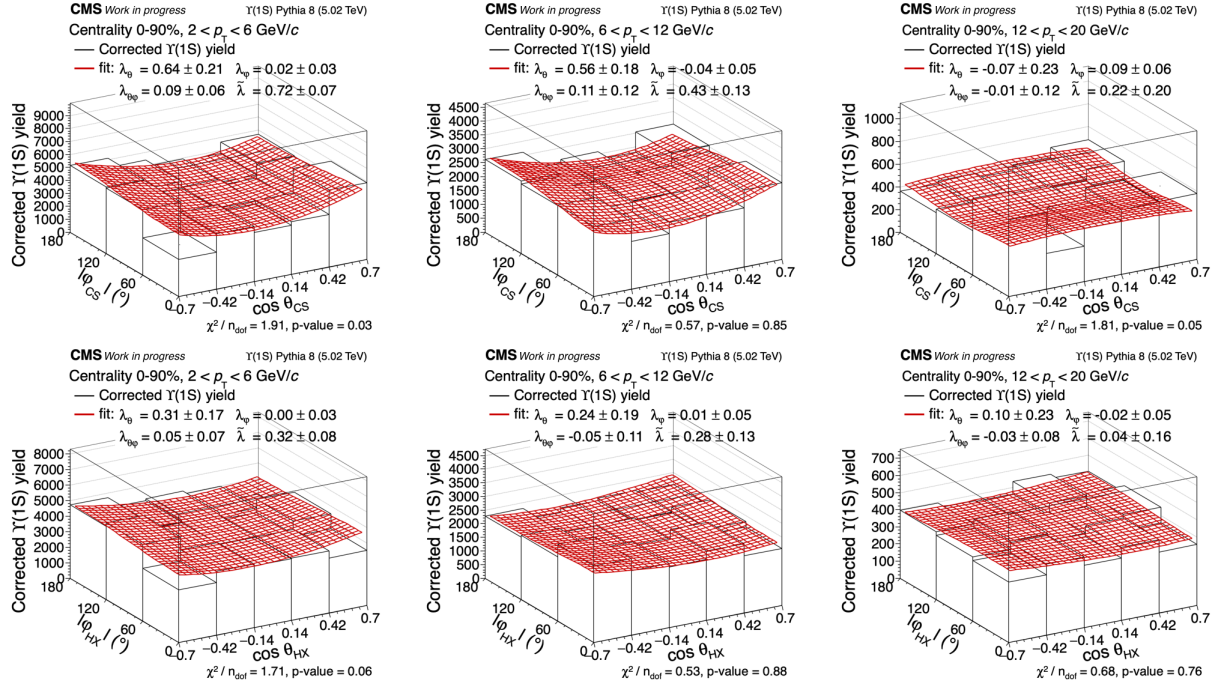
Figure F.2: Polarization parameter extraction fits (red mesh) are shown as 3D lego plots in the CS (top row) and HX (bottom row) frames. Each column corresponds to a different p_T analysis bin: (left) $2 < p_T^{\mu\mu} < 6 \, \text{GeV}/c$, (middle) $6 < p_T^{\mu\mu} < 12 \, \text{GeV}/c$, and (right) $12 < p_T^{\mu\mu} < 20 \, \text{GeV}/c$.

Appendix G

Pseudo-experiments

Figures G.1–G.30 are the complete set of pseudo-experiment results across all $(p_\mathrm{T}^{\mu\mu}, \cos\theta, \varphi)$ bins.

Figure G.1: Pseudo-experiment results using the nominal fit model (first column), an alternative signal model (second column), and an alternative background model (third column) for $2 < p_\mathrm{T} < 6\,\mathrm{GeV}/c$, $0.42 < \cos\theta < 0.70$ bins in the CS frame.

Figure G.2: Pseudo-experiment results using the nominal fit model (first column), an alternative signal model (second column), and an alternative background model (third column) for $2 < p_T < 6 \, \text{GeV}/c$, $0.14 < \cos\theta < 0.42$ bins in the CS frame.

Figure G.3: Pseudo-experiment results using the nominal fit model (first column), an alternative signal model (second column), and an alternative background model (third column) for $2 < p_\mathrm{T} < 6\,\mathrm{GeV}/c$, $-0.14 < \cos\theta < 0.14$ bins in the CS frame.

Figure G.4: Pseudo-experiment results using the nominal fit model (first column), an alternative signal model (second column), and an alternative background model (third column) for $2 < p_T < 6\,\mathrm{GeV}/c$, $-0.42 < \cos\theta < -0.14$ bins in the CS frame.

Figure G.5: Pseudo-experiment results using the nominal fit model (first column), an alternative signal model (second column), and an alternative background model (third column) for $2 < p_T < 6\,\mathrm{GeV}/c$, $-0.70 < \cos\theta < -0.42$ bins in the CS frame.

Figure G.6: Pseudo-experiment results using the nominal fit model (first column), an alternative signal model (second column), and an alternative background model (third column) for $6 < p_{\mathrm{T}} < 12\,\mathrm{GeV}/c$, $0.42 < \cos\theta < 0.70$ bins in the CS frame.

Figure G.7: Pseudo-experiment results using the nominal fit model (first column), an alternative signal model (second column), and an alternative background model (third column) for $6 < p_\mathrm{T} < 12 \, \mathrm{GeV}/c$, $0.14 < \cos\theta < 0.42$ bins in the CS frame.

Figure G.8: Pseudo-experiment results using the nominal fit model (first column), an alternative signal model (second column), and an alternative background model (third column) for $6 < p_\mathrm{T} < 12\,\mathrm{GeV}/c$, $-0.14 < \cos\theta < 0.14$ bins in the CS frame.

Figure G.9: Pseudo-experiment results using the nominal fit model (first column), an alternative signal model (second column), and an alternative background model (third column) for $6 < p_{\mathrm{T}} < 12\,\mathrm{GeV}/c$, $-0.42 < \cos\theta < -0.14$ bins in the CS frame.

Figure G.10: Pseudo-experiment results using the nominal fit model (first column), an alternative signal model (second column), and an alternative background model (third column) for $6 < p_\mathrm{T} < 12\,\mathrm{GeV}/c$, $-0.70 < \cos\theta < -0.42$ bins in the CS frame.

Figure G.11: Pseudo-experiment results using the nominal fit model (first column), an alternative signal model (second column), and an alternative background model (third column) for $12 < p_{\mathrm{T}} < 20 \, \mathrm{GeV}/c$, $0.42 < \cos\theta < 0.70$ bins in the CS frame.

Figure G.12: Pseudo-experiment results using the nominal fit model (first column), an alternative signal model (second column), and an alternative background model (third column) for $12 < p_{\mathrm{T}} < 20\,\mathrm{GeV}/c$, $0.14 < \cos\theta < 0.42$ bins in the CS frame.
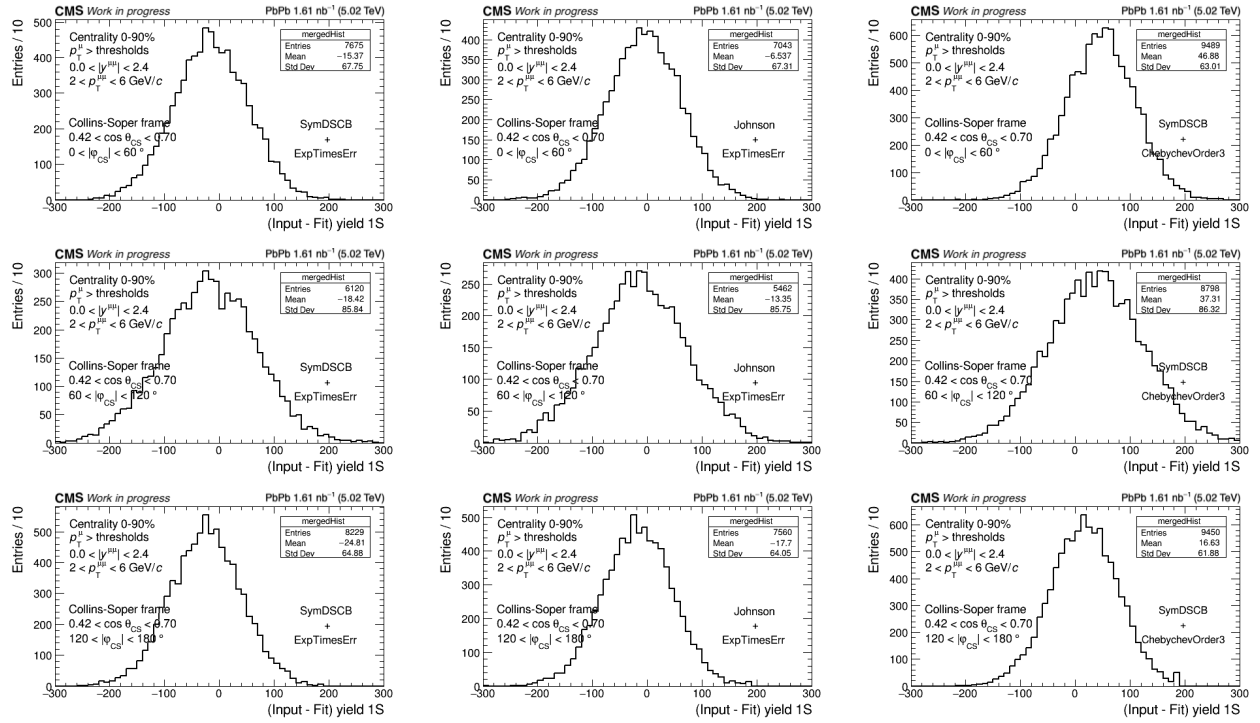
Figure G.13: Pseudo-experiment results using the nominal fit model (first column), an alternative signal model (second column), and an alternative background model (third column) for $12 < p_\mathrm{T} < 20\,\mathrm{GeV}/c$, $-0.14 < \cos\theta < 0.14$ bins in the CS frame.

Figure G.14: Pseudo-experiment results using the nominal fit model (first column), an alternative signal model (second column), and an alternative background model (third column) for $12 < p_{\mathrm{T}} < 20\,\mathrm{GeV}/c$, $-0.42 < \cos\theta < -0.14$ bins in the CS frame.
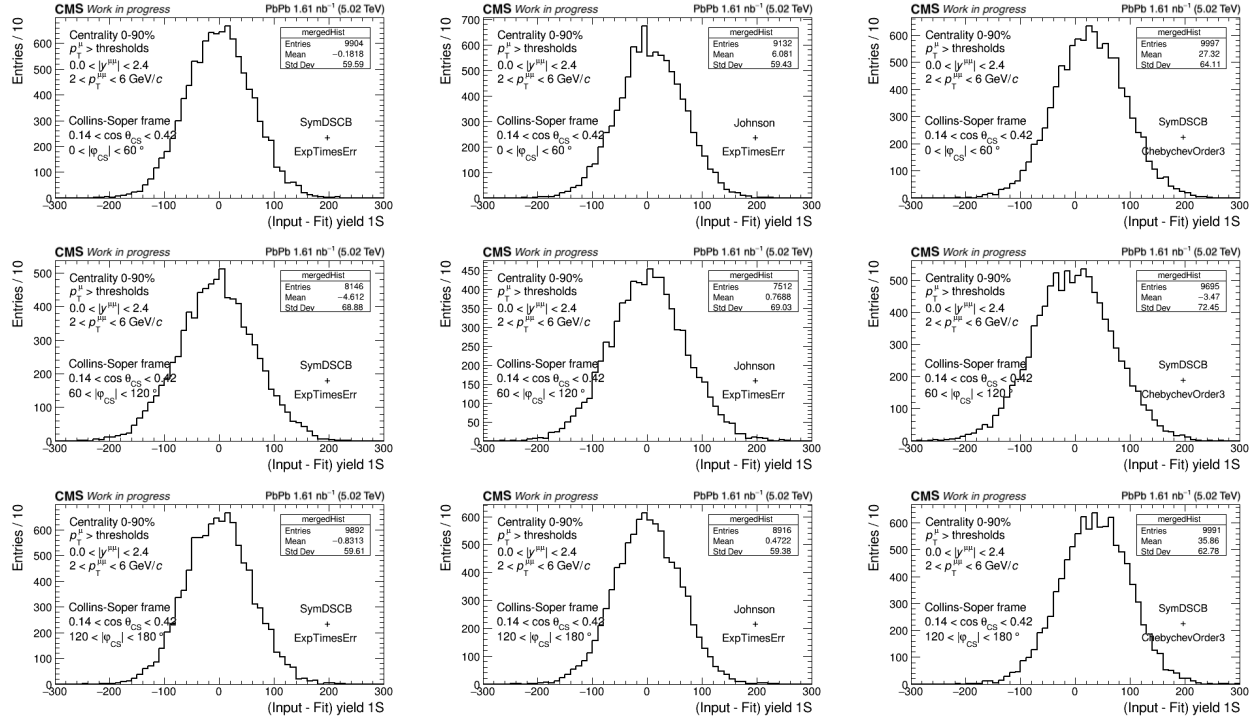
Figure G.15: Pseudo-experiment results using the nominal fit model (first column), an alternative signal model (second column), and an alternative background model (third column) for $12 < p_T < 20\,\mathrm{GeV}/c$, $-0.70 < \cos\theta < -0.42$ bins in the CS frame.
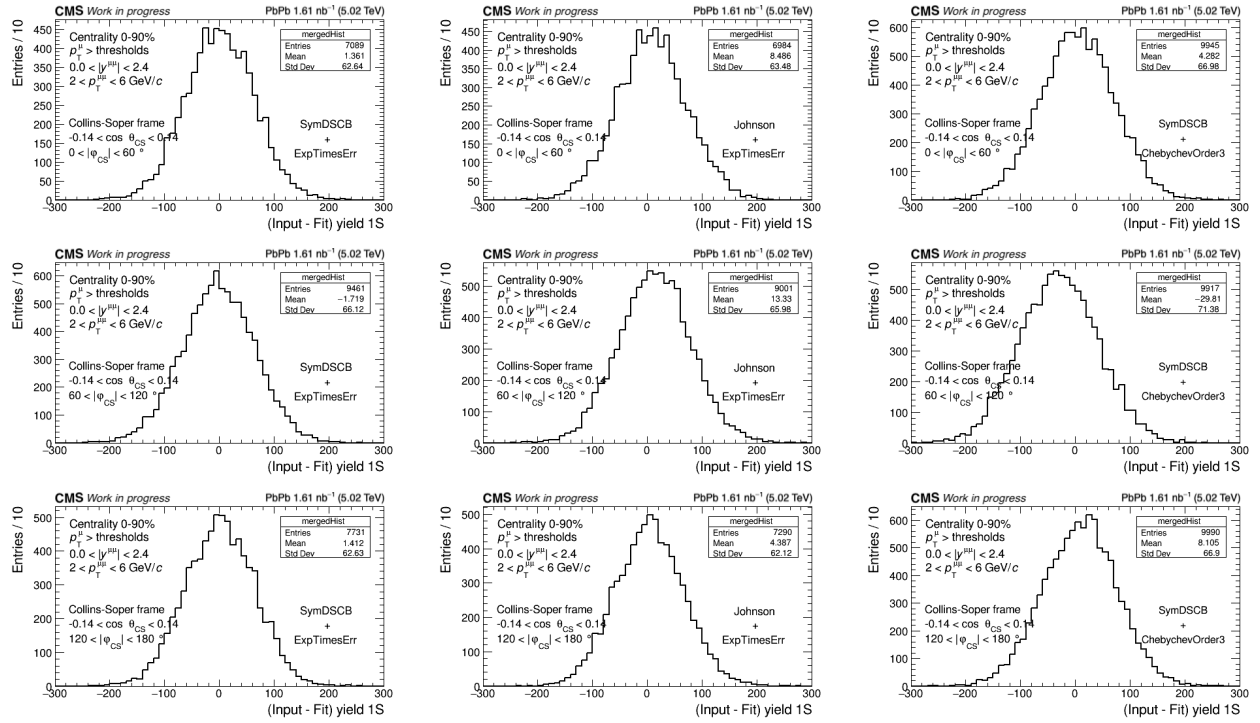
Figure G.16: Pseudo-experiment results using the nominal fit model (first column), an alternative signal model (second column), and an alternative background model (third column) for $2 < p_T < 6\,\mathrm{GeV}/c$, $0.42 < \cos\theta < 0.70$ in the HX frame.
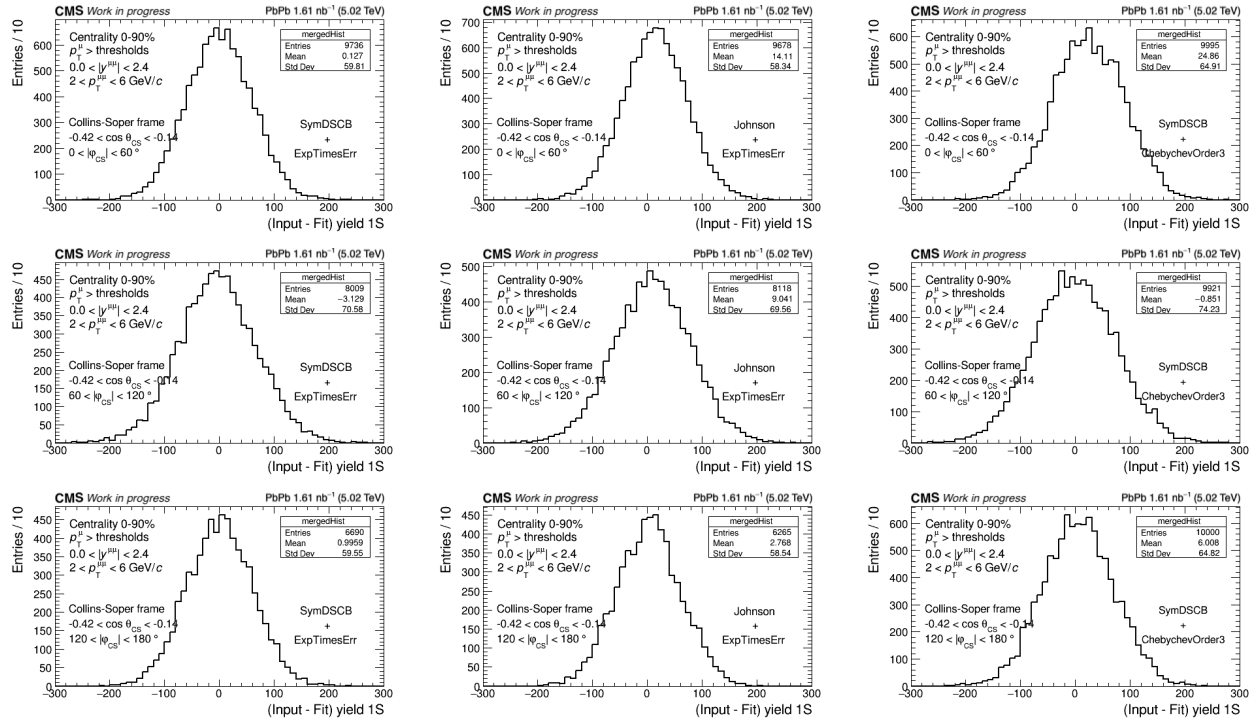
Figure G.17: Pseudo-experiment results using the nominal fit model (first column), an alternative signal model (second column), and an alternative background model (third column) for $2 < p_T < 6\,\mathrm{GeV}/c$, $0.14 < \cos\theta < 0.42$ in the HX frame.
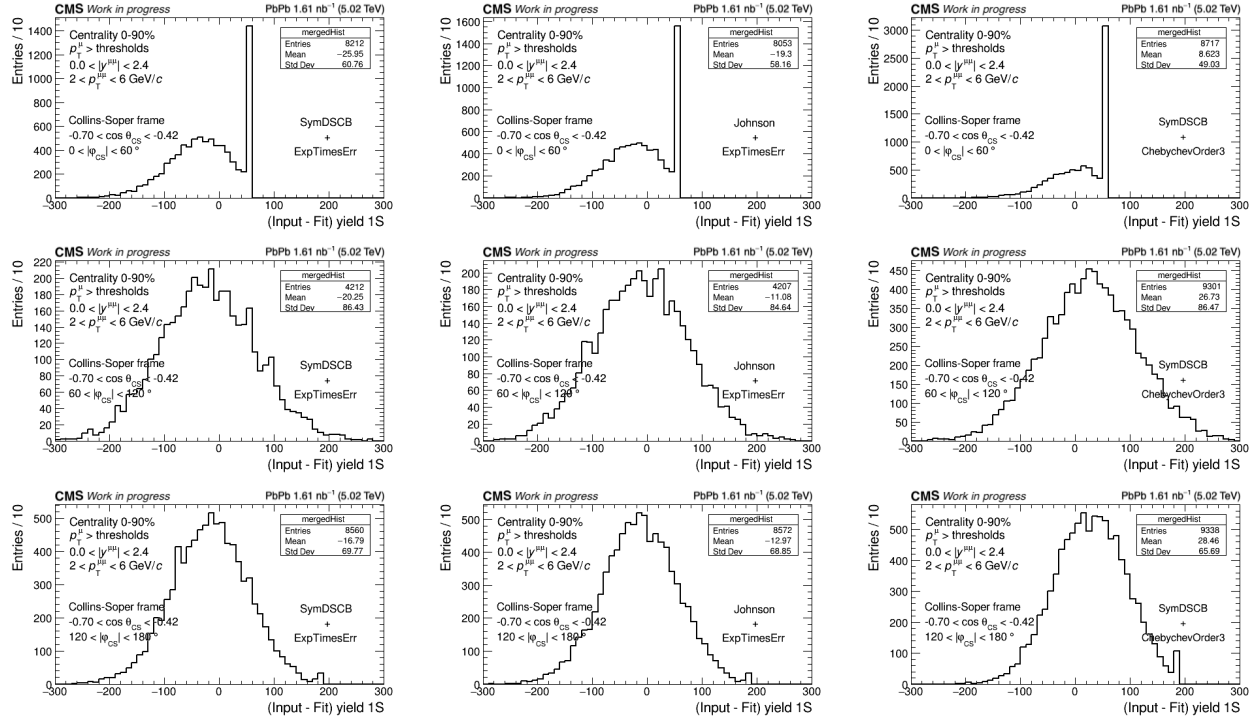
Figure G.18: Pseudo-experiment results using the nominal fit model (first column), an alternative signal model (second column), and an alternative background model (third column) for $2 < p_\mathrm{T} < 6\,\mathrm{GeV}/c$, $-0.14 < \cos\theta < 0.14$ in the HX frame.
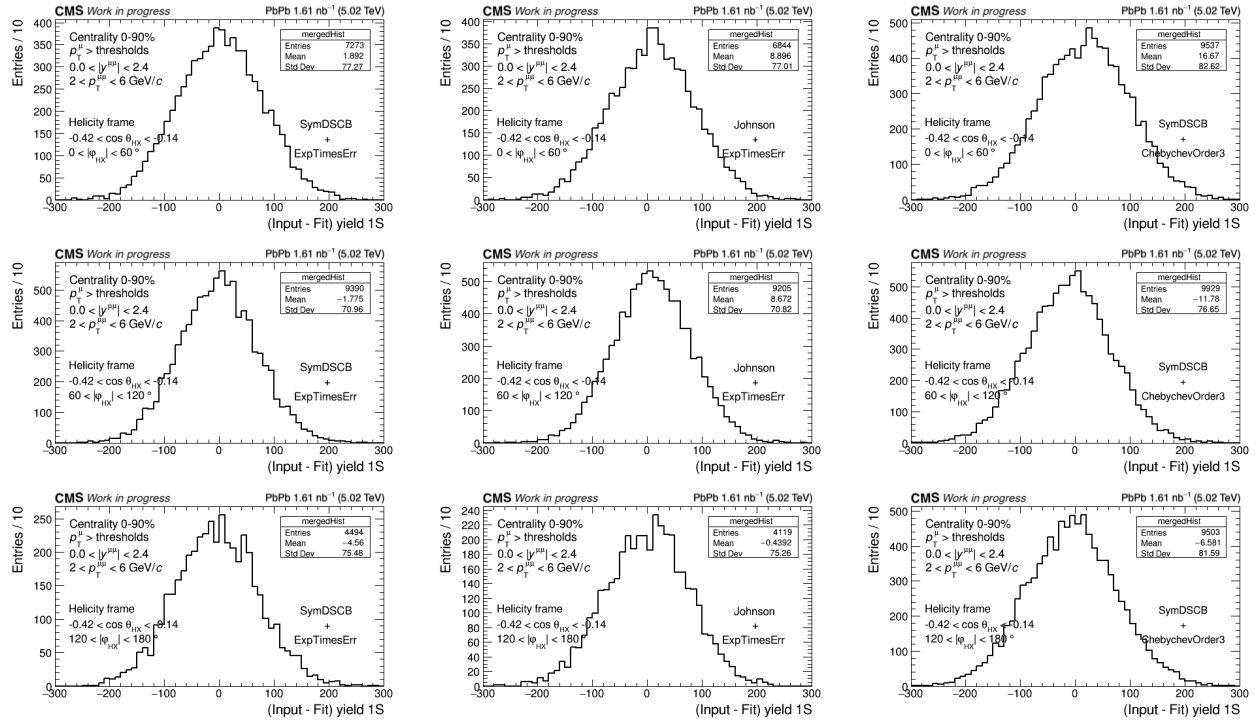
Figure G.19: Pseudo-experiment results using the nominal fit model (first column), an alternative signal model (second column), and an alternative background model (third column) for $2 < p_T < 6\,\mathrm{GeV}/c$, $-0.42 < \cos\theta < -0.14$ in the HX frame.
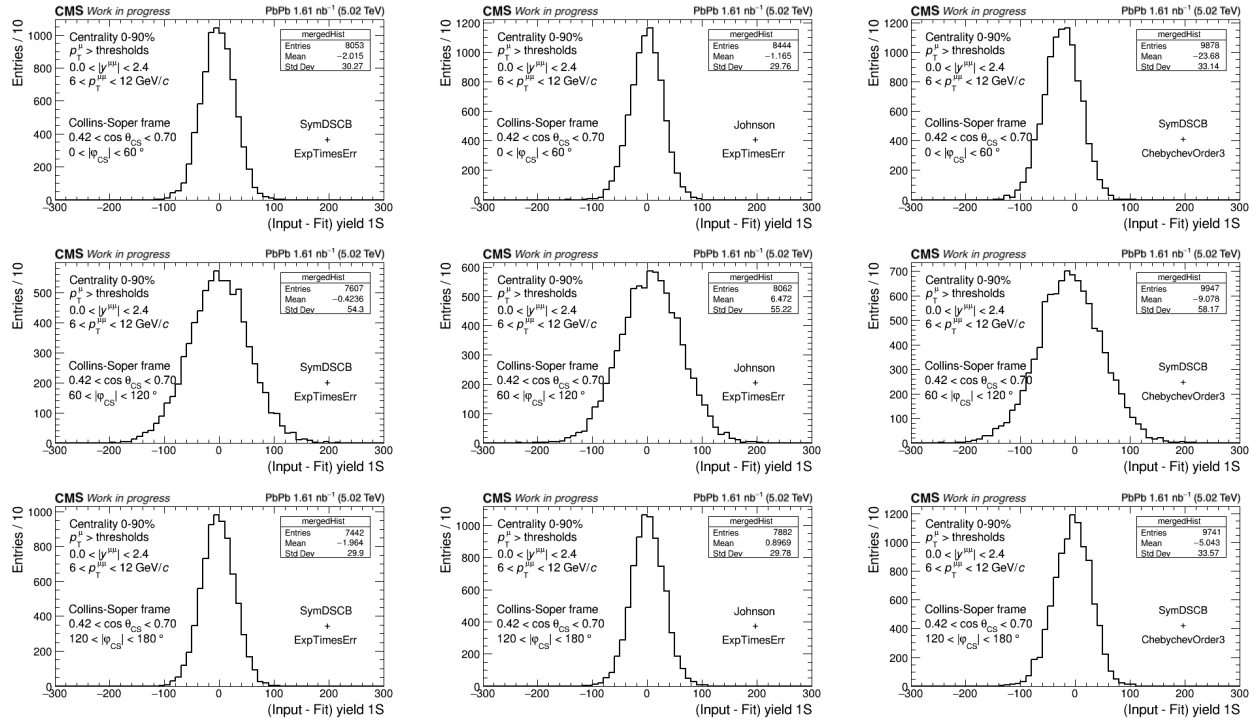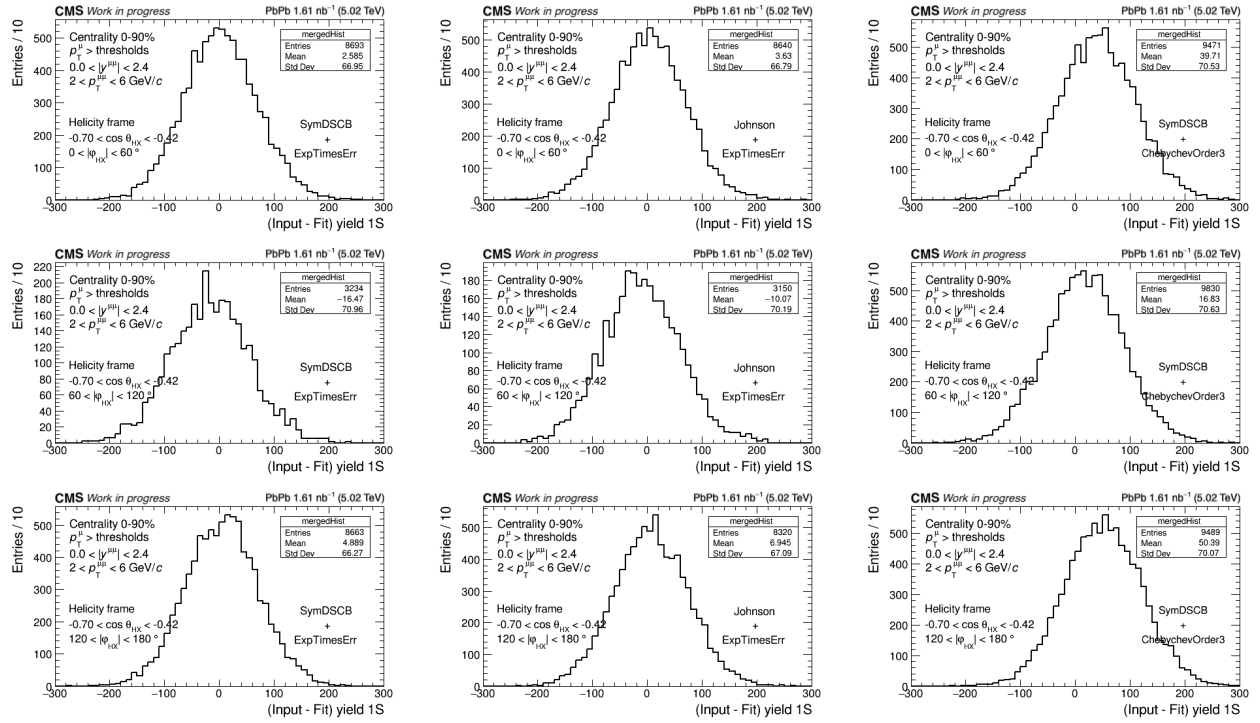
Figure G.20: Pseudo-experiment results using the nominal fit model (first column), an alternative signal model (second column), and an alternative background model (third column) for $2 < p_T < 6\,\mathrm{GeV}/c$, $-0.70 < \cos\theta < -0.42$ in the HX frame.
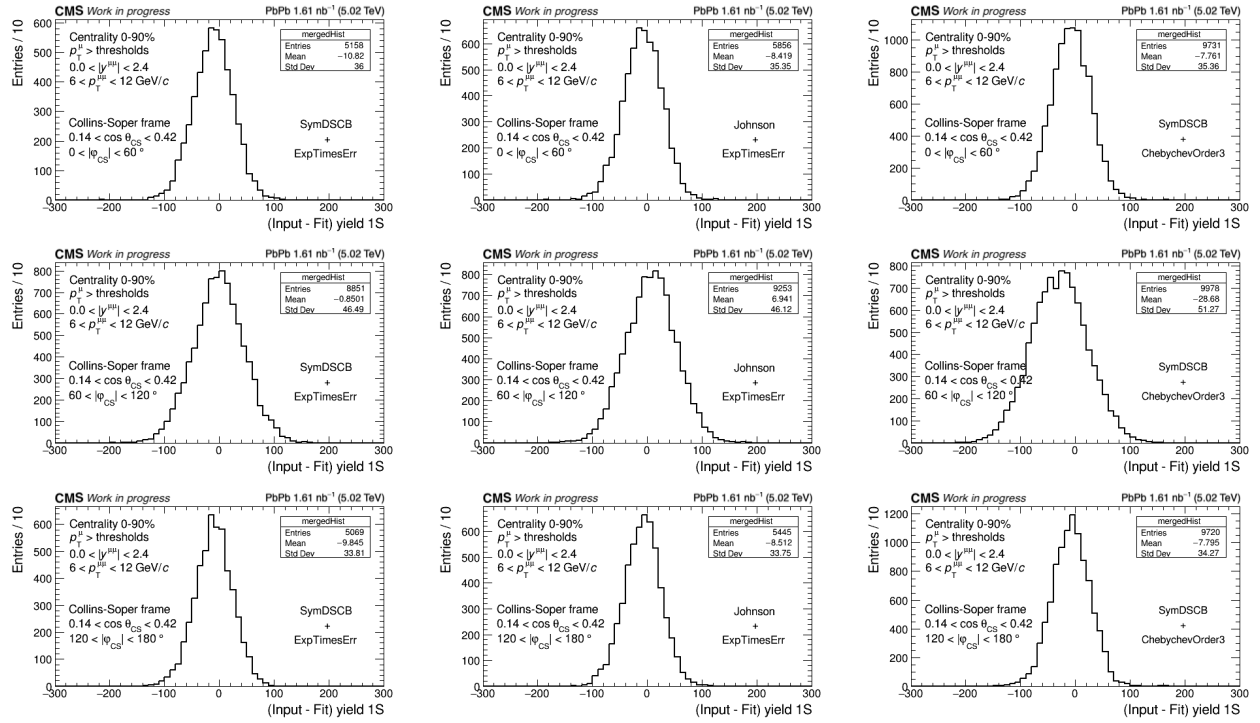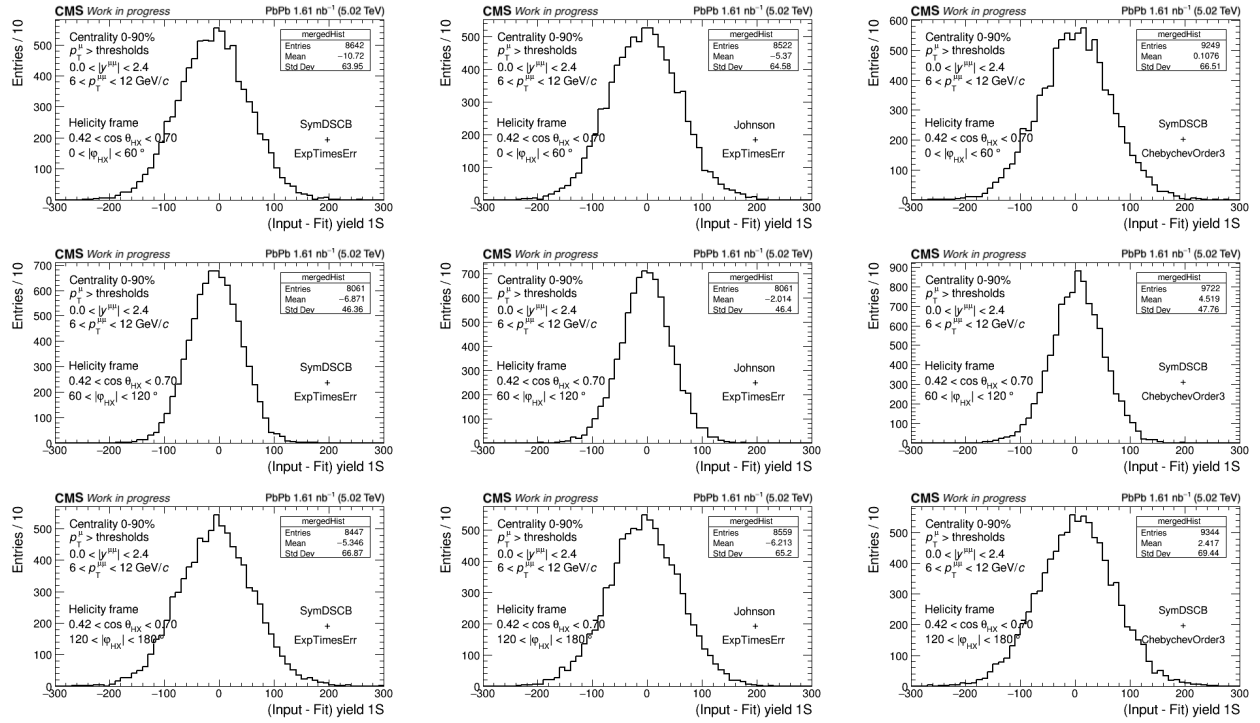
Figure G.21: Pseudo-experiment results using the nominal fit model (first column), an alternative signal model (second column), and an alternative background model (third column) for $6 < p_{\mathrm{T}} < 12\,\mathrm{GeV}/c$, $0.42 < \cos\theta < 0.70$ in the HX frame.
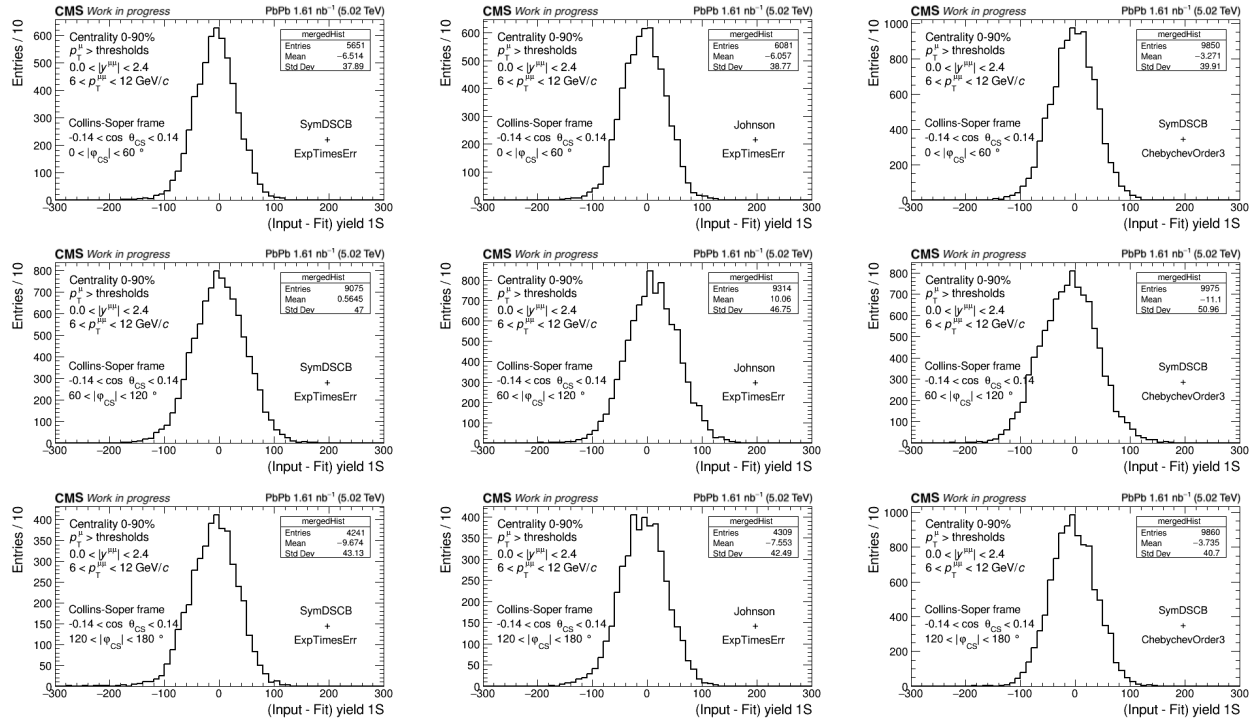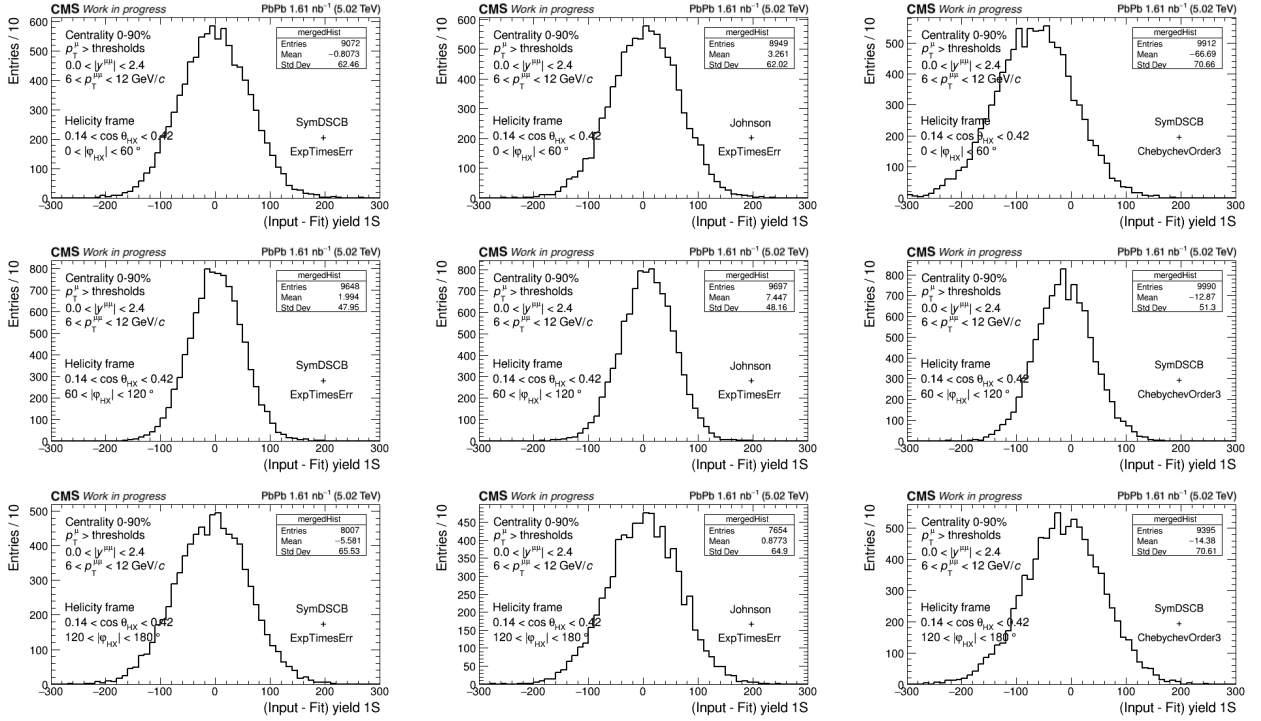
Figure G.22: Pseudo-experiment results using the nominal fit model (first column), an alternative signal model (second column), and an alternative background model (third column) for $6 < p_T < 12\,\mathrm{GeV}/c$, $0.14 < \cos\theta < 0.42$ in the HX frame.
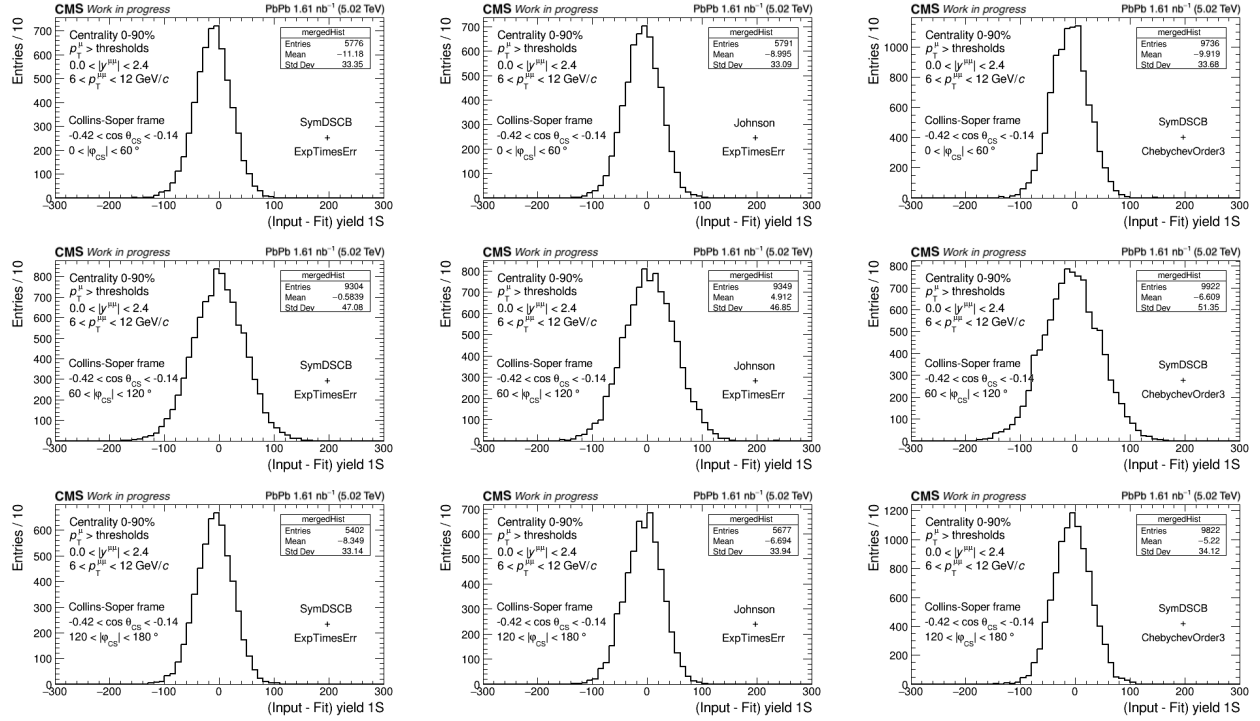
181
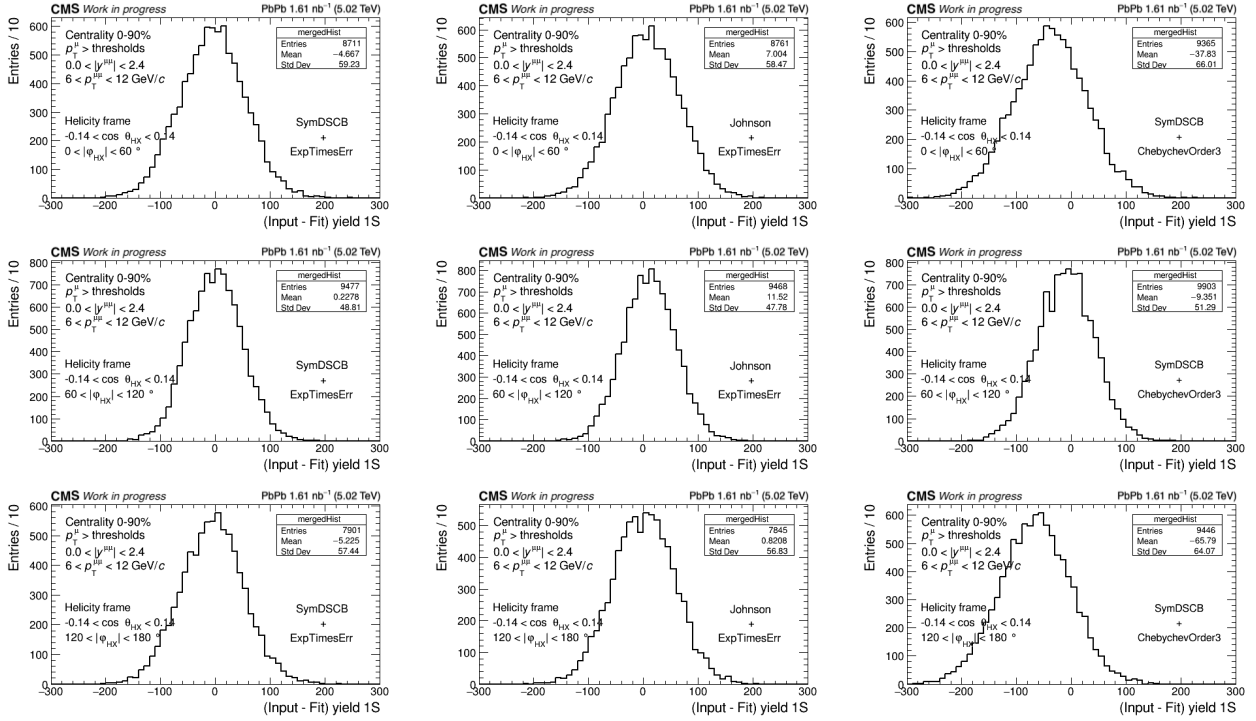
Figure G.23: Pseudo-experiment results using the nominal fit model (first column), an alternative signal model (second column), and an alternative background model (third column) for $6 < p_T < 12\,\mathrm{GeV}/c$, $-0.14 < \cos\theta < 0.14$ in the HX frame.
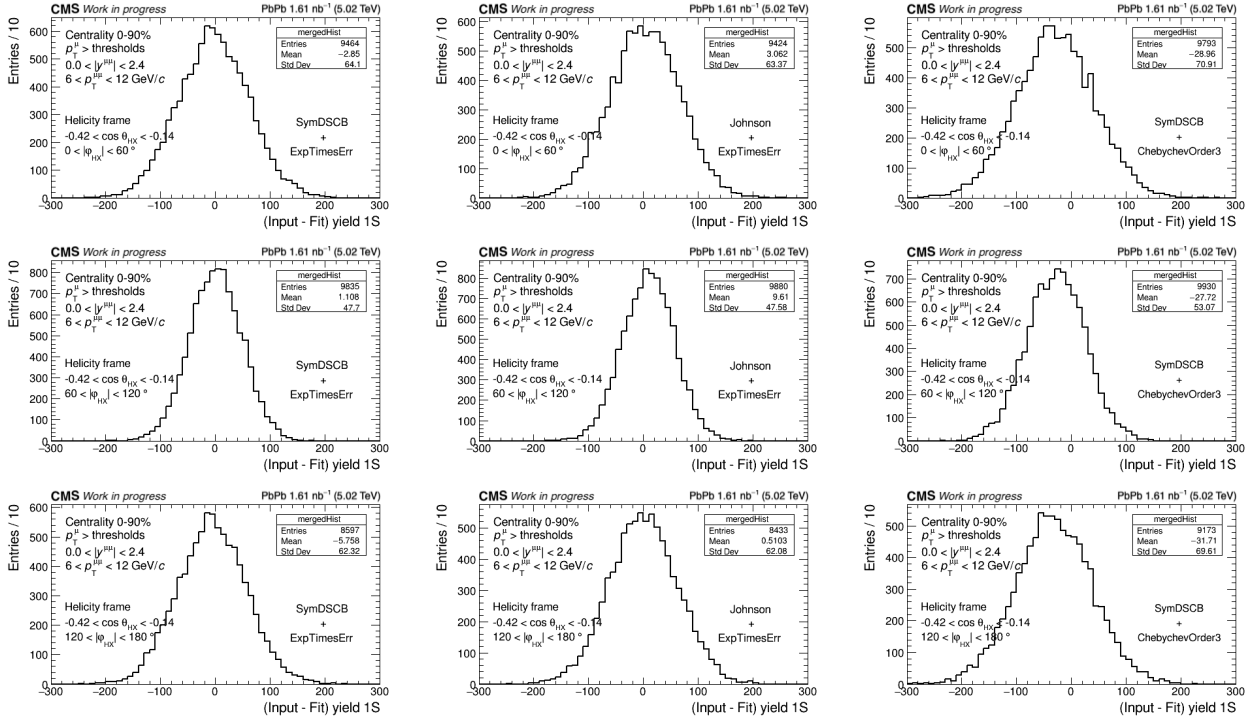
Figure G.24: Pseudo-experiment results using the nominal fit model (first column), an alternative signal model (second column), and an alternative background model (third column) for $6 < p_T < 12\,\text{GeV}/c$, $-0.42 < \cos\theta < -0.14$ in the HX frame.
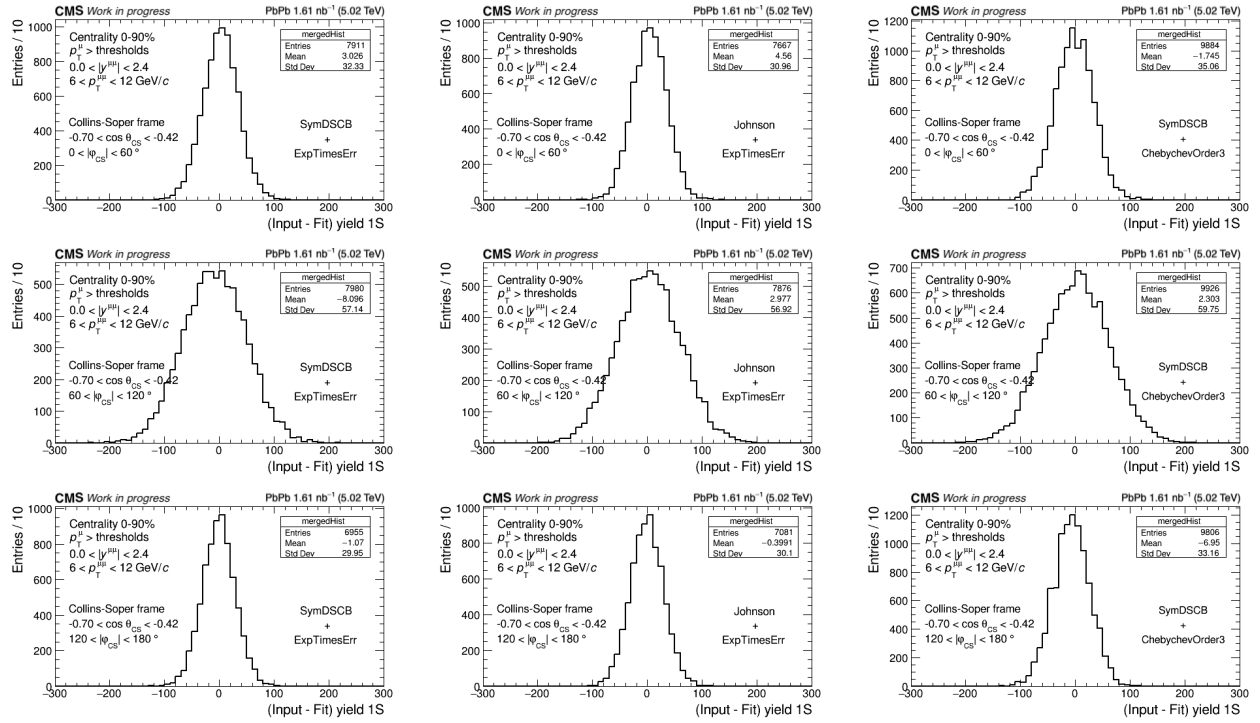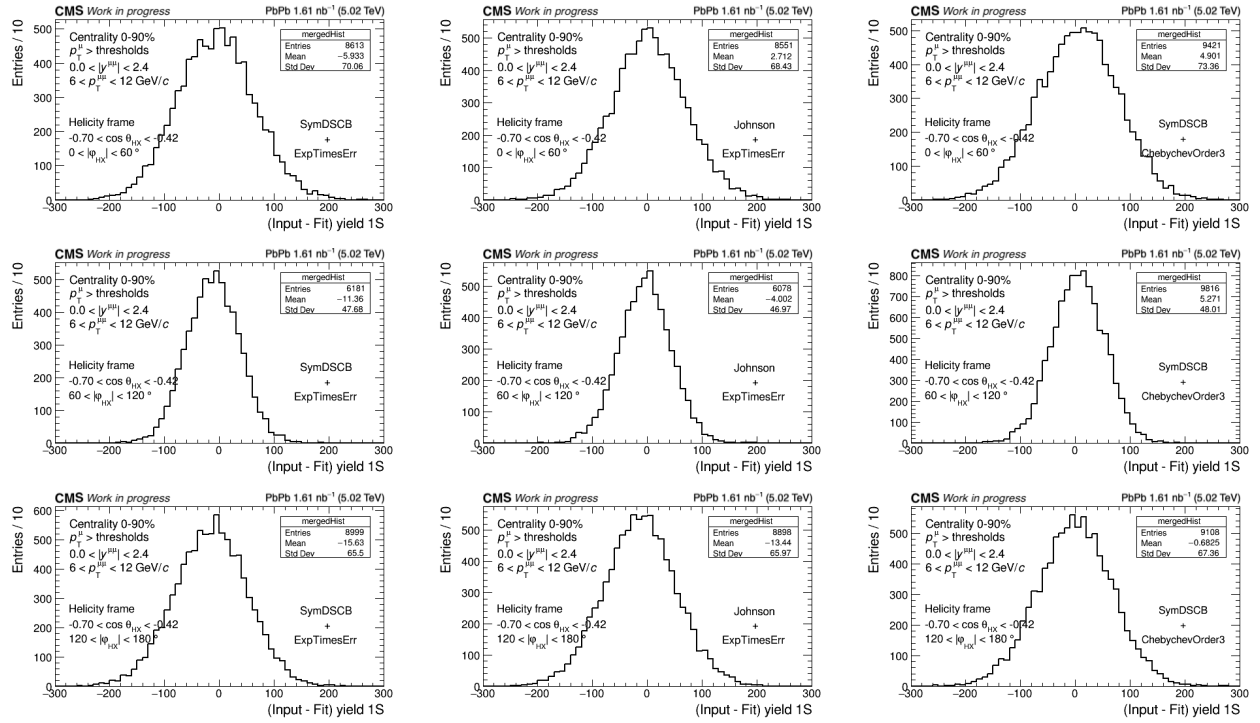
Figure G.25: Pseudo-experiment results using the nominal fit model (first column), an alternative signal model (second column), and an alternative background model (third column) for $6 < p_{\mathrm{T}} < 12 \, \mathrm{GeV}/c$, $-0.70 < \cos\theta < -0.42$ in the HX frame.
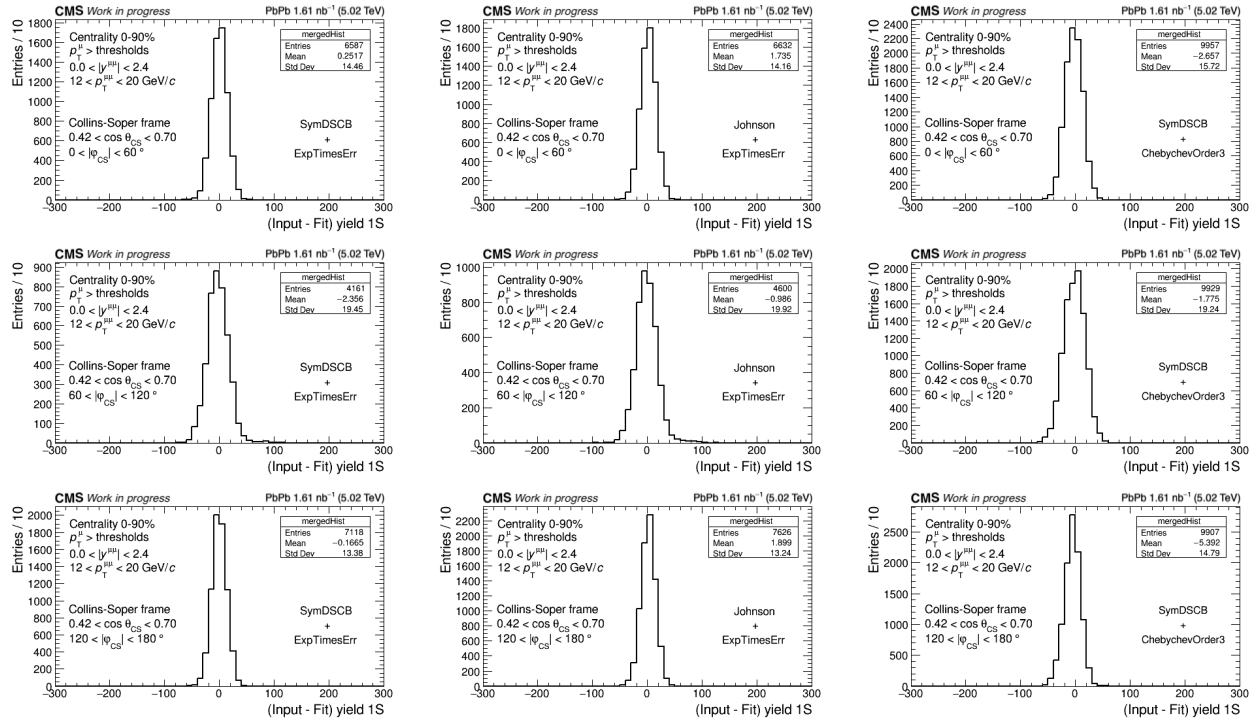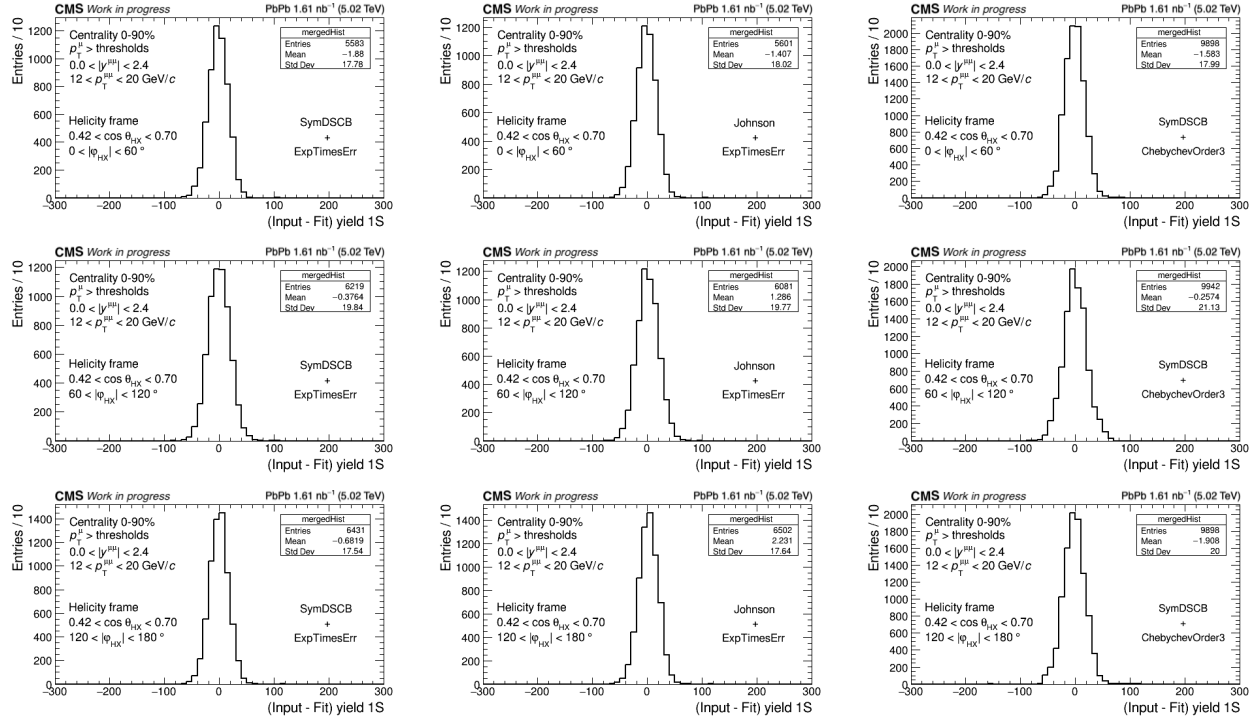
Figure G.26: Pseudo-experiment results using the nominal fit model (first column), an alternative signal model (second column), and an alternative background model (third column) for $12 < p_T < 20\,\mathrm{GeV}/c$, $0.42 < \cos\theta < 0.70$ in the HX frame.
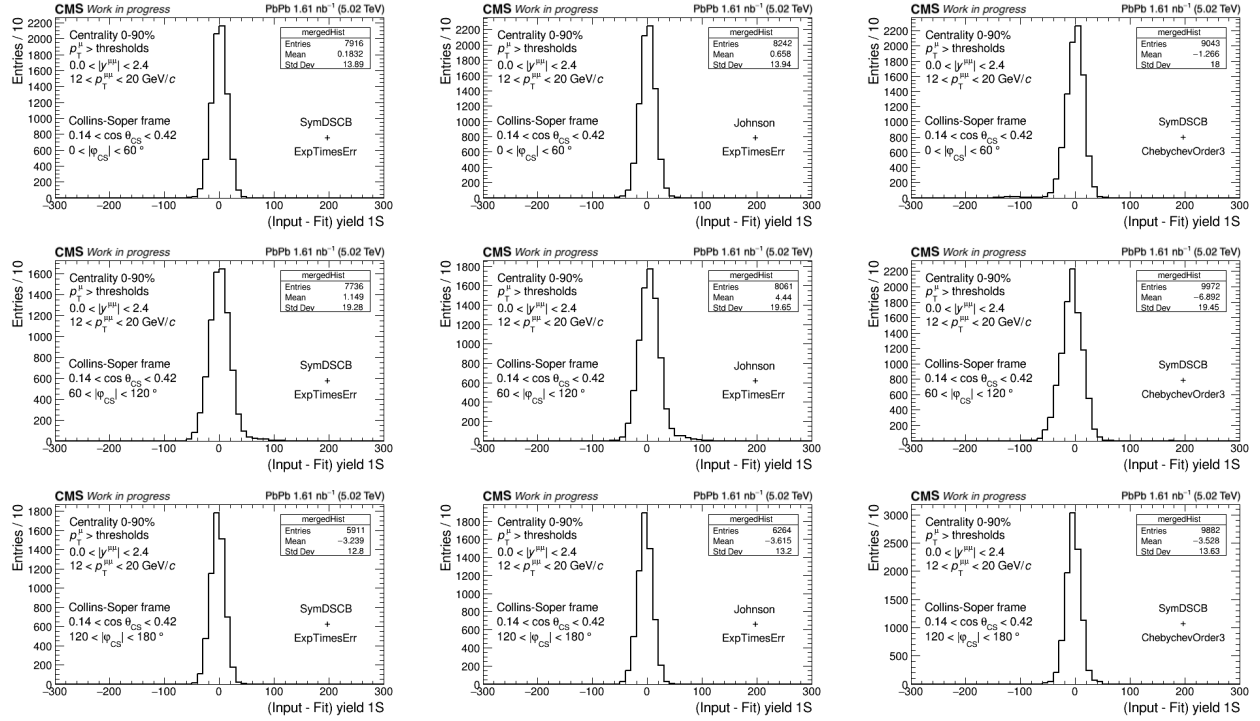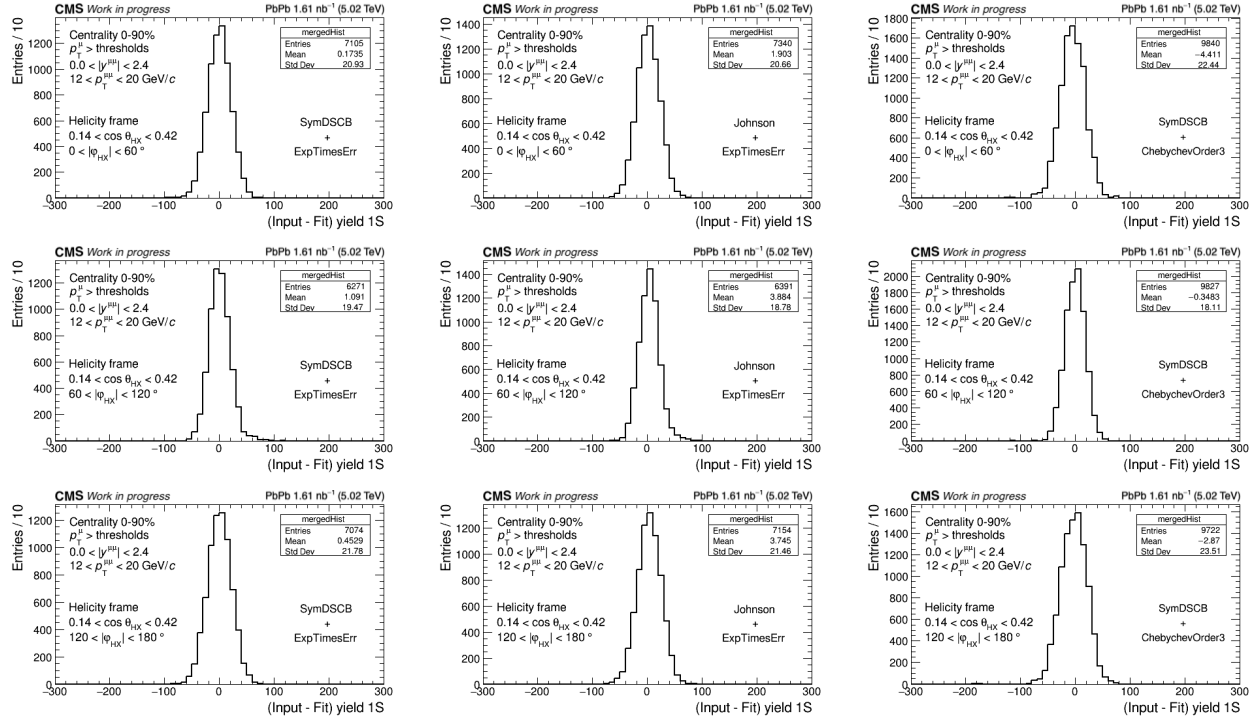
Figure G.27: Pseudo-experiment results using the nominal fit model (first column), an alternative signal model (second column), and an alternative background model (third column) for $12 < p_{\mathrm{T}} < 20\,\mathrm{GeV}/c$, $0.14 < \cos\theta < 0.42$ in the HX frame.
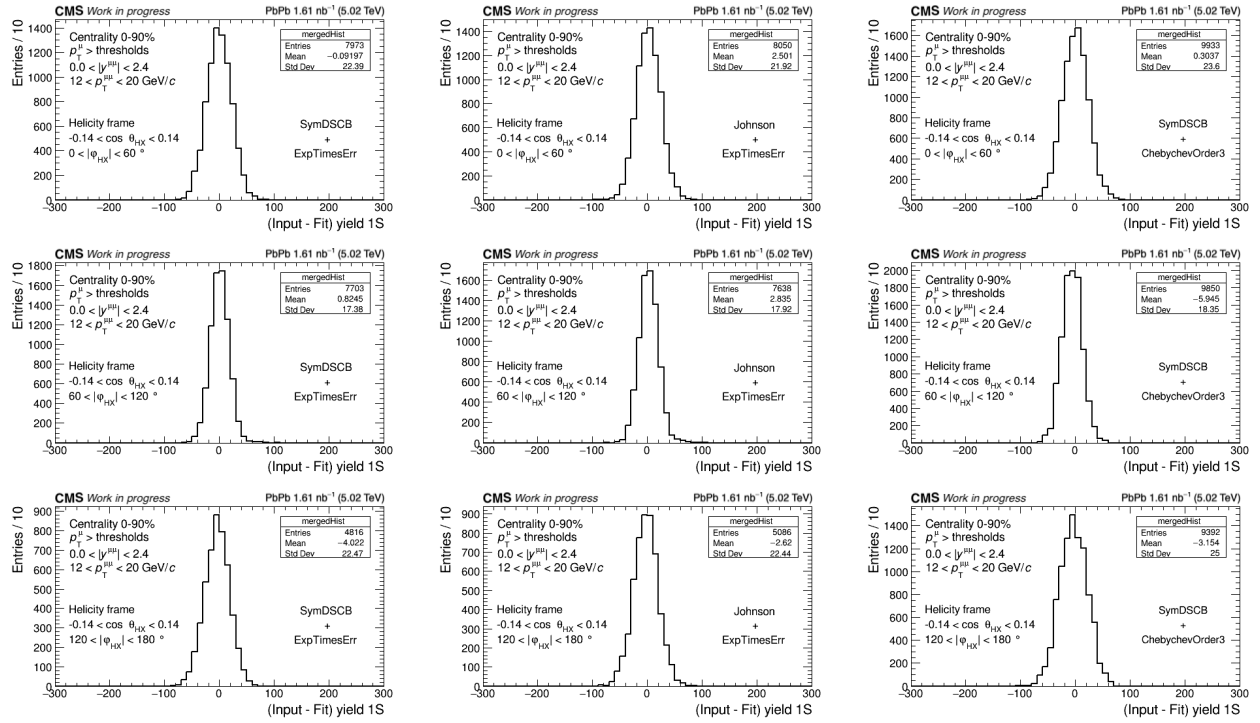
Figure G.28: Pseudo-experiment results using the nominal fit model (first column), an alternative signal model (second column), and an alternative background model (third column) for $12 < p_T < 20\,\mathrm{GeV}/c$, $-0.14 < \cos\theta < 0.14$ in the HX frame.
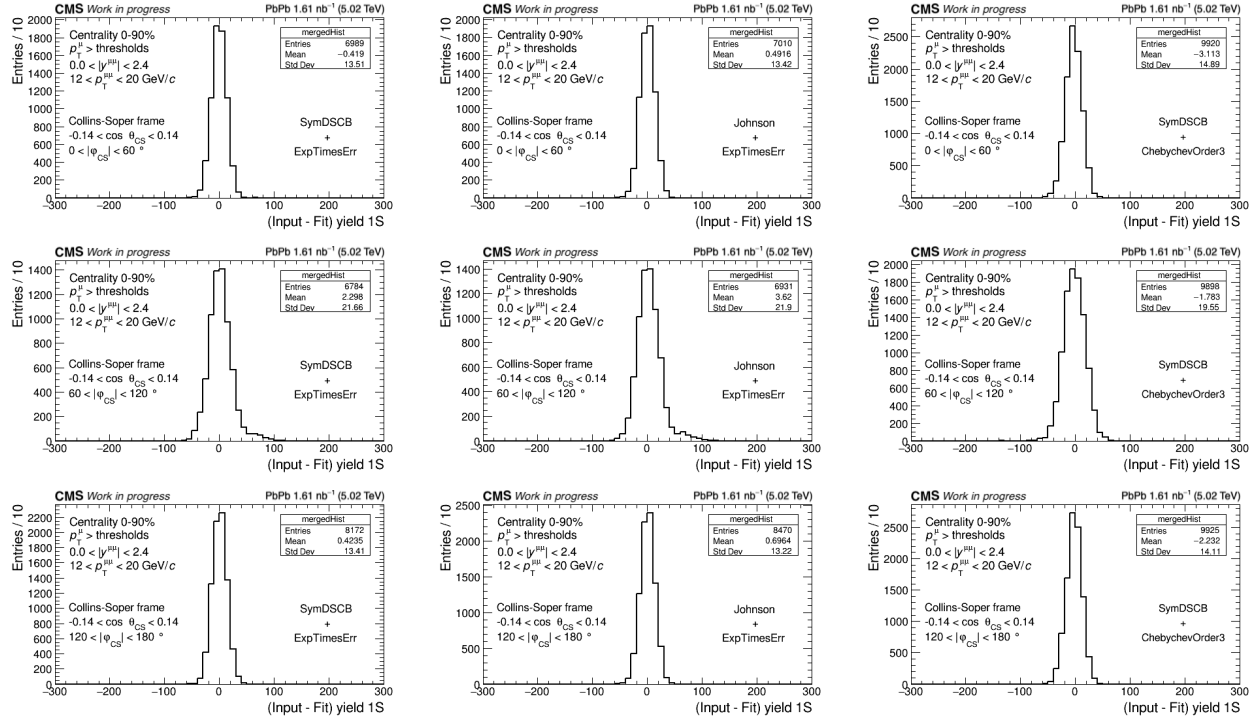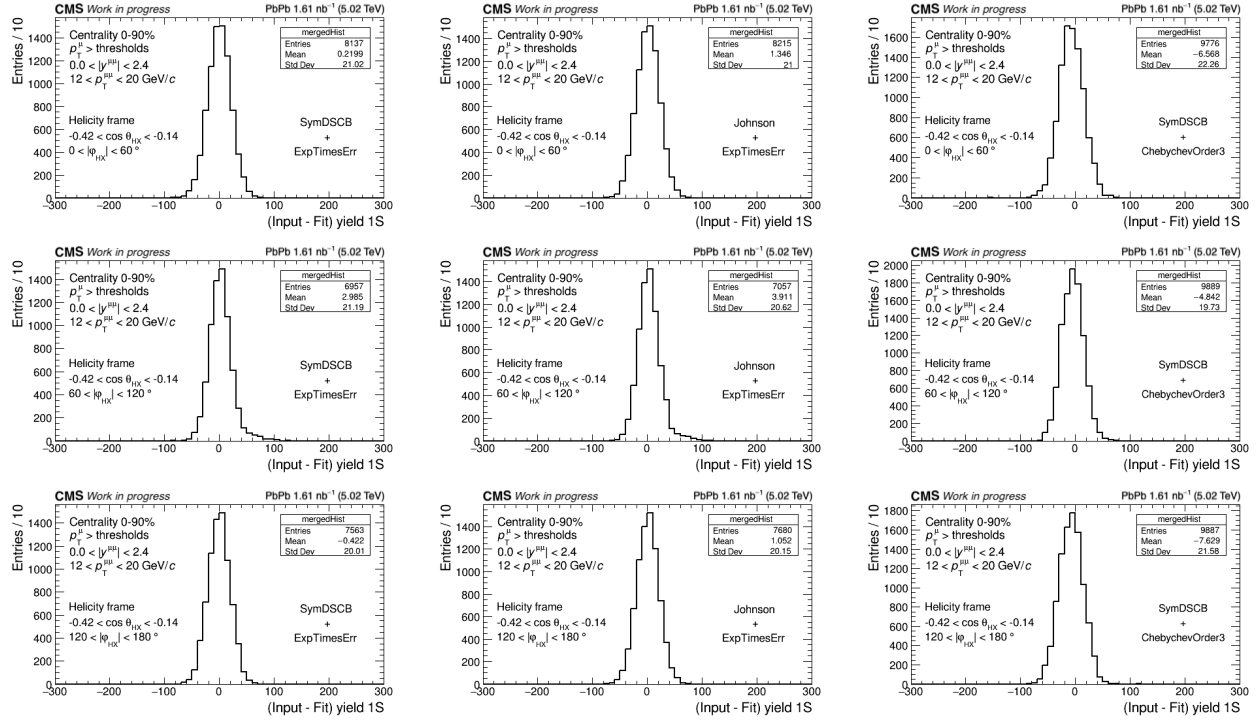
Figure G.29: Pseudo-experiment results using the nominal fit model (first column), an alternative signal model (second column), and an alternative background model (third column) for $12 < p_T < 20\,\mathrm{GeV}/c$, $-0.42 < \cos\theta < -0.14$ in the HX frame.
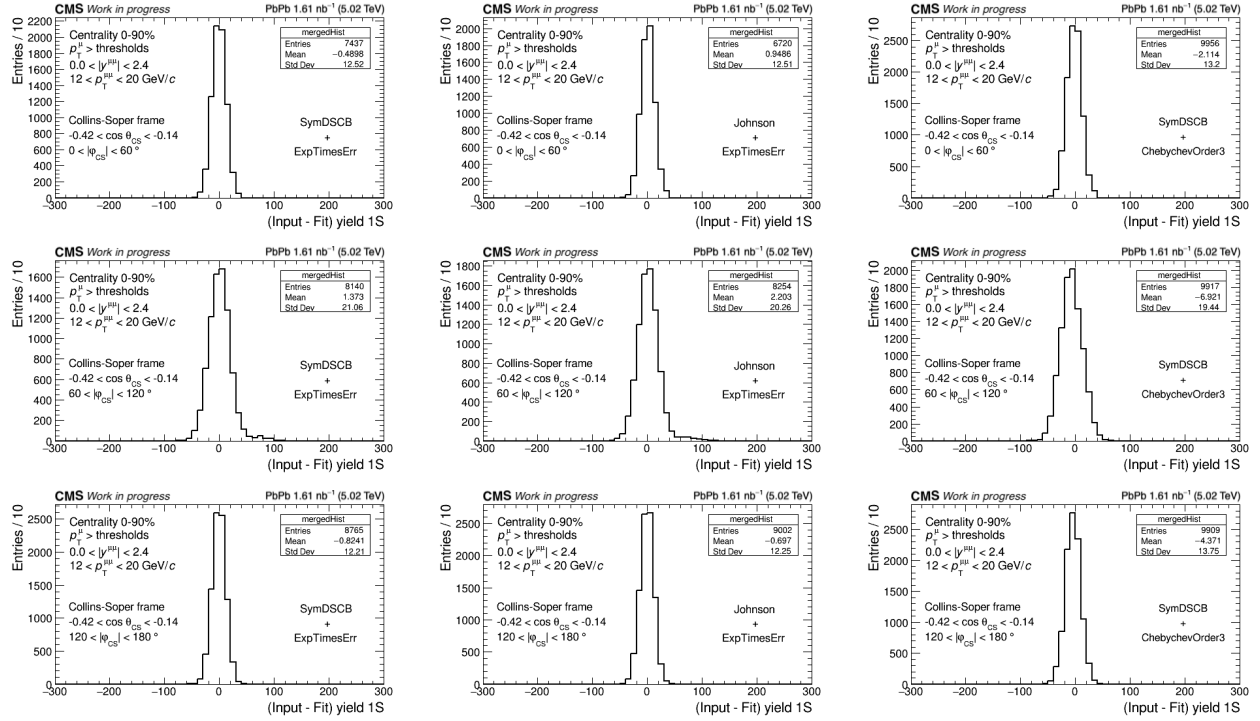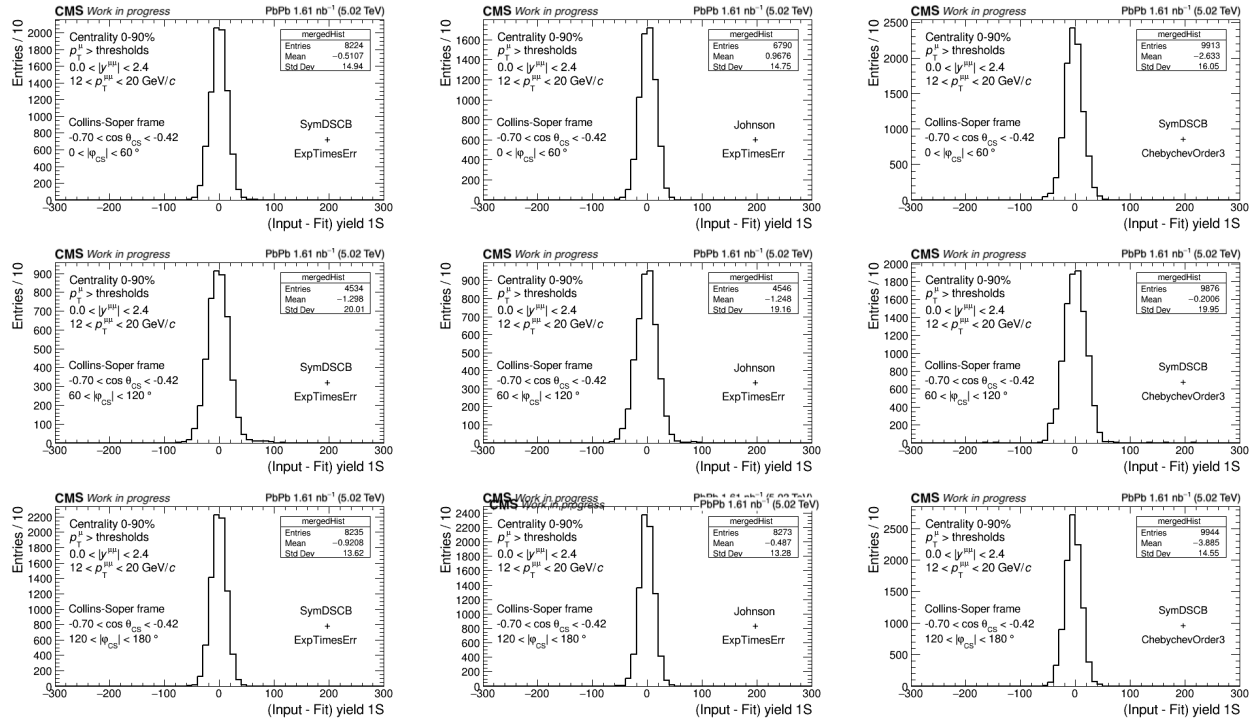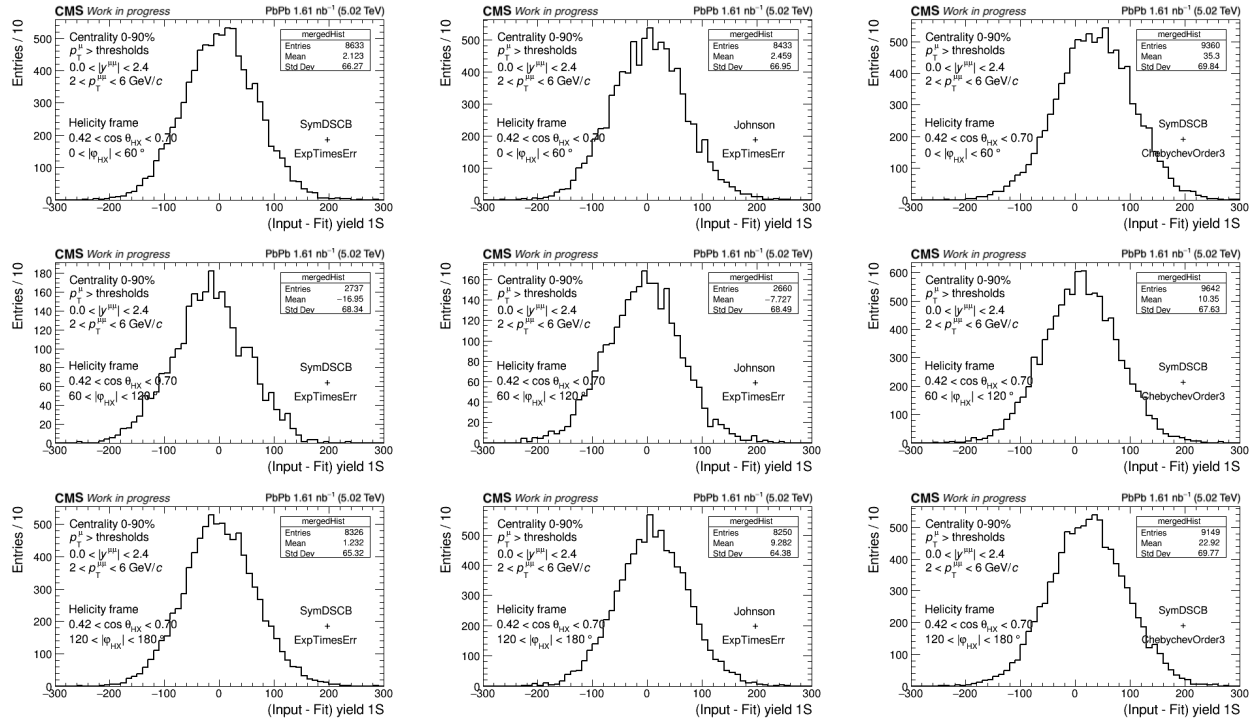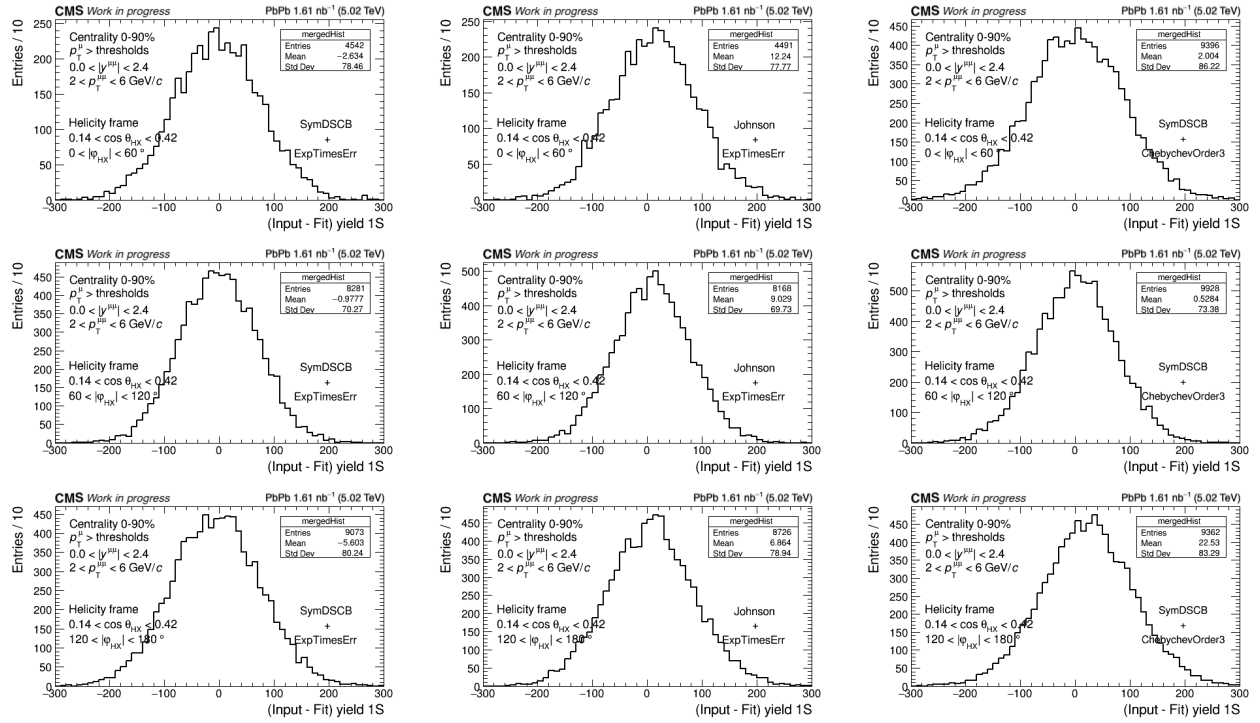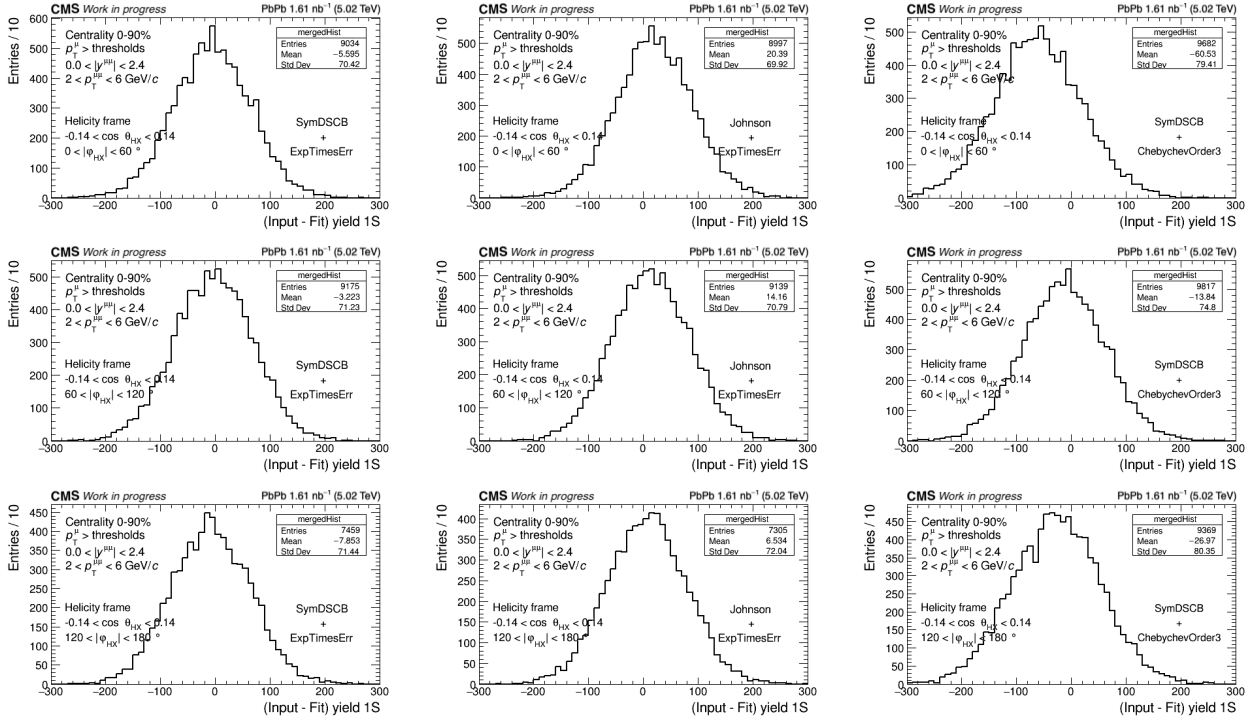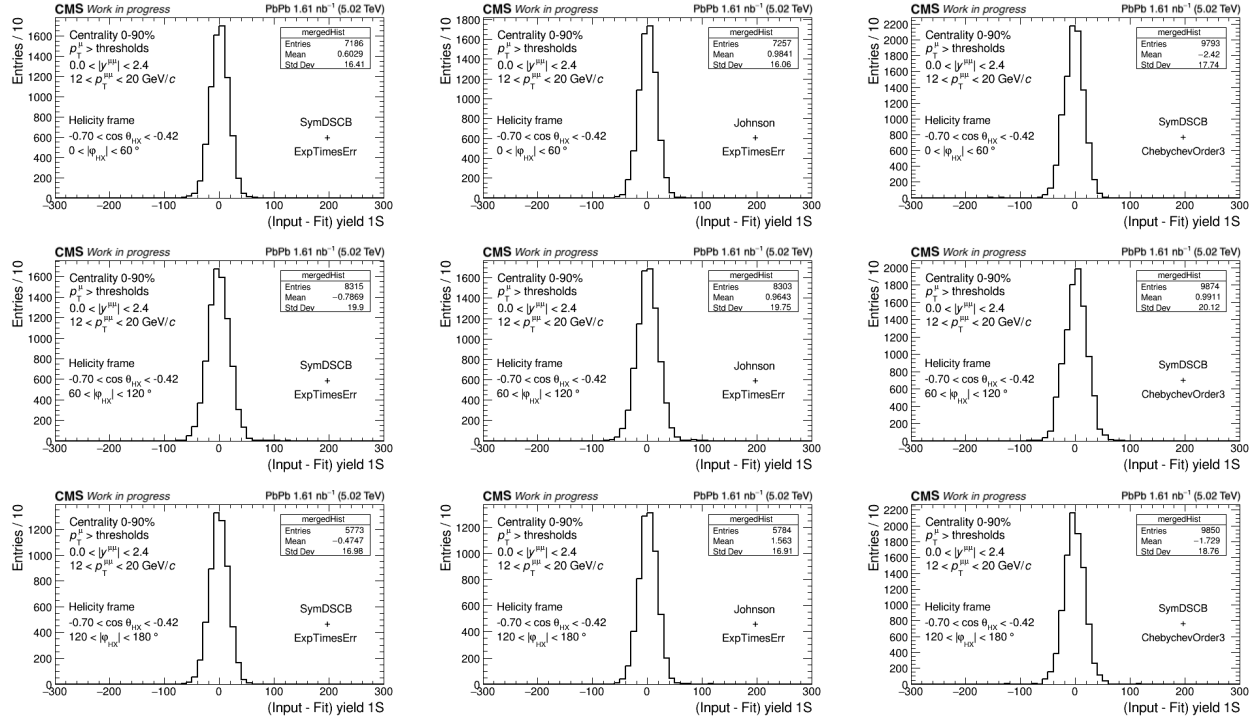
Figure G.30: Pseudo-experiment results using the nominal fit model (first column), an alternative signal model (second column), and an alternative background model (third column) for $12 < p_T < 20\,\mathrm{GeV}/c$, $-0.70 < \cos\theta < -0.42$ in the HX frame.

Bibliography

[1] E. V. Shuryak. "Quantum Chromodynamics and the Theory of Superdense Matter." In: *Phys. Rept.* 61 (1980), pp. 71–158. DOI: `10.1016/0370-1573(80)90105-2`.

[2] J. C. Collins and M. J. Perry. "Superdense Matter: Neutrons or Asymptotically Free Quarks?" In: *Phys. Rev. Lett.* 34 (1975), p. 1353. DOI: `10.1103/PhysRevLett.34.1353`.

[3] U. Heinz and R. Snellings. "Collective flow and viscosity in relativistic heavy-ion collisions." In: *Ann. Rev. Nucl. Part. Sci.* 63 (2013), pp. 123–151. DOI: `10.1146/annurev-nucl-102212-170540`.

[4] Alexei Bazavov. "The QCD equation of state." In: *Nuclear Physics A* 931 (2014). QUARK MATTER 2014, pp. 867–871. ISSN: 0375-9474. DOI: `10.1016/j.nuclphysa.2014.08.073`.

[5] S. Borsanyi et al. "Full result for the QCD equation of state with 2+1 flavors." In: *Phys. Lett. B* 730 (2014), pp. 99–104. DOI: `10.1016/j.physletb.2014.01.007`.

[6] Xiaojian Du, Mengge He, and Ralf Rapp. "Color screening and regeneration of bottomonia in high-energy heavy-ion collisions." In: *Phys. Rev. C* 96.5 (2017), p. 054901. DOI: `10.1103/PhysRevC.96.054901`. arXiv: `1706.08670`.

[7] Estia Eichten et al. "Quarkonia and their transitions." In: *Rev. Mod. Phys.* 80 (3 Sept. 2008), pp. 1161–1193. DOI: `10.1103/RevModPhys.80.1161`.

[8] A. Andronic et al. "Comparative study of quarkonium transport in hot QCD matter." In: *Eur. Phys. J. A* 60.4 (2024), p. 88. DOI: `10.1140/epja/s10050-024-01306-6`. arXiv: `2402.04366 [nucl-th]`.

[9] B. L. Ioffe and D. E. Kharzeev. "Quarkonium polarization in heavy ion collisions as a possible signature of the quark gluon plasma." In: *Phys. Rev. C* 68 (2003), p. 061902. DOI: `10.1103/PhysRevC.68.061902`. arXiv: `hep-ph/0306176`.

[10] Pietro Faccioli et al. "Towards the experimental clarification of quarkonium polarization." In: *Eur. Phys. J. C* 69.3 (2010), pp. 657–673. DOI: `10.1140/epjc/s10052-010-1420-5`.

[11] Wikipedia contributors. *Color charge — Wikipedia, The Free Encyclopedia*. [Online; accessed 2-September-2025]. 2025. URL: `https://en.wikipedia.org/w/index.php?title=Color_charge&oldid=1292167782`.

[12] D. J. Gross and F. Wilczek. "Ultraviolet Behavior of Non-Abelian Gauge Theories." In: *Phys. Rev. Lett.* 30 (1973), pp. 1343–1346. DOI: `10.1103/PhysRevLett.30.1343`.

[13] H. David Politzer. "Reliable Perturbative Results for Strong Interactions?" In: *Phys. Rev. Lett.* 30 (1973), pp. 1346–1349. DOI: `10.1103/PhysRevLett.30.1346`.

[14] Mark Thomson. *Modern Particle Physics*. Cambridge University Press, 2013. ISBN: 9781107034266. DOI: `10.1017/CBO9781139525367`.

[15] S. Bethke. "Determination of the QCD coupling α_s." In: *J. Phys. G* 26 (2000), R27. DOI: `10.1088/0954-3899/26/7/201`. arXiv: `hep-ex/0004021`.

[16] Rajesh Kumar et al. "Theoretical and experimental constraints for the equation of state of dense and hot matter." In: *Living Reviews in Relativity* 27.1 (2024), p. 3. ISSN: 1433-8351. DOI: `10.1007/s41114-024-00049-6`.

[17] Ramona Vogt. *Ultrarelativistic Heavy-Ion Collisions.* Elsevier, 2007. ISBN: 9780444521965. DOI: `10.1016/B978-0-444-52196-5.X5000-2`.

[18] P. Kovtun, D. T. Son, and A. O. Starinets. "Viscosity in Strongly Interacting Quantum Field Theories from Black Hole Physics." In: *Phys. Rev. Lett.* 94 (2005), p. 111601. DOI: `10.1103/PhysRevLett.94.111601`.

[19] ALICE Collaboration. "Elliptic flow of charged particles in Pb-Pb collisions at 2.76 TeV." In: *Phys. Rev. Lett.* 105 (2010), p. 252302. DOI: `10.1103/PhysRevLett.105.252302`.

[20] Md Hasanujjaman. "Effects of Critical Point on Quark Gluon Plasma." arXiv:2307.14601 [nucl-th]. PhD thesis. University of Calcutta, 2022. URL: `https://doi.org/10.48550/arXiv.2307.14601`.

[21] ALICE Collaboration. "Charged-Particle Multiplicity Density at Midrapidity in Central Pb-Pb Collisions at $\sqrt{s_{NN}} = 2.76$ TeV." In: *Phys. Rev. Lett.* 105 (2010), p. 252301. DOI: `10.1103/PhysRevLett.105.252301`.

[22] L. Evans and P. Bryant. "LHC Machine." In: *JINST* 3 (2008), S08001. DOI: `10.1088/1748-0221/3/08/S08001`.

[23] O. Bruning, H. Burkhardt, and S. Myers. "The Large Hadron Collider." In: *Prog. Part. Nucl. Phys.* 67 (2012), pp. 705–734. DOI: `10.1016/j.ppnp.2012.03.001`.

[24] T. Matsui and H. Satz. "J/ψ Suppression by Quark-Gluon Plasma Formation." In: *Phys. Lett. B* 178 (1986), pp. 416–422. DOI: `10.1016/0370-2693(86)91404-8`.

[25] J.F. Gunion and R. Vogt. "Determining the existence and nature of the quark-gluon plasma by Upsilon suppression at the LHC." In: *Nucl. Phys. B* 492.1 (1997), pp. 301–337. ISSN: 0550-3213. DOI: `10.1016/S0550-3213(97)80037-5`.

[26] R. Vogt. "Shadowing effects on J/ψ and Υ production at energies available at the CERN Large Hadron Collider." In: *Phys. Rev. C* 92 (2015), p. 034909. DOI: `10.1103/PhysRevC.92.034909`.

[27] CMS Collaboration. "Observation of Sequential Upsilon Suppression in PbPb Collisions." In: *Phys. Rev. Lett.* 109 (2012). [Erratum: Phys.Rev.Lett. 120, 199903 (2018)], p. 222301. DOI: `10.1103/PhysRevLett.109.222301`. arXiv: `1208.2826 [nucl-ex]`.

[28] CMS Collaboration. "Suppression of $\Upsilon(1S), \Upsilon(2S)$ and $\Upsilon(3S)$ production in PbPb collisions at $\sqrt{s_{NN}} = 2.76$ TeV." In: *Phys. Lett. B* 770 (2017), pp. 357–379. DOI: `10.1016/j.physletb.2017.04.031`. arXiv: `1611.01510 [nucl-ex]`.

[29] ALICE Collaboration. "Suppression of $\Upsilon(1S)$ at forward rapidity in Pb–Pb collisions at $\sqrt{s_{NN}} = 2.76$ TeV." In: *Phys. Lett. B* 738 (2014), pp. 361–372. DOI: `10.1016/j.physletb.2014.10.028`. arXiv: `1405.4493 [nucl-ex]`.

[30] M. Aaboud et al. "Measurement of $\Upsilon(nS)$ production in Pb+Pb and *pp* collisions at $\sqrt{s_{NN}} = 5.02$ TeV with the ATLAS detector." In: *Phys. Lett. B* 790 (2019), pp. 595–614. DOI: `10.1016/j.physletb.2019.01.024`. arXiv: `1812.11317 [nucl-ex]`.

[31] CMS Collaboration. "Measurement of the azimuthal anisotropy of $\Upsilon(1S)$ and $\Upsilon(2S)$ mesons in PbPb collisions at $\sqrt{s_{NN}} = 5.02$ TeV." In: *Phys. Lett. B* 819 (2021), p. 136385. DOI: `10.1016/j.physletb.2021.136385`. arXiv: `2006.07707 [hep-ex]`.

[32] CMS Collaboration. "Observation of the $\Upsilon(3S)$ Meson and Suppression of Υ States in PbPb Collisions at $\sqrt{s_{NN}} = 5.02$ TeV." In: *Phys. Rev. Lett.* 133.2 (2024), p. 022302. DOI: `10.1103/PhysRevLett.133.022302`. arXiv: `2303.17026 [hep-ex]`.

[33] S. Navas et al. "Review of particle physics." In: *Phys. Rev. D* 110.3 (2024), p. 030001. DOI: `10.1103/PhysRevD.110.030001`.

[34] Geoffrey T. Bodwin, Eric Braaten, and G. Peter Lepage. "Rigorous QCD analysis of inclusive annihilation and production of heavy quarkonium." In: *Phys. Rev. D* 51 (1995). [Erratum: Phys.Rev.D 55, 5853 (1997)], pp. 1125–1171. DOI: `10.1103/PhysRevD.55.5853`. arXiv: `hep-ph/9407339`.

[35] M. B. Einhorn and S. D. Ellis. "Hadronic Production of the New Resonances: Probing Gluon Distributions." In: *Phys. Rev. D* 12 (1975), p. 2007. DOI: `10.1103/PhysRevD.12.2007`.

[36] M. Gluck, J. F. Owens, and E. Reya. "Gluon Contribution to Hadronic J/psi Production." In: *Phys. Rev. D* 17 (1978), p. 2324. DOI: `10.1103/PhysRevD.17.2324`.

[37] Vincent Cheung and Ramona Vogt. "Polarization of prompt J/ψ and $\Upsilon(1S)$ production in the color evaporation model." In: *Phys. Rev. D* 96.5 (2017), p. 054014. DOI: `10.1103/PhysRevD.96.054014`. arXiv: `1706.07686 [hep-ph]`.

[38] S. P. Baranov and A. V. Lipatov. "Prompt charmonia production and polarization at LHC in the NRQCD with k_T-factorization. Part III: J/ψ meson." In: *Phys. Rev. D* 96.3 (2017), p. 034019. DOI: `10.1103/PhysRevD.96.034019`. arXiv: `1611.10141 [hep-ph]`.

[39] Vincent Cheung and Ramona Vogt. "Production and polarization of prompt $\Upsilon(n\mathrm{S})$ in the improved color evaporation model using the k_T-factorization approach." In: *Phys. Rev. D* 99.3 (2019), p. 034007. DOI: `10.1103/PhysRevD.99.034007`. arXiv: `1811.11570 [hep-ph]`.

[40] Eric Braaten, Bernd A. Kniehl, and Jungil Lee. "Polarization of prompt J/ψ at the Tevatron." In: *Phys. Rev. D* 62 (2000), p. 094005. DOI: `10.1103/PhysRevD.62.094005`. arXiv: `hep-ph/9911436`.

[41] T. Affolder et al. "Measurement of J/ψ and $\psi(2S)$ Polarization in $p\bar{p}$ Collisions at $\sqrt{s} = 1.8$ TeV." In: *Phys. Rev. Lett.* 85 (2000), pp. 2886–2891. DOI: `10.1103/PhysRevLett.85.2886`. arXiv: `hep-ex/0004027`.

[42] A. Abulencia et al. "Polarization of J/ψ and ψ_{2S} Mesons Produced in $p\bar{p}$ Collisions at $\sqrt{s} = 1.96$-TeV." In: *Phys. Rev. Lett.* 99 (2007), p. 132001. DOI: `10.1103/PhysRevLett.99.132001`. arXiv: `0704.0638 [hep-ex]`.

[43] CMS Collaboration. "Measurement of the Prompt J/ψ and $\psi(2S)$ Polarizations in pp Collisions at $\sqrt{s} = 7$ TeV." In: *Phys. Lett. B* 727 (2013), pp. 381–402. DOI: `10.1016/j.physletb.2013.10.055`. arXiv: `1307.6070 [hep-ex]`.

[44] CMS Collaboration. "Measurement of the $Y(1S), Y(2S)$ and $Y(3S)$ Polarizations in pp Collisions at $\sqrt{s} = 7$ TeV." In: *Phys. Rev. Lett.* 110.8 (2013), p. 081802. DOI: `10.1103/PhysRevLett.110.081802`. arXiv: `1209.2922 [hep-ex]`.

[45] R Aaij et al. "Measurement of J/ψ polarization in pp collisions at $\sqrt{s} = 7$ TeV." In: *Eur. Phys. J. C* 73.11 (2013), p. 2631. DOI: `10.1140/epjc/s10052-013-2631-3`. arXiv: `1307.6379 [hep-ex]`.

[46] Roel Aaij et al. "Measurement of the Υ polarizations in pp collisions at $\sqrt{s} = 7$ and 8 TeV." In: *JHEP* 12 (2017), p. 110. DOI: `10.1007/JHEP12(2017)110`. arXiv: `1709.01301 [hep-ex]`.

[47] ALICE Collaboration. "Measurement of the inclusive J/ ψ polarization at forward rapidity in pp collisions at $\sqrt{\mathbf{s}} = \mathbf{8}$ TeV." In: *Eur. Phys. J. C* 78.7 (2018), p. 562. DOI: `10.1140/epjc/s10052-018-6027-2`. arXiv: `1805.04374 [hep-ex]`.

[48] Mathias Butenschoen and Bernd A. Kniehl. "Reconciling J/ψ production at HERA, RHIC, Tevatron, and LHC with NRQCD factorization at next-to-leading order." In:

Phys. Rev. Lett. 106 (2011), p. 022003. DOI: `10.1103/PhysRevLett.106.022003`. arXiv: `1009.5662 [hep-ph]`.

[49]   Yan-Qing Ma, Kai Wang, and Kuang-Ta Chao. "A complete NLO calculation of the J/ψ and ψ' production at hadron colliders." In: *Phys. Rev. D* 84 (2011), p. 114001. DOI: `10.1103/PhysRevD.84.114001`. arXiv: `1012.1030 [hep-ph]`.

[50]   Mathias Butenschoen and Bernd A. Kniehl. "J/psi polarization at Tevatron and LHC: Nonrelativistic-QCD factorization at the crossroads." In: *Phys. Rev. Lett.* 108 (2012), p. 172002. DOI: `10.1103/PhysRevLett.108.172002`. arXiv: `1201.1872 [hep-ph]`.

[51]   Kuang-Ta Chao et al. "J/ψ Polarization at Hadron Colliders in Nonrelativistic QCD." In: *Phys. Rev. Lett.* 108 (2012), p. 242004. DOI: `10.1103/PhysRevLett.108.242004`. arXiv: `1201.2675 [hep-ph]`.

[52]   Yu Feng et al. "Complete study on polarization of $\Upsilon(nS)$ hadroproduction at QCD next-to-leading order." In: *Chin. Phys. C* 45.1 (2021), p. 013117. DOI: `10.1088/1674-1137/abc682`. arXiv: `2009.03028 [hep-ph]`.

[53]   N. A. Abdulov and A. V. Lipatov. "Bottomonium production and polarization in the NRQCD with k_T-factorization. III: $\Upsilon(1S)$ and $\chi_b(1P)$ mesons." In: *Eur. Phys. J. C* 81.12 (2021), p. 1085. DOI: `10.1140/epjc/s10052-021-09880-5`. arXiv: `2011.13401 [hep-ph]`.

[54]   Hao Han et al. "$\Upsilon(nS)$ and $\chi_b(nP)$ production at hadron colliders in nonrelativistic QCD." In: *Phys. Rev. D* 94.1 (2016), p. 014028. DOI: `10.1103/PhysRevD.94.014028`. arXiv: `1410.8537 [hep-ph]`.

[55]   ALICE Collaboration. "First measurement of quarkonium polarization in nuclear collisions at the LHC." In: *Phys. Lett. B* 815 (2021), p. 136146. DOI: `10.1016/j.physletb.2021.136146`. arXiv: `2005.11128 [nucl-ex]`.

[56] Pietro Faccioli and Carlos Lourenço. *Particle Polarization in High Energy Physics: An Introduction and Case Studies on Vector Particle Production at the LHC*. Springer, Dec. 2022. DOI: 10.1007/978-3-031-08876-6.

[57] CERN Service graphique. *Overall view of the LHC*. 2014. URL: https://cds.cern.ch/record/1708849?ln=en.

[58] Oliver S. Brüning et al., eds. *LHC Design Report*. CERN, 2004. ISBN: 9789290832249. URL: https://cds.cern.ch/record/782076?ln=en.

[59] Maximilien Brice. *Cross section of an LHC dipole in the tunnel*. 2011. URL: https://cds.cern.ch/record/1365795.

[60] AC Team. *Diagram of an LHC dipole magnet*. 1999. URL: https://cds.cern.ch/record/40524.

[61] S. Claudet et al. "Cryogenic and Vacuum Systems for the LHC." In: *Proceedings of the 19th International Cryogenic Engineering Conference*. 2002. URL: https://cds.cern.ch/record/473367.

[62] Lyndon Evans. *The Large Hadron Collider: A Marvel of Technology*. Geneva: CERN, 2009.

[63] L. Rossi. "Superconducting Magnets for the LHC." In: *Proceedings of the Particle Accelerator Conference*. 2003. URL: https://cds.cern.ch/record/621120.

[64] ALICE Collaboration. *ALICE Technical Design Report*. 2004. URL: https://cds.cern.ch/record/628137.

[65] CMS Collaboration. "The CMS experiment at the CERN LHC." In: *JINST* 3 (2008), S08004. DOI: 10.1088/1748-0221/3/08/S08004.

[66] CERN. *LHC Long-Term Schedule*. Accessed: 2025-08-23. 2024. URL: https://lhc-commissioning.web.cern.ch/schedule/LHC-long-term.htm.

[67] Jean-Luc Caron. *LHC layout. Schema general du LHC.* AC Collection. Legacy of AC. Pictures from 1992 to 2002. 1997. URL: `https://cds.cern.ch/record/841573`.

[68] Ewa Lopienska. *The CERN accelerator complex, layout in 2022.* 2022. URL: `https://cds.cern.ch/record/2800984`.

[69] M. Benedikt et al. "The CERN Accelerator Complex." In: *CERN Brochure.* 2018. URL: `https://cds.cern.ch/record/2628845`.

[70] Joram Berger. "Search for the Higgs Boson Produced via Vector-Boson Fusion in the Decay Channel H $\to \tau\tau$." Ph.D. thesis. Karlsruhe Institute of Technology, 2014. URL: `https://inspirehep.net/literature/1775935`.

[71] Hoch, Michael and Brice, Maximilien (for the CMS Collaboration). *A full-scale cross section photograph of the CMS detector at CERN.* Photograph (CMS Photos Collection), CERN Document Server, record 1474902. Licensed under CC-BY-4.0. Aug. 2008. URL: `https://cds.cern.ch/record/1474902`.

[72] Dominik Wilhelm Haitz. "Precision Studies of Proton Structure and Jet Energy Scale with the CMS Detector at the LHC." PhD thesis. KIT, Karlsruhe, 2016. DOI: `10.5445/IR/1000055680`.

[73] CMS Collaboration. "Commissioning and performance of the CMS silicon strip tracker with cosmic ray muons." In: *JINST* 5.03 (2010), T03008. DOI: `10.1088/1748-0221/5/03/T03008`.

[74] Julien Marius Ordan and Maximilien Brice. *CMS tracker.* General Photo. 2021. URL: `https://cds.cern.ch/record/2778000`.

[75] CMS Collaboration. *The CMS tracker system project: Technical Design Report.* Tech. rep. CERN, 1998. URL: `https://cds.cern.ch/record/368412`.

[76] CMS Collaboration. *CMS Technical Design Report for the Pixel Detector Upgrade.* Tech. rep. CERN-LHCC-2012-016, CMS-TDR-11. CERN, 2012. URL: `https://cds.cern.ch/record/1481838`.

[77] CMS Collaboration. *Tracking — Identifying tracks (CMS Detector Intro).* Accessed: 2025-08-25. URL: `https://cms.cern/detector/identifying-tracks`.

[78] CMS Collaboration. "Performance and Operation of the CMS Electromagnetic Calorimeter." In: *JINST* 5 (2010), T03010. DOI: `10.1088/1748-0221/5/03/T03010`.

[79] CMS Collaboration. *CMS Physics: Technical Design Report Volume 1: Detector Performance and Software.* Tech. rep. CERN-LHCC-2006-001, CMS-TDR-8-1. Figures available as CMS-PHO-GEN-2006-001. Geneva: CERN, 2006. DOI: `10.2172/878629`.

[80] CMS Collaboration. *CMS, The Electromagnetic Calorimeter: Technical Design Report.* Tech. rep. CERN-LHCC-97-033. CERN, 1997. URL: `https://cds.cern.ch/record/349375`.

[81] A. Ghezzi et al. "CMS barrel electromagnetic calorimeter: performance of the avalanche photodiode readout." In: *Nucl. Instrum. Meth. A* 518 (2004), pp. 607–609. DOI: `10.1016/j.nima.2003.11.213`.

[82] S. K. Dasu et al. "Performance of vacuum phototriodes for the CMS electromagnetic calorimeter endcaps." In: *Nucl. Instrum. Meth. A* 518 (2004), pp. 607–609. DOI: `10.1016/j.nima.2003.11.212`.

[83] Maximilien Brice / CERN. *Installation of an ECAL Barrel supermodule inside CMS.* Accessed: 2025-08-25. URL: `https://cds.cern.ch/record/1431477`.

[84] CMS Collaboration. *Schematic layout of the HCAL detectors (side-view).* Accessed: 2025-08-25. URL: `https://cms-opendata-workshop.github.io/workshop2023-lesson-cms-detector/04-hcal/index.html`.

[85] CMS Collaboration. *The CMS hadron calorimeter project: Technical Design Report.* Tech. rep. CERN, 1997. URL: https://cds.cern.ch/record/357153.

[86] CMS Collaboration. *The CMS magnet project: Technical Design Report.* Tech. rep. CERN-LHCC-97-010, CMS-TDR-1. CERN, 1997. URL: https://cds.cern.ch/record/331056.

[87] CMS Collaboration. "Performance of the CMS muon detector and muon reconstruction with proton-proton collisions at $\sqrt{s} = 13$ TeV." In: *JINST* 13 (2018), P06015. DOI: 10.1088/1748-0221/13/06/P06015. arXiv: 1804.04528 [physics.ins-det].

[88] CMS Collaboration. "Performance of the CMS Drift-Tube Chamber Local Trigger with Cosmic Rays." In: *JINST* 5 (2010), T03017. DOI: 10.1088/1748-0221/5/03/T03017.

[89] CMS Collaboration. "Performance of the CMS muon trigger system in proton-proton collisions at $\sqrt{s} = 13$ TeV." In: *JINST* 16 (2021), P07019. DOI: 10.1088/1748-0221/16/07/P07019.

[90] CMS Collaboration. "Performance of the CMS Cathode Strip Chambers with Cosmic Rays." In: *JINST* 5 (2010), T03018. DOI: 10.1088/1748-0221/5/03/T03018.

[91] CMS Collaboration. *CMS Technical Design Report for the Muon Endcap GEM Upgrade.* Tech. rep. CERN, 2015. URL: https://cds.cern.ch/record/2021453.

[92] CMS Collaboration. "First results from the GEM detectors installed in CMS during the 2021 LHC run." In: *JINST* 17 (2022), P03020. DOI: 10.1088/1748-0221/17/03/P03020.

[93] Benjamin Radburn-Smith. *L1T Tutorial Introduction.* CMS L1 Trigger Tutorial, Indico. Presented at the CMS L1 Trigger Tutorial, 23 July 2021. 2021. URL: https:

//indico.cern.ch/event/1060362/contributions/4455919/attachments/
2286720/3886663/L1TutorialIntro_BRS_20210723_v1.pdf.

[94]   Joschka Phillip Lingemann. "Upgrade of the global muon trigger at the CMS exper-
       iment." PhD thesis. RWTH Aachen University, 2016. URL: https://publications.
       rwth-aachen.de/record/670489.

[95]   CMS Collaboration. *WorkBook: High-Level Trigger Tutorial.* Accessed: 2025-08-30.
       2025. URL: https://twiki.cern.ch/twiki/bin/view/CMSPublic/WorkBookHLTTu
       torial.

[96]   CMS Collaboration. "Performance of CMS muon reconstruction from proton-proton
       to heavy ion collisions." In: *JINST* 19.09 (2024), P09012. DOI: 10.1088/1748-0221/
       19/09/P09012. arXiv: 2404.17377 [hep-ex].

[97]   CMS Collaboration. *3.3.1 Data Formats and Data Tiers.* Accessed: 2025-07-31. URL:
       https://twiki.cern.ch/twiki/bin/view/CMSPublic/WorkBookDataFormats.

[98]   CMS Collaboration. *CMS OMS Run Summary for Runs 325530–327802.* Accessed
       on August 5, 2025. 2025. URL: https://cmsoms.cern.ch/cms/runs/summary?cms_
       run_to=327802&cms_run_from=325530&cms_run_sequence=GLOBAL-RUN.

[99]   Yongsun Kim et al. *Measurement of the anisotropic flow of upsilon mesons in PbPb
       collisions at 5.02 TeV.* CMS Analysis Note CMS-AN-2019/001. CMS internal docu-
       ment. Archive Hash: fa68620. CMS Collaboration, Oct. 2019.

[100] CMS Collaboration. "Description and performance of track and primary-vertex recon-
       struction with the CMS tracker." In: *JINST* 9 (2014), P10009. DOI: 10.1088/1748-
       0221/9/10/P10009. arXiv: 1405.6569 [physics.ins-det].

[101] CMS Collaboration. "Extraction and validation of a new set of CMS PYTHIA8 tunes from underlying-event measurements." In: *Eur. Phys. J. C* 80.1 (2020), p. 4. DOI: 10.1140/epjc/s10052-019-7499-4. arXiv: 1903.12179 [hep-ex].

[102] I. P. Lokhtin and A. M. Snigirev. "A Model of jet quenching in ultrarelativistic heavy ion collisions and high-p_T hadron spectra at RHIC." In: *Eur. Phys. J. C* 45 (2006), pp. 211–217. DOI: 10.1140/epjc/s2005-02426-3. arXiv: hep-ph/0506189.

[103] S. Agostinelli et al. "GEANT4—a simulation toolkit." In: *Nucl. Instrum. Meth. A* 506 (2003), p. 250. DOI: 10.1016/S0168-9002(03)01368-8.

[104] CMS Collaboration. *CMS Data Aggregation System (DAS)*. Accessed on August 5, 2025. 2025. URL: https://cmsweb.cern.ch/das/.

[105] CMS Collaboration. *HiDilepton Working Area TWiki: CMSSW_11_2_X Setup*. Accessed on August 5, 2025. 2025. URL: https://twiki.cern.ch/twiki/bin/view/CMS/HiDileptonWorkingAreaSetting#CMSSW_11_2_X.

[106] CMS HIN Dilepton Group. *OniaTree Analyzer Configuration for PbPb Prompt Data, CMSSW_11_2_X*. Accessed on August 5, 2025. 2025. URL: https://github.com/CMS-HIN-dilepton/cmssw/blob/OniaTree_11_2_X/HiAnalysis/HiOnia/test/hioniaanalyzer_PbPbPrompt_112X_DATA_cfg.py.

[107] Gurpreet Singh Chahal. *Tutorial for CMS Analysts about Monte Carlo Management (McM) and production Monitoring platform (pMp)*. 2017. URL: https://indico.cern.ch/event/674156/contributions/2758128/attachments/1570281/2476808/Tutorial_for_CMSanalysts_Gurpreet.pdf.

[108] CMS Collaboration. *CMS MC Production Workflow Documentation*. Managed by the CMS PdmV group. Accessed on August 5, 2025. 2025. URL: https://cms-pdmv.gitbook.io/project.

[109] Shengquan Tuo et al. *Centrality and Event Plane Reconstruction for PbPb 2018 Data at 5.02 TeV*. CMS Analysis Note CMS-AN-2018/287. Internal document, for CMS use only. Archive Date: 2020-03-06, Hash: 7ab2ad7. CMS Collaboration, Mar. 2020.

[110] CMS Collaboration. "Measurement of nuclear modification factors of $\Upsilon(1S)$, $\Upsilon(2S)$, and $\Upsilon(3S)$ mesons in PbPb collisions at $\sqrt{s_{NN}} = 5.02$ TeV." In: *Phys. Lett. B* 790 (2019), pp. 270–293. DOI: `10.1016/j.physletb.2019.01.006`.

[111] F. James and M. Roos. "Minuit: A System for Function Minimization and Analysis of the Parameter Errors and Correlations." In: *Comput. Phys. Commun.* 10 (1975), pp. 343–367. DOI: `10.1016/0010-4655(75)90039-9`.

[112] Rene Brun and Fons Rademakers. "ROOT — An object oriented data analysis framework." In: *Nucl. Instrum. Meth. A* 389 (1997), pp. 81–86. DOI: `10.1016/S0168-9002(97)00048-X`.

[113] R. Brun, F. Rademakers, et al. *ROOT Data Analysis Framework, TEfficiency class.* Accessed: 2025-08-19. URL: `https://root.cern.ch/doc/master/classTEfficiency.html`.

[114] Ota Kukral Andre Stahl Emilien Chapon. *Dimuon Performance Studies in 2018 PbPb and 2017 pp 5.02 TeV Data*. CMS Analysis Note CMS-AN-2018/316. Internal document, available on the CMS Information Server. Updated version v5 dated 18 August 2022. CMS Collaboration, Dec. 2018.

[115] CMS HIN Dilepton Group. *MuonAnalysis-TagAndProbe: Tag and Probe weights for PbPb*. Accessed on August 17, 2025. 2020. URL: `https://github.com/CMS-HIN-dilepton/MuonAnalysis-TagAndProbe/blob/62e934924e9a9cc8e47db0d1657c5b57650fc852/macros/tnp_weight_lowptPbPb.h#L535`.

[116] Louis Lyons. *Statistics for Nuclear and Particle Physicists*. Cambridge University Press, 1986. ISBN: 9780521379342. URL: https://cds.cern.ch/record/1023964.

[117] N. L. Johnson. "Systems of Frequency Curves Generated by Methods of Translation." In: *Biometrika* 36.1/2 (1949), pp. 149–176. ISSN: 00063444, 14643510. URL: http://www.jstor.org/stable/2332539 (visited on 09/05/2025).

[118] ROOT Team. *RooJohnson Class Reference*. https://root.cern/doc/v636/classRooJohnson.html. ROOT v6.36 documentation; accessed 2025-09-05.

[119] M. Abramowitz and I. A. Stegun. *Handbook of Mathematical Functions*. Dover Publications, 1972. Chap. 22.3.

[120] ROOT Team. *RooChebychev Class Reference*. https://root.cern.ch/doc/master/classRooChebychev.html. ROOT documentation (RooFit). 2025. (Visited on 09/05/2025).

[121] Vincent Cheung and Ramona Vogt. "Quarkonium polarization in Pb + Pb collisions in the improved color evaporation model." In: *Phys. Rev. C* 105 (2022), p. 055202. DOI: 10.1103/PhysRevC.105.055202.